

Channel Adaptive Waveforms with Homo- or Heterogeneous Configurations per Cell

An FBMC-OQAM based evaluation

Von der Fakultät für Elektrotechnik und Informatik
der Gottfried Wilhelm Leibniz Universität Hannover
zur Erlangung des akademischen Grades
Doktor-Ingenieurin/Doktor-Ingenieur
(abgekürzt: Dr.-Ing.)
genehmigte Dissertation

von

Dipl.-Ing. Martin Fuhrwerk

geboren am 17. Februar 1982
in Wismar

2018

1. Referentin/Referent: Prof. Dr. Jürgen Peissig
 2. Referentin/Referent: Univ.Prof. Dr.techn. Markus Rupp (TU Wien)
- Tag der Promotion: 16 Oktober 2018

What counts in life is not the mere fact that we lived.
It is the difference we have made to the lives of
others that will determine the significance of the life we lead.

— Nelson Mandela (May 18, 2002)

For Marina, Leevke and Thorge who kept me going, as well as
Chris and family rewarding my life in an unexpected manner.

In loving memory of Elli Alma Ottilie Fuhrwerk.

1926 – 2013

ABSTRACT

In the upcoming fifth generation cellular networks, a large variety of application scenarios is planned to be covered. These range from machine-to-machine (M2M) communication with low latency, low data-rate, high reliability and a massive number of devices per cell up to very high capacity applications with data rates greater than 1 Gbit/s for a small amount of users. Due to this, an improved flexibility and efficiency of the deployed communication systems are set into focus to support the severely diverging requirements. One approach to enhance the efficiency is the deployment of waveforms which are more robust against signal spreading due to dispersive communication channels. Here, the filterbank multicarrier approach has been shown to be a promising candidate to replace the state-of-the-art CP-OFDM scheme. Additionally, the waveform of current communication systems is selected to provide the best performance in a certain amount of channel environments. Here, the design of communication systems matching their present channel environment offers some potential gains, as the present-day approach utilizes the available channel capacity sub-optimally.

This thesis proposes and evaluates a new approach to design mobile communication systems called channel adaptive waveforms, in which a systems waveform in terms of subcarrier spacing and prototype filter function is optimized to match the properties of the utilized communication channel. For this purpose, the effects on data and pilot symbols transmitted over doubly dispersive channels are characterized using the (cross-)ambiguity function and the statistical properties of the communication channel. Additionally, prototype filter functions for the filterbank multicarrier system are selected based on their reconstruction performance in doubly dispersive channels. Based on these results, the practical feasibility of the proposed approach is investigated for cellular networks with homogeneous system configurations per cell. Here, all users in a cell utilize the same subcarrier spacing and prototype filter function, whereby each cell is allowed to be configured differently. With the assumption of perfect channel knowledge at the receiver, the evaluation results confirm that this system design provides significant performance gains compared to a “one-fits-all” system design approach as LTE. To obtain insight into the effects of imperfect channel knowledge, a scattered pilot based channel estimation according to the least squares approach is considered. In this regard, the channel estimation error for different scattered pilot schemes proposed in literature is derived and evaluated based on analytical expressions as well as Monte-Carlo simulations. Here, the results show that for the investigated scattered pilot schemes the performance gains of channel adaptive waveforms are

reduced significantly due to residual channel estimation errors. To counteract these performance degradations, some improvements for the scattered pilot schemes are discussed briefly. Based on these results, the channel adaptive waveform approach is extended to a system setup which allows for heterogeneous system configurations per cell. For this, the related channel capacity gains are investigated for both down- and uplink transmissions. In this context, the optimization problem to maximize the capacity within a cell as well as important optimization constraints are proposed and discussed. Simulation results for a selected scenario show that channel adaptive waveforms with heterogeneous system configurations per cell provide a close to optimal channel capacity. Furthermore, the analysis of down- and uplink scenarios proves that the performance of the heterogeneous approach is basically independent from the direction of transmission.

In conclusion, the outcome of this thesis shows that the application of channel adaptive waveforms in communication systems is advantageous compared to the current "one-fits-all" system design approach. For applications with a high range of channel characteristics such as cellular networks, the results indicate that channel adaptive waveforms provide significant performance gains in terms of bit-error-rates and channel capacity without the need for complex receiver structures such as multi-tap equalizers. Due to the excellent localization of the prototype filter functions applied in filterbank multicarrier systems, the amount of required guard bands is very limited. Thus, it is possible to deploy cellular networks which allow user-specific subcarrier spacing and prototype filter functions within in a single cell without sacrificing the performance gains.

Keywords: Channel Adaptive Systems, Filterbank Multicarrier, Channel Capacity, Intrinsic Interference

ZUSAMMENFASSUNG

In den Mobilfunknetzen der kommenden fünften Generation soll eine Vielzahl verschiedener Anwendungsszenarien abgedeckt werden. Diese reichen von Maschinen zu Maschinen (M2M) Kommunikation mit geringer Latenzzeit, niedriger Datenrate, hoher Zuverlässigkeit und einer enormen Anzahl von Geräten pro Zelle bis zu Anwendungen mit sehr hohen Datenraten größer als 1 Gbit/s für eine geringe Anzahl von Nutzern. Aus diesem Grund wird eine verbesserte Flexibilität und Effizienz der eingesetzten Kommunikationssysteme in den Mittelpunkt gestellt, um die extrem unterschiedlichen Anforderungen zu ermöglichen. Ein Ansatz zur Verbesserung der Effizienz ist die Bereitstellung von Wellenformen, die robuster gegen die Signalverbreitung aufgrund von dispersiven Kommunikationskanälen sind. In diesem Zusammenhang wurde gezeigt, dass filterbankbasierte Mehrträgerverfahren vielversprechende Kandidaten sind, um das aktuell vielfach eingesetzte CP-OFDM Schema zu ersetzen. Zudem werden die Wellenformen aktueller Kommunikationssysteme so ausgewählt, dass eine ausreichende Leistung in verschiedenen Umgebungen garantiert ist. An dieser Stelle bietet das Design von Kommunikationssystemen, die an ihre aktuelle Umgebung angepasst sind, potentielle Vorteile, da der gegenwärtige Ansatz die verfügbare Kanalkapazität nicht vollständig ausnutzt.

In dieser Dissertation wird ein neuartiger Ansatz zum Entwurf von mobilen Kommunikationssystemen vorgestellt und evaluiert, der innerhalb dieser Arbeit als kanaladaptive Wellenform bezeichnet wird. Dabei wird die Wellenform eines Systems in Bezug auf Unterträgerabstand und Prototypfilterfunktion passend zu den Eigenschaften des verwendeten Kommunikationskanals optimiert. Zu diesem Zweck werden die Auswirkungen auf Daten- und Pilotsymbole, die über doppel-dispersive Kanäle übertragen werden, unter Verwendung der (Kreuz-)Ambiguityfunktion und der statistischen Eigenschaften des Kommunikationskanals charakterisiert. Zusätzlich werden die Prototypfilterfunktionen für das filterbankbasierte Mehrträgersystem auf Basis ihrer Rekonstruktionsperformanz in doppel-dispersiven Kanälen ausgewählt. Von diesen Ergebnissen ausgehend wird die praktische Relevanz des vorgeschlagenen Ansatzes für zelluläre Netze mit homogenen Systemkonfigurationen pro Zelle untersucht. Bei diesem Ansatz verwenden alle Benutzer in einer Zelle den gleichen Unterträgerabstand und die gleichen Prototypfunktionen, wobei jede Zelle eines Netzwerks anders konfiguriert werden kann. Für die Annahme einer perfekten Kanalkennntnis beim Empfänger bestätigen die Evaluationsergebnisse, dass dieses Designkonzept signifikante Leistungssteigerungen im Vergleich zu einem "One-fits-all"-Designansatz wie LTE bietet. Um einen Einblick in die Auswirkungen von

unvollkommenem Kanalwissen zu erhalten, wird eine Kanalschätzung mit verteilten Piloten nach der Methode der kleinsten Quadrate in Betracht gezogen. Hierfür wird der Kanalschätzungsfehler für verschiedene in der Literatur vorgeschlagene Schemata von verteilten Piloten hergeleitet und basierend auf analytischen Ausdrücken sowie Monte-Carlo-Simulationen bewertet. Die entsprechenden Ergebnisse für die untersuchten Schemata zeigen, dass die Leistungssteigerungen von kanaladaptiven Wellenformen aufgrund von Restfehlern der Kanalschätzung signifikant reduziert sind. Um diesen Leistungsverschlechterungen entgegenzuwirken, werden einige Verbesserungen für Systeme mit verteilten Piloten diskutiert. Basierend auf diesen Ergebnissen wird der bisherige Ansatz der kanaladaptiven Wellenform erweitert, um heterogene Systemkonfigurationen pro Zelle zu ermöglichen. Dazu werden die zugehörigen Kapazitätsgewinne sowohl für Down- als auch Uplink-Übertragungen untersucht. In diesem Zusammenhang wird das Optimierungsproblem zur Maximierung der Kapazität innerhalb einer Zelle vorgestellt sowie wichtige Randbedingungen diskutiert. Simulationsergebnisse für ein ausgewähltes Szenario zeigen, dass kanaladaptive Wellenformen mit heterogenen Systemkonfigurationen pro Zelle eine nahezu optimale Kanalkapazität bereitstellen. Darüber hinaus zeigt die Analyse von Down- und Uplink-Szenarien, dass die Performanz des heterogenen Ansatzes prinzipiell unabhängig von der Übertragungsrichtung ist.

Zusammenfassend zeigen die Ergebnisse dieser Arbeit, dass die Anwendung von kanaladaptiven Wellenformen in Kommunikationssystemen vorteilhaft im Vergleich zum aktuellen "One-fits-all" Ansatz ist. Für Anwendungen mit stark heterogenen Kanaleigenschaften wie beispielsweise zelluläre Netze zeigen die Ergebnisse, dass kanaladaptive Wellenformen signifikante Leistungssteigerungen in Bezug auf Bitfehlerraten und Kanalkapazität bereitstellen, ohne komplexe Empfängerstrukturen wie Multi-tap Entzerrer zu benötigen. Aufgrund der exzellenten Lokalisierung der Prototypfilterfunktionen, die in filterbankbasierten Mehrträgersystemen angewendet werden, ist die Menge der erforderlichen Schutzbänder sehr begrenzt. Somit ist es möglich, zelluläre Netze zu implementieren, die nahezu ohne Kapazitätsverluste nutzerspezifische Unterträgerabstände und Prototypfilterfunktionen innerhalb einer einzelnen Zelle ermöglichen.

Schlagwörter: Kanalangepasste Systeme, Filterbankbasierte Mehrträgerverfahren, Kanalkapazität, Intrinsische Interferenz

CONTENTS

GLOSSARY OF SYMBOLS	xi
GLOSSARY OF ACRONYMS	xxv
I DISSERTATION	1
1 INTRODUCTION	3
1.1 Motivation	3
1.2 Thesis contribution and outline	4
2 FUNDAMENTALS OF MULTICARRIER SYSTEMS AND PROBLEM DESCRIPTION	7
2.1 Mobile communication systems	7
2.1.1 Communication channels	8
2.1.2 Modeling of data transmission	10
2.1.3 System design for imperfect transmission conditions	13
2.1.4 Classification of MC modulation schemes	15
2.1.5 Arising research question	18
2.2 Related work	19
2.2.1 Channel Adaptive Modulation and coding (CAM)	19
2.2.2 Channel Adaptive Loading (CAL)	20
2.2.3 Channel Adaptive Waveform (CAW)	20
2.3 Problem statement	21
3 SYSTEM MODEL, PFFs AND SIR	23
3.1 Discrete-time transmission model	23
3.2 Representation of demodulated symbols	24
3.2.1 FBMC-OQAM	27
3.2.2 (CP-)OFDM	28
3.3 Pulse shaping	29
3.3.1 PHYDYAS	31
3.3.2 EGF based IOTA	31
3.3.3 Hermite	36
3.3.4 Rectangular (CP-OFDM)	36
3.4 Reconstruction performance	39
3.4.1 CP-OFDM	39
3.4.2 FBMC-OQAM	39
3.5 Considerations on the SIR in doubly dispersive channels	41
3.6 Concluding remarks	46
4 CAW WITH HOMOGENEOUS CONFIGURATIONS PER CELL	49
4.1 Reconstruction performance	49
4.2 System level performance with perfect CSIR	52
4.2.1 Considerations for the practical relevance of the SIR gains	53

4.2.2	Influence of channel equalization	55
4.3	Channel capacity	59
4.4	CAW with imperfect Channel State Information at the Receiver (CSIR)	62
4.4.1	Scattered pilots based on AP	65
4.4.2	Scattered pilots based on DS	70
4.4.3	System level simulations	75
4.5	Concluding remarks	79
5	CAW WITH HETEROGENEOUS CONFIGURATIONS PER CELL	81
5.1	Heterogeneous CAW in cellular DL	82
5.1.1	System model	83
5.1.2	Channel capacity gains	85
5.2	Heterogeneous CAW in cellular UL	92
5.2.1	System model	93
5.2.2	Channel capacity gains	94
5.3	Concluding remarks	98
6	CONCLUSIONS AND FUTURE WORKS	99
II APPENDIX		101
A	MULTICARRIER SYSTEMS	103
A.1	Inherent orthogonality for real and even symmetric PFFs	103
A.2	Derivation of the received demodulated symbol	104
A.3	Mean interference power of received symbol	106
A.4	Symbol modulation for scattered pilots	107
A.5	Co-user symbol and subcarrier offsets	108
B	CHANNEL MODELING	111
B.1	Harmonization of channel models	111
B.2	Channel scenarios	111
B.3	Considerations for Monte-Carlo simulations	112
C	DS SCHEME RELATED DERIVATIONS	115
C.1	Channel estimation error for DS scheme	115
C.2	Channel estimation error dependencies in the DS scheme	118
C.3	DS scheme matrices	120
C.3.1	General solution	121
C.3.2	Solution specific to isotropic PFFs	122
BIBLIOGRAPHY		125
INDEX		137
LIST OF FIGURES		139
LIST OF TABLES		140
SCIENTIFIC CAREER		143
LIST OF PUBLICATIONS		145

GLOSSARY OF SYMBOLS

Greek Symbols		
Symbol	Set	Description
α	\mathbb{R}	Spreading parameter for PFFs based on EGF.
$\alpha_{\mu,\kappa}[\tau, \nu], \alpha[\tau, \nu]$	\mathbb{R}	Effective ambiguity functions in AP and DS scheme.
$\underline{\alpha}[\tau_l, \nu]$	$\mathbb{C}^{1 \times \Lambda}$	Vector of ambiguity function values for specific channel path delay τ_l and frequency offset ν .
$\underline{\alpha}_p^{\tilde{k}}[\tau_l, \nu], \underline{\alpha}_p^{\tilde{k}'}[\tau_l, \nu]$	$\mathbb{C}^{1 \times \Lambda}$	Vector of phase-shifted ambiguity function values for specific channel path delay τ_l and frequency offset ν .
β	\mathbb{R}	Direction parameter of a PFF.
β_{norm}	\mathbb{R}	Direction parameter of a PFF normalized to the lattice grid.
β_λ	\mathbb{R}	Weighting coefficient for calculation of auxiliary symbol in DS scheme. Element of $\underline{\beta}$.
$\underline{\beta}$	$\mathbb{R}^{1 \times \Lambda - 1}$	Weighting coefficient vector for calculation of auxiliary symbol in DS scheme.
γ	\mathbb{N}^+	Overlapping factor in PFF design.
γ_f	\mathbb{R}^+	Fairness factor for capacity optimization in heterogeneous CAW scenarios.
δ	\mathbb{R}	Delay-Doppler product of a communication channel, i.e. $\delta = \tau_{\text{rms}} f_D$.
$\delta_{x,y}$	\mathbb{N}	Kronecker-Delta with respect to x and y .
$\delta(t), \delta[n]$	\mathbb{N}	Continuous- and discrete-time Dirac delta function.
$\Delta \varepsilon_C, \Delta \varepsilon_H$	\mathbb{R}	Cancellation and channel estimation error ratio of AP and DS scheme.
$\varepsilon_{H,x}$	\mathbb{R}	Channel estimation error (MSE) for scheme x .
$\varepsilon_{C,x}$	\mathbb{R}	Cancellation error (MSE) induced by symbols considered in interference mitigation scheme x .
$\varepsilon_{T,x}$	\mathbb{R}	Residual channel estimation error (MSE) induced by symbols not considered in scheme x .

Greek Symbols (cont.)

Symbol	Set	Description
$\varepsilon_{H,a}^{DS}$	\mathbb{R}	Part of the channel estimation error induced by auto-correlation of a specific symbol.
$\varepsilon_{H,c}^{DS}$	\mathbb{R}	Part of the channel estimation error induced by cross-correlation of a specific symbol with another spread data symbol.
$\varepsilon_{H,max}$	\mathbb{R}	Approximated upper channel estimation error bound for a throughput utilization $> 90\%$ for a specific MCS.
ζ_u	\mathbb{N}	Frequency domain oversampling factor of user u , i.e. $\zeta_u = K_v K_u / \nu_0$.
$\theta_{m,k}, \theta_\lambda$	\mathbb{C}	Phase shift to establish/remove real-field orthogonality in FBMC-OQAM, i.e. $\theta_{m,k} = j^{m+k}$.
κ, κ'	\mathbb{Z}	Subcarrier index offset.
κ_λ	\mathbb{Z}	Subcarrier index offset for symbol with index λ in DS scheme.
κ_a	\mathbb{Z}	Subcarrier index offset of the auxiliary pilot symbol $\rho_{m,k}$.
λ, λ'	\mathbb{N}	Symbol index for spread symbols of the DS scheme, i.e. $\lambda : \{\lambda = 1, \dots, \Lambda\} \rightarrow \{(\mu, \kappa)_\lambda\}$.
Λ	\mathbb{N}	Number of spread symbols for DS scheme.
μ, μ'	\mathbb{Z}	MC symbol index offset.
μ_a	\mathbb{Z}	MC symbol index offset of the auxiliary pilot symbol $\rho_{m,k}$.
ν	\mathbb{R}	Normalized frequency (offset), i.e. $\nu = fT_s$.
ν_0	\mathbb{R}	Normalized subcarrier spacing (normalized to $1/T$).
ν_u	\mathbb{R}	Normalized CFO of user u .
$\nu_{u,u'}$	\mathbb{R}	Normalized frequency offset between users u and u' .
ξ	\mathbb{R}	Heisenberg-Gabor uncertainty or T-F-uncertainty, $0 < \xi \leq 1$.
$\rho_{m,k}$	\mathbb{R}	Transmitted auxiliary pilot symbol.
$\tilde{\rho}_{\tilde{m},\tilde{k}}$	\mathbb{C}	Observed channel-distorted (without noise) auxiliary pilot symbol.
$\rho_{\tilde{m},\tilde{k}}$	\mathbb{C}	Observed ideal (without channel and noise) auxiliary pilot symbol.

Greek Symbols (cont.)

Symbol	Set	Description
σ_t, σ_f	\mathbb{R}	Dispersion (standard deviation) of a PFF in time and frequency domain.
σ_β^2	\mathbb{R}	Amplification factor of average auxiliary data symbol power for DS scheme, i.e. $\sigma_\beta^2 = \sigma_{DS}^2 / \sigma_d^2$.
$\sigma_{AP}^2, \sigma_{DS}^2$	\mathbb{R}	Average power of auxiliary data symbol for AP and DS schemes.
σ_d^2, σ_p^2	\mathbb{R}	Average power of data and pilot symbols.
σ_S^2	\mathbb{R}	Average power of received unequalized data and pilot symbols.
σ_I^2	\mathbb{R}	Average interference power of received unequalized data and pilot symbols.
$\sigma_{\mu, \mu'}^{\kappa, \kappa'}(\tilde{m}, \tilde{k})$	\mathbb{C}	Element of system dependent channel cross-correlation matrix.
τ	\mathbb{Z}	Discrete-time channel path delay, i.e. $t_\Delta = \tau T_s$.
τ_l	\mathbb{Z}	Discrete-time channel path delay of channel tap l .
τ_0	\mathbb{R}	Normalized MC symbol period (normalized to T).
$\bar{\tau}$	\mathbb{R}	Continuous-time mean delay of the propagation channel.
τ_{\max}	\mathbb{R}	Continuous-time maximum excess delay of the propagation channel.
τ_{rms}	\mathbb{R}	Continuous-time delay spread of the propagation channel.
τ_s	\mathbb{Z}	Discrete-time STO induced by synchronization.
τ_u	\mathbb{R}	Discrete-time STO offset of user u .
$\tau_{u, u'}$	\mathbb{R}	Time offset between users u and u' .
$\phi_p(\tilde{k}, \mu, \kappa)$	\mathbb{C}	Lattice position (μ, κ) depended phase shifts of ambiguity function.
$\phi_d(\tilde{k}, \tau_l), \phi_d(\kappa, \tau_l)$	\mathbb{C}	Channel delay τ_l depended phase shift of ambiguity function.
\underline{X}_λ	$\mathbb{R}^{1 \times \Lambda}$	λ -th row vector of spreading matrix \underline{C} .
\underline{X}	$\mathbb{R}^{\Lambda \times \Lambda}$	Covariance matrix of spread data symbols in DS scheme.
$\underline{X}_1, \underline{X}_2$	$\mathbb{R}^{x \times y}$	Partial matrices of covariance matrix \underline{X} . The dimension depends on the applied spreading matrix \underline{C} and the applied PFF.

Latin Symbols

Symbol	Set	Description
$\mathbf{a}_{m,k}$ ($\mathbf{a}_{u,m,k}$), \mathbf{a}_λ	\mathbb{R} or \mathbb{C}	Transmitted data or pilot symbol (of user u).
$\tilde{\mathbf{a}}_{\tilde{m},\tilde{k}}$ ($\tilde{\mathbf{a}}_{u,\tilde{m},\tilde{k}}$)	\mathbb{C}	Observed channel-distorted (without noise) data or pilot symbol (of user u).
$\hat{\mathbf{a}}_{\tilde{m},\tilde{k}}$	\mathbb{C}	Observed equalized (without noise) data or pilot symbol.
$\check{\mathbf{a}}_{\tilde{m},\tilde{k}}$ ($\check{\mathbf{a}}_{u,\tilde{m},\tilde{k}}$)	\mathbb{C}	Desired part of observed channel-distorted (without noise) data or pilot symbol $\tilde{\mathbf{a}}_{\tilde{m},\tilde{k}}$ ($\tilde{\mathbf{a}}_{u,\tilde{m},\tilde{k}}$).
$A[\tau, \nu]$	\mathbb{C}	Discrete-time ambiguity function.
$A_{\mu,\kappa}[\tau, \nu]$, $A_\lambda[\tau, \nu]$	\mathbb{C}	Discrete-time ambiguity function for a specific symbol offset (μ, κ) , i.e. $A_{\mu,\kappa}[\tau, \nu] = A[\mu M_0 + \tau, \kappa K_0 + \nu]$.
$A_{\mu,\kappa}^k[\tau, \nu]$, $A_\lambda^k[\tau, \nu]$	\mathbb{C}	Subcarrier k specific phase-shifted discrete-time ambiguity function.
$A_{\tilde{m},\tilde{k}}^{u,u'}[\tau, \nu]$	\mathbb{C}	Discrete-time (cross-)ambiguity function between users u and u' . For $u = u'$, $A_{\tilde{m},\tilde{k}}^{u,u'}[\tau, \nu] = A_{\tilde{m},\tilde{k}}[\tau, \nu]$.
$\underline{\mathbf{a}}$	$\mathbb{R}^{\Lambda \times 1}$	Vector of spread data symbols.
b	\mathbb{R}	Pilot boost factor (power).
B	\mathbb{R}	Bandwidth mode of LTE system.
$B(f, f_\Delta)$	\mathbb{C}	Continuous-time Doppler-variant transfer function.
B_c	\mathbb{R}	Coherence bandwidth of a communication channel.
$\underline{\mathbf{B}}$	$\mathbb{R}^{\Lambda \times \Lambda}$	Reduced covariance matrix of data symbols to be spread with DS scheme, i.e. $\underline{\mathbf{B}} = \underline{\mathbf{B}}_I - \underline{\mathbf{I}}_\Lambda$.
$\underline{\mathbf{B}}_I$	$\mathbb{R}^{\Lambda \times \Lambda}$	Covariance matrix of data symbols to be spread with DS scheme.
$c_{\lambda,\lambda'}$	\mathbb{R}	Element of spreading matrix $\underline{\mathbf{C}}$.
C	\mathbb{R}	Normalized channel capacity according to the Shannon-Hartley-Theorem in bit/s/Hz.
C_g (\bar{C}_g)	\mathbb{R}	Gain (bound) in terms of normalized channel capacity in relation to an FBMC-OQAM system with LTE parametrization.
C_{eff}	\mathbb{R}	Efficiency of capacity gain utilization, i.e. $C_{\text{eff}} = C_g / \bar{C}_g$.

Latin Symbols (cont.)

Symbol	Set	Description
$C_{\text{LTE}}^{s_c}$	\mathbb{R}	Normalized channel capacity of an FBMC-OQAM system with LTE parametrization for channel scenario s_c .
$C_{\text{opt}}^{s_c}$	\mathbb{R}	Normalized channel capacity of an FBMC-OQAM system with homogeneous CAW and optimal parametrization for channel scenario s_c .
$C_{u,\text{opt}}$	\mathbb{R}	Normalized channel capacity of an FBMC-OQAM system with heterogeneous CAW and optimal parametrization for channel a given scenario.
$C_{\text{opt}}(\mathbf{u})$	\mathbb{R}	Normalized channel capacity of user (group) \mathbf{u} of an FBMC-OQAM system with heterogeneous CAW and optimal parametrization for a given channel scenario.
C_{ref}	\mathbb{R}	Reference cell capacity to determine C_g in a heterogeneous CAW scenario.
$C_{\bar{m},\bar{k}}$	\mathbb{R}	Interference (amplitude) induced by symbols considered by interference mitigation scheme.
C_s, C_o	\mathbb{R}	Slope and ordinate intercept of linear function.
\underline{c}_λ	$\mathbb{R}^{\wedge \times 1}$	λ -th column vector of spreading matrix \underline{C} .
\underline{C}	$\mathbb{R}^{\wedge \times \wedge}$	Spreading matrix in DS scheme.
d_λ	\mathbb{R}	Data symbols to be spread in DS scheme.
d_Λ	\mathbb{R}	Auxiliary data symbol of DS scheme.
\underline{d}	$\mathbb{R}^{\wedge \times 1}$	Vector of data symbols to be spread in DS scheme.
$D(\tau, \nu)$ ($D_u(\tau, \nu)$)	\mathbb{C}	Discrete-time Doppler-variant channel impulse response or spreading function (of user \mathbf{u}).
$f[n]$ ($f_u[n]$)	\mathbb{R}	Discrete-time PFF (of user \mathbf{u}), i.e. $f[n] := f(nT_s); -\gamma K/2 \leq n < \gamma K/2$
f_c	\mathbb{R}	Carrier frequency.
$f_k[n]$ ($f_{u,k}[n]$)	\mathbb{C}	Discrete-time PFF $f[n]$ (of user \mathbf{u}) modulated to subcarrier k .
$f_k(t)$	\mathbb{C}	Continuous-time PFF $f(t)$ modulated to subcarrier k .

Latin Symbols (cont.)

Symbol	Set	Description
$f_{m,k}$	\mathbb{C}	Transmitter “T-F logon”; Continuous- or discrete-time T-F shifted version of PFF $f(t)$.
f_d	\mathbb{R}	Doppler shift.
f_Δ	\mathbb{R}	Frequency offset (in ACFs).
f_D	\mathbb{R}	Maximum Doppler shift.
\bar{f}_d	\mathbb{R}	Mean Doppler shift.
$f_{d,rms}$	\mathbb{R}	Doppler spread.
F_0	\mathbb{R}	Subcarrier spacing, i.e. $F_0 = \nu_0/T$; Spans lattice grid in frequency domain.
F'_0	\mathbb{R}	Effective subcarrier spacing for forced orthogonality in staggered lattice modulation schemes, i.e. $F'_0 = 2F_0$.
\mathbb{F}	\mathbb{R}	Set of PFF $f_u[n]$, i.e. $\forall u \in \mathcal{U} : f_u[n] \in \mathbb{F}$.
$g[n]$	\mathbb{R}	Discrete-time receiver PFF, i.e. $g[n] := g(nT_s)$; $-\gamma K/2 \leq n < \gamma K/2$.
$g(t)$	\mathbb{R}	Continuous-time receiver PFF.
$g_{\tilde{k}}[n]$ ($g_{u,\tilde{k}}[n]$)	\mathbb{C}	Discrete-time receive PFF $g[n]$ (of user u) modulated to subcarrier \tilde{k} .
$g_{m,k}$	\mathbb{C}	Receiver “T-F logon”; Continuous- or discrete-time T-F shifted version of PFF $g(t)$.
$g_\alpha[n]$	\mathbb{R}	Discrete-time square root of Gaussian function with spreading parameter α .
$h[\tau, n]$ ($h_u[\tau, n]$)	\mathbb{C}	Discrete-time time-variant channel impulse response (of user u).
$h(\Delta t, t)$	\mathbb{C}	Continuous-time time-variant channel impulse response.
$h_l[n]$	\mathbb{C}	Discrete-time time-variant attenuation coefficient of channel tap l .
$H(f, t)$	\mathbb{C}	Continuous-time time-variant CTF or T-F transfer function.
$H_{\tilde{m},\tilde{k}}(\mu, \kappa)$	\mathbb{C}	Observed system dependent frequency domain channel coefficient for symbol and subcarrier offset μ and κ .

Latin Symbols (cont.)

Symbol	Set	Description
$H_{\tilde{m},\tilde{k}}^{u,u'}(\mu, \kappa)$	\mathbb{C}	By user u observed system dependent frequency domain channel coefficient for symbol and subcarrier offset μ and κ transmitted in DL for user u' .
$\mathcal{H}_{\tilde{m},\tilde{k}}^{u,u'}(\mu, \kappa)$	\mathbb{C}	For user u observed system dependent frequency domain channel coefficient for symbol and subcarrier offset μ and κ transmitted in UL by user u' .
$H_{\tilde{m},\tilde{k}}(m, k)$	\mathbb{C}	Observed system dependent frequency domain channel coefficient for data symbols transmitted at MC symbol m and subcarrier k .
$\tilde{H}_{\tilde{m},\tilde{k}}$	\mathbb{C}	Estimated system dependent frequency domain channel coefficient.
$\hat{H}_{\tilde{m},\tilde{k}}$	\mathbb{C}	Effective frequency domain channel coefficient for symbols considered for interference mitigation by AP scheme.
i, i'	\mathbb{Z}	General indexing variable.
$i_{\tilde{m},\tilde{k}}(i_{u,\tilde{m},\tilde{k}})$	\mathbb{C}	Intrinsic interference part of observed channel-distorted (without noise) data or pilot symbol $\tilde{a}_{\tilde{m},\tilde{k}}$ (of user u).
$\hat{i}_{\tilde{m},\tilde{k}}$	\mathbb{C}	Intrinsic interference part of channel-distorted (without noise) data or pilot symbol used to evaluate the reconstruction performance in FBMC-OQAM systems.
\mathbf{I}_Λ	$\mathbb{N}^{\Lambda \times \Lambda}$	Identity matrix of size Λ .
k	\mathbb{N}^+	Subcarrier index, $k = 1, \dots, K$, $k = K$ corresponds to center (DC) subcarrier.
\tilde{k}	\mathbb{N}^+	Subcarrier index for demodulation.
K	\mathbb{N}^+	Overall number of subcarriers, even valued.
K_0	\mathbb{R}	Normalized subcarrier spacing, i.e. $K_0 = \nu_0 T_s / T = \nu_0 / K$.
K_r	\mathbb{R}	Ratio of spectrum allocated for two different users.
K_u	\mathbb{R}	Normalized subcarrier spacing of user u , i.e. $K_u = \nu_0 T_s / T_u = \nu_0 \zeta_u / K_v$.
K_v	\mathbb{N}^+	Overall number of virtual subcarriers, i.e. $\forall u : K_v = \nu_0 \zeta_u / K_u$.
$\mathbb{K} (\mathbb{K}_u)$	\mathbb{N}^+	Set of allocated subcarriers (of user u).

Latin Symbols (cont.)

Symbol	Set	Description
\mathbb{K}_u^I	\mathbb{N}^+	Initial set of allocated subcarriers of user u .
$\tilde{\mathbb{K}} (\tilde{\mathbb{K}}_u)$	\mathbb{Z}	Set of subcarrier offsets (of user u).
$\mathbb{K}_g^{u,u'}$	\mathbb{N}	Number of virtual guard carriers used as guard band between users u and u' .
l	\mathbb{Z}	Discrete-time channel tap index.
L	\mathbb{N}^+	Number of channel taps.
L_t	\mathbb{R}	PDP truncation factor.
L_p	\mathbb{N}^+	Discrete-time PFF length.
$L_H(\Delta t, \Delta f)$	\mathbb{R}	Auto-correlation function of time-variant transfer function $H(f, t)$, i.e. $L_H(\Delta t, \Delta f) = \mathbb{E}[H(f, t)H^*(f - \Delta f, t - \Delta t)]$. Also known as time-frequency correlation function.
m	\mathbb{Z}	MC symbol index for modulation.
\tilde{m}	\mathbb{Z}	MC symbol index for demodulation.
M	\mathbb{N}^+	Modulation order of M -QAM.
M_0	\mathbb{N}^+	Discrete-time MC symbol period, i.e. $M_0 = \tau_0 T / T_s = \tau_0 K$.
M_u	\mathbb{N}^+	Discrete-time MC symbol period of user u , i.e. $M_u = \tau_0 / K_u = \tau_0 K_v / (\nu_0 \zeta_u)$.
$\mathbb{M} (\mathbb{M}_u)$	\mathbb{Z}	Set of allocated MC symbols (of user u).
$\tilde{\mathbb{M}} (\tilde{\mathbb{M}}_u)$	\mathbb{Z}	Set of MC symbol offsets μ (of user u).
n	\mathbb{Z}	Discrete-time sample index, i.e. $t = nT_s$.
$n(t)$	\mathbb{C}	Additive noise.
$n_{\tilde{m}, \tilde{k}}$	\mathbb{C}	Filtered additive noise at demodulated symbol $\tilde{a}_{\tilde{m}, \tilde{k}}$.
N_{bin}	\mathbb{N}^+	Number of bins to represent a given signal in frequency domain with a certain accuracy.
$N_{\text{bin, DPSD}}$	\mathbb{N}^+	Number of bins to represent a given Doppler PSD with a certain accuracy.
$N_{\text{Byte}, x}$	\mathbb{N}^+	Number of bytes required to store x .
N_P	\mathbb{N}^+	Number of different sampling patterns of the cross-ambiguity function in heterogeneous CAW scenarios.

Latin Symbols (cont.)

Symbol	Set	Description
N_{CIR}	\mathbb{N}^+	Number of samples per channel tap to represent the time-variant channel impulse response $h[\tau, n]$.
N_{H}	\mathbb{N}^+	Number of considered isotropic Hermite functions for calculation of the Hermite PFF.
σ_{T}	\mathbb{R}	Scaling factor of base symbol duration for heterogeneous CAW.
\underline{O}_x	$\mathbb{N}^{x \times x}$	Zero matrix of size x .
$p_{m,k}$	\mathbb{R}	Transmitted pilot symbol.
$\tilde{p}_{\tilde{m},\tilde{k}}$	\mathbb{C}	Observed channel-distorted (without noise) pilot symbol.
$p_{\tilde{m},\tilde{k}}$	\mathbb{C}	Observed ideal (without channel and noise) pilot symbol.
$p[n]$	\mathbb{R}	Discrete-time base functions for derivation of the PFFs.
$P_{\text{D}}(\Delta f), P_{\text{D}}(\nu)$	\mathbb{R}	Continuous- and discrete time Doppler power spectral density.
$P_{\text{h}}(\Delta t), P_{\text{h}}(\tau)$	\mathbb{R}	Continuous- and discrete time power delay profile.
$\mathcal{P}_{\mu,\kappa}^{u,u'}$	\mathbb{R}	Average power collected in DL by user u on symbol position (\tilde{m}, \tilde{k}) from relative lattice position (μ, κ) allocated by user u' .
$\mathcal{P}_{\mu,\kappa}^{u,u'}$	\mathbb{R}	Average power collected in UL for user u on symbol position (\tilde{m}, \tilde{k}) from relative lattice position (μ, κ) allocated by user u' .
$q_x, q_{i,\alpha,\nu_0}, q_{i',1/\alpha,\tau_0}$	\mathbb{R}	Weighting factors used in PFF calculations.
$r[n] (r_u[n])$	\mathbb{C}	AFB input signal in discrete-time domain (of user u), i.e. $r[n] := r(nT_s)$.
$r(t)$	\mathbb{C}	AFB input signal in continuous-time domain.
r_1, r_2, r_3	\mathbb{C}	Values of effective ambiguity functions at data positions for DS scheme.
$R_{\tilde{m},\tilde{k}}$	\mathbb{R}	Interference (amplitude) induced by symbols not considered by interference mitigation scheme.
\underline{R}	$\mathbb{R}^{x \times y}$	Rotation matrix.
$s[n] (s_u[n])$	\mathbb{C}	SFB output signal in discrete-time domain (of user u), i.e. $s[n] := s(nT_s)$.

Latin Symbols (cont.)

Symbol	Set	Description
$s(t)$	\mathbb{C}	SFB output signal in continuous-time domain.
s_c	$\{A, B, C\}$	Specific channel scenario (see Appendix B.2).
$s_{c,u}$	$\{A, B, C\}$	Channel scenario specific to user u (see Appendix B.2).
$\tilde{s}_{\tilde{m},\tilde{k}}$	\mathbb{C}	Channel-distorted (without noise) data or pilot symbol used to evaluate the reconstruction performance in FBMC-OQAM systems.
$\check{s}_{\tilde{m},\tilde{k}}$	\mathbb{C}	Desired part of channel-distorted (without noise) data or pilot symbol used to evaluate the reconstruction performance in FBMC-OQAM systems.
$S(\Delta t, \Delta f), S(\tau, \nu)$	\mathbb{R}	Continuous- and discrete-time channel scattering function, i.e. $S(\tau, \nu) = \mathbf{E}[D(\tau, \nu) ^2]$.
\mathcal{S}	$\mathbb{Z}^{ \tilde{\mathcal{M}} \times \tilde{\mathcal{K}} }$	Set of lattice position tuples (μ, κ) of allocated symbols, i.e. $\mathcal{S} = \tilde{\mathcal{M}} \times \tilde{\mathcal{K}}$.
\mathcal{S}_u	$\mathbb{Z}^{ \tilde{\mathcal{M}}_u \times \tilde{\mathcal{K}}_u }$	Set of lattice position tuples (μ, κ) of symbols allocated by user u , i.e. $\mathcal{S}_u = \tilde{\mathcal{M}}_u \times \tilde{\mathcal{K}}_u$.
\mathcal{S}_N	\mathbb{Z}	Set of lattice position tuples (μ, κ) of allocated symbols neighboring the reference symbol, i.e. $\mathcal{S}_N = \mathcal{S} \setminus (0, 0)$.
$\mathcal{S}_{N,u}$	\mathbb{Z}	Set of lattice position tuples (μ, κ) of user u of allocated symbols neighboring the reference symbol, i.e. $\mathcal{S}_{N,u} = \mathcal{S}_u \setminus (0, 0)$.
\mathcal{S}_C	$\mathbb{Z}^{x \times y}$	Set of lattice position tuples (μ, κ) of allocated symbols considered in the interference mitigation scheme, i.e. $\mathcal{S}_C \subseteq \mathcal{S}_N$.
\mathcal{S}_R	$\mathbb{Z}^{x \times y}$	Set of lattice position tuples (μ, κ) of allocated symbols not considered in the interference mitigation scheme, i.e. $\mathcal{S}_R = \mathcal{S}_N \setminus \mathcal{S}_C$.
SINR_e	\mathbb{R}	Tolerated SINR error for a specific modulation order.
SIR	\mathbb{R}	SIR after the demodulation process.
SIR_{ZF}	\mathbb{R}	SIR after ZF equalization.
t	\mathbb{R}	Continuous-time time variable.
t_d	\mathbb{R}	Continuous-time channel path delay.
t_Δ	\mathbb{R}	Continuous-time time offset (in ACFs).
T	\mathbb{R}	MC symbol duration, i.e. $T = K T_s$.

Latin Symbols (cont.)

Symbol	Set	Description
T_{LTE}	\mathbb{R}	MC symbol duration of LTE, i.e. $T_{\text{LTE}} = 66.7 \mu\text{s}$.
T_{opt}	\mathbb{R}	MC symbol duration optimized to match the channel properties.
T_{c}	\mathbb{R}	Coherence time of the communication channel.
$T_{\text{CP}}, T_{\text{ZP}}$	\mathbb{R}	Duration of CP and ZP.
T_{s}	\mathbb{R}	Sampling period at SFB output and AFB input.
T_{u}	\mathbb{R}	MC symbol duration of user u .
T_0	\mathbb{R}	Continuous-time transmit period of MC symbols, i.e. $T_0 = \tau_0 T$; Spans lattice grid in time domain.
T'_0	\mathbb{R}	Effective continuous-time transmit period for forced orthogonality in staggered lattice modulation schemes, i.e. $T'_0 = 2T_0$.
\mathbb{T}	$\mathbb{Z}^{ \mathbb{M} \times \mathbb{K} }$	Set of lattice position tuples (m, k) of allocated symbols, i.e. $\mathbb{T} = \mathbb{M} \times \mathbb{K}$.
\mathbb{T}_{u}	$\mathbb{Z}^{ \mathbb{M}_{\text{u}} \times \mathbb{K}_{\text{u}} }$	Set of lattice position tuples (m, k) of allocated symbols for user u , i.e. $\mathbb{T}_{\text{u}} = \mathbb{M}_{\text{u}} \times \mathbb{K}_{\text{u}}$.
\mathbb{T}_{s}	\mathbb{R}	Set of symbol durations T_{u} , i.e. $\forall u \in \mathbb{U} : T_{\text{u}} \in \mathbb{T}_{\text{s}}$.
u, u'	\mathbb{N}^+	User (group) index.
\mathbb{U}	\mathbb{N}^+	Set of users (or user groups).
$u_{u, \tilde{m}, \tilde{k}}$	\mathbb{C}	Co-user interference part of observed channel-distorted (without noise) data or pilot symbol $\tilde{a}_{\tilde{m}, \tilde{k}}$ of user u .
$\mathbb{U}_{\text{c}, u}$	\mathbb{N}^+	Set of co-users of user u , i.e. $\mathbb{U}_{\text{c}, u} = \mathbb{U} \setminus u$.
v	\mathbb{R}	User velocity.
$x_{\lambda, \lambda'}$	\mathbb{R}	Element of Covariance matrix \underline{X} .

Mathematical symbols, constants, functions and operators

Symbol	Description
e	Eulers number.
j	Imaginary unit, i.e. $j = \sqrt{-1}$.
π	Number Pi.
c	Speed of light.
$*$	Linear convolution operator.
\Leftrightarrow	Equivalence of equations.
\times	Cartesian product of sets.
\propto	Indicator for proportionality.
\in, \notin	Element of, not element of.
\wedge	Logical AND operator.
\uparrow_x	Upsampling by the factor of x .
\downarrow_x	Downsampling by the factor of x .
(x, y)	Ordered pair or 2-tuple.
$(x, y)_z$	Indexed 2-tuple, i.e. $z : \{1, \dots, Z\} \rightarrow \{(x, y)_z\}; A_z \equiv A_{x, y}$.
x^*	Complex conjugate of x .
\underline{x}^T	Transpose of \underline{x} .
\underline{x}^H	Conjugate transpose of \underline{x} .
$\underline{A} \setminus \underline{B}$	Relative complement of \underline{A} with respect to set \underline{B} , i.e. $\underline{A} \setminus \underline{B} = \{x \in \underline{A} \mid x \notin \underline{B}\}$.
$ x $	Absolute value of x .
$ \mathbb{X} $	Cardinality of set \mathbb{X} .
$\lceil x \rceil$	Map x to subsequent integer $y \in \mathbb{Z}$ with $x \leq y < x + 1$.
$[y, z]$	Closed interval, i.e. $[x, y] = \{x \mid y \leq x \leq z\}$.
$]y, z[$	Open interval, i.e. $]x, y[= \{x \mid y < x < z\}$.
$\langle x, y \rangle$	Inner product of $x(z)$ and $y(z)$, i.e. $\int x(z)y^*(z)dz$.
$E[x]$	Expected value of x .
$T_{t_\Delta} F_{f_\Delta}$	T-F shift operator.
H	T-F dispersive channel operator.
$m_x\{y(z)\}$	x -th normalized moment of function $y(z)$, i.e. $m_x\{y(z)\} = (\int z^x y(z) dz) / (\int y(z) dz)$.

Mathematical symbols, constants, functions and operators (cont.)

Symbol	Description
$\mathbf{M}_x\{y(z)\}$	x -th normalized central moment of function $y(z)$, i.e. $\mathbf{M}_x\{y(z)\} = (\int (z - \mathbf{m}_1\{y(z)\})^x y(z) dz) / (\int y(z) dz)$.
$\mathbf{R}_x(y, y', z, z')$	ACF of function $x(y, z)$.
$\mathbf{C}_{wx}(y, y', z, z')$	CCF of functions $w(y, z)$ and $x(y, z)$.
$\text{sinc } x$	Cardinal sine (sinc), $\text{sinc } x = \frac{\sin \pi x}{\pi x}$.
$\log_y x$	Logarithm of x with base y .
$\text{cov}(X, Y)$	Covariance of random processes X and Y , i.e. $\text{cov}(X, Y) = \mathbf{E}[X] \mathbf{E}[Y] - \mathbf{E}[XY]$.
$\arg \max_x y(x)$	Get argument x which maximizes function $y(x)$.
$\arg \min_x y(x)$	Get argument x which minimizes function $y(x)$.
$\inf\{\mathbf{X}\}$	Infimum (lower bound) of set \mathbf{X} .
$\sup\{\mathbf{X}\}$	Supremum (upper bound) of set \mathbf{X} .
$\Re\{x\}, \Im\{x\}$	Real and imaginary parts of x .
$\mathcal{F}_x\{f(x, y)\}$	Continuous-time Fourier transform of function $f(x, y)$ over x .
$\mathcal{F}_x\{f[x, y]\}$	DTFT of function $f[x, y]$ over x .
$\mathcal{F}_x^{-1}\{f(x, y)\}$	Continuous-time inverse Fourier transform of function $f(x, y)$ over x .
$\mathcal{F}_x^{-1}\{f[x, y]\}$	Inverse DTFT of function $f[x, y]$ over x .
$\mathbb{N}, \mathbb{Z}, \mathbb{Q}, \mathbb{R}, \mathbb{C}$	Sets of natural, integer, rational, real and complex numbers.
\mathbb{N}^+	Set of natural numbers excluding zero, i.e. $\mathbb{N}^+ = \mathbb{N} \setminus \{0\}$.
\mathbb{R}^+	Set of non-negative real numbers, i.e. $\mathbb{R}^+ = \{x \in \mathbb{R} : x \geq 0\}$.
$\mathbb{L}^2(\mathbb{R})$	Lebesgue space of the 2-norm for real valued functions.

GLOSSARY OF ACRONYMS

3GPP	3rd Generation Partnership Project
5G	5th Generation
ACF	AutoCorrelation Function
AFB	Analysis FilterBank
AP	Auxiliary Pilot
ASB	Adaptive Subcarrier Bandwidth
AWGN	Additive White Gaussian Noise
BER	Bit Error Rate
BIIM	Basic Iterative Interference Mitigation
BPSK	Binary Phase-Shift Keying
CAL	Channel Adaptive Loading [per subcarrier]
CAM	Channel Adaptive Modulation and coding
CAPS	Channel Adaptive Pulse Shaping
CASS	Channel Adaptive Subcarrier Spacing
CAW	Channel Adaptive Waveform
CCF	CrossCorrelation Function
CFO	Carrier Frequency Offset
CIR	Channel Impulse Response
CMT	Cosine-modulated MultiTone
CP	Cyclic Prefix
CP-OFDM	Cyclic Prefix Orthogonal Frequency-Division Multiplexing
CPP	Composite Pilot Pairs
CSI	Channel State Information
CSIR	Channel State Information at the Receiver
CTF	Channel Transfer Function
DFT	Discrete Fourier Transform
DFT-s-OFDM	DFT-spread OFDM
DL	DownLink
DPSD	Doppler Power Spectral Density

DRM	Digital Radio Modiale
DS	Data Spreading
DTFT	Discrete-Time Fourier Transform
DVB	Digital Video Broadcasting
DVB-T	Terrestrial Digital Video Broadcasting
DVB-T2	2nd generation Terrestrial Digital Video Broadcasting
EGF	Extended Gaussian Function
FBMC	FilterBank MultiCarrier
FBMC-OQAM	FBMC with OQAM subcarrier modulation
FBMC/OQAM	Synonym for FBMC-OQAM
FBMC-QAM	FBMC with QAM subcarrier modulation
FD	Frequency Domain
FER	Frame Error Rate
FFT	Fast Fourier Transform
FFT-FBMC	FBMC-OQAM with FFT precoding
FMT	Filtered MultiTone
F-OFDM	Filtered OFDM
FTN	Faster Than Nyquist
GFDM	Generalized Frequency-Division Multiplexing
HTx	Hilly Terrain channel model
i.i.d.	independent and identically distributed
IBI	Inter-Block Interference
ICI	Inter-Carrier Interference
IOTA	Isotropic Orthogonal Transform Algorithm
ISI	Inter-Symbol Interference
LDPC	Low Density Parity Check
LOFDM	Lattice-OFDM
LS	Least Squares
LTE	Long-Term Evolution
M2M	Machine-to-Machine
MAC	Medium Access Control
MC	MultiCarrier
MCS	Modulation and Coding Scheme

MIMO	Multiple-Input Multiple-Output
MMSE	Minimum Mean-Squared Error
MSE	Mean-Squared Error
MTC	Machine-Type Communication
MU	Multi-User
NC-OFDM	Non-Contiguous OFDM
OFDM	Orthogonal Frequency-Division Multiplexing
OOB	Out-Of-Band
OQAM	Offset Quadrature Amplitude Modulation
OFDM/OQAM	Synonym for FBMC-OQAM
OFDM-OQAM	Synonym for FBMC-OQAM
OQAM-OFDM	Synonym for FBMC-OQAM
OQAM/OFDM	Synonym for FBMC-OQAM
PAM	Pulse Amplitude Modulation
PAPR	Peak-to-Average Power Ratio
PC	Pilot Clustering
PDP	Power Delay Profile
PPF	Prototype Filter Function
P-OFDM	Pulse-shaped OFDM
PHYDYAS	PHYSical layer for DYnamic spectrum AccesS and cognitive radio
PPN	PolyPhase Network
POP	Pairs of Pilots
PSD	Power Spectral Density
QAM	Quadrature Amplitude Modulation
QAM-FBMC	FBMC with QAM subcarrier modulation
QoS	Quality of Service
RAM	Random Access Memory
Rax	Rural area channel model
RC	Raised Cosine
RLC	Radio Link Control
RRC	[square]Root Raised Cosine
RX	Receiver
SC-FDMA	Single-Carrier Frequency-Division Multiple Access

SFB	Synthesis FilterBank
sinc	Cardinal sine
SINR	Signal-to-Interference-plus-Noise Ratio
SIR	Signal-to-Interference Ratio [or reconstruction performance]
SMT	Staggered MultiTone
SNR	Signal-to-Noise Ratio
STO	Symbol Timing Offset
TD	Time Domain
TDMA	Time-Division Multiple Access
T-F	Time-Frequency
Tux	Typical urban channel model
TX	Transmitter
UFMC	Universal-Filtered MultiCarrier
UL	UpLink
US	Uncorrelated Scattering
VDSL	Very high speed Digital Subscriber Line
VSB	Vestigial Side-Band modulation
WH	Weyl-Heisenberg
WiMAX	Worldwide Interoperability for Microwave Access
WLAN	Wireless Local Area Network
w.r.t.	with respect to
WSS	Wide Sense Stationary
WSSUS	Wide Sense Stationary Uncorrelated Scattering
ZF	Zero Forcing
ZP	Zero-Padded
ZP-OFDM	Zero-Padded OFDM

Part I
DISSERTATION

INTRODUCTION

An ever growing demand for high data rates with the ubiquitous need for mobility drives recent wireless communication systems to deliver adequate solutions. Besides the application of multiple antenna scheme technologies as well as establishing an increased cell density, an efficient utilization of available time and frequency resources can provide a significant contribution towards a more efficient utilization of spectrum. An additional critical issue for upcoming mobile communication systems is the increased demand for flexibility and efficiency necessary to support heterogeneous system requirements to use the scarce and expensive spectrum as efficient as possible [48, 74, 108]. Nowadays, MultiCarrier (MC) systems such as Long-Term Evolution (LTE) [60], Terrestrial Digital Video Broadcasting (DVB-T) [22] and Wireless Local Area Networks (WLANs) [47] are based on Cyclic Prefix Orthogonal Frequency-Division Multiplexing (CP-OFDM) [10, 84] and have been designed to provide an optimal trade-off between spectral efficiency and high Quality of Service (QoS) over a wide range of different channel scenarios. For future mobile communication systems, this “one-fits-all” approach no longer is favored [74], as this approach only provides a suboptimal trade-off between system capacity and robustness. Additionally, its performance in terms of capacity degrades considerably if a system is not operating in one of the target channel scenarios.

1.1 MOTIVATION

One approach to enhance mobile communication systems is the utilization of modulation schemes with the capability of Channel Adaptive Pulse Shaping (CAPS). This has been proven to maximize the system capacity for a given symbol duration and subcarrier configuration [55]. For this, modulation schemes allowing the usage of arbitrary Prototype Filter Functions (PFFs) such as Generalized Frequency-Division Multiplexing (GFDM) [31], FBMC with OQAM subcarrier modulation (FBMC-OQAM) [93] and Universal-Filtered MultiCarrier (UFMC) [99] are required. These schemes also have been considered for the upcoming 5th Generation (5G) cellular network [25, 87, 107]. Additionally, utilizing proper PFFs allows to reduce side lobes significantly and thus improves the coexistence capabilities of mobile communication systems with adjacent or in-band interferers [100].

However, the PFF applied for CAPS cannot be spread arbitrarily in time or frequency domain to prevent increased latency or out-of-band emission. Thus, the performance gains achieved by CAPS are limited. A design paradigm for CP-OFDM systems with Time-Division Multiple Access (TDMA) called Adaptive Subcarrier Bandwidth (ASB) which

overcomes this limitation has been proposed by Das et al. [16]. Here, the subcarrier bandwidth for a given time slot is adapted in dependence on the user velocity.

1.2 THESIS CONTRIBUTION AND OUTLINE

A joint application of both Channel Adaptive Subcarrier Spacing (CASS) and CAPS to mobile communication systems called Channel Adaptive Waveforms (CAWs) allows for an increased flexibility in system design. Additionally, PFFs with reduced side lobes in combination with inter-user guard bands enable the deployment of heterogeneous system configurations per time slot. Thus, an increased flexibility in user and resource scheduling is supported which is a crucial aspect in cellular radio systems. To support the research of CAW, this thesis contributes analytical and simulation based results for FBMC-OQAM and CP-OFDM systems operating in doubly dispersive channels which are summarized in the following.

- *A novel system design concept for homo- and heterogeneous channel scenarios¹ per cell is proposed that combats system performance degradations induced by doubly dispersive channels.*
- *The measure “reconstruction performance” (Signal-to-Interference Ratio (SIR) after the Analysis FilterBank (AFB)) is introduced and compared to the equivalent Signal-to-Interference-plus-Noise Ratio (SINR) after channel equalization.*
- *Numerical performance gains for homogeneous CAW applied to FBMC-OQAM systems are provided and compared to the performance of classical CP-OFDM systems based on LTE parameters.*
- *The cell-wide capacity gains for homo- and heterogeneous CAW configurations are evaluated for perfect synchronization at receiver side to verify the CAW concept.*
- *The applicability of CAW in the presence of imperfect channel knowledge based on channel estimation by use of scattered pilots is evaluated for selected schemes of interference mitigation on pilot symbols. Therefore, closed form expressions for the channel estimation error are derived.*
- *The co-user interference for heterogeneous CAW in DownLink (DL) and UpLink (UL) transmissions is analyzed and the amount of inter-user guard-bands is determined.*

These contributions are described in the remaining part of this thesis, which is organized as follows.

¹ For simplicity, in this thesis CAW scenarios with only one system configuration per cell are referred to as homogeneous CAW, whereas scenarios with individual configuration per user or user group are referred to as heterogeneous CAW.

In Chapter 2 a theoretical survey on the theory of Gabor frames and MC communication systems is provided. Then, the optimal system design in doubly dispersive channels is discussed, followed by a classification of well known and frequently discussed MC modulation schemes. The chapter concludes with the formulation of the research question, a discussion of the related work and the presentation of the problem statement.

In Chapter 3, generic system and channel models for Staggered MultiTone (SMT) based MC systems are introduced, followed by a description of PFFs suggested for FBMC-OQAM systems. Finally, the reconstruction performance for FBMC-OQAM and CP-OFDM systems is defined and some considerations on the parameter space investigated within this thesis are given.

In Chapter 4 the performance gains in terms of the reconstruction performance of the AFB, uncoded Bit Error Rate (BER) as well as channel capacity are evaluated for homogeneous CAW assuming perfect channel knowledge. Then, based on these results the impact of imperfect channel knowledge at the receiver is studied for scattered pilot based channel estimation for different schemes of interference mitigation on pilot symbols. Therefore, analytical expressions for the channel estimation error are derived, compared with Monte-Carlo simulation based results and the performance limitations are analyzed. Afterwards, different techniques for channel estimation performance enhancements are discussed and evaluated.

In Chapter 5 the application of CAW to cells with heterogeneous channel scenarios and thus heterogeneous system configurations per cell is evaluated for cellular DL and UL transmissions. Therefore, the system model from Chapter 3 is extended to derive analytical expressions for the calculation of the co-user interference. Additionally, the optimization problem to maximize the capacity per cell is formulated and different optimization constraints are discussed. Subsequently, the capacity gains for selected scenarios and the required amount of inter-user guard bands are determined.

In Chapter 6 the outcome of this thesis is summarized and an outlook on future work is provided.

FUNDAMENTALS OF MULTICARRIER SYSTEMS AND PROBLEM DESCRIPTION

In this chapter a brief survey on the theory of mobile communication systems is provided. This comprises important properties of the communication channel considered in this thesis and an introduction to Gabor or Weyl-Heisenberg (WH) frames. Additionally, design constraints for mobile communication systems are presented and various current MC schemes are reviewed. Afterwards, the research question for this thesis is formulated and the related work is discussed. The chapter is concluded by the presentation of the problem statement.

2.1 MOBILE COMMUNICATION SYSTEMS

To enable a well-founded design of communication systems, it is necessary to understand the fundamentals of the physical behavior of the transmission medium, i.e. the propagation channel and impairments of the channel access technology, e.g. oscillator imperfections, as well as their impact on the transmitted signal. Neglecting the receiver noise it can be shown, that for a given transmit signal $s(t)$ which is distorted by a linear propagation channel, the received signal $r(t)$ can be described by a weighted superposition of Time-Frequency (T-F) shifts of $s(t)$ [41, 62]:

$$r(t) = \iint D(t_d, f_d) s(t - t_d) e^{j2\pi f_d t} df_d dt_d, \quad (2.1a)$$

where $D(t_d, f_d)$ is the channel spreading function which characterizes the complex weight associated to a specific delay t_d and Doppler shift f_d . An alternative representation based on operators is given by

$$r(t) = (\mathbf{H}s)(t) \quad (2.1b)$$

$$= \iint D(t_d, f_d) (\mathbf{T}_{t_d} \mathbf{F}_{f_d} s)(t) df_d dt_d, \quad (2.1c)$$

where (2.1b) with the T-F dispersive channel operator \mathbf{H} is also known as the basic input-output relation of a T-F dispersive channel [62]. The operator $\mathbf{T}_{t_d} \mathbf{F}_{f_d}$ is used to represent the time and Doppler shifts:

$$(\mathbf{T}_{t_d} \mathbf{F}_{f_d} s)(t) = s(t - t_d) e^{j2\pi f_d t}. \quad (2.1d)$$

2.1.1 Communication channels

Besides the channel spreading function $D(t_d, f_d)$, which characterizes the energy spread of a communication channel in the delay-Doppler domain, the channel can be described in the T-F domain by calculating the two-dimensional Fourier transform of the spreading function $D(t_d, f_d)$ as follows [6]:

$$H(f, t) = \iint D(t_d, f_d) e^{-j2\pi(ft_d - tf_d)} dt_d df_d. \quad (2.2)$$

The resulting time-variant Channel Transfer Function (CTF) $H(t, f)$ can be interpreted as the time-dependent attenuation factor of a specific frequency component of a signal transmitted through this channel. Performing a one-dimensional (inverse) Fourier transform of either $D(t_d, f_d)$ or $H(t, f)$, one obtains the time-variant Channel Impulse Response (CIR) $h(t_d, t)$

$$h(t_d, t) = \int D(t_d, f_d) e^{j2\pi tf_d} df_d \quad (2.3a)$$

$$= \int H(f, t) e^{j2\pi ft_d} df \quad (2.3b)$$

and the Doppler-variant CTF $B(f, f_d)$

$$B(f, f_d) = \int D(t_d, f_d) e^{-j2\pi ft_d} dt_d \quad (2.4a)$$

$$= \int H(f, t) e^{-j2\pi tf_d} dt. \quad (2.4b)$$

Thereby, the time-variant CIR $h(t_d, t)$ characterizes the signal attenuation of a certain propagation path t_d at a specific time t and the Doppler-variant transfer function $B(f, f_d)$ defines the frequency f specific Doppler shift f_d .

These characteristic functions of propagation channels can be used, if the investigation of a specific channel realization is of interest. For real channels, this can be assumed for most wired connections, where in general the channel characteristics, e.g. propagation delay, frequency and/or mode dispersion, are quasi-static over time and known beforehand or can be easily obtained by measurements. However, this is not true for mobile communication channels and phenomenon as hardware dependent time and frequency offsets as well as phase noise, as these are strongly dependent on environmental parameters such as location, temperature and time. Therefore, the characteristic functions described before are often modeled by two-dimensional random processes. Most of practical channels are Wide Sense Stationary (WSS) over a sufficient area [6, 40, 63, 67], so that the AutoCorrelation Function (ACF) \mathbf{R}_H of the T-F transfer function $H(f, t)$, i.e. the T-F

correlation function $L_H(f_\Delta, t_\Delta)$, only depends on the time and frequency offsets t_Δ and f_Δ and not the current time t and frequency f , respectively:

$$\begin{aligned} \mathbf{R}_H(f, f + f_\Delta, t, t + t_\Delta) &= \mathbf{E}[H(f, t)H^*(f - f_\Delta, t - t_\Delta)] \\ &= L_H(f_\Delta, t_\Delta). \end{aligned} \quad (2.5)$$

Thus, the second order statistics of the WSS propagation channels are constant. Additionally, for most communication channels the different scatterers are uncorrelated (Uncorrelated Scattering (US)) [6, 40, 63, 67]. With the Dirac delta function $\delta(t_d - t'_d)$ the ACF \mathbf{R}_D of the channel spreading function $D(t_d, f_d)$ yields

$$\begin{aligned} \mathbf{R}_D(t_d, t'_d, f_d, f'_d) &= \mathbf{E}[D(t_d, f_d)D^*(t'_d, f'_d)] \\ &= S(t_d, f_d)\delta(t_d - t'_d)\delta(f_d - f'_d), \end{aligned} \quad (2.6)$$

whereby $S(t_d, f_d)$ is known as the channel scattering function. As for the deterministic system functions $D(f_d, t_d)$ and $H(f, t)$, the second order moments $S(t_d, f_d)$ and $L_H(f_\Delta, t_\Delta)$ of the statistical propagation channel are related via a two-dimensional Fourier transform [6, 40, 63, 67]

$$S(t_d, f_d) = \iint L_H(f_\Delta, t_\Delta) e^{-j2\pi(f_d t_\Delta - t_d f_\Delta)} dt_\Delta df_\Delta. \quad (2.7)$$

The Wide Sense Stationary Uncorrelated Scattering (WSSUS) property of many communication channels is an important simplification in communication theory, as it reduces the complexity of system descriptions and thus simplifies their analysis.

As the second order moments for WSSUS channels still depend on two parameters, for the derivation of channel models it has been shown to be practical to derive functions which only depend on one parameter. This is done by calculation of the Power Delay Profile (PDP) and the Doppler Power Spectral Density (DPSD), which are used to characterize and define channel models, cf. [11, 20, 26]. The PDP $P_h(t_d)$ defines the average power received on a propagation path with delay t_d irrespective of any Doppler shifts. Accordingly, the DPSD $P_D(f_d)$ describes the average power distribution in dependence of a Doppler shift f_d . To calculate the PDP and DPSD of a channel, several solutions have been proposed in literature [67]. Here, the PDP $P_h(t_d)$ and DPSD $P_D(f_d)$ are calculated based on the channel scattering function $S(t_d, f_d)$ according to

$$\text{PDP:} \quad P_h(t_d) = \int S(t_d, f_d) df_d \quad (2.8a)$$

$$\text{DPSD:} \quad P_D(f_d) = \int S(t_d, f_d) dt_d. \quad (2.8b)$$

For some practical channels it can be reasonable to use a propagation path specific description of the DPSD, e.g. [26]. However, although the derivations in this thesis are appli-

cable to channels with arbitrary PDP and DPSD definitions, the results presented in this thesis are based on channel models with only one DPSD function, e.g. [20].

Usually, different channels are compared based on a few key parameters, which provide a rough idea about the time and frequency domain characteristics of the propagation channel. In time domain, these are the mean delay $\bar{\tau}$, the delay spread τ_{rms} and the maximum excess delay τ_{max} , which are given by [67]

$$\begin{aligned}\bar{\tau} &= \mathbf{m}_1\{P_h(t_d)\} \\ &= \frac{\int P_h(t_d)t_d dt_d}{\int P_h(t_d) dt_d}\end{aligned}\quad (2.9a)$$

$$\begin{aligned}\tau_{\text{rms}} &= \sqrt{\mathbf{M}_2\{P_h(t_d)\}} \\ &= \sqrt{\frac{\int P_h(t_d)t_d^2 dt_d}{\int P_h(t_d) dt_d} - \bar{\tau}^2}\end{aligned}\quad (2.9b)$$

$$\tau_{\text{max}} = \sup\{t_d \in \mathbb{R} \mid P_h(t_d) > 0\}.\quad (2.9c)$$

Here, \mathbf{M}_2 and \mathbf{m}_1 are the normalized 2nd-order central and normalized 1st-order moments. The corresponding frequency domain characteristics are the mean Doppler shift \bar{f}_d , the Doppler spread $f_{d,\text{rms}}$ and the maximum Doppler shift f_D , which can be calculated according to [67]:

$$\begin{aligned}\bar{f}_d &= \mathbf{m}_1\{P_D(f_d)\} \\ &= \frac{\int P_D(f_d)f_d df_d}{\int P_D(f_d) df_d}\end{aligned}\quad (2.9d)$$

$$\begin{aligned}f_{d,\text{rms}} &= \sqrt{\mathbf{M}_2\{P_D(f_d)\}} \\ &= \sqrt{\frac{\int P_D(f_d)f_d^2 df_d}{\int P_D(f_d) df_d} - \bar{f}_d^2}\end{aligned}\quad (2.9e)$$

$$f_D = \max\left\{\left|\inf\{f_d \in \mathbb{R} \mid P_D(f_d) > 0\}\right|, \sup\{f_d \in \mathbb{R} \mid P_D(f_d) > 0\}\right\}.\quad (2.9f)$$

In Figure 2.1, the subset of characteristic functions and parameters of channels used within this thesis and their relationships are depicted. A complete overview of all characteristic functions, parameters and their relationships is provided in [51, 67].

2.1.2 Modeling of data transmission

In 1946, Gabor proposed the usage of T-F shifts of a PFF $f(t) \in \mathbb{L}^2(\mathbb{R})$, so called ‘‘T-F logons’’ $f_{m,k}$ [38], to model the modulation of independent and identically distributed (i.i.d.) data symbols $a_{m,k}$ onto communication signals (e.g. [8, 45, 54, 62, 64, 83]):

$$s(t) = \sum_{(m,k) \in \mathbb{T}} a_{m,k} f_{m,k}.\quad (2.10)$$

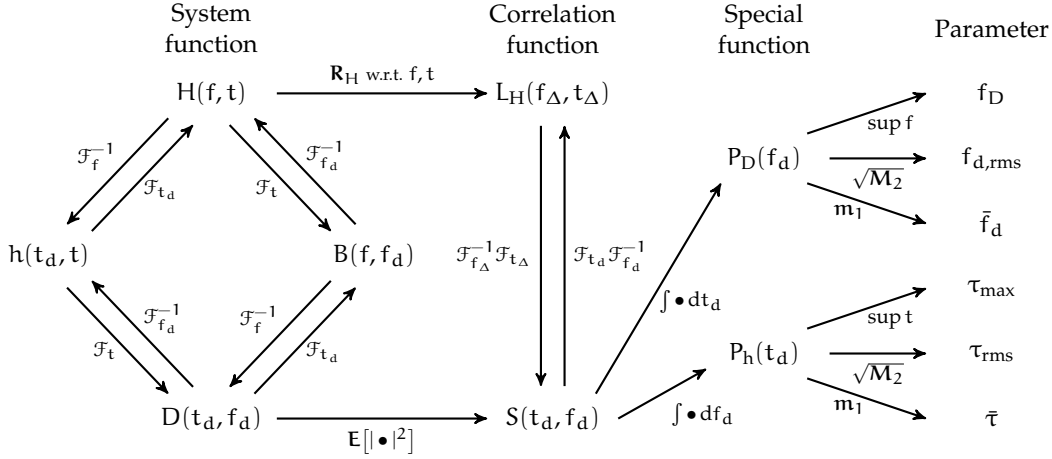


Figure 2.1: Subset of characteristic functions, parameters and relationships of WSSUS communication channels used within this thesis. A complete picture is provided in [51, 67].

Here, T_0 and F_0 are the symbol period and subcarrier spacing, which define the sampling positions or lattice grid of the T-F plane as depicted in Figure 2.2. $m \in \mathbb{M}$ and $k \in \mathbb{K}$ are the symbol and subcarrier indices out of the sets of allocated symbols \mathbb{M} and subcarriers \mathbb{K} , respectively. For the sake of generality it is assumed that $\forall m \in \mathbb{M} : \mathbb{K} = \text{const.}$, such that $\mathbb{T} = \mathbb{M} \times \mathbb{K}$ denotes the set of transmit position tuples (m, k) . The “T-F logon” $f_{m,k}$ is given by

$$\begin{aligned} f_{m,k} &= (\mathbf{T}_{mT_0} \mathbf{F}_{kF_0} f)(t) \\ &= f(t - mT_0) e^{j2\pi k F_0 (t - mT_0)}, \end{aligned} \quad (2.11)$$

whereby the set of all T-F shifts of $f(t)$, i.e. $\{f_{m,k}\}_{m,k \in \mathbb{Z}}$, is also known as a WH set [62]. To demodulate the transmitted data symbol in the receiver at symbol and subcarrier index \tilde{m} and \tilde{k} , the inner product of the received signal with T-F shifts $g_{\tilde{m},\tilde{k}}(t) = (\mathbf{T}_{\tilde{m}T_0} \mathbf{F}_{\tilde{k}F_0} g)(t)$ of a receiver PFF $g(t) \in \mathbb{L}^2(\mathbb{R})$ has to be calculated. Thus, the received symbol $\tilde{a}_{\tilde{m},\tilde{k}}$ is obtained by

$$\begin{aligned} \tilde{a}_{\tilde{m},\tilde{k}} &= \langle r, g_{\tilde{m},\tilde{k}} \rangle \\ &= \int r(t) g_{\tilde{m},\tilde{k}}^* dt. \end{aligned} \quad (2.12)$$

Without loss of generality, any system exposed to a T-F or doubly dispersive channel $h(t_\Delta, t)$ and additive noise $n(t)$, the received symbol can be separated into a desired part $\check{a}_{\tilde{m},\tilde{k}}$, an interference part $i_{\tilde{m},\tilde{k}}$ and filtered noise $n_{\tilde{m},\tilde{k}}$:

$$\tilde{a}_{\tilde{m},\tilde{k}} = \check{a}_{\tilde{m},\tilde{k}} + i_{\tilde{m},\tilde{k}} + n_{\tilde{m},\tilde{k}}, \quad (2.13)$$

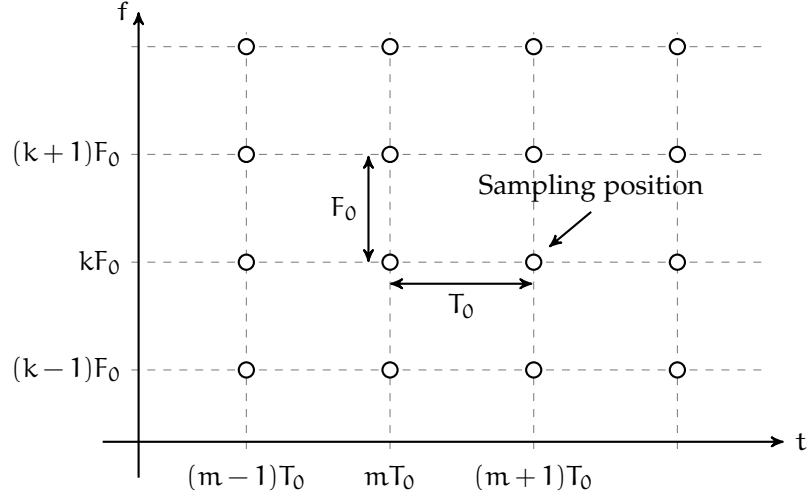


Figure 2.2: Sampling of the T-F plane.

with

$$\check{a}_{\tilde{m},\tilde{k}} = a_{\tilde{m},\tilde{k}} \langle \mathbf{H}f_{\tilde{m},\tilde{k}}, g_{\tilde{m},\tilde{k}} \rangle \quad (2.14a)$$

$$i_{\tilde{m},\tilde{k}} = \sum_{(m,k) \in \{\mathbb{T} \setminus (\tilde{m},\tilde{k})\}} a_{\tilde{m},\tilde{k}} \langle \mathbf{H}f_{m,k}, g_{\tilde{m},\tilde{k}} \rangle \quad (2.14b)$$

and

$$n_{\tilde{m},\tilde{k}} = \langle \mathbf{n}, g_{\tilde{m},\tilde{k}} \rangle. \quad (2.14c)$$

A fundamental design constraint in the absence of noise is the maximization of $\check{a}_{\tilde{m},\tilde{k}}$ and the minimization of $i_{\tilde{m},\tilde{k}}$ with assumption of a perfect propagation channel, i.e. $h(t_\Delta, t) = \delta(t)$ such that $\check{a}_{\tilde{m},\tilde{k}} = a_{m,k}$. This is guaranteed in case $f_{m,k}$ and $g_{\tilde{m},\tilde{k}}$ satisfy the biorthogonality condition:

$$\langle f_{m,k}, g_{\tilde{m},\tilde{k}} \rangle = \delta_{m-\tilde{m},k-\tilde{k}}, \quad (2.15)$$

where $\delta_{m-\tilde{m},k-\tilde{k}}$ is the Kronecker-Delta with respect to $m - \tilde{m}$ and $k - \tilde{k}$. This is also known as the Nyquist constraints [28]. For $a_{m,k} \in \mathbb{C}$, biorthogonality can only be established for $T_0 F_0 \geq 1$, which may be a drawback during system design, as the capacity of a communication system is maximized for a critically sampled lattice grid, i.e. $T_0 F_0 = 1$ [54]. However, the Balian-Low theorem [18] induces that it is not possible to design well-localized PFFs for $a_{m,k} \in \mathbb{C}$ and $T_0 F_0 = 1$, which can be matched to the channel spreading function $D(t_\Delta, f_\Delta)$ to minimize $i_{\tilde{m},\tilde{k}}$ (cf. [28] and Section 2.1.3). Instead, for $T_0 F_0 = 1$ the Balian-Low theorem dictates the application of badly localized PFFs, e.g. sinus cardinalis and rectangular functions, which have the drawback of a poor energy containment in

time or frequency domain and suffer from the inability to match the channel spreading function $D(t_\Delta, f_\Delta)$ [83].

A solution to overcome the restrictions induced by the Balian-Low theorem, i.e. to design communication systems with a critically sampled lattice grid in combination with a well-localized PFF, is the staggering of lattices for real valued data symbols ($a_{m,k} \in \mathbb{R}$) and usage of even symmetric PFFs, i.e. $f(t) = f(-t)$ and $g(t) = g(-t)$ [8, 9, 19, 29, 55]. Lattice staggering stands for the separation and T-F shifted transmission of the In- and Quadrature-Phase, i.e. cosine and sine, components of a signal. As shown in Appendix A.1, even symmetric PFFs provide the property of inherent orthogonality in either the real- or imaginary-field, regardless of the exact shape of the PFFs. However, the lattice positions providing real or imaginary orthogonality are not distributed uniformly (cf. Figure A.1). Therefore, to enable lattice staggering the lattice positions $(2m, 2k)$ have to be forced to be zero by an appropriate PFF design, which results in the effective subcarrier spacing F'_0 and symbol duration T'_0 given by

$$F'_0 = 2F_0 \quad (2.16a)$$

$$T'_0 = 2T_0. \quad (2.16b)$$

For the analysis of the relationship between PFF properties and lattice grid density, the Balian-Low theorem only considers lattice positions, and thus the related T-F product, with orthogonality forced by PFF design. With use of even symmetric PFFs the resulting effective T-F product is $F'_0 T'_0 = 2$. Thus, well-localized PFFs can be applied to each deployed lattice. As the lattices of both the In- and Quadrature-phase components are orthogonal to each other, both can be transmitted simultaneously, as long as a time offset of T_0 is applied. Consequently, lattice staggering allows the application of well-localized PFFs and the maximum channel capacity can still be utilized [83].

2.1.3 System design for imperfect transmission conditions

As mentioned before, a fundamental constraint in the design of communications systems is the maximization of the power ratio between the information bearing signal part and the incurred interference and noise. In general, the transmitted data as well as the interference and noise can be assumed to be stochastic processes. Therefore, the design constraint also well known as SINR yields

$$\text{SINR} = \frac{\mathbf{E}\left[|\check{a}_{\check{m},\check{k}}|^2\right]}{\mathbf{E}\left[|\check{i}_{\check{m},\check{k}}|^2\right] + \mathbf{E}\left[|\check{n}_{\check{m},\check{k}}|^2\right]}. \quad (2.17)$$

Assuming interference free transmission, i.e. $i_{\bar{m},\bar{k}} = 0$, it can be shown that the Signal-to-Noise Ratio (SNR) is maximized for $g(t) = f(t)$ ¹, which is known as matched filtering [40, 67]. On the other hand, for doubly dispersive channels it can be beneficial to design bi-orthogonal PFFs $g(t) \neq f(t)$ to minimize $\mathbb{E}[|i_{\bar{m},\bar{k}}|^2]$ [54].

To achieve a robust transmission over doubly dispersive channels, without a statement on the amount of potential gains (or losses in case of a non-optimal configuration), previous studies proved that the direction parameter $\beta \in [0, \infty)$ of a PFF used for pulse shaping as well as the selection of the lattice grid defined by T_0 and F_0 should match the statistical properties of the channel environment as follows [28, 54, 55, 62, 83]:

$$\text{lattice adaptation:} \quad \frac{T_0}{F_0} \propto \frac{\tau_{\text{rms}}}{f_D} \quad (2.18a)$$

$$\text{PFF adaptation:} \quad \beta \propto \frac{\tau_{\text{rms}}}{f_D}. \quad (2.18b)$$

The direction parameter β determines the energy spread of a PFF in the T-F plane. It is defined by [24]

$$\beta = \frac{\sigma_t}{\sigma_f}, \quad (2.19a)$$

with

$$\sigma_t = \sqrt{\mathbf{M}_2\{|f(t)|\}} \quad (2.19b)$$

and

$$\sigma_f = \sqrt{\mathbf{M}_2\{|\mathcal{F}_t\{f(t)\}|\}}, \quad (2.19c)$$

where σ_t and σ_f are the standard deviation (or dispersion) of the applied PFF in time- and frequency domain, respectively. An alternative definition of the direction parameter is the normalized direction parameter β_{norm} , which represents the energy spread of a PFF in relation to the lattice grid. It is defined according to

$$\beta_{\text{norm}} = \frac{\beta}{\frac{T_0}{F_0}} = \frac{\sigma_t F_0}{T_0 \sigma_f}. \quad (2.19d)$$

¹ Here, the matched filter is defined for demodulation by use of the inner product (cf. (2.12)). This definition differs from the common convolution based demodulation $\tilde{a}_{\bar{m},\bar{k}} = (r(t) * g_{\bar{m},\bar{k}}) \downarrow_T$, for which $g(t) = f^*(-t)$.

To avoid confusion, in this thesis the terms *isotropic*, *Time Domain (TD) spread* and *Frequency Domain (FD) spread* PFF refer to the normalized direction parameter β_{norm} :

$$\begin{aligned} \text{isotropic:} & \quad \beta_{\text{norm}} = 1 \\ \text{TD spread:} & \quad \beta_{\text{norm}} > 1 \\ \text{FD spread:} & \quad \beta_{\text{norm}} < 1. \end{aligned}$$

The exact relation for lattice and PFF adaptation depends on the statistic of the target channels as well as the lattice grid structure and PFF. For rectangular lattice grids and Gaussian PFF, which is not (bi-)orthogonal and thus not the optimal choice for MC modulation schemes, in literature the following conditions are derived for flat fading channels (2.20a) [30], uniform PDP and DPSD (2.20b) [27] and exponential PDP with Jakes DPSD (2.20c) [27]:

$$S(t_d, f_d) = \delta(t_d)\delta(f_d) \quad \Rightarrow \quad \beta = \frac{\tau_{\text{max}}}{f_D} \quad (2.20a)$$

$$S(t_d, f_d) = \frac{1}{2\tau_{\text{max}}f_D} \quad \Rightarrow \quad \beta = \frac{T_0}{F_0} = \frac{\tau_{\text{max}}}{f_D} \quad (2.20b)$$

$$S(t_d, f_d) = \frac{e^{-\frac{t_d}{\tau_{\text{rms}}}}}{\tau_{\text{rms}}} \frac{1}{\pi f_D \sqrt{1 - \left(\frac{f_d}{f_D}\right)^2}} \quad \Rightarrow \quad \beta = \frac{T_0}{F_0} = \frac{3\tau_{\text{rms}}}{2f_D}. \quad (2.20c)$$

At the cost of increased receiver complexity, hexagonal lattice grids, which increase the minimum distance between two lattice points and thus improve the protection against Inter-Carrier Interference (ICI) and Inter-Symbol Interference (ISI), are investigated in [44, 96].

2.1.4 Classification of MC modulation schemes

Based on the selected lattice grid structure (e.g. rectangular, hexagonal, etc.) and density (i.e T-F product), PFF characteristics (localization, direction, etc.) and data sets (\mathbb{R} or \mathbb{C}), different modulation schemes have been defined. Figure 2.3 presents the most familiar modulation schemes with a rectangular lattice grid, which are briefly discussed in the following.

2.1.4.1 OFDM

Orthogonal Frequency-Division Multiplexing (OFDM) is based on the work of Saltzberg and Chang [10, 84] and can be simply implemented by application of (inverse) Fast Fourier Transforms (FFTs) [104]. Plain OFDM utilizes a rectangular PFF with duration T at the transmitter and receiver, and thus has the ability to transmit complex data symbols. Plain OFDM is the only scheme in the OFDM family, which has the T-F product $T_0F_0 =$

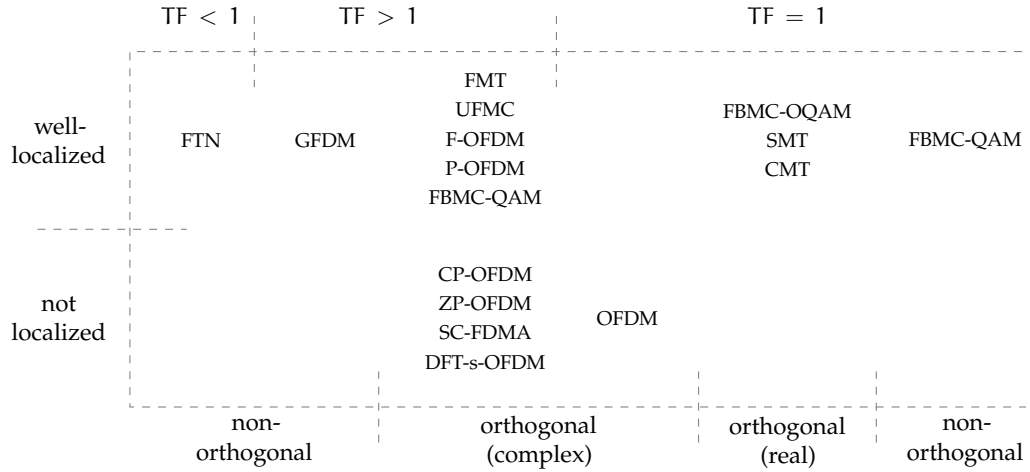


Figure 2.3: Classification of popular MC modulation schemes based on T-F grid, PFF localization and orthogonality.

$T \cdot 1/T = 1$. Due to vulnerability of the rectangular PFF to multipath propagation, Zero-Padded OFDM (ZP-OFDM) and CP-OFDM have been introduced, whereby CP-OFDM is a bi-orthogonal MC scheme, as the transmit and receive filters have the length $T_0 = T + T_{CP}$ and $T_0 = T$, respectively. For applications with high Peak-to-Average Power Ratio (PAPR) restrictions, such as in mobile transmitters, the PAPR of OFDM schemes can be reduced by Discrete Fourier Transform (DFT) spreading as done in Single-Carrier Frequency-Division Multiple Access (SC-FDMA) or DFT-spread OFDM (DFT-s-OFDM).

2.1.4.2 Block-wise filtered OFDM

For all communication systems, the Out-Of-Band (OOB) emissions are a crucial design aspect and often regulated. Current (CP-)OFDM systems, e.g. LTE and WLAN sacrifice some subcarriers for inter-system guard bands, thus allowing an analog or digital filtering of the whole signal to reduce the OOB emission. Besides windowed OFDM, which applies a time domain windowing of each separate OFDM symbol, in the recent years different OFDM based modulation schemes have been proposed. All these modulation schemes have in common, that they utilize a T-F product $T_0 F_0 > 1$. Based on ZP-OFDM, in 2013 Vakilian et al. proposed the UFMC scheme [99, 106]. In UFMC, the spectrum of a transmit signal is divided into distinct blocks, which are filtered individually by a not necessarily orthogonal filter of length $T + T_{ZP}$, e.g. Dolph-Chebyshev or other optimized filters [102, 103], such that the orthogonality between the different blocks may be destroyed and Inter-Block Interference (IBI) is introduced. As UFMC preserves the orthogonality within each block, this modulation scheme can be considered as orthogonal. To relax the filter design constraints, Filtered OFDM (F-OFDM) has been proposed [1, 113]. Similar to UFMC, the filtering is performed for independent blocks of spectrum with non-orthogonal filters. As F-OFDM utilizes a Cyclic Prefix (CP) and allows filter lengths $T_{CP} < T_F < T$, IBI and ISI is introduced, which has to be taken into account during filter and system design.

2.1.4.3 Subcarrier-wise filtered OFDM

Besides block-wise filtering, different OFDM based modulation schemes using subcarrier-wise filtering with or without CP have been proposed. As stated by the Balian-Low theorem, transmitting complex data symbols using well-localized filtering results in either undersampled lattice grids with $T_0F_0 > 1$ or non-orthogonal transmissions. Both approaches have been discussed in literature. In [110, 111], FBMC with Quadrature Amplitude Modulation (QAM) subcarrier modulation (FBMC-QAM) or QAM-FBMC schemes with $T_0F_0 = 1$ have been proposed. They utilize real as well as complex valued PFFs and provide a limited SIR of about 20 dB (ref. Section 3.4) in Additive White Gaussian Noise (AWGN) channels and thus may not be suitable for high throughput applications. In [69, 70, 114], orthogonal modulation schemes with $T_0F_0 > 1$ have been proposed as FBMC-QAM and Pulse-shaped OFDM (P-OFDM). It should be noted that the modulation schemes proposed in [69, 70, 110] apply some kind of lattice staggering, as they utilize subcarrier specific PFFs. Some of these PFFs have increased OOB emissions, thus limiting their applicability to scenarios with high spectral containment requirements, e.g. spectrum pooling (Non-Contiguous OFDM (NC-OFDM)) [105].

Another approach with subcarrier-wise filtering is Filtered MultiTone (FMT), which has been a candidate for application in Very high speed Digital Subscriber Line (VDSL) [12, 68]. Despite to the previous described schemes with $T_0F_0 > 1$, which spread the lattice in time domain ($T_0 > T$), FMT increased the subcarrier spacing ($F_0 > F$), and applies filters which do not overlap in frequency domain.

2.1.4.4 Staggered lattice grids

Modulation schemes with $T_0F_0 = 1$ in combination with well-localized PFFs and real-field (bi-)orthogonality are Cosine-modulated MultiTone (CMT), SMT and FBMC-OQAM [28, 29]. SMT is the continuous-time description of FBMC-OQAM, which is also known under the synonyms OFDM/OQAM, OFDM-OQAM, OQAM-OFDM, OQAM/OFDM and FBMC/OQAM, with $F_0 = F$ and $T_0 = 0.5T$. An approach with FFT based precoding, which enables Multiple-Input Multiple-Output (MIMO) for FBMC-OQAM has been proposed as FFT-FBMC [112]. CMT establishes the orthogonality by selecting the lattice grid parameters as $F_0 = 0.5F$ and $T_0 = T$. While CMT, which is also dedicated to Vestigial Side-Band modulation (VSB), is only capable of transmitting Pulse Amplitude Modulation (PAM) symbols, FBMC-OQAM enables the transmission of Quadrature Amplitude Modulation (QAM) type signals [29, 83]. As these modulation schemes only provide real-field orthogonality, additional effort is required to enable estimation and equalization of signal distortions induced by dispersive propagation channels as well as Symbol Timing Offset (STO) and Carrier Frequency Offset (CFO).

2.1.4.5 *Special non-orthogonal MC modulation schemes*

A non-orthogonal modulation scheme with an effective T-F product $T_0F_0 \geq 1$, transmission of complex data symbols and well-localized PFF is GFDM [31]. Here, the CP is applied to a block of certain numbers of OFDM symbols and the subcarrier-wise filtering is based on a circular convolution with a PFF kernel. The PFF is designed to overlap with neighboring subcarriers. Therefore, the ICI needs to be canceled out by additional processing after the demodulation at the receiver [17, 39].

In 1975 Mazo showed for single-carrier systems, that it is possible to design communication systems with $T_0F_0 < 1$, i.e. Faster Than Nyquist (FTN) systems, without a loss in BER. This so called Mazo limit depends on the applied modulation order and PFF [59], e.g. for sinc pulses and Binary Phase-Shift Keying (BPSK), the Mazo limit yields $T_0 = 0.801T$. In [80–82], the concept of Mazo has been extended to MC systems. However, to achieve the Mazo limit a somewhat “perfect receiver” is required [83].

2.1.5 *Arising research question*

In the previous section, a brief introduction in communication channels, the design of MC systems and the classification of recent MC modulation schemes has been provided. It is shown, that the lattice grid as well as the PFF of the communication system should match the statistical properties of the communication channel. However, in literature there is no statement on the amount of potential gains (or losses in case of non-optimal system configurations) and its practical relevance.

Currently deployed communication systems utilizing MC modulation mainly rely on CP-OFDM, e.g. LTE, DVB-T and WLAN, and thus are only capable of matching their lattice grid to the statistics of the target channel scenarios. Based on the properties of the previously discussed MC schemes, the only one with well-localized and orthogonal PFFs in combination with the maximum lattice grid density of $T_0F_0 = 1$ is FBMC-OQAM, which also has been considered as modulation scheme for the upcoming fifth generation cellular network 5G. Thus, the following research question is formulated.

Can an optimized system adaption in terms of a combined lattice grid and PFF adaptation, that matches the properties of the utilized communication channel, provide relevant performance gains?

To answer this question, a novel system design concept for homo- and heterogeneous channel scenarios per cell is proposed and its performance gains in terms of SIR, BER and system capacity are evaluated. To account for limitations in practical systems, the effects of channel estimation are considered.

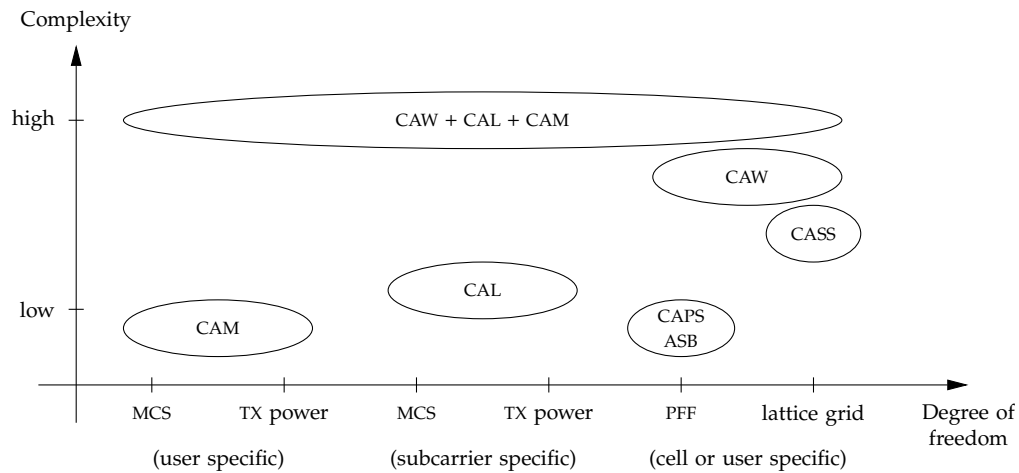


Figure 2.4: System complexity categorization of channel adaptivity schemes² based on the utilized degrees of freedom.

2.2 RELATED WORK

Generally, there exist several different approaches to adapt a communication system to the behavior of the utilized communication channels. As depicted in Figure 2.4, channel adaptation approaches can be categorized into the three different groups Channel Adaptive Modulation and coding (CAM), Channel Adaptive Loading (CAL) and CAW, which are discussed briefly in the following.

2.2.1 Channel Adaptive Modulation and coding (CAM)

CAM is the state-of-the-art approach to adapt systems to the utilized channel. It is widely adopted in current communication systems such as WLAN, Worldwide Interoperability for Microwave Access (WiMAX) and LTE. The underlying system design follows a “one-fits-all” approach, which means that system parameters in terms of lattice grid and PFF of a communication system are designed to provide a trade-off in system performance in all target channel scenarios. Here, the channel adaptivity is obtained by adjusting the applied modulation order, the code rate of the channel coder and the transmit power, e.g. known as Modulation and Coding Scheme (MCS) in LTE, to the present channel environment and SNR to maximize the effective throughput defined in bit/s/Hz. Thereby, all subcarriers of a user in a system utilize the same MCS which can vary over time as the underlying channel changes. Under high SNR conditions the system performance is restricted by the global configuration of the lattice grid and PFF which may not match the channel properties and thus is suboptimal.

² ASB: Adaptive Subcarrier Bandwidth, CAL: Channel Adaptive Loading, CAM: Channel Adaptive Modulation and coding, CAPS: Channel Adaptive Pulse Shaping, CASS: Channel Adaptive Subcarrier Spacing, CASS: Channel Adaptive Subcarrier Spacing

2.2.2 Channel Adaptive Loading (CAL)

CAL can be considered as a generalization of the state-of-the-art CAM approach, whereby the MCS and transmit power are selected subcarrier wise instead of the equal subcarrier configuration used in CAM. This significantly improves channel capacity in multipath channels with more than one channel tap resolvable at the receiver, where the (time-variant) CTF $H(f, t)$ and thus the SNR per subcarrier becomes frequency-variant. A comparison of different CAL approaches has been done by Chung et al. [88] and the references therein. Compared to CAM, the system performance is improved but still suboptimal, as the lattice grid and PFF are not matched to the channel properties as suggested by theory (cf. Section 2.1.3). CAL suffers from the need of accurate channel estimation and low latency transmission of the Channel State Information (CSI) to the transmitter, which complicates its application to wireless communication channels. In wired communications where the channel can be assumed to be invariant over a sufficiently long time, the low latency CSI feedback constraint is not relevant. Thus, it is much less complicated to apply CAL to wired communication systems. A widely adopted wired communication system using CAL is VDSL [94].

2.2.3 Channel Adaptive Waveform (CAW)

In CAW, the adaptivity of communication systems is based on matching the lattice grid and PFF to the characteristics of the utilized channel to maximize the SINR and thus channel capacity [28, 54, 55, 62, 83]. Furthermore, CAW enables receiver structures without the need for complex interference cancellation mechanisms, as the interference may be reduced sufficiently. The channel adaptivity schemes CAM or CAL can be applied additionally to combat capacity losses induced by fading. CAW can be deployed in different forms, which are

- sole adaptation of the PFF, which is referred to as CAPS within this thesis;
- sole adaptation of the lattice grid, which is referred to as CASS within this thesis;
- combined adaptation of the PFF and lattice grid, which is referred as CAW within this thesis.

For CP-OFDM, a CASS approach called ASB has been proposed by Das et al. [16] to combat the ICI induced by Doppler effects. They show that the system throughput can be improved by 10% to 30%.

In [64], Matz et al. investigated the SIR gains of optimized PFFs for P-OFDM and compared the performance with classical CP-OFDM. Based on DVB-T and Digital Radio Modiale (DRM) systems the authors showed that optimizing the PFFs can significantly improve the system performance compared to the standardized CP-OFDM based DVB-T and DRM systems [21, 22].

An approach to adapt a PFF to varying channel conditions is proposed in [96] by Strohmer et al. Furthermore, they propose the application of generalized lattice schemes for P-OFDM systems which is called Lattice-OFDM (LOFDM) and provides an SINR gain of approximately 1 dB compared to P-OFDM with optimized PFFs.

In [15], Das et al. presented an approach in which the intrinsic interference induced by doubly dispersive channels is shaped by non-(bi)orthogonal PFFs. Thereby, the equalization requires two turbo equalizers and thus significantly increased receiver complexity. Compared to the LOFDM approach by Strohmer et al. [96], the SINR can be improved by up to 1 dB. Compared to classical CP-OFDM the SINR gain yields approximately 2.5 dB.

Inspired by some of the work presented in this thesis, Schaich et al. discussed the application of CASS to enable the support of velocities of up to 500 km/h [3] in UFMC systems. In [85] the authors evaluated the applicability of a Multi-User (MU) UFMC system, proving that the inter-user interference suppression of UFMC is superior compared to CP-OFDM. In a follow up publication [86], the authors showed the related gains in terms of spectral efficiency and proposed frame designs which are appropriate to the 5G recommendations [48].

2.3 PROBLEM STATEMENT

Even though the related work provides different approaches to the topic of channel adaptive modulation and waveforms, several aspects are still required to be investigated. Thus, the research question is split into the following sub-questions:

1. *What are the quantitative performance gains of CAW in practical doubly dispersive channels?*
2. *How does imperfect channel knowledge effect the performance gains of CAW?*
3. *Is there a benefit for the application of CAW in cells with heterogeneous channel scenarios?*
4. *What amount of inter-user guard bands is required for DL and UL transmissions with heterogeneous CAW?*

Each of the above mentioned questions is investigated in the following chapters to provide a comprehensive answer to the research question. Therefore, CAW is investigated in the context of cellular networks.

In this chapter, a description of the applied unified discrete-time system model for FBMC-OQAM and CP-OFDM is provided and the utilized channel model is introduced. The effects on a demodulated symbol being transmitted over doubly dispersive channels are derived based on the characteristics of the PFFs and the statistical properties of the communication channel. This is followed by a description and discussion of various PFFs suggested for FBMC-OQAM as well as their main characteristics. Additionally, the reconstruction performance in terms of SIR is defined for both FBMC-OQAM and CP-OFDM. Finally, the set of parameters considered in this thesis is presented.

3.1 DISCRETE-TIME TRANSMISSION MODEL

In this thesis, a critically sampled discrete-time system model with the sampling period T_s , symbol duration T and total number of subcarriers K is considered, i.e. $T_s = T/K$ and $t = nT_s$, which is depicted in Figure 3.1. Here, the main focus of interest is laid on the effects of the intrinsic interference in FBMC-OQAM systems caused by the propagation channel. Thus, the receiver noise is not considered. To improve readability, the sampling period is neglected in the following and brackets are used instead of parenthesis to indicate discrete-time functions, i.e. $r[n] := r(nT_s)$.

Considering the time-variant multipath channel $h[\tau, n]$ of path delay τ with $t_d = \tau T_s$ as well as (2.1), (2.10) and (2.11), the received signal $r[n]$ of a subcarrier-wise filtered MC modulation scheme is obtained by

$$r[n] = h[\tau, n] * s[n], \quad (3.1)$$

where the transmit signal $s[n]$ is given by

$$s[n] = \sum_{(m,k) \in \mathbb{T}} \theta_{m,k} \alpha_{m,k} f_k[n - mM_0] \quad (3.2a)$$

with

$$f_k[n] = f[n] e^{j2\pi k K_0 n}. \quad (3.2b)$$

Here, $f_k[n]$ is the discrete-time modulated PFF. $\tau_0 = T_0/T$ and $\nu_0 = F_0 T$ are the normalized symbol and subcarrier spacing spanning the lattice grid, respectively. $K_0 = \nu_0/K =$

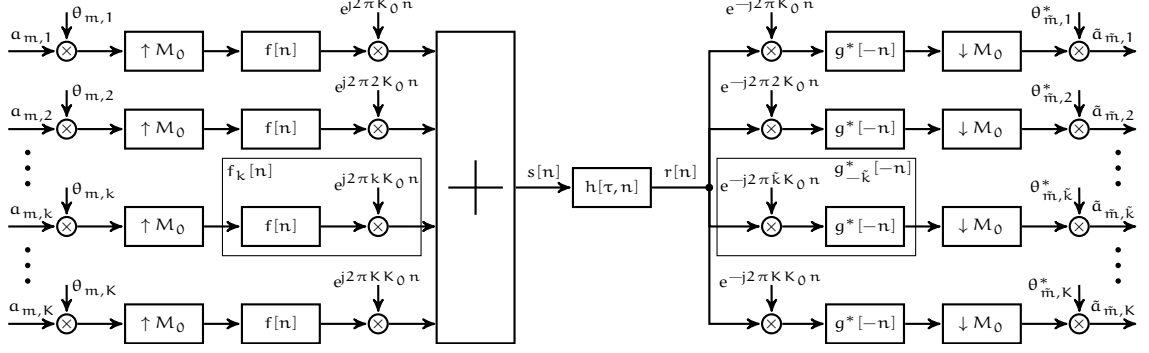


Figure 3.1: Generic discrete-time and filtering (convolution¹) based transceiver chain for a (bi-)orthogonal multicarrier scheme with K subcarriers and a lattice grid defined by the symbol spacing M_0 and subcarrier spacing K_0 . The weighting factor $\theta_{m,k}$ is a phase shift which is used to establish the real-field orthogonality in staggered lattice grid schemes (symbols $a_{m,k} \in \mathbb{R}$).

$\nu_0 T_s/T$ and $M_0 = \tau_0 K = \tau_0 T/T_s$ define the discrete-time subcarrier and symbol spacing. $\theta_{m,k}$ is a phase shift which can be used to establish the real orthogonality condition.

The discrete-time channel is modeled by a time-variant tapped delay line with a maximum Doppler shift f_D and L separate channel taps, which is given as follows [67]:

$$h[\tau, n] = \sum_{l=0}^{L-1} h_l[n] \delta[\tau - \tau_l]. \quad (3.3)$$

Thereby, the discrete-time time-variant complex valued attenuation coefficient $h_l[n]$ of channel tap index l is defined by $h_l[n] = h[\tau_l, n]$.

3.2 REPRESENTATION OF DEMODULATED SYMBOLS

Referring to (2.12), the unequalized data or pilot symbol $\tilde{a}_{\tilde{m},\tilde{k}}$ is obtained by projecting the received signal $r[n]$ onto T-F shifted versions of the receive PFF $g[n]$. Additionally, the phase shift $\theta_{m,k}$ has to be compensated. Accordingly and with assumption of perfect synchronization to the first channel tap $l = 0$, $\tilde{a}_{\tilde{m},\tilde{k}}$ is obtained by

$$\begin{aligned} \tilde{a}_{\tilde{m},\tilde{k}} &= \theta_{\tilde{m},\tilde{k}}^* \langle r, g_{\tilde{m},\tilde{k}} \rangle = \theta_{\tilde{m},\tilde{k}}^* \left(r[n] * g_{\tilde{k}}^*[n - \tilde{m}M_0] \right) \Big|_{M_0} \\ &= \theta_{\tilde{m},\tilde{k}}^* \sum_n \sum_{(m,k) \in \mathbb{T}} \theta_{m,k} a_{m,k} \left(h[\tau, n] * f_k[n - mM_0] \right) g_{\tilde{k}}^*[n - \tilde{m}M_0], \end{aligned} \quad (3.4a)$$

with \tilde{m} and \tilde{k} being the symbol and subcarrier index of the demodulated received symbol, respectively, and the receive PFF given as

$$g_{\tilde{k}}^*[n - \tilde{m}M_0] = g^*[n - \tilde{m}M_0] e^{-j2\pi \tilde{k} K_0 (n - \tilde{m}M_0)}. \quad (3.4b)$$

¹ Here, the receiver filter $g[n]$ is defined according to (2.12).

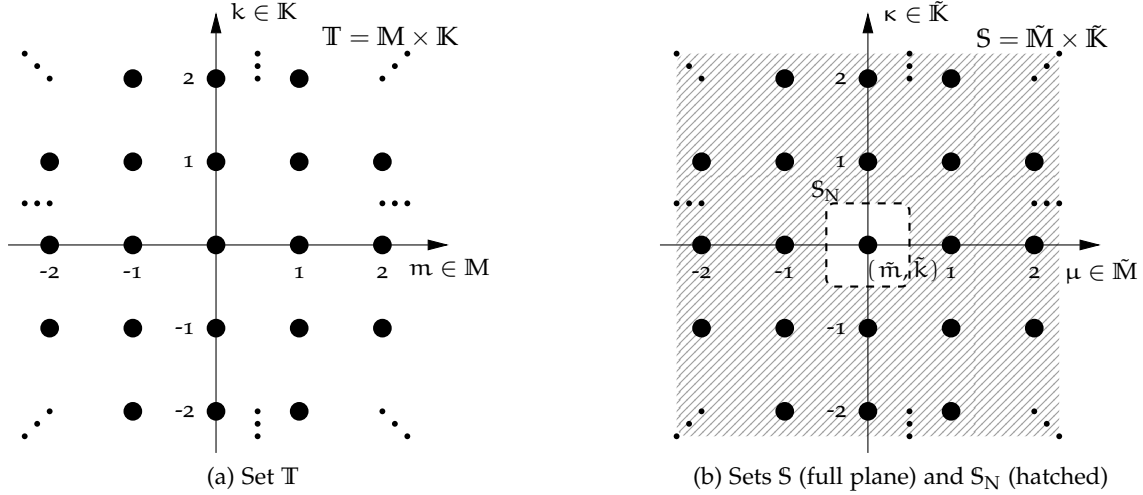


Figure 3.2: Sets of lattice position for Transmitter (TX) symbols (left) and the ones related to the Receiver (RX) symbol at position (\tilde{m}, \tilde{k}) (right).

As long as $2f_D T_s < 1$, the Discrete-Time Fourier Transform (DTFT) can be applied to $h[\tau, n]$ [67]. Therefore, and by consideration of (3.3), (3.4a) yields

$$\begin{aligned}
 \tilde{a}_{\tilde{m}, \tilde{k}} &= \theta_{\tilde{m}, \tilde{k}}^* \sum_n g_{\tilde{k}}^*[n - \tilde{m}M_0] \sum_{(m,k) \in \mathbb{T}} \left(\theta_{m,k} a_{m,k} \sum_{l=0}^{L-1} h[\tau_l, n] f_k[n - \tau_l - mM_0] \right) \\
 &= \theta_{\tilde{m}, \tilde{k}}^* \sum_n g_{\tilde{k}}^*[n - \tilde{m}M_0] \sum_{(m,k) \in \mathbb{T}} \left(\theta_{m,k} a_{m,k} \right. \\
 &\quad \left. \cdot \sum_{l=0}^{L-1} \int_{-f_D T_s}^{f_D T_s} D[\tau_l, \nu] e^{j2\pi n \nu} f_k[n - \tau_l - mM_0] d\nu \right), \quad (3.5)
 \end{aligned}$$

with the normalized frequency ν and the Doppler-variant channel impulse response or spreading function $D[\tau_l, \nu]$, which is given by

$$D[\tau_l, \nu] = \sum_{n=-\infty}^{\infty} h[\tau_l, n] e^{-j2\pi n \nu}. \quad (3.6)$$

By introduction of the symbol index offset $\mu = m - \tilde{m}$, the subcarrier offset $\kappa = k - \tilde{k}$ and the associated sets of available offsets $\tilde{\mathbb{M}} = \mathbb{M} - \tilde{m}$ and $\tilde{\mathbb{K}} = \mathbb{K} - \tilde{k}$, the lattice grid related to $\tilde{a}_{\tilde{m}, \tilde{k}}$ can be described by the set of lattice position tuples $(\mu, \kappa) \in \mathbb{S}$ with $\mathbb{S} = (\tilde{\mathbb{M}} \times \tilde{\mathbb{K}})^2$.

² An overview of the different sets of symbol positions in the T-F domain is given in Figure 3.2.

Moreover, with definition of the set of neighboring symbols as $S_N = S \setminus (0, 0)$, $\tilde{a}_{\tilde{m}, \tilde{k}}$ yields (cf. Appendix A.2)

$$\begin{aligned} \tilde{a}_{\tilde{m}, \tilde{k}} &= \sum_{(\mu, \kappa) \in S} \theta_{\mu, \kappa} a_{\tilde{m}+\mu, \tilde{k}+\kappa} \sum_{l=0}^{L-1} \int_{-f_D T_s}^{f_D T_s} D[\tau_l, \nu] e^{j2\pi \tilde{m} M_0 \nu} A_{\mu, \kappa}^{\tilde{k}}[\tau_l, \nu] d\nu \\ &= \underbrace{a_{\tilde{m}, \tilde{k}} H_{\tilde{m}, \tilde{k}}(0, 0)}_{\check{a}_{\tilde{m}, \tilde{k}}} + \underbrace{\sum_{(\mu, \kappa) \in S_N} \theta_{\mu, \kappa} a_{\tilde{m}+\mu, \tilde{k}+\kappa} H_{\tilde{m}, \tilde{k}}(\mu, \kappa)}_{i_{\tilde{m}, \tilde{k}}}. \end{aligned} \quad (3.7)$$

Here, $\check{a}_{\tilde{m}, \tilde{k}}$ is the desired unequalized signal and $i_{\tilde{m}, \tilde{k}}$ includes the intrinsic ISI and ICI, respectively. Additionally, the system dependent effective channel coefficient $H_{\tilde{m}, \tilde{k}}(\mu, \kappa)$ is given by

$$H_{\tilde{m}, \tilde{k}}(\mu, \kappa) = \sum_{l=0}^{L-1} \int_{-f_D T_s}^{f_D T_s} D[\tau_l, \nu] e^{j2\pi \tilde{m} M_0 \nu} A_{\mu, \kappa}^{\tilde{k}}[\tau_l, \nu] d\nu, \quad (3.8)$$

where the phase shifted discrete-time (cross-)ambiguity function $A_{\mu, \kappa}^{\tilde{k}}[\tau_l, \nu]$ is defined by

$$A_{\mu, \kappa}^{\tilde{k}}[\tau_l, \nu] = e^{-j2\pi K_0 (\tilde{k}+\kappa)(\mu M_0 + \tau_l)} A[\mu M_0 + \tau_l, \kappa K_0 + \nu] \quad (3.9a)$$

$$= \phi_p(\tilde{k}, \mu, \kappa) \phi_d(\tilde{k}, \tau_l) \phi_d(\kappa, \tau_l) A[\mu M_0 + \tau_l, \kappa K_0 + \nu]. \quad (3.9b)$$

Thereby, the discrete-time (cross-)ambiguity function $A[\tau, \nu]$ as well as the phase factors $\phi_p(\tilde{k}), \phi_d(\tilde{k}, \tau_l)$ and $\phi_d(\kappa, \tau_l)$ are calculated as follows:

$$A[\tau, \nu] = \sum_{n=-\infty}^{\infty} f[n - \tau] g^*[n] e^{j2\pi \nu n} \quad (3.9c)$$

$$\phi_p(\tilde{k}, \mu, \kappa) = e^{-j2\pi \mu M_0 K_0 (\tilde{k}+\kappa)} \quad (3.9d)$$

$$\phi_d(\tilde{k}, \tau_l) = e^{-j2\pi K_0 \tilde{k} \tau_l} \quad (3.9e)$$

$$\phi_d(\kappa, \tau_l) = e^{-j2\pi K_0 \kappa \tau_l}. \quad (3.9f)$$

From (3.9) it can be deduced, that the effects on any received symbol depends on the subcarrier \tilde{k} where it is transmitted on, the relative position of neighboring symbols (μ, κ) as well as the delay τ_l of the observed propagation channel path.

For the generation of results based on Monte-Carlo simulations, the computer-aided calculation of the effective channel coefficients $H_{\tilde{m}, \tilde{k}}(\mu, \kappa)$ according to (3.8) can be inefficient, as the time-variant CIR has to have a sufficient length N_{CIR} to provide an adequate resolution in frequency domain, which in dependance of the investigated channel parameters can require a lot of Random Access Memory (RAM). Exemplary values for the memory consumption for different parameter settings are provided in Appendix B.3.

Therefore, in Monte-Carlo based simulations $H_{\tilde{m},\tilde{k}}(\mu, \kappa)$ is calculated based on the usage of the time-variant CIR $h[\tau, n]$. To this end, (A.9) is rearranged as

$$H_{\tilde{m},\tilde{k}}(\mu, \kappa) = \sum_{\tau} \sum_{n=-\infty}^{\infty} h[\tau, n + \tilde{m}M_0] f[n - \tau - \mu M_0] g^*[n] e^{j2\pi K_0 \kappa (n - \tau - \mu M_0)}. \quad (3.10)$$

3.2.1 FBMC-OQAM

To establish the real-field (bi-)orthogonality for FBMC-OQAM systems, the phase shift in (2.10) is given by

$$\theta_{m,k} = j^{m+k} \quad (3.11a)$$

and the symbol alphabet for the transmit symbols $a_{m,k}$ is restricted to

$$a_{m,k} \in \mathbb{R}. \quad (3.11b)$$

For FBMC-OQAM, orthogonal as well as bi-orthogonal schemes have been proposed [90]. To limit the parameter space in this thesis, the investigations are restricted to orthogonal PFFs, thus $f[n] = g[n]$. As mentioned before (cf. Section 2.1.2 and Appendix A.1), FBMC-OQAM uses lattice staggering such that $M_0 = 0.5K$ and $K_0 = 1/K$. Therefore, (3.9d) reduces to

$$\begin{aligned} \phi_p(\tilde{k}, \mu, \kappa) &= e^{j\pi\mu(\tilde{k}+\kappa)} \\ &= (-1)^{\mu(\tilde{k}+\kappa)}, \end{aligned} \quad (3.12)$$

which indicates that for FBMC-OQAM systems the intrinsic interference $i_{\tilde{m},\tilde{k}}$ of a received symbol $\tilde{a}_{\tilde{m},\tilde{k}}$ depends on the allocated position (\tilde{m}, \tilde{k}) of the lattice grid, even for the case of a non-dispersive channel. The related patterns of sign change are depicted in Figure 3.3. This has to be considered for algorithms handling the intrinsic interference such as the Auxiliary Pilot (AP) scheme, which is a possible scheme to mitigate the interference on pilot symbols (see Section 4.4.1).

To recover the transmitted symbol, the interference has to be removed by eliminating the imaginary value and the channel effects on the demodulated symbol $\tilde{a}_{\tilde{m},\tilde{k}}$ have to be reverted. For channel equalization, different schemes such as Zero Forcing (ZF), Minimum Mean-Squared Error (MMSE) or multi-tap equalizers can be applied. Due to its simplicity, in this thesis the ZF equalizer is utilized. Additionally, applying the ZF equalizer provides a lower performance bound which can be used in the future to compare

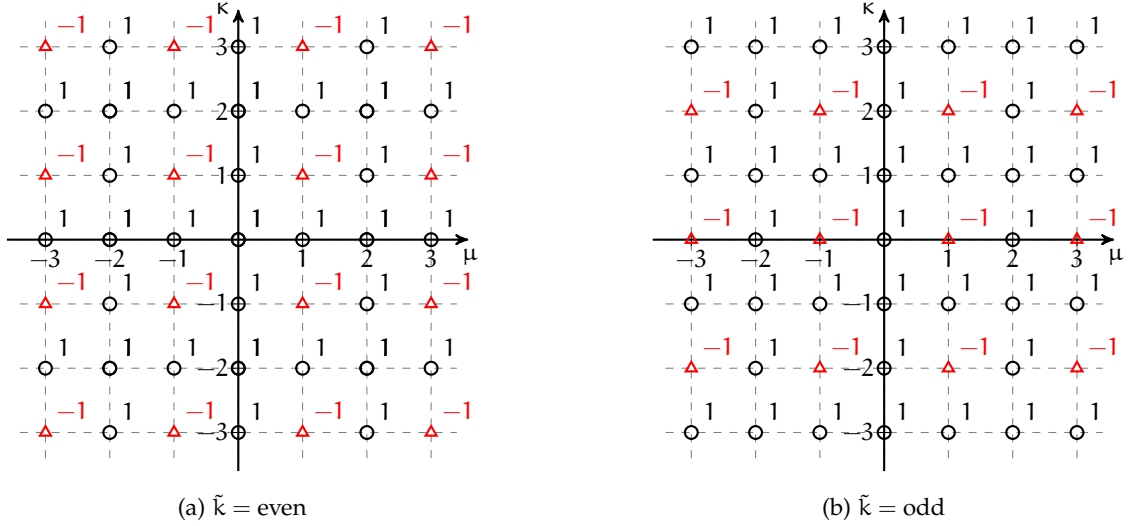


Figure 3.3: Sign change patterns of the intrinsic interference in FBMC-OQAM systems. Lattice positions with sign changes are indicated by triangles.

the gains of more sophisticated receiver algorithms such as multi-tap equalizers [101]. Therefore, the received FBMC-OQAM symbol $\hat{a}_{\tilde{m}, \tilde{k}}$ is obtained by

$$\hat{a}_{\tilde{m}, \tilde{k}} = a_{\tilde{m}, \tilde{k}} + \Re \left\{ \sum_{(\mu, \kappa) \in \mathcal{S}_N} \theta_{\mu, \kappa} a_{\tilde{m} + \mu, \tilde{k} + \kappa} \frac{H_{\tilde{m}, \tilde{k}}(\mu, \kappa)}{H_{\tilde{m}, \tilde{k}}(0, 0)} \right\}. \quad (3.13)$$

3.2.2 (CP-)OFDM

Contrary to FBMC-OQAM, in (CP-)OFDM systems all transmit symbols are complex, i.e. $a_{m, k} \in \mathbb{C}$, and no phase shift is required:

$$\theta_{m, k} = 1. \quad (3.14)$$

Plain OFDM is an orthogonal modulation scheme with $T_0 = T$ and $F_0 = 1/T$, which utilizes rectangular PFFs according to

$$f[n] = g[n] = \begin{cases} \frac{1}{\tilde{K}} & -\frac{\tilde{K}}{2} \leq n < \frac{\tilde{K}}{2} \\ 0 & \text{otherwise.} \end{cases} \quad (3.15)$$

Therefore, for plain OFDM (3.9d) reduces to

$$\begin{aligned} \phi_p(\tilde{k}, \mu, \kappa) &= e^{2j\pi\mu(\tilde{k} + \kappa)} \\ &= 1. \end{aligned} \quad (3.16)$$

Accordingly, for plain OFDM systems operating in non-dispersive channels, the intrinsic interference can be assumed to be independent of the allocated subcarrier.

Similar to FBMC-OQAM, the transmitted symbol is recovered by reverting the channel effects with a ZF equalizer:

$$\hat{a}_{\tilde{m},\tilde{k}} = a_{\tilde{m},\tilde{k}} + \sum_{(\mu,\kappa) \in \mathcal{S}_N} a_{\tilde{m}+\mu,\tilde{k}+\kappa} \frac{H_{\tilde{m},\tilde{k}}(\mu,\kappa)}{H_{\tilde{m},\tilde{k}}(0,0)}. \quad (3.17)$$

However, plain OFDM has a major drawback in time-dispersive channels. Due to the rectangular PFF, plain OFDM suffers from high ISI and ICI (cf. Section 3.3). Thus, in 1971 Weinstein and Ebert suggested the application of a Cyclic Prefix (CP) to OFDM to remove the ISI [104], which can be implemented easily by extension of the transmit filter

$$f[n] = \begin{cases} \frac{1}{K} & -\left(\frac{K}{2} + \lceil T_{\text{CP}}/T_s \rceil\right) \leq n < \frac{K}{2} \\ 0 & \text{otherwise,} \end{cases} \quad (3.18)$$

with $T_{\text{CP}} \geq \tau_{\text{max}}$. It is easy to see that the introduction of the CP stretches the lattice grid in time domain, i.e. $T_0 = T + T_{\text{CP}}$, and thus decreases the spectral efficiency. Accordingly, for CP-OFDM (3.9d) yields

$$\begin{aligned} \phi_p(\tilde{k}, \mu, \kappa) &= e^{2j\pi\mu \frac{T+T_{\text{CP}}}{T} (\tilde{k}+\kappa)} \\ &= e^{2j\pi\mu \frac{T_{\text{CP}}}{T} (\tilde{k}+\kappa)}, \end{aligned} \quad (3.19)$$

which similar to FBMC-OQAM may require attention in some receiver algorithms.

3.3 PULSE SHAPING

Referring to Section 2.1.3, the PFFs of a transmission system are a critical part in system design to enable a robust transmission in (doubly) dispersive channels. Generally, all PFF can be categorized in one of the following three classes: time-limited, band-limited and localized, which are discussed in the following.

TIME-LIMITED are PFFs defined with a finite duration and thus are simple to implement, as no additional effort is required. However, due to their finite duration, time-limited PFFs have an unlimited spectrum. Most common representatives of this group are the rectangular, Hamming, Hanning, (exact) Blackman and PHYDYAS PFFs [5, 46].

BAND-LIMITED PFFs theoretically provide a perfect spectral containment of the signal energy. However, this results in an infinite duration which requires special treatment in practical implementation to limit implementation costs and spectral regrowth induced

by the time limitation. Well known representatives of band-limited PFFs are the Cardinal sine (sinc), which has a rectangular function in frequency domain, as well as the Raised Cosine (RC) and the Root Raised Cosine (RRC) functions [76].

LOCALIZED PFFs aren't limited in either the time or frequency domain. Contrary to time- and band-limited PFFs, localized PFFs attempt to concentrate the signal energy in time as well as frequency domain to maximize the Heisenberg-Gabor uncertainty. For a given PFF $f(t)$, the Heisenberg-Gabor uncertainty or T-F-localization ξ is defined as [7, 28]:

$$\xi = \frac{1}{4\pi\sigma_t\sigma_f} \leq 1. \quad (3.20)$$

The PFF with the optimal T-F-localization $\xi = 1$ is the Gaussian PFF with spreading factor $\alpha = 1$. Other localized PFFs are the Isotropic Orthogonal Transform Algorithm (IOTA), Extended Gaussian Function (EGF) and Hermite PFFs [43, 55, 92], which all are orthogonalized Gaussian functions.

In practical systems, the performance of PFFs is often effected by implementation constraints such as filter length and bit widths to limit hardware costs, energy consumption and latency, which result in quantization noise and spectral regrowth. For FBMC-OQAM systems, the filter length is usually defined by the so called overlapping factor γ , which specifies the filter length L_p in terms of the amount of overlapping symbols:

$$L_p = \gamma K. \quad (3.21)$$

In general and considering the transceiver model presented in Figure 3.1, γ can be selected as $\gamma \in \mathbb{Q}$. However, compared to the given system model, the implementation complexity can be reduced significantly by realizing the filtering process with PolyPhase Networks (PPNs) [93]. As the PPN approach results in an implementation complexity which is $\propto \lceil \gamma \rceil$, it is reasonable to restrict γ to $\gamma \in \mathbb{N}^+$.

The PFFs $f[n]$ applied in this work are derived from not necessary time-limited base PFFs $p[n]$ proposed in literature for FBMC-OQAM systems as follows:

$$f[n] = \begin{cases} p[n], & -\frac{\gamma K}{2} \leq n < \frac{\gamma K}{2} \\ 0, & \text{otherwise.} \end{cases} \quad (3.22)$$

As base PFFs $p[n]$, different Nyquist pulses, namely PHYDYAS [5] or Mirabbasi-Martin [66], an IOTA PFF based on EGF [92] and the Hermite pulse shape [43], are considered, which are shortly discussed hereinafter. For completeness and to allow a comparison between FBMC-OQAM and CP-OFDM, the properties of the rectangular PFF of CP-OFDM are presented, too.

γ	q_0	q_1	q_2	q_3	q_4	β	β_{norm}	ξ
3	1	0.91143783	0.41143783			0.8	1.6	0.89059
4	1	0.97195983	$\sqrt{2}/2$	0.23514695		0.83693	1.6739	0.88389
5	1	0.99184131	0.86541624	0.50105361	0.12747868	0.88252	1.765	0.86715

Table 3.1: Coefficients for the parametrization of the PHYDYAS PFF given in (3.23) and the resulting direction and T-F localization parameters. Additional coefficients for $\gamma \in [1, 8]$ are given in [5, 61, 66, 100].

3.3.1 PHYDYAS

The PHYDYAS PFF, which has been intensively studied within the PHYSical layer for DYnamic spectrum AccesS and cognitive radio (PHYDYAS) project, is a time limited Nyquist filter obtained by frequency sampling. It has been optimized to provide a superior stop band attenuation. Due to this property, the PHYDYAS PFF is a good choice for spectrum sharing scenarios such as NC-OFDM and cognitive radio. The discrete-time PFF $p[n]$ can be described by a truncated Fourier series with coefficients q_i according to [5]

$$p[n] = q_0 + 2 \sum_{i=1}^{\gamma-1} q_i \cos \left[\frac{2\pi i n}{\gamma K} \right]. \quad (3.23)$$

For $\gamma \in [3, 5]$, the coefficients q_i and the direction parameter β , the normalized direction parameter β_{norm} as well as the T-F-localization parameter ξ are given in Table 3.1 and the related ambiguity functions as well as the transferfunctions $F(\nu) = \mathcal{F}_n\{f[n]\}$ are depicted in Figure 3.4. From these results, it can be stated, that increasing the overlapping factor γ on the one hand improves the frequency selectivity of the PHYDYAS PFF, but on the other hand degrades the T-F localization.

3.3.2 EGF based IOTA

As mentioned before, the Gaussian PFF holds the property of ideal energy localization in the T-F plane, but does not satisfy the Nyquist constraints given by (2.15). Therefore, the IOTA is used to transform the non-orthogonal Gaussian function into a PFF which is orthogonal after matched filtering at the receiver [55]. Thereby, the localization property of the Gaussian function is kept. In [79] it is shown that the IOTA results in a closed-form expression based on the family of Extended Gaussian Functions (EGFs). In this thesis, the

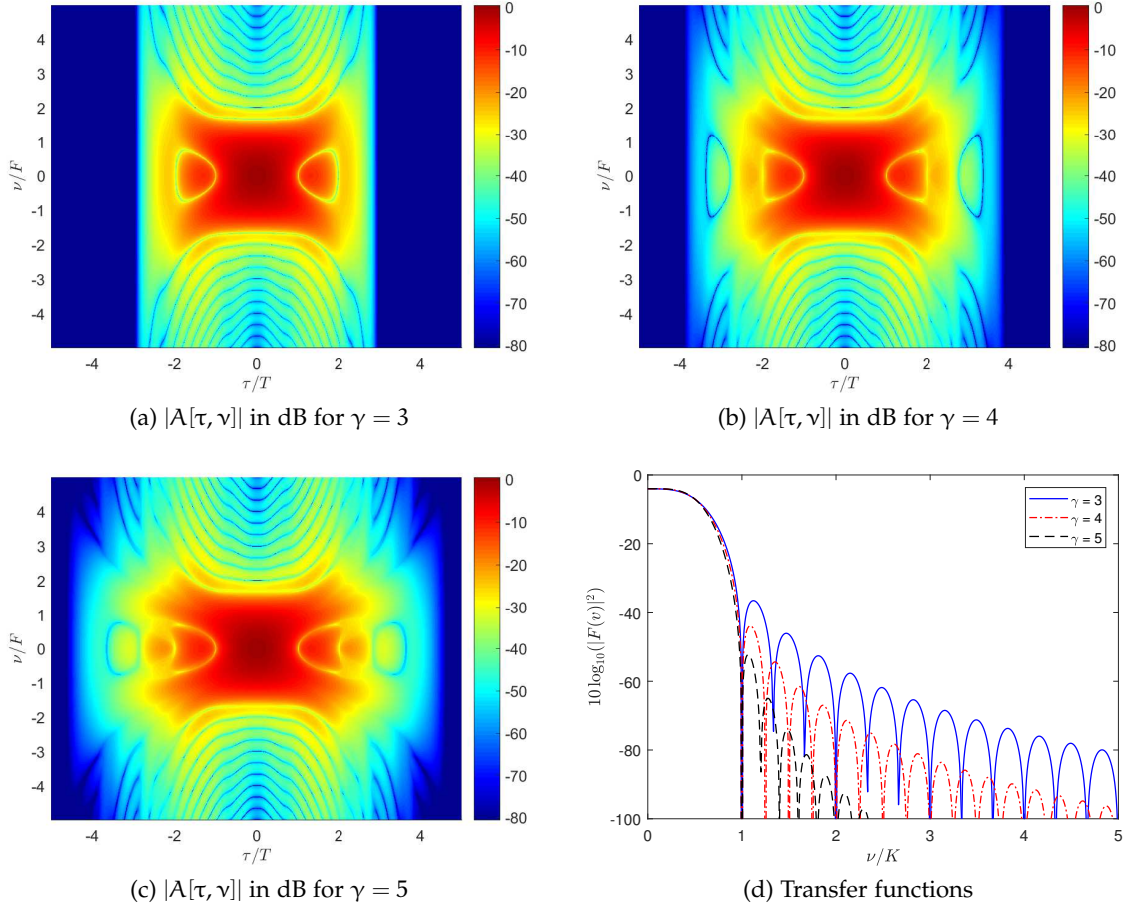


Figure 3.4: Ambiguity functions and the related transfer functions $F(\nu) = \mathcal{F}_n\{f[n]\}$ for PHYDYAS PFFs with $\gamma = [3, 5]$.

EGFs based closed-form solution proposed by Pierre Siohan et al. [92] is used to calculate the IOTA. It is given as

$$\begin{aligned}
 p[n, \alpha] = & \frac{1}{2} \sum_{i=0}^{\infty} q_{i, \alpha, \nu_0} \left(g_{\alpha} \left[\frac{n}{K} + \frac{i}{\nu_0} \right] + g_{\alpha} \left[\frac{n}{K} - \frac{i}{\nu_0} \right] \right) \\
 & \cdot \sum_{i'=0}^{\infty} q_{i', 1/\alpha, \tau_0} \cos \left[\frac{2\pi i' n}{M_0} \right]
 \end{aligned} \tag{3.24a}$$

with

$$g_{\alpha}[n] = (2\alpha)^{\frac{1}{4}} e^{-\pi\alpha n^2} \tag{3.24b}$$

Here α is the spreading factor of the discrete-time square root of Gaussian function $g_{\alpha}[n]$, which is used to adjust the power spreading in the time-frequency grid. $q_{\{\cdot\}}$ are real valued weighting coefficients, which can be calculated as given in [92]. In this thesis, all coefficients $q_{\{\cdot\}}$ are calculated with the maximal available accuracy provided by [92].

γ	$\alpha = 1$			$\alpha = 2$			$\alpha = 3$		
	β	β_{norm}	ξ	β	β_{norm}	ξ	β	β_{norm}	ξ
3	0.77628	1.5526	0.80002	0.4994	0.9988	0.97611	0.35453	0.70905	0.93878
4	0.86007	1.7201	0.87249	0.49998	0.99995	0.97695	0.35453	0.70906	0.93878
5	0.87098	1.742	0.87254	0.5	1	0.97694	0.35453	0.70906	0.93878

Table 3.2: Direction and T-F localization parameters for the EGF PFF with $\alpha \in \{1, 2, 3\}$ and $\gamma \in [3, 5]$.

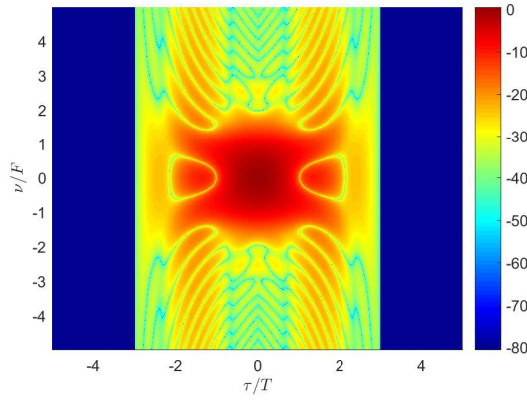
For the overlapping factor $\gamma \in [3, 5]$ and the spreading factor $\alpha \in [1, 3]$, the direction parameter β , the normalized direction parameter β_{norm} as well as the T-F-localization parameter ξ are given in Table 3.2 and the related ambiguity functions as well as the transfer functions $F(\nu) = \mathcal{F}_n\{f[n]\}$ are depicted in Figure 3.5. It can be stated, that increasing the overlapping factor γ reduces the spectral regrowth due to filter truncation, especially for $\alpha = 1$. It should be noted that the closed-form solution proposed in [92] is only strictly equivalent to the general solution presented in [2, 55] for

$$0.528\nu_0^2 \leq \alpha \leq \frac{1}{0.528\nu_0^2}. \quad (3.25a)$$

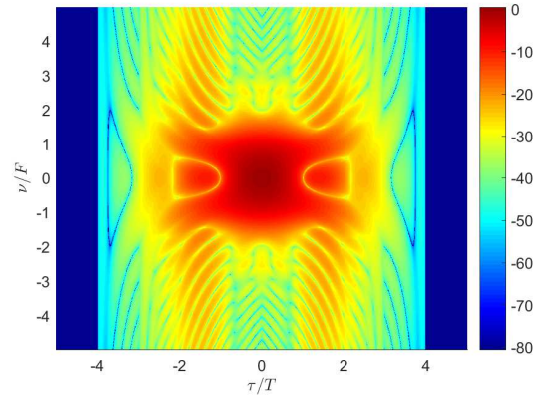
For FBMC-OQAM with $\nu_0 = 1$ this bound yields

$$0.528 \leq \alpha \leq 1.89, \quad (3.25b)$$

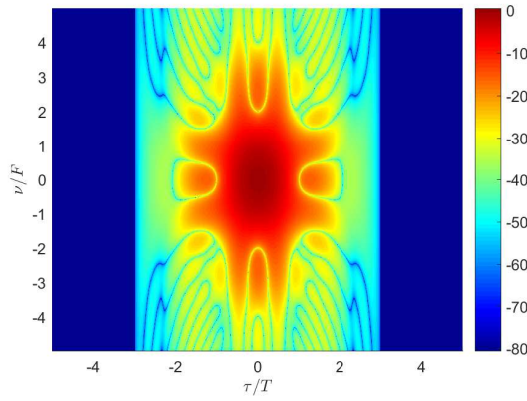
which shows that the presented closed-form solution for the IOTA is only optimal for PFFs with a direction parameter $\beta > 1$. As the localization parameter for $\alpha = \{2, 3\}$ is still significantly better than the one of the PHYDYAS PFF, this suboptimal solution of the IOTA is assumed to be suitable for further investigations.



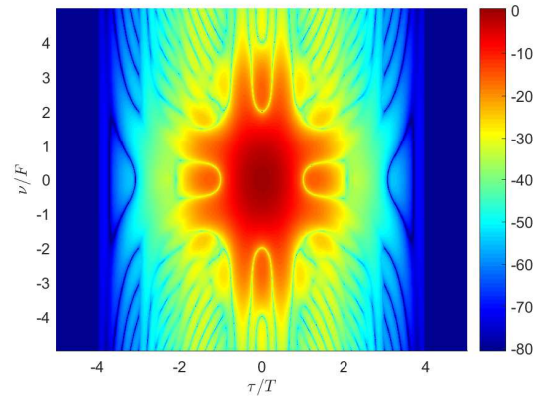
(a) $|A[\tau, \nu]|$ in dB for $\gamma = 3$ and $\alpha = 1$



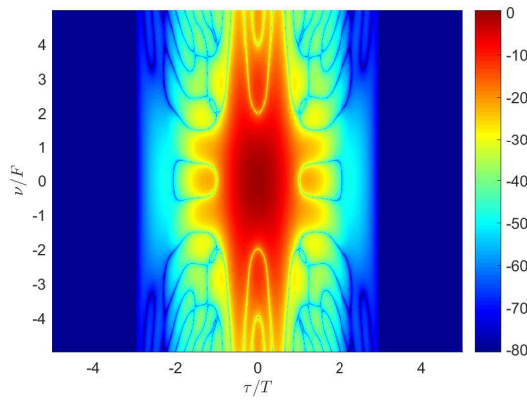
(b) $|A[\tau, \nu]|$ in dB for $\gamma = 4$ and $\alpha = 1$



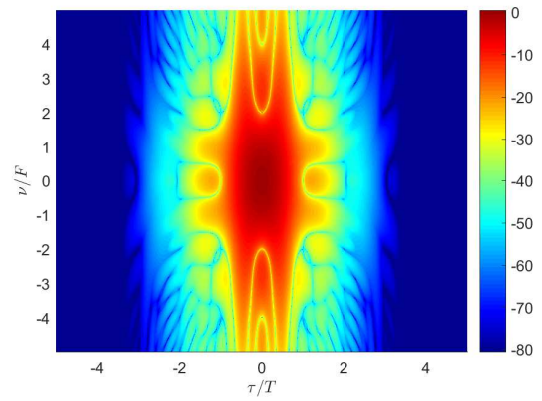
(c) $|A[\tau, \nu]|$ in dB for $\gamma = 3$ and $\alpha = 2$



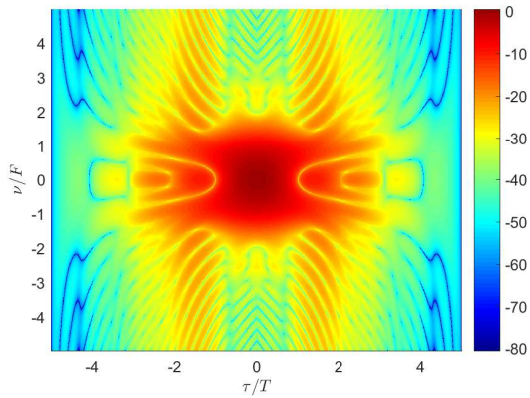
(d) $|A[\tau, \nu]|$ in dB for $\gamma = 4$ and $\alpha = 2$



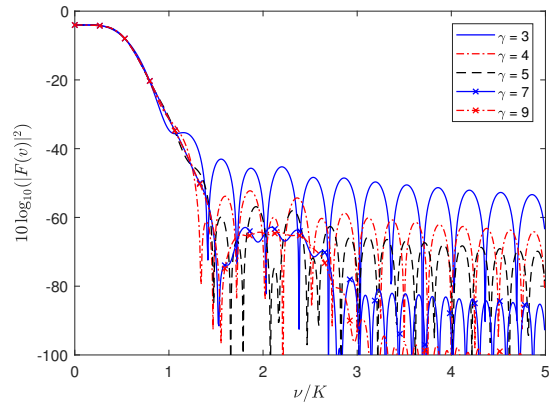
(e) $|A[\tau, \nu]|$ in dB for $\gamma = 3$ and $\alpha = 3$



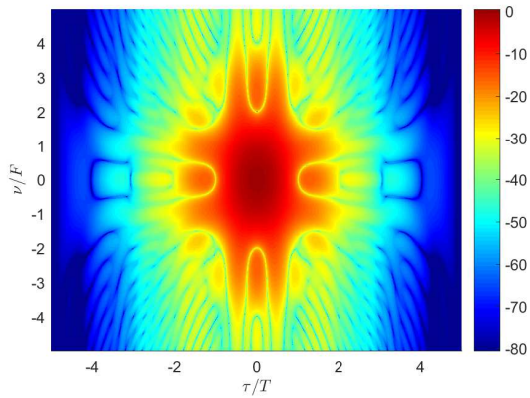
(f) $|A[\tau, \nu]|$ in dB for $\gamma = 4$ and $\alpha = 3$



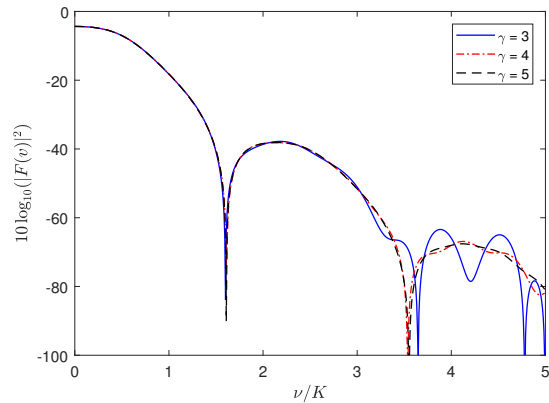
(g) $|A[\tau, \nu]|$ in dB for $\gamma = 5$ and $\alpha = 1$



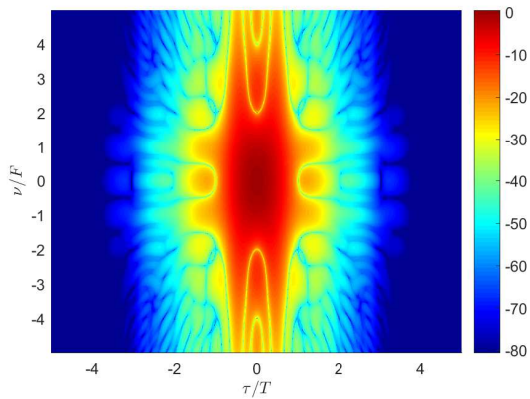
(h) Transfer functions for $\alpha = 1$



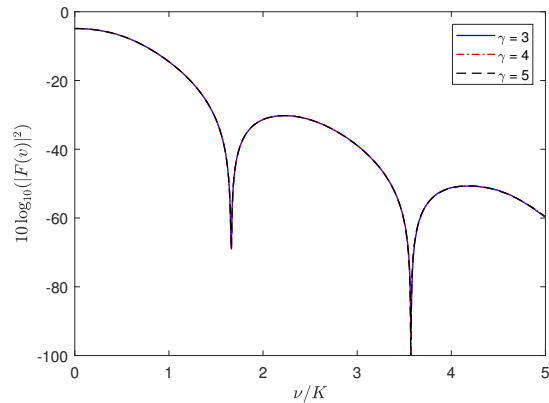
(i) $|A[\tau, \nu]|$ in dB for $\gamma = 5$ and $\alpha = 2$



(j) Transfer functions for $\alpha = 2$



(k) $|A[\tau, \nu]|$ in dB for $\gamma = 5$ and $\alpha = 3$



(l) Transfer functions for $\alpha = 3$

Figure 3.5: Ambiguity functions for EGF PFFs with $\gamma = [3, 5]$ and $\alpha \in \{1, 2, 3\}$ as well as the related transfer functions $F(\nu) = \mathcal{F}_n\{f[n]\}$. To indicate the truncation effects for EGFs with $\alpha = 1$, the transfer functions for this configuration is plotted for $\gamma \in \{3, 4, 5, 7, 9\}$

q_0	q_4	q_8	q_{12}	q_{16}
1.185 089 9	$-2.290 172 1 \cdot 10^{-3}$	$-8.664 261 9 \cdot 10^{-6}$	$-3.738 021 9 \cdot 10^{-9}$	$1.145 201 4 \cdot 10^{-12}$

Table 3.3: Weighting factors q_{4i} for the calculation of the Hermite PFF given in (3.26).

$\gamma = 3$			$\gamma \in \{4, 5\}$		
β	β_{norm}	ξ	β	β_{norm}	ξ
0.499 98	0.999 96	0.979 62	0.5	1	0.979 65

Table 3.4: Direction and T-F localization parameters of the Hermite PFF for $\gamma \in [3, 5]$.

3.3.3 Hermite

Similar to the IOTA PFF the Hermite PFF is based on orthogonalization of the Gaussian function. However, until now there exists only an isotropic solution for the Hermite PFF. To build the Hermite PFF, the Gaussian function is weighted with isotropic Hermite functions to achieve orthogonality at the required positions in the T-F plane [43]:

$$p[n] = \sum_{i=0}^{N_H-1} q_{4i} H_{4i} \left(2\sqrt{\pi} \frac{n}{K} \right) \quad (3.26a)$$

with

$$H_i[n] = e^{-\frac{n^2}{2}} \left[\frac{d^i}{dt^i} e^{-\left(\frac{t}{T_s}\right)^2} \right]_{t=nT_s}. \quad (3.26b)$$

Here, q_{4i} are the weighting factors reported in [43] and shown in Table 3.3, $\frac{d^i}{dt^i}$ is the i -th derivation with respect to t and $N_H = 4$ is the number of isotropic Hermite functions used to construct the Hermite PFF. For $\gamma \in [3, 5]$, the coefficients q_i and the direction parameter β , the normalized direction parameter β_{norm} as well as the T-F-localization parameter ξ are given in Table 3.4 and the related ambiguity functions as well as the transfer functions $F(\nu) = \mathcal{F}_n\{f[n]\}$ are depicted in Figure 3.6. The results show, that the Hermite PFF provides a slightly better localization property compared to the isotropic EGF PFFs ($\alpha = 2$), in case both PFF are truncated to the same filter length L_p .

3.3.4 Rectangular (CP-OFDM)

In CP-OFDM systems two different rectangular PFFs are applied. On RX side a standard rectangular function as defined in (3.15) and at the TX an extended rectangular function according to (3.18) are used. It is well-known that the transfer function of a rectangular

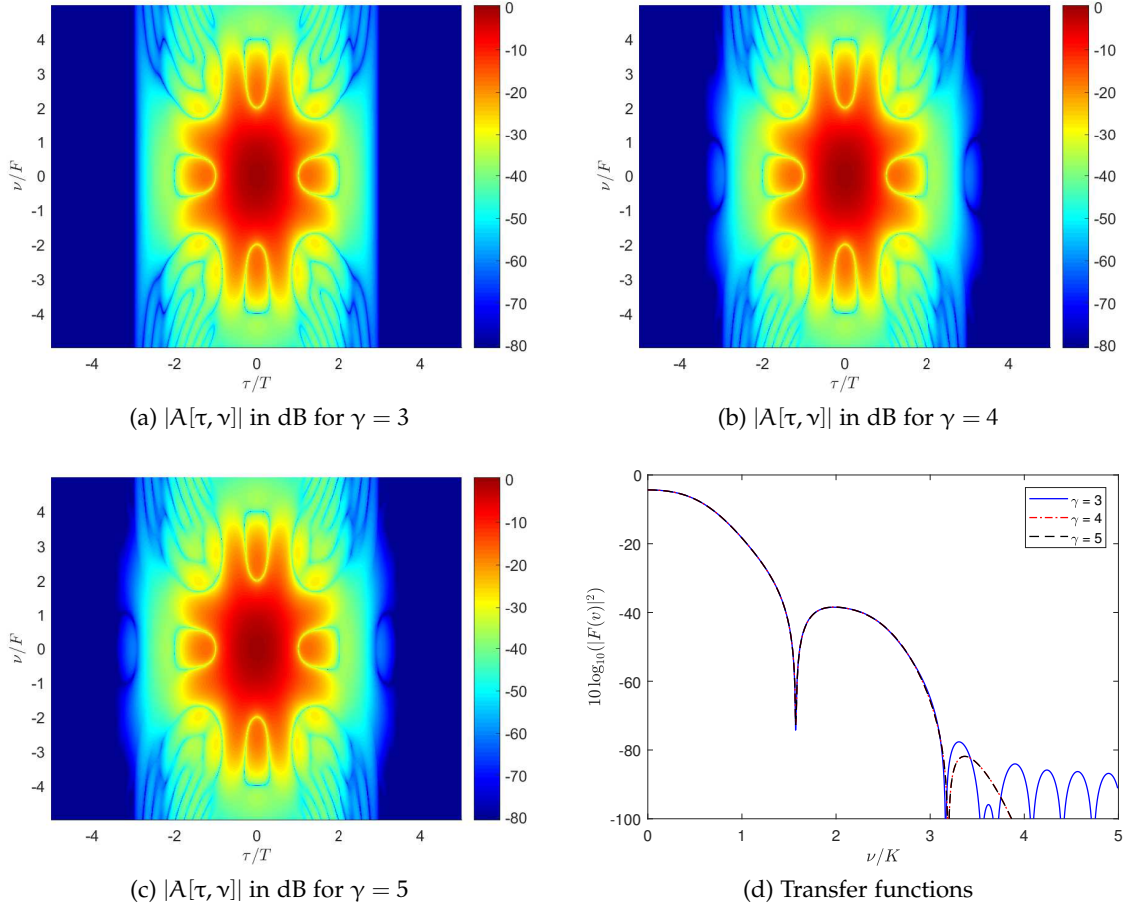


Figure 3.6: Ambiguity functions for Hermite PFFs with $\gamma = [3, 5]$ and the related transfer functions $F(\nu) = \mathcal{F}_n\{f[n]\}$.

function is the sinc function, which has a normalized central second-order moment of infinity:

$$\begin{aligned}
 \sigma_f &= \sqrt{\mathbf{M}_2 \left\{ \left| \frac{T + T_{CP}}{T} \operatorname{sinc} \left(\omega \frac{T + T_{CP}}{2} \right) \right| \right\}} \\
 &= \sqrt{\int_{-\infty}^{\infty} f^2 \left| \operatorname{sinc} \left(2\pi f \frac{T + T_{CP}}{2} \right) \right|^2 df} \\
 &= \frac{1}{2\pi \frac{T + T_{CP}}{2}} \sqrt{\int_{-\infty}^{\infty} \left| \sin \left(2\pi f \frac{T + T_{CP}}{2} \right) \right|^2 df} \\
 &= \infty.
 \end{aligned} \tag{3.27a}$$

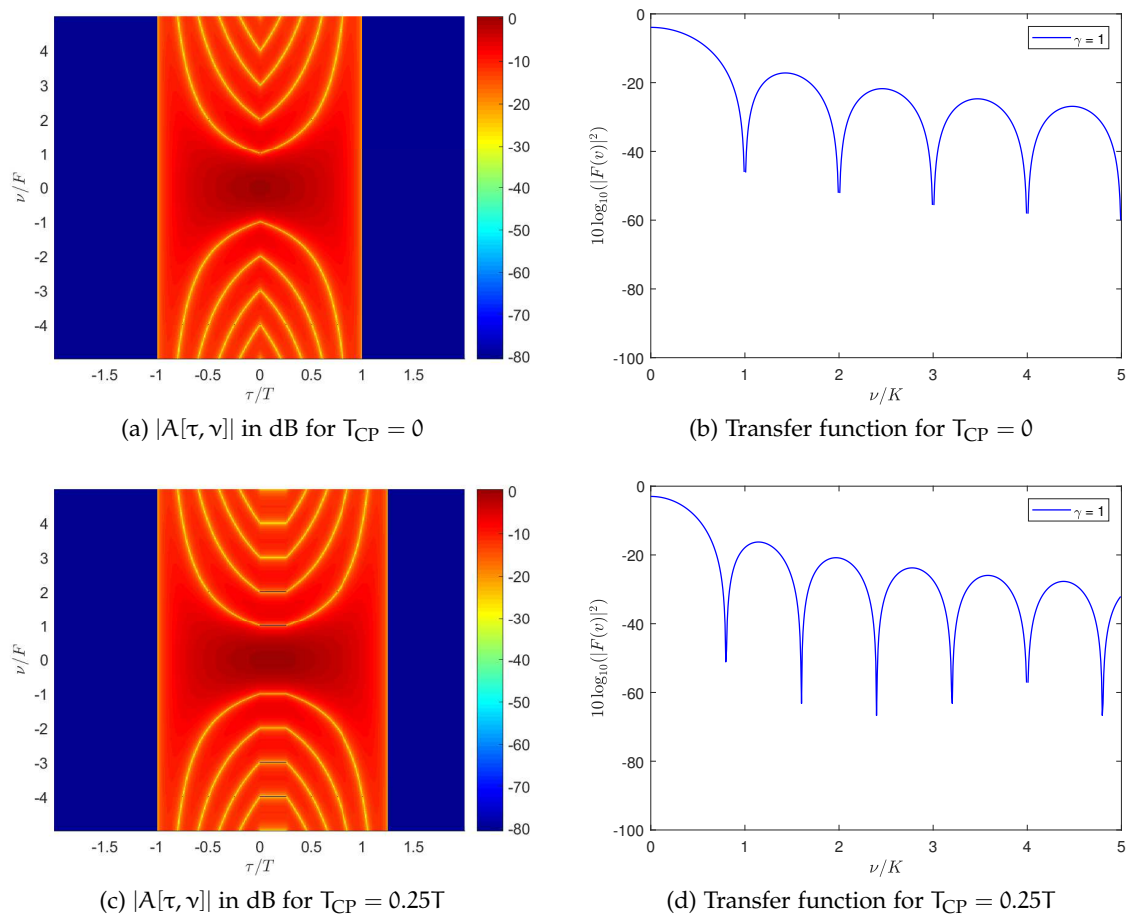


Figure 3.7: Ambiguity functions for rectangular PFFs with $T_{CP}/T \in \{0, 0.25\}$ and the related transfer functions $F(\nu) = \mathcal{F}_n\{f[n]\}$.

Thus, both the direction parameter β and the T-F localization ξ of the rectangular function are given as

$$\beta = 0 \quad (3.27b)$$

$$\xi = 0. \quad (3.27c)$$

For completeness, Figure 3.7 depicts the ambiguity and transfer functions for $T_{CP} = 0$ and $T_{CP} = 0.25T$. Comparing these pictures with the ones of the PFF discussed for FBMC-OQAM, both the high energy spreading and out-of-band radiation of CP-OFDM are evident.

3.4 RECONSTRUCTION PERFORMANCE

In Section 2.1.3 a general constraint for the design of communication systems has been given, which however lacks an exact definition. To enable a measure for a fair comparison of the performance of different MC modulation schemes and PFFs in the presence of (doubly) dispersive channels, the reconstruction performance in terms of SIR has been proposed. It considers the amount of useful signal power σ_S^2 as well as the quantity of intrinsic interference power σ_I^2 induced by the demodulation in the AFB at the receiver. Similar to the well-known SNR, the SIR is defined as the ratio of these powers:

$$\text{SIR} = \frac{\sigma_S^2}{\sigma_I^2}. \quad (3.28)$$

It considers both the useful and interfering power which can be exploited or has to be tackled by the receiver, respectively. Therefore, the SIR can be considered to be a useful measure to optimize the system configuration in terms of symbol duration T , applied PFF, required channel equalizer complexity and channel coding.

3.4.1 CP-OFDM

Considering the definition of the useful signal $\check{\alpha}_{\tilde{m},\tilde{k}}$ and interference signal part $i_{\tilde{m},\tilde{k}}$ given in (3.7), the SIR of CP-OFDM systems is given by

$$\text{SIR} = \frac{\mathbf{E} \left[|\check{\alpha}_{\tilde{m},\tilde{k}}|^2 \right]}{\mathbf{E} \left[|i_{\tilde{m},\tilde{k}}|^2 \right]}, \quad (3.29a)$$

which, referring to Appendix A.3, yields

$$\text{SIR} = \frac{\sum_{l=0}^{L-1} \int_{-f_D T_s}^{f_D T_s} S[\tau_l, \nu] |A_{0,0}[\tau_l, \nu]|^2 d\nu}{\sum_{(\mu,\kappa) \in \mathcal{S}_N} \sum_{l=0}^{L-1} \int_{-f_D T_s}^{f_D T_s} S[\tau_l, \nu] |A_{\mu,\kappa}[\tau_l, \nu]|^2 d\nu}. \quad (3.29b)$$

3.4.2 FBMC-OQAM

As stated before each received FBMC-OQAM symbol consists of a desired part $\check{\alpha}_{\tilde{m},\tilde{k}}$ and intrinsic interference $i_{\tilde{m},\tilde{k}}$, which for non-dispersive propagation channels can be removed perfectly considering the real part after demodulation and channel equalization. Thus, the real and imaginary parts of the received FBMC-OQAM symbols can be denoted as

quasi-orthogonal data and interference spaces, respectively, which are defined by the corresponding parts of the ambiguity function.

$$\begin{aligned}
\tilde{a}_{\tilde{m},\tilde{k}} &= \underbrace{\sum_{l=0}^{L-1} \int_{-f_D T_s}^{f_D T_s} D[\tau_l, \nu] e^{j2\pi\tilde{m}M_0\nu} \sum_{(\mu,\kappa) \in \mathcal{S}} a_{\tilde{m}+\mu, \tilde{k}+\kappa} \Re\left\{\theta_{\mu,\kappa} A_{\mu,\kappa}^{\tilde{k}}[\tau_l, \nu]\right\} d\nu}_{\text{data space } (\tilde{s}_{\tilde{m},\tilde{k}})} \\
&+ j \underbrace{\sum_{l=0}^{L-1} \int_{-f_D T_s}^{f_D T_s} D[\tau_l, \nu] e^{j2\pi\tilde{m}M_0\nu} \sum_{(\mu,\kappa) \in \mathcal{S}} a_{\tilde{m}+\mu, \tilde{k}+\kappa} \Im\left\{\theta_{\mu,\kappa} A_{\mu,\kappa}^{\tilde{k}}[\tau_l, \nu]\right\} d\nu}_{\text{interference space}}.
\end{aligned} \tag{3.30}$$

To provide a fair comparison with CP-OFDM, which is not subject to an interference space, it is reasonable that the calculation of the reconstruction performance at the AFB of FBMC-OQAM systems only evaluates the signal part $\tilde{s}_{\tilde{m},\tilde{k}}$ lying in the data space.

$$\begin{aligned}
\tilde{s}_{\tilde{m},\tilde{k}} &= \sum_{l=0}^{L-1} \int_{-f_D T_s}^{f_D T_s} D[\tau_l, \nu] e^{j2\pi\tilde{m}M_0\nu} \sum_{(\mu,\kappa) \in \mathcal{S}} a_{\tilde{m}+\mu, \tilde{k}+\kappa} \Re\left\{\theta_{\mu,\kappa} A_{\mu,\kappa}^{\tilde{k}}[\tau_l, \nu]\right\} d\nu \\
&= a_{\tilde{m},\tilde{k}} \underbrace{\sum_{l=0}^{L-1} \int_{-f_D T_s}^{f_D T_s} D[\tau_l, \nu] e^{j2\pi\tilde{m}M_0\nu} \Re\left\{A_{0,0}^{\tilde{k}}[\tau_l, \nu]\right\} d\nu}_{\tilde{s}_{\tilde{m},\tilde{k}}} \\
&+ \underbrace{\sum_{(\mu,\kappa) \in \mathcal{S}_N} a_{\tilde{m}+\mu, \tilde{k}+\kappa} \sum_{l=0}^{L-1} \int_{-f_D T_s}^{f_D T_s} D[\tau_l, \nu] e^{j2\pi\tilde{m}M_0\nu} \Re\left\{\theta_{\mu,\kappa} A_{\mu,\kappa}^{\tilde{k}}[\tau_l, \nu]\right\} d\nu}_{\hat{i}_{\tilde{m},\tilde{k}}}.
\end{aligned} \tag{3.31}$$

Thus, considering the useful signal $\tilde{s}_{\tilde{m},\tilde{k}}$ and interference signal $\hat{i}_{\tilde{m},\tilde{k}}$ lying in the data space, the SIR of FBMC-OQAM systems is given by

$$\text{SIR} = \frac{\mathbb{E}\left[|\tilde{s}_{\tilde{m},\tilde{k}}|^2\right]}{\mathbb{E}\left[|\hat{i}_{\tilde{m},\tilde{k}}|^2\right]}, \tag{3.32a}$$

which yields

$$\text{SIR} = \frac{\sum_{l=0}^{L-1} \int_{-f_D T_s}^{f_D T_s} |S[\tau_l, \nu]| \Re\left\{A_{0,0}^{\tilde{k}}[\tau_l, \nu]\right\}^2 d\nu}{\sum_{(\mu,\kappa) \in \mathcal{S}_N} \sum_{l=0}^{L-1} \int_{-f_D T_s}^{f_D T_s} |S[\tau_l, \nu]| \Re\left\{\theta_{\mu,\kappa} A_{\mu,\kappa}^{\tilde{k}}[\tau_l, \nu]\right\}^2 d\nu}. \tag{3.32b}$$

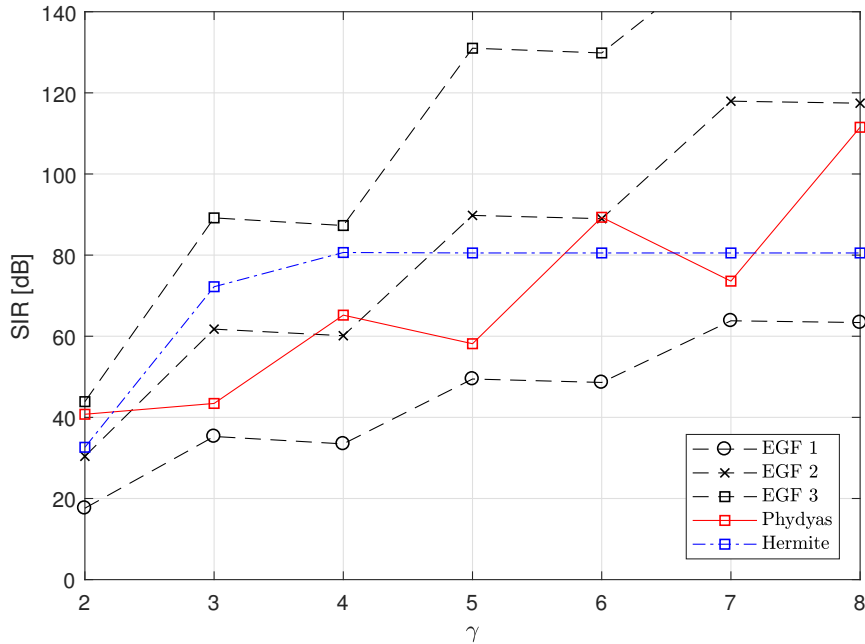


Figure 3.8: Reconstruction performance of FBMC-OQAM systems with different PFFs in dependence on the overlapping factor γ in an AWGN channel.

A similar representation of the SIR in matrix notation based on correlation of the time-variant CIR $h[\tau, n]$ has been presented in [73]. It has to be noted that due to the complex nature of the ambiguity function not only the intrinsic interference from the interference space is spread to the data space but also some parts of the data space are spread to the interference space. Thus, compared to CP-OFDM the SIR of FBMC-OQAM systems comprises an additional power loss of the desired signal part. Sample SIR values for FBMC-OQAM systems in AWGN channels, i.e. $S[\tau_l, \nu] = \delta[\tau_l]\delta(\nu)$, utilizing PFFs discussed in Section 3.3 are depicted in Figure 3.8 and discussed in the following sections.

3.5 CONSIDERATIONS ON THE SIR IN DOUBLY DISPERSIVE CHANNELS

As discussed in the previous section, the reconstruction performance of a communication system on one hand depends on the applied PFF as well as the deployed lattice grid. On the other hand, the SIR is influenced by the second order statistics of the underlying channel, i.e. the channel scattering function $S[\tau, \nu]$. In literature a manifold amount of channel models with arbitrary fading characteristics and complexity is described. Referring to the problem statement of this thesis, the focus of the presented investigations is in the context of cellular networks. Therefore, the channel model used here relies upon the Rayleigh fading channel model with exponential decay PDP and Jakes DPSD $P_D(\nu)$, which is frequently used to model communication channels, especially for cellular networks [20, 26]. To enable a more straightforward performance comparison within this thesis, the channel scenarios defined in [20] are mapped onto a common WSSUS channel model

based on Rayleigh fading as shown in Appendix B. The related discrete-time models are given by [67]:

$$\text{Exponential decay PDP} \quad P_h[\tau] = \frac{1}{\frac{\tau_{\text{rms}}}{T_s}} e^{-\frac{\tau T_s}{\tau_{\text{rms}}}} = \frac{1}{K\tau_{\text{rms}}/T} e^{-\frac{\tau}{K\tau_{\text{rms}}/T}} \quad (3.33a)$$

$$\begin{aligned} \text{Jakes DPSD} \quad P_D(\nu) &= \frac{1}{\pi f_D T_s \sqrt{1 - \left(\frac{\nu}{f_D T_s}\right)^2}} \\ &= \frac{K}{\pi f_D T \sqrt{1 - \left(\frac{K\nu}{f_D T}\right)^2}}. \end{aligned} \quad (3.33b)$$

With the WSSUS assumption, the related channel scattering function is defined as

$$S[\tau, \nu] = P_h[\tau]P_D(\nu). \quad (3.34a)$$

Thus, for the tapped-delay line model used here the channel scattering function yields

$$S[\tau, \nu] = \sum_{l=0}^{L-1} \frac{1}{\pi\tau_{\text{rms}}f_D} e^{-\frac{\tau_l}{K\tau_{\text{rms}}/T}} \frac{1}{\sqrt{1 - \left(\frac{K\nu}{f_D T}\right)^2}} \delta[\tau - \tau_l]. \quad (3.34b)$$

An important insight obtained from (3.34b) is the fact that the channel scattering function $S[\tau, \nu]$ can be described as a function of the normalized delay spread τ_{rms}/T and normalized maximum Doppler shift $f_D T$. Thus, the SIR of a transmission system does not depend on the actual real world channel and system parameters T , τ_{rms} and f_D , but on their relation to each another, which enables a generalized analysis of CAW.

Exemplary results for the resulting reconstruction performance of CP-OFDM with a Cyclic Prefix length of 7% (CP length of LTE) and FBMC-OQAM systems with the PFFs discussed in Section 3.3 are depicted in Figure 3.9. Here, contour plots are selected to ease the analysis of the underlying three-dimensional data. Having a more detailed look on the SIR results presented in Figure 3.9 one can see, that compared to FBMC-OQAM the CP significantly improves the robustness to multipath channels and thus is superior over FBMC-OQAM as long as the delay spread τ_{rms} is less than about 1% of the symbol duration T . In case the delay spread increases, the SIR of CP-OFDM systems decreases considerably and FBMC-OQAM can provide a better reconstruction performance.

For FBMC-OQAM the figures show the dependence of the SIR on the utilized PFF as predicted by theory (cf. Section 2.1.3). The more a PFF is spread in TD, the larger is the robustness against multipath propagation and the higher is the vulnerability against Doppler spread. As the investigated PDP and DPSD are of different shape, the contour plots of the SIR for the isotropic PFF (here: Hermite and EGF with $\alpha = 2$) do not show any symmetry properties.

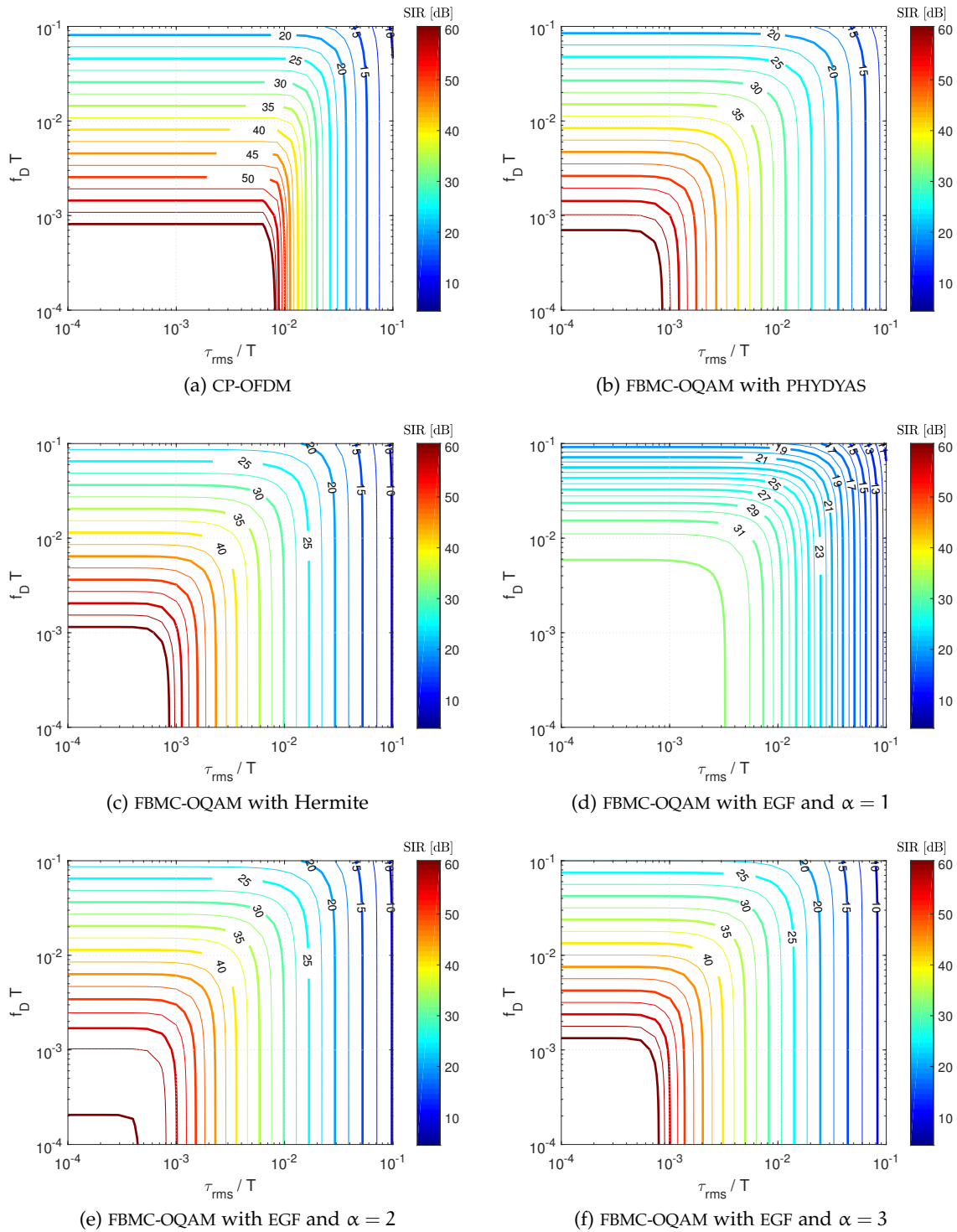


Figure 3.9: SIR in dB for CP-OFDM with $T_{CP}/T = 0.07$ and FBMC-OQAM for overlapping factor $\gamma = 4$, $K = 256$ and different PFFs.

The type of presentation used in Figure 3.9 (irrespective to the measure, e.g. SIR, BER, etc.) can be used in several ways to analyze the influence of varying system or channel parameters on the system performance. These are briefly described in the following:

VERTICAL SECTIONS can be used to analyze the influence of the subcarrier spacing $1/T$, user velocity or carrier frequency in a certain environment. Therefore, the normalized delay spread τ_{rms}/T is kept constant and the normalized maximum Doppler shift $f_D T$, which is a function of the user velocity v and the carrier frequency f_c is varied. With the speed of light c , this well-known relationship is given by [67]

$$f_D T = f_c \frac{v}{c} T. \quad (3.35)$$

This analysis method has been carried out in [35]. Therein, the performance in terms of SIR, BER and data rate is compared for LTE like CP-OFDM and FBMC-OQAM systems operating in COST 207 channel environments [26].

HORIZONTAL SECTIONS are useful to investigate the influence of multipath propagation at a certain user velocity and normalized maximum Doppler shift. On one hand horizontal sections can be used to analyze the performance of a communication system with a defined symbol duration which is deployed in different channel environments. On the other hand, these kinds of sections are useful to examine the effects of tuning the symbol duration of a communication system for a given delay spread.

DIAGONAL SECTIONS provide a special tool for the investigation of CAW, which is briefly derived in the following. Any linear section in the discussed type of plots can be described by the definition of a linear function with arbitrary slope C_m and ordinate intercept C_s :

$$\begin{aligned} \log_{10}(f_D T) &= C_m \log_{10}(\tau_{\text{rms}}/T) + C_s \\ \Leftrightarrow \log_{10}(f_D) + \log_{10}(T) &= C_m \log_{10}(\tau_{\text{rms}}) - C_m \log_{10}(T) + C_s \\ \Leftrightarrow \log_{10}(f_D) + (1 + C_m) \log_{10}(T) &= C_m \log_{10}(\tau_{\text{rms}}) + C_s. \end{aligned} \quad (3.36a)$$

For the slope $C_m = -1$, the section is completely characterized by the delay-Doppler product δ of a channel given by

$$\delta = f_D \tau_{\text{rms}} \quad (3.36b)$$

and therefore independent of the symbol duration T :

$$\begin{aligned}
 & \log_{10}(f_D) + \log_{10}(\tau_{\text{rms}}) = C_s \\
 \Leftrightarrow & \log_{10}(f_D \tau_{\text{rms}}) = C_s \\
 \Leftrightarrow & \log_{10}(\delta) = C_s \quad . \quad (3.36c)
 \end{aligned}$$

Thus, diagonal sections with a slope of -1 can either be used to investigate a communication system operating in channels with a common delay-Doppler product and identical Doppler Power Spectral Density (PSD) and PDP shapes, or to examine the performance in a defined channel in dependence on the selected symbol duration T . The latter property of the diagonal sections renders them a perfect choice to examine the influence of the symbol duration T on the performance of a communication system which is operating in a defined transmission scenario (CASS), in which the carrier frequency f_c , user velocity v and channel properties, i.e. Doppler PSD and PDP, are well known. It has to be noted that for CP-OFDM systems the diagonal sections are of limited use. In CP-OFDM systems, the CP length is usually selected in dependence on the present delay spread of a channel to minimize the intrinsic interference induced by multi-path propagation. This design constraint in CP-OFDM conflicts with the investigation purpose of the diagonal sections, i.e. influence of the symbol duration, thus resulting in a two-dimensional optimization problem.

In Figure 3.10, exemplary diagonal sections for FBMC-OQAM systems with the PHYDYAS PFF operating in LTE related channel environments [20] are depicted. The results presented here indicate that a “one-fits-all” system design approach only provides suboptimal SIR performance in many practical channel scenarios. As already stated in Section 2.1.3 the waveform should be matched to the channel properties to improve the performance of communication systems which operate in heterogeneous channel environments. In practical systems this can be implemented by two different approaches:

- *Homogeneous CAW* - A single symbol duration and PFF configuration is applied to all users in a cell which covers homogenous user behavior and channel property distributions.
- *Heterogeneous CAW* - A specific symbol duration and PFF configurations is applied for every user or user group in a cell with heterogeneous user behavior and channel property distributions. Each group of users with similar behavior and channel properties may utilize the same symbol duration and PFF configuration.

The gains of the different CAW implementation approaches in terms of SIR, BER and system capacity are investigated in the following chapters.

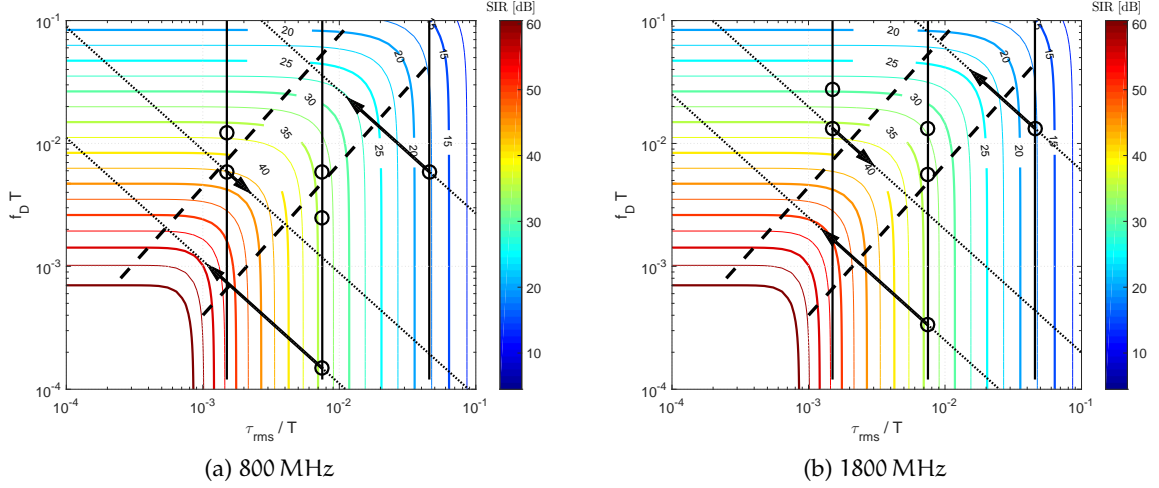


Figure 3.10: SIR as a function of the normalized delay spread τ_{rms}/T and normalized maximum Doppler shift $f_D T$ of an FBMC-OQAM system with $K = 256$ subcarriers, operating in channels with exponential PDP and Jakes Doppler PSD. The vertical lines indicate the SIR values for the channel environments derived in Appendix B (left: Rax, middle: Tux, right: HTx), which are achievable by an LTE like system with standard conform symbol duration T . The circles show the resulting operation points for the default mobile speeds [20] at the typical frequency bands for LTE in Europe. The area between the dashed diagonals indicates the optimal operation region in terms of SIR after the AFB of an FBMC-OQAM system utilizing the PHYDYAS PFF. The dotted diagonals depict the SIR values for a certain operation point, if the symbol duration T of the LTE system is adjusted to maximize the SIR. The arrows indicate the direction of available SIR gains for the channel scenarios and user velocities investigated in this thesis (see Appendix B.2).

3.6 CONCLUDING REMARKS

In the previous sections a unified system model for FBMC-OQAM and CP-OFDM systems has been described. The effects on a symbol transmitted over doubly dispersive channels are characterized based on the (cross-)ambiguity function and the statistical properties of the communication channel. Various PFFs proposed for the application in FBMC-OQAM systems and their properties have been presented and the reconstruction performance or SIR for FBMC-OQAM and CP-OFDM has been defined and evaluated for AWGN and doubly dispersive channels.

Recalling Section 3.3, there exists a wide range of configurations to design FBMC-OQAM systems. As the investigation of all these parameter settings results in an unmanageable amount of outputs, it is beneficial to reduce this parameter space to an arguable set. For completeness, the relevant characteristics, namely direction parameter, T-F localization and reconstruction performance, of the parameter settings under discussion, i.e. PFF and overlapping factor, are summarized in Table 3.5.

To avoid a noticeable degradation in system performance such as BER, the SIR beyond the AFB should be significantly higher than the SNR (i.e. greater than 10 dB). For cur-

PPF	γ	β_{norm}	ξ	SIR in AWGN [dB]	spreading type
PHYDYAS	3	1.6	0.89059	43.43	TD
	4	1.6739	0.88389	65.2	
	5	1.765	0.86715	58.15	
EGF $\alpha = 1$	3	1.5526	0.80002	35.29	
	4	1.7201	0.87249	33.46	
	5	1.742	0.87254	49.46	
Hermite	3	0.99996	0.97962	72.21	isotropic
	4	1	0.97965	80.64	
	5	1	0.97965	80.53	
EGF $\alpha = 2$	3	0.9988	0.97611	61.75	
	4	0.99995	0.97695	60.13	
	5	1	0.97694	89.79	
EGF $\alpha = 3$	3	0.70905	0.93878	89.18	FD
	4	0.70905	0.93878	87.3	
	5	0.70906	0.93878	131	
Rectangular		0	0	∞	

Table 3.5: Key characteristics of the PFFs discussed in Section 3.3

rent mobile communication systems such as LTE Advanced Pro [75] and 2nd generation Terrestrial Digital Video Broadcasting (DVB-T2), the highest modulation order in DL is 256-QAM. In dependence on the applied channel coding, a sufficient uncoded BER can be assumed to be in the range of $1 \cdot 10^{-2}$ to $1 \cdot 10^{-1}$, which requires an SINR of approximately 21 to 28 dB (AWGN) and 24 to 36 dB (Rayleigh) (cf. Table 4.3), respectively. For SNR limited transmissions, this requires an SIR which is significantly larger than the necessary SNR. Here, an error of

$$1 - \frac{\text{SINR}}{\text{SNR}} < 0.1 \quad (3.37)$$

is considered to be acceptable, which requires an SIR larger than 46 dB. This can be achieved approximately by all PFFs and overlapping factors, except for the EGF with $\alpha = 1$. As the PHYDYAS PFF has similar properties in terms of T-F localization and direction parameter in combination with a significantly improved reconstruction performance, the EGF with $\alpha = 1$ will not be considered for investigation within this thesis. To preserve the possibility of adjusting systems to a channel scenario which requires a TD spread PFF ($\beta_{\text{norm}} > 1$), the PHYDYAS PFF is considered within this thesis. As it has an SIR for $\gamma = 3$ of only approximately 43 dB in AWGN channels, this value for the overlapping factor γ will not be investigated in this thesis, as it can be supposed to provide an insufficient performance in (doubly) dispersive channels. From implementation point of view,

a small overlapping factor is preferable to reduce hardware cost and power consumption of mobile devices. On the contrary, higher values for the overlapping factor in general improve the reconstruction performance and reduce the out-of-band emissions (compare Table 3.5, Figure 3.8 and Section 3.3). However, selecting $\gamma = 5$ for the remaining PFFs only improves the related characteristics in a range which is of little practical relevance. Thus, in this thesis the overlapping factor is selected to be $\gamma = 4$, as it provides a good compromise between implementation costs and provided PFF characteristics.

A comparison of the direction and T-F localization parameters as well as the SIR of the EGF with $\alpha = 2$ and Hermite PFFs shows that all these characteristics can be considered as identical for both PFF except for the reconstruction performance. For $\gamma = 4$, the Hermite PFF provides a significantly higher SIR. Thus, in this thesis only the PHYDYAS, the EGF with $\alpha = 3$ and the Hermite PFFs are considered. Investigations and performance comparisons including all PFFs discussed in Section 3.3 are provided in [34–36].

In this chapter, the performance gains of CAW with homogeneous but environmental specific system configurations per cell are compared to the classical “one-fits-all” system design, in which all users in all cells utilize the same waveform (i.e. subcarrier spacing and PFF). Therefore, the reconstruction performance of the PFFs discussed in Section 3.3 is evaluated for practical doubly dispersive channels. This is followed by a system level analysis of the achievable performance gains in terms of uncoded BER and channel capacity with the assumption of perfect Channel State Information at the Receiver (CSIR). Afterwards, the influence of imperfect CSIR on the performance gains is determined for selected state-of-the-arts channel estimation algorithms and performance improvements are discussed briefly. All FBMC-OQAM related results are compared with the performance of an LTE like CP-OFDM system. Parts of the concepts and results presented in this chapter have been published in [32–34].

4.1 RECONSTRUCTION PERFORMANCE

By application of diagonal sections (see Section 3.5) to the reconstruction performance curves depicted in Figure 3.9, the SIR of FBMC-OQAM system with different PFFs operating in the same channel can be compared. For the channel scenarios $s_c = \{A, B, C\}$ defined in Appendix B.2, the resulting SIR curves are depicted in Figure 4.1. It should be noted that such kinds of plots provide two types of abscissas. At the bottom, the normalized delay spread is shown with increasing values from left to right. The corresponding abscissa for the normalized maximum Doppler shift is located at the top of the plots with increasing the values from right to left. For the abscissas, the upper bound is selected such that the delay spread τ_{rms} as well as the maximum Doppler shift f_D are restricted to a maximum of 10% of the symbol duration and subcarrier spacing, respectively. The related lower bounds are derived with the help of the delay-Doppler product δ . For reference, the vertical dashed and the horizontal purple lines indicate the normalized delay spread and reconstruction performance of a state-of-the-art CP-OFDM based LTE system, respectively.

The results presented in Figure 4.1 show three different effects, which may be relevant for the design of mobile communication systems. First, the performance differences for Doppler dominated scenarios, i.e. $f_D T > \tau_{\text{rms}} T$, and for multi-path propagation dominated scenarios, i.e. $f_D T < \tau_{\text{rms}} T$, is unbalanced. This mismatch can be explained by the different shapes of the PDP, the DPSD and the ambiguity functions of the PFFs, which additionally lead to curves with disparate slopes. Second, according to the results all

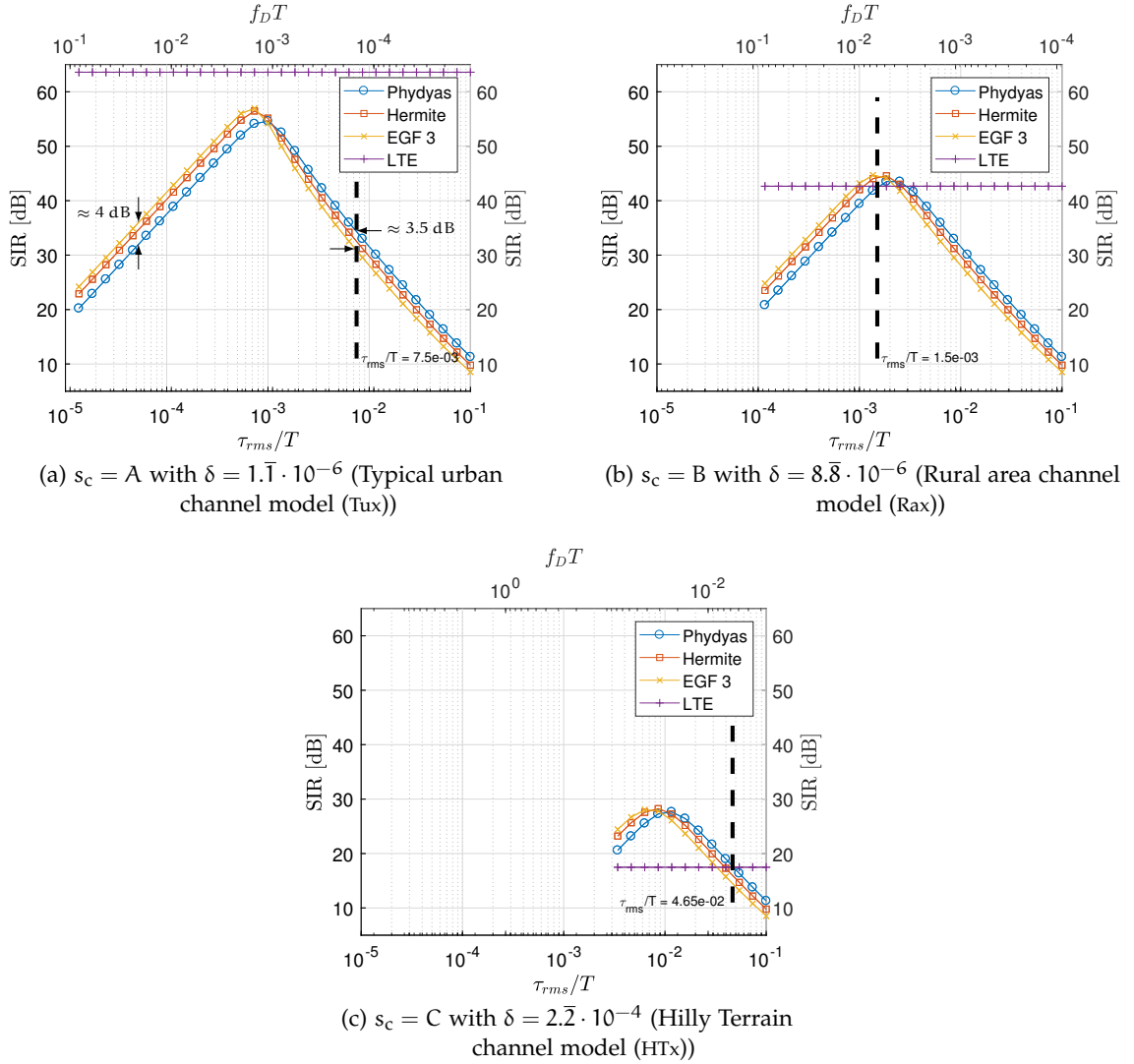


Figure 4.1: SIR of FBMC-OQAM systems in dependence on symbol duration T and channel scenarios s_c . The vertical dashed and the horizontal purple lines indicate the normalized delay spread and SIR of a state-of-the-art CP-OFDM based LTE system with $T_{CP} = 0.07T$.

investigated PFFs provide approximately the same maximum SIR, which may limit the usefulness of CAPS. A more in-depth analysis of this effect is provided in the subsequent sections of this thesis. The third outcome is that a common symbol duration configuration for FBMC-OQAM systems as for LTE results in severe SIR losses in channel scenarios A and C.

To enable a quantitative analysis of CAW based on the reconstruction performance, the SIR values for FBMC-OQAM and CP-OFDM systems with LTE parametrization ($T = 66.7 \mu\text{s}$) are provided in Table 4.1. A major conclusion to be drawn from these results is that a selection of the PFF according to the channel properties in combination with a fixed symbol duration (CAPS) can result in an SIR improvement of about 4 dB. This is assumed to be significant as it results in a considerable gain in BER and channel capacity (cf.

s_c	$\tau_{\text{rms}}/T_{\text{LTE}}$	SIR [dB]			LTE
		PHYDYAS	Hermite	EGF 3	
A	$7.5 \cdot 10^{-3}$	34.3	32.5	30.9	63.8
B	$1.5 \cdot 10^{-3}$	42.5	44.4	44.8	42.5
C	$4.5 \cdot 10^{-2}$	17.8	16.2	14.6	17.6

Table 4.1: SIR for an FBMC-OQAM or CP-OFDM based LTE system operating in channel scenarios s_c (ref. to Appendix B.2).

s_c	PFF	T_{opt} [μs]	$\tau_{\text{rms}}/T_{\text{opt}}$	SIR [dB]
A	PHYDYAS	546	$9.16 \cdot 10^{-4}$	54.8
	Hermite	651	$7.68 \cdot 10^{-4}$	56.5
	EGF 3	730	$6.85 \cdot 10^{-4}$	57.1
B	PHYDYAS	46	$2.16 \cdot 10^{-3}$	43.8
	Hermite	59	$1.71 \cdot 10^{-3}$	44.6
	EGF 3	68	$1.48 \cdot 10^{-3}$	44.8
C	PHYDYAS	280	$1.07 \cdot 10^{-2}$	27.7
	Hermite	358	$8.37 \cdot 10^{-3}$	28.3
	EGF 3	423	$7.09 \cdot 10^{-3}$	28.1

Table 4.2: SIR and corresponding $\tau_{\text{rms}}/T_{\text{opt}}$ in dependence on PFFs and channel scenarios.

Sections 4.2 and 4.3 as well as [33, 34]). Another important outcome is the fact, that suboptimal PFF selections result in considerable performance degradations.

As mentioned before, the SIR performance of FBMC-OQAM systems with LTE symbol duration is far from optimal in channel scenarios A and C. Only in scenario B, the achieved SIR is close to optimal. The SIR can be improved significantly by using the channel scenario specific symbol duration T_{opt} (CASS), which provides the maximum SIR for a given channel scenario and PFF. T_{opt} for an arbitrary PFF can be obtained by solving the following optimization problem:

$$T_{\text{opt}} = \arg \max_{T} \text{SIR}. \quad (4.1)$$

In this thesis, this optimization problem is solved numerically. Here, the normalized delay spread and maximum Doppler shift axes are sampled such that the differences of the selected optimum symbol duration T_{opt} to its predecessor and successor are less than 0.04 dB, which relates to an error smaller than $1 \cdot 10^{-2}$. The resulting optimal symbol durations T_{opt} , normalized delay spreads $\tau_{\text{rms}}/T_{\text{opt}}$ and reconstruction performance are summarized in Table 4.2. Compared to the reconstruction performance with LTE

parametrization, these results show SIR gains of about 24 dB and 11 dB in channel scenarios A and C, respectively, whereby the exact SIR gains depends on the applied PFF.

Comparing the reconstruction performance of FBMC-OQAM with state-of-the-art LTE shows that in urban scenarios CP-OFDM is superior to that of FBMC-OQAM due to the cyclic prefix and low Doppler spreads, even for the case that CASS is applied. However, for increased velocities (or carrier frequencies), the performance of CP-OFDM decreases significantly. For the investigated rural case with $v = 120$ km/h and a reduced delay spread compared to the urban scenario, FBMC-OQAM slightly outperforms CP-OFDM by approximately 2 dB. In the hilly terrain of channel scenario C, the performance of the LTE system is heavily deteriorated as the length of the CIR is longer than the CP. In this scenario, the performance of both MC modulation schemes provide a similar reconstruction performance.

4.2 SYSTEM LEVEL PERFORMANCE WITH PERFECT CSIR

The results discussed in the previous section indicate that the performance of FBMC-OQAM systems can be improved significantly by use of CAW. In this section, the effects of CAW on the BER are investigated. Therefore, the error floors for the uncoded BERs with perfect CSIR are evaluated using ZF equalization, which provides not only a lower performance bound but also offers a simple receiver structure. Additionally, the BER is evaluated in the absence of noise. A follow up discussion on the impacts of imperfect CSIR is provided in Section 4.4.

A major challenge for an analysis of the impact of communication channels on the system level performance is the dependency on the applied channel coding schemes, such as convolutional, turbo, Low Density Parity Check (LDPC) or polar codes based schemes, which has a severe influence on BERs and thus Frame Error Rates (FERs) and effective throughput. However, all channel coding schemes require a suitable uncoded BER to provide a sufficient BER improvement. Therefore, in this thesis the system level performance is carried out based on the uncoded BER.

A second challenge is the assessment of the practical relevance of the obtained BER values. For this purpose, the work flow depicted in Figure 4.2 is applied. To this, the performance curves of LTE systems in AWGN channels provided in [77] are considered. Assuming that the SNR values at the intersections of the throughput curves of consecutive MCS are used for switching between the in the communication system applied MCSs, one obtains the lower SINR bound for a certain MCS. Based on these SINR values, the upper BER bound for AWGN channels can be calculated [76]. Thereof, the lower SINR bound for Rayleigh channels can be derived by calculation of the BER curves [91]¹. In Table 4.3 the

¹ Here, the BERs in AWGN and Rayleigh fading channels are obtained by using the `BERAWGN` and `BERFADING` functions provided by Matlab.

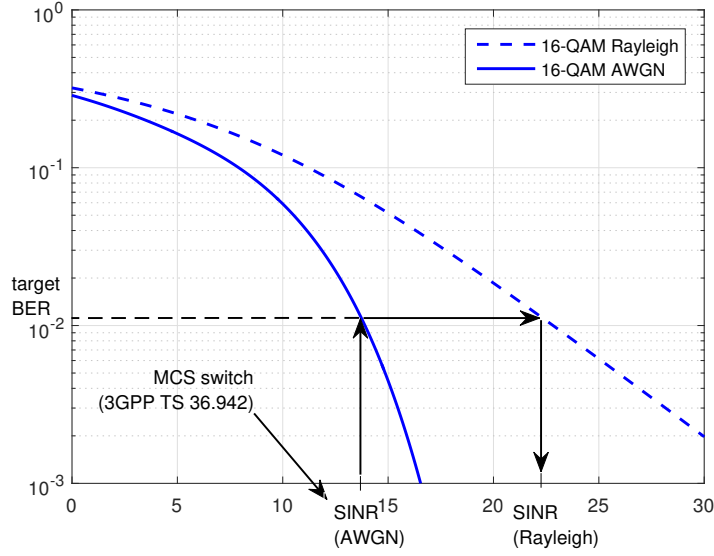


Figure 4.2: Work flow for the determination of practically relevant BER and SINR values for Rayleigh fading channels.

MCS along with the corresponding uncoded BER and SINR values are given. Based on these results, for the presented investigations a target uncoded BER of $5 \cdot 10^{-2}$ is considered.

4.2.1 Considerations for the practical relevance of the SIR gains

From this outcome, an upper SIR bound can be derived such that in the presence of noise the system performance is mainly limited by the SNR and not the SIR, i.e. $\text{SINR} \approx \text{SNR}$. The related necessary reconstruction performance values are summarized in Table 4.4. With the tolerated SINR error SINR_e defined by

$$\text{SINR} \geq (1 - \text{SINR}_e)\text{SNR} \quad (4.2a)$$

and (2.17), the upper SIR bound is obtained according to

$$\begin{aligned} (1 - \text{SINR}_e)\text{SNR} &\leq \frac{1}{\frac{1}{\text{SIR}} + \frac{1}{\text{SNR}}} \\ \Leftrightarrow \frac{1}{(1 - \text{SINR}_e)\text{SNR}} &\geq \frac{1}{\text{SIR}} + \frac{1}{\text{SNR}} \\ \Leftrightarrow \frac{1}{(1 - \text{SINR}_e)\text{SNR}} - \frac{1}{\text{SNR}} &\geq \frac{1}{\text{SIR}} \\ \Leftrightarrow \left(\frac{1}{(1 - \text{SINR}_e)} - 1 \right) \frac{1}{\text{SNR}} &\geq \frac{1}{\text{SIR}} \\ \Leftrightarrow \frac{\text{SINR}_e}{(1 - \text{SINR}_e)} \frac{1}{\text{SNR}} &\geq \frac{1}{\text{SIR}} \\ \Leftrightarrow \text{SIR} &\geq \text{SNR} \left(\frac{1}{\text{SINR}_e} - 1 \right). \end{aligned} \quad (4.2b)$$

M-QAM	MCS	SINR [dB] (AWGN)	QAM (uncoded)	SINR [dB] (Rayleigh)
4	1 to 7	-5.5 to 5	0.3 to $3.77 \cdot 10^{-2}$	-4.2 to 10.7
16	8 to 10	7 to 11.5	0.12 to $3.48 \cdot 10^{-2}$	10 to 17
64	11 to 13	14 to 17	$8 \cdot 10^{-2}$ to $3.57 \cdot 10^{-2}$	17.5 to 22

Table 4.3: Approximated SINR values in AWGN and Rayleigh fading channels and the related uncoded BERs required for $> 90\%$ throughput for certain LTE MCSs according to [77].

M-QAM	4	16	64	256	1024	4096
SINR [dB]	9.3	15.1	20.2	25.2	30.2	35.2
SIR [dB] (SINR _e = 10 %)	18.8	24.6	29.7	34.7	39.7	44.7
SIR [dB] (SINR _e = 1 %)	29.3	35.1	40.2	45.2	50.2	55.2

Table 4.4: Target SINR and related minimum SIR values for 1 % and 10 % SINR tolerance (SINR_e) for an uncoded BER of $5 \cdot 10^{-2}$ in Rayleigh fading channels.

SINR _e \ s _c	LTE			FBMC-OQAM (T _{LTE})			FBMC-OQAM (T _{opt})		
	A	B	C	A	B	C	A	B	C
10 %	> 4096	1024	4	256	4096	4	> 4096	4096	64
1 %	> 4096	64	< 4	16	256	< 4	4096	256	4

Table 4.5: Estimated available modulation order M in dependence on the channel scenario and tolerated SINR error.

Based on the SIR results from the previous section (cf. Tables 4.1 and 4.2), the maximally possible modulation order M can be derived. For the given channel scenarios and SINR tolerances, the estimated modulation orders are presented in Table 4.5. These results show, that CAW enables significantly higher modulation orders compared to a “one-fits-all” system design. Additionally, the results indicate that FBMC-OQAM with CAW surpasses the performance of state-of-the-art LTE. However, this kind of estimation method does not account for the applied equalizer and the question on the accuracy and thus validity of this system performance estimation method arises. Therefore, in the following section the BER is evaluated by Monte-Carlo simulations and the equivalent SINR for Rayleigh channels is determined and compared to the SIR.

4.2.2 Influence of channel equalization

In the previous section, a method for the determination of the communication channel induced performance bounds of FBMC-OQAM and CP-OFDM systems based on the reconstruction performance has been proposed. Here, the validity of this method is analyzed considering ZF equalization. Therefore, in this section the SINR after equalization is determined by Monte-Carlo based simulations and compared to the SIR values obtained in the previous sections.

The BER results are obtained by Monte-Carlo simulations with $K = 256$, which were carried out for $4 \cdot 10^2$ channel realizations with $4 \cdot 10^2$ transmitted FBMC-OQAM symbols each. In order to equalize the data symbols, the effective channel coefficients $H_{m,\tilde{k}}(0,0)$ are calculated according to (3.10). The resulting BER floor values of FBMC-OQAM systems operating in the investigated channel scenarios are depicted in Figure 4.3. As for the SIR plots, the horizontal lines indicate the BER of a state-of-the-art CP-OFDM based LTE system with a CP length of $0.07T$ and the vertical lines show the normalized delay spreads and maximum Doppler shifts for FBMC-OQAM systems with the standard LTE symbol duration of $T_{\text{LTE}} = 1/15$ ms. The results show, that the basic relationship discussed in Section 3.5 can be transferred to the BER performance: For scenarios B and C, FBMC-OQAM with proper PFF selection performs better than CP-OFDM. However, FBMC-OQAM is outperformed significantly in scenario A.

For completeness, Table 4.6 provides the error floors for uncoded BERs in Rayleigh fading channels for FBMC-OQAM and CP-OFDM systems with the LTE symbol duration T_{LTE} as well as for the optimized symbol duration T_{opt} for selected higher order QAM symbol alphabets. Here, the Monte-Carlo based simulations are conducted with $8 \cdot 10^3$ FBMC-OQAM or CP-OFDM symbols per channel realization to improve the accuracy of the numeric results compared to the results presented in Figure 4.3. The results show, that the application of CAPS provides a significant BER improvement. For the investigated PFFs, the uncoded BER gain yields a factor of approximately 2, which in [34] has been shown to turn into a BER gain larger than factor of 4 if a convolutional channel coding with code rate $2/3$ as deployed in DVB-T [22] is used.

The application of CASS with the optimized symbol durations T_{opt} given in Table 4.2 results in the BER values displayed in Table 4.6. They show, that in scenarios A and C, CASS reduces the error floors for the uncoded BER by about 2 and 1 orders of magnitude, respectively. In contrast, the BER floor reduction gains in scenario B are insignificant due to the for this scenario close to optimal symbol duration of LTE, which already has been indicated by the investigations on the SIR.

The resulting SINR values as well as the SINR estimation error ΔSINR defined as

$$\Delta\text{SINR}[\text{dB}] = \text{SINR}[\text{dB}] - \text{SIR}[\text{dB}] \quad (4.3)$$

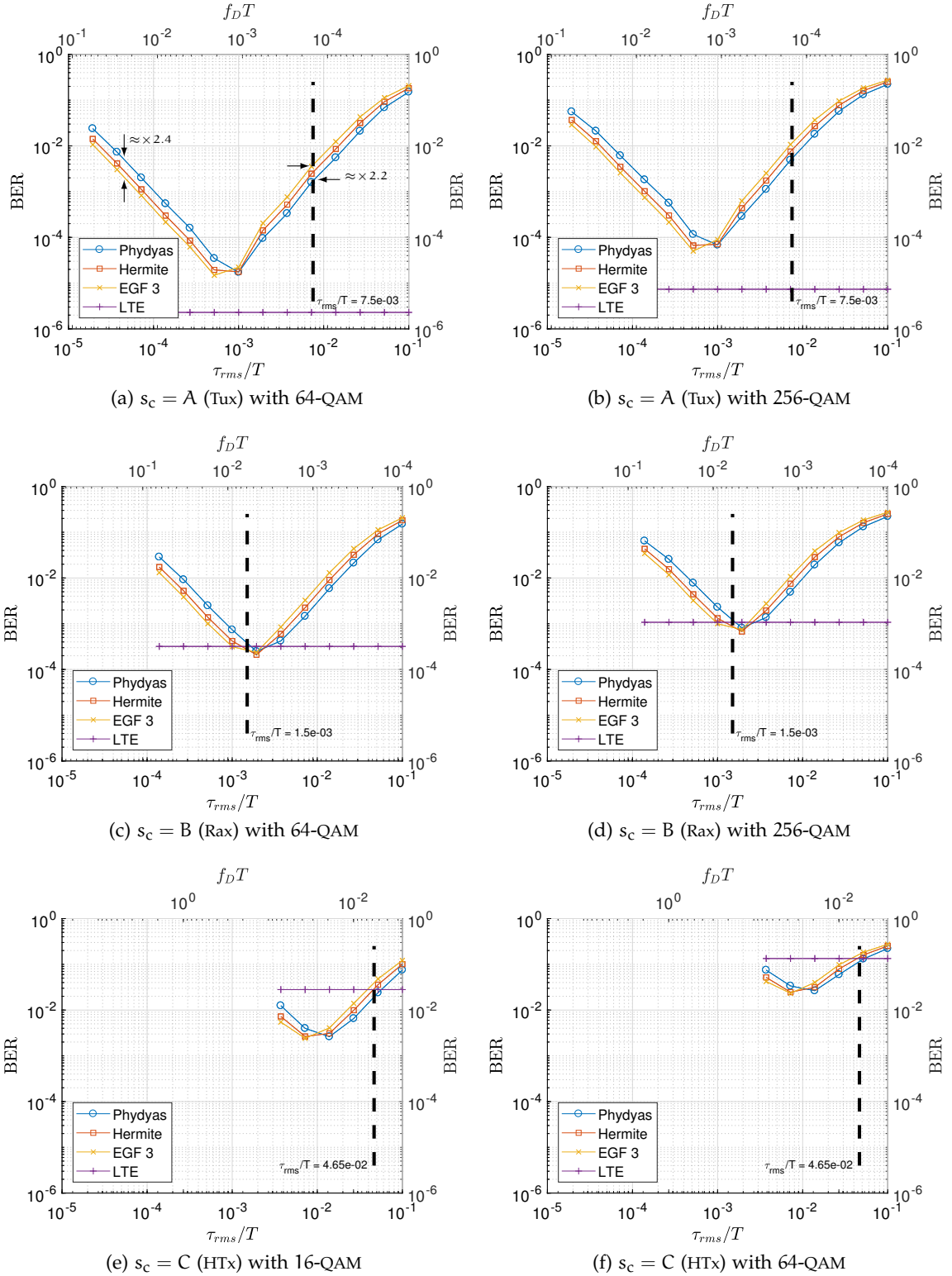


Figure 4.3: BER of FBMC-QAM systems with selected modulation order M in dependence on symbol duration T and channel scenarios s_c . The vertical dashed and the horizontal purple lines indicate the normalized delay spread and BER of a state-of-the-art CP-OFDM based LTE system with $T_{CP} = 0.07T$, respectively.

s_c	M	BER						
		for T_{LTE}				for T_{opt}		
		PHYDYAS	Hermite	EGF 3	LTE	PHYDYAS	Hermite	EGF 3
A	64	$1.6 \cdot 10^{-3}$	$2.3 \cdot 10^{-3}$	$3.4 \cdot 10^{-3}$	$2.6 \cdot 10^{-6}$	$2.0 \cdot 10^{-5}$	$1.4 \cdot 10^{-5}$	$1.3 \cdot 10^{-5}$
	256	$5.1 \cdot 10^{-3}$	$7.6 \cdot 10^{-3}$	$1.1 \cdot 10^{-2}$	$8.6 \cdot 10^{-6}$	$6.4 \cdot 10^{-5}$	$4.7 \cdot 10^{-5}$	$4.2 \cdot 10^{-5}$
	1024	$1.6 \cdot 10^{-2}$	$2.4 \cdot 10^{-2}$	$3.3 \cdot 10^{-2}$	$3.0 \cdot 10^{-5}$	$2.1 \cdot 10^{-4}$	$1.5 \cdot 10^{-4}$	$1.4 \cdot 10^{-4}$
	4096	$4.3 \cdot 10^{-2}$	$5.7 \cdot 10^{-2}$	$7.2 \cdot 10^{-2}$	$9.8 \cdot 10^{-5}$	$7.2 \cdot 10^{-4}$	$5.2 \cdot 10^{-4}$	$4.7 \cdot 10^{-4}$
B	64	$3.4 \cdot 10^{-4}$	$2.2 \cdot 10^{-4}$	$2.0 \cdot 10^{-4}$	$3.3 \cdot 10^{-4}$	$2.5 \cdot 10^{-4}$	$2.1 \cdot 10^{-4}$	$2.0 \cdot 10^{-4}$
	256	$1.1 \cdot 10^{-3}$	$7.2 \cdot 10^{-4}$	$6.7 \cdot 10^{-4}$	$1.1 \cdot 10^{-3}$	$8.2 \cdot 10^{-4}$	$6.9 \cdot 10^{-4}$	$6.7 \cdot 10^{-4}$
	1024	$3.6 \cdot 10^{-3}$	$2.3 \cdot 10^{-3}$	$2.2 \cdot 10^{-3}$	$3.5 \cdot 10^{-3}$	$2.7 \cdot 10^{-3}$	$2.2 \cdot 10^{-3}$	$2.2 \cdot 10^{-3}$
	4096	$1.1 \cdot 10^{-2}$	$7.5 \cdot 10^{-3}$	$7.0 \cdot 10^{-3}$	$1.1 \cdot 10^{-2}$	$8.4 \cdot 10^{-3}$	$7.2 \cdot 10^{-3}$	$7.0 \cdot 10^{-3}$
C	16	$1.8 \cdot 10^{-2}$	$2.6 \cdot 10^{-2}$	$3.7 \cdot 10^{-2}$	$2.8 \cdot 10^{-2}$	$2.5 \cdot 10^{-3}$	$2.3 \cdot 10^{-3}$	$2.4 \cdot 10^{-3}$
	64	$5.4 \cdot 10^{-2}$	$7.3 \cdot 10^{-2}$	$9.4 \cdot 10^{-2}$	$7.2 \cdot 10^{-2}$	$8.3 \cdot 10^{-3}$	$7.5 \cdot 10^{-3}$	$7.7 \cdot 10^{-3}$
	256	$1.1 \cdot 10^{-1}$	$1.4 \cdot 10^{-1}$	$1.6 \cdot 10^{-1}$	$1.3 \cdot 10^{-1}$	$2.5 \cdot 10^{-2}$	$2.2 \cdot 10^{-2}$	$2.3 \cdot 10^{-2}$
	1024	$1.7 \cdot 10^{-1}$	$2.0 \cdot 10^{-1}$	$2.2 \cdot 10^{-1}$	$2.0 \cdot 10^{-1}$	$5.9 \cdot 10^{-2}$	$5.4 \cdot 10^{-2}$	$5.5 \cdot 10^{-2}$

Table 4.6: BERs floors for FBMC-OQAM and CP-OFDM systems with LTE or channel specific symbol duration operating in channel scenarios s_c (ref. to Appendix B.2).

s_c	M	SINR [dB] (Δ SINR [dB])						
		for T_{LTE}				for T_{opt}		
		PHYDYAS	Hermite	EGF 3	LTE	PHYDYAS	Hermite	EGF 3
A	64	36.3 (2)	34.5 (2)	32.9 (2)	64.1 (0.3)	55.3 (0.5)	56.7 (0.2)	57.2 (0.1)
	256	36.3 (2)	34.4 (1.9)	32.7 (1.8)	64.1 (0.3)	55.4 (0.6)	56.7 (0.2)	57.2 (0.1)
	1024	36.1 (1.8)	34.3 (1.8)	32.6 (1.7)	64 (0.2)	55.4 (0.6)	56.8 (0.3)	57.2 (0.1)
	4096	36.1 (1.8)	34.3 (1.8)	32.7 (1.8)	64.1 (0.3)	55.4 (0.6)	56.8 (0.3)	57.2 (0.1)
B	64	42.9 (0.4)	44.8 (0.4)	45.2 (0.4)	43 (0.5)	44.3 (0.5)	45 (0.4)	45.1 (0.3)
	256	42.9 (0.4)	44.9 (0.5)	45.2 (0.4)	43 (0.5)	44.3 (0.5)	45 (0.4)	45.2 (0.4)
	1024	43 (0.5)	44.9 (0.5)	45.2 (0.4)	43.1 (0.6)	44.3 (0.5)	45.1 (0.5)	45.2 (0.4)
	4096	43.2 (0.7)	45 (0.6)	45.3 (0.5)	43.3 (0.8)	44.4 (0.6)	45.2 (0.6)	45.3 (0.5)
C	16	20.2 (2.4)	18.4 (2.2)	16.7 (2.1)	18 (0.4)	28.9 (1.2)	29.4 (1.1)	29.2 (1.1)
	64	19.8 (2)	18 (1.8)	16.5 (1.9)	18.2 (0.6)	28.9 (1.2)	29.4 (1.1)	29.2 (1.1)
	256	19.9 (2.1)	18.1 (1.9)	16.5 (1.9)	18.3 (0.7)	28.9 (1.2)	29.4 (1.1)	29.3 (1.2)
	1024	20 (2.2)	18.2 (2)	16.7 (2.1)	18.5 (0.9)	29.2 (1.4)	29.7 (1.4)	29.6 (1.4)

Table 4.7: Equivalent SINR for the obtained BER values and the related SINR estimation error Δ SINR.

are given in Table 4.7². It can be seen, that there is a small mismatch between the reconstruction performance defined in Section 3.4 and the effective SINR after equalization. This is due to the fact, that the effective SINR is determined with assumption of uncorrelated interference, which is not perfectly true as briefly discussed in the following.

1. For ZF equalization, the interference part of the received symbol is linked with the actual effective channel coefficient $H_{\tilde{m},\tilde{k}}(0,0)$ of the desired symbol part, i.e.

$$\hat{a}_{\tilde{m},\tilde{k}} = \Re\left\{\frac{\tilde{a}_{\tilde{m},\tilde{k}}}{H_{\tilde{m},\tilde{k}}(0,0)}\right\} = a_{\tilde{m},\tilde{k}} + \Re\left\{\sum_{(\mu,\kappa)\in\mathcal{S}_N} \theta_{\mu,\kappa} a_{\tilde{m}+\mu,\tilde{k}+\kappa} \frac{H_{\tilde{m},\tilde{k}}(\mu,\kappa)}{H_{\tilde{m},\tilde{k}}(0,0)}\right\}, \quad (4.4)$$

where $\hat{a}_{\tilde{m},\tilde{k}}$ is the equalized data symbol. Thus, the average interference power after demodulation and equalization is subject to the statistical dependence between the effective channel coefficients $H_{\tilde{m},\tilde{k}}(\mu,\kappa)$ and $H_{\tilde{m},\tilde{k}}(0,0)$. As all channel coefficients consider the same scatterers $D[\tau_l, \nu]$ (weighted with different factors), the statistical dependence is inherent. To qualify the degree of correlation, the coherence bandwidth B_c and coherence time T_c can be considered. For Rayleigh fading channels these measures yield [63]

$$\text{Coherence bandwidth} \quad B_c = \frac{1}{\tau_{\text{rms}}} \quad (4.5a)$$

$$\text{Coherence time} \quad T_c = \frac{\sqrt{2}}{f_D}. \quad (4.5b)$$

For all investigated scenarios, both the coherence bandwidth B_c and coherence time T_c are significantly larger than one subcarrier spacing $1/T$ and symbol duration T (cf. Appendix B.2), respectively.

2. Due to the shape of the ambiguity function, the main interference is generated by only a small amount of symbols. This results in a slow convergence of the central limit theorem and thus the distribution of the intrinsic interference can significantly differ from a normal distribution [72].

However, the results in Table 4.7 indicate that the reconstruction performance can serve as a suitable approximation for the SIR after ZF equalization. As $\text{SINR} \geq \text{SIR}$, the SIR can be considered as a lower bound for the system performance. This also is supported by the results presented in [72], which show that the assumption of normally distributed interference results in a slightly increased BER. Thus, in the remaining part of this thesis the SIR is used as approximation of the effective SINR. It should be noted that the SIR based results and conclusion are only valid for equalizers and receiver structures, which do not suppress or remove the intrinsic interference such as multi-tap equalizers (e.g. [101]).

² The equivalent SINR values for Rayleigh fading channels have been determined using the BERFADING function of MATLAB.

s_c	$\tau_{\text{rms}}/T_{\text{LTE}}$	$C_{\text{LTE}}^{\text{sc}}$ [bit/s/Hz] (SIR [dB])			
		PHYDYAS	Hermite	EGF 3	LTE
A	$7.5 \cdot 10^{-3}$	11.4 (34.3)	10.8 (32.5)	10.2 (30.9)	19.8 (63.8)
B	$1.5 \cdot 10^{-3}$	14.1 (42.5)	14.7 (44.4)	14.9 (44.8)	13.2 (42.5)
C	$4.5 \cdot 10^{-2}$	6.0 (17.8)	5.4 (16.2)	4.9 (14.6)	5.5 (17.6)

Table 4.8: $C_{\text{LTE}}^{\text{sc}}$ (and SIR) for an FBMC-OQAM or CP-OFDM based LTE system operating in channel scenarios s_c (see Appendix B.2). The capacity values of the LTE system account for the CP.

4.3 CHANNEL CAPACITY

In this section, the channel capacity of homogeneous CAW is investigated. As discussed in the last preceding section, the SIR can be considered as a lower bound of the effective SINR after equalization. Therefore, the SIR is used to determine the channel capacity based on the well-known Shannon-Hartley theorem. For the noise free case and with (3.32b) and (3.28), the channel capacity of FBMC-OQAM systems is calculated according to [89]

$$C = \log_2(1 + \text{SIR}). \quad (4.6a)$$

To account for the capacity losses in CP-OFDM systems induced by the insertion of the CP, the corresponding effective channel capacity yields

$$C = \frac{T}{T + T_{\text{CP}}} \log_2(1 + \text{SIR}). \quad (4.6b)$$

The resulting channel capacities of FBMC-OQAM systems operating in the investigated channel scenarios are depicted in Figure 4.4. As for the SIR plots, the horizontal lines indicate the channel capacity of a state-of-the-art CP-OFDM based LTE system with a CP length of $0.07T$ and the vertical lines the normalized delay spreads and maximum Doppler shifts for FBMC-OQAM systems with the standard LTE symbol duration of $T_{\text{LTE}} = 1/15$ ms. With this configuration, a CP-OFDM or FBMC-OQAM system can utilize a channel capacity $C_{\text{LTE}}^{\text{sc}}$ of about 5 to 20 bit/s/Hz (cf. Table 4.8). For the discussed channel scenarios and the symbol duration of LTE, the PHYDYAS PFF is the best choice for FBMC-OQAM, as it performs best in scenarios A and C with only a moderate performance loss in scenario B. In addition, it can be noted that for the given subcarrier spacing and the investigated scenarios only two different PFFs, i.e. PHYDYAS and EGF 3, are required to utilize CAPS as proposed in [34].

The results presented in Figure 4.4 and Table 4.8 indicate that a unified symbol duration for all channel scenarios leads to suboptimal channel capacity utilization in scenarios A and C. This can be improved significantly by a system design approach in which all users in a cell have the same system configuration, which is optimized for the present

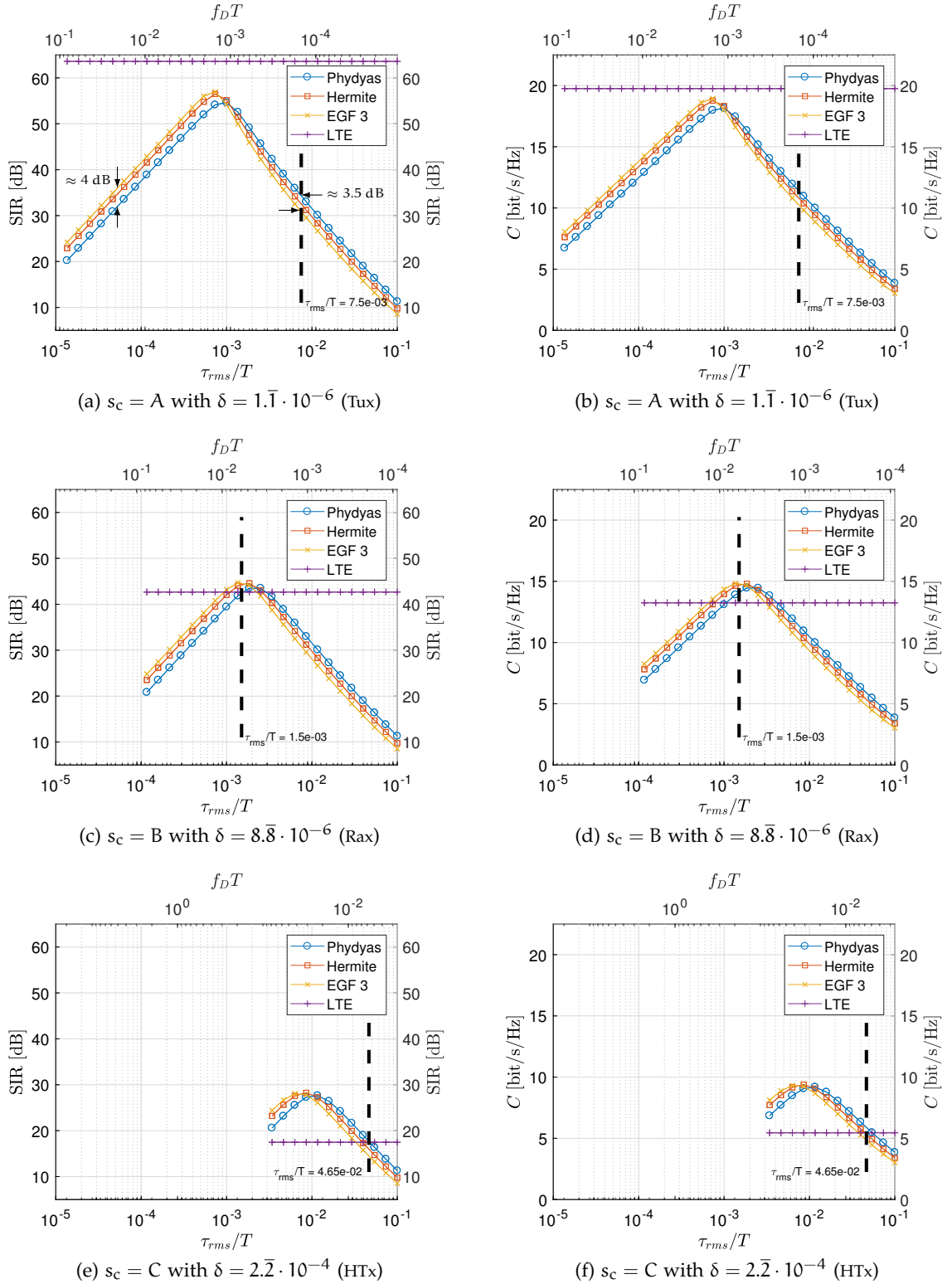


Figure 4.4: SIR (left side) and related channel capacity C (right side) of FBMC-OQAM systems in dependence on symbol duration T and channel scenarios s_c . The vertical dashed and the horizontal purple lines indicate the normalized delay spread and SIR or channel capacity of a state-of-the-art CP-OFDM based LTE system with $T_{CP} = 0.07T$, respectively.

s_c	PPF	$T_{\text{opt}} [\mu\text{s}]$	$\tau_{\text{rms}}/T_{\text{opt}}$	SIR [dB]	$C_{\text{opt}}^{\text{sc}} [\text{bit/s/Hz}]$	$C_{\text{opt}}^{\text{sc}}/C_{\text{LTE}}^{\text{sc}}$
A	PHYDYAS	546	$9.16 \cdot 10^{-4}$	54.8	18.2	1.6
	Hermite	651	$7.68 \cdot 10^{-4}$	56.5	18.8	1.74
	EGF 3	730	$6.85 \cdot 10^{-4}$	57.1	19.0	1.86
B	PHYDYAS	46	$2.16 \cdot 10^{-3}$	43.8	14.5	1.03
	Hermite	59	$1.71 \cdot 10^{-3}$	44.6	14.8	1.01
	EGF 3	68	$1.48 \cdot 10^{-3}$	44.8	14.9	1
C	PHYDYAS	280	$1.07 \cdot 10^{-2}$	27.7	9.2	1.53
	Hermite	358	$8.37 \cdot 10^{-3}$	28.3	9.4	1.74
	EGF 3	423	$7.09 \cdot 10^{-3}$	28.1	9.4	1.92

Table 4.9: SIR and $C_{\text{opt}}^{\text{sc}}$ and corresponding $\tau_{\text{rms}}/T_{\text{opt}}$ in dependence on PFFs and channel scenarios.

channel environment and user behavior characteristics, i.e. homogeneous CAW. To obtain the channel capacity gains for this homogeneous CAW approach, the optimal channel capacity $C_{\text{opt}}^{\text{sc}}$ is calculated by optimizing (4.6a) with respect to the symbol duration T and utilized PFF and considering (3.32b):

$$C_{\text{opt}}^{\text{sc}} = \arg \max_{T, f[n]} \log_2 (1 + \text{SIR}). \quad (4.7)$$

Here, this optimization process depends on three different base functions, i.e. the PFFs. Thus, (4.7) is evaluated numerically. The resulting channel capacities $C_{\text{opt}}^{\text{sc}}$, optimized symbol durations T_{opt} and the related normalized delay spreads $\tau_{\text{rms}}/T_{\text{opt}}$ are given in Table 4.9 and contrasted in Figure 4.5. As depicted, in scenario B the channel capacity gains are limited to about 3%, as the symbol duration of LTE is close to optimal for the Rax channel [32]. However, in scenarios A and C the gains of CAPS compared to the “one-fits-all” approach are approximately 85% and 90%, respectively. For a cellular network covering only the investigated scenarios, it is not necessary to deploy homogeneous CAW, as for all cases CAPS in combination with the EGF 3 PFF delivers the optimal performance.

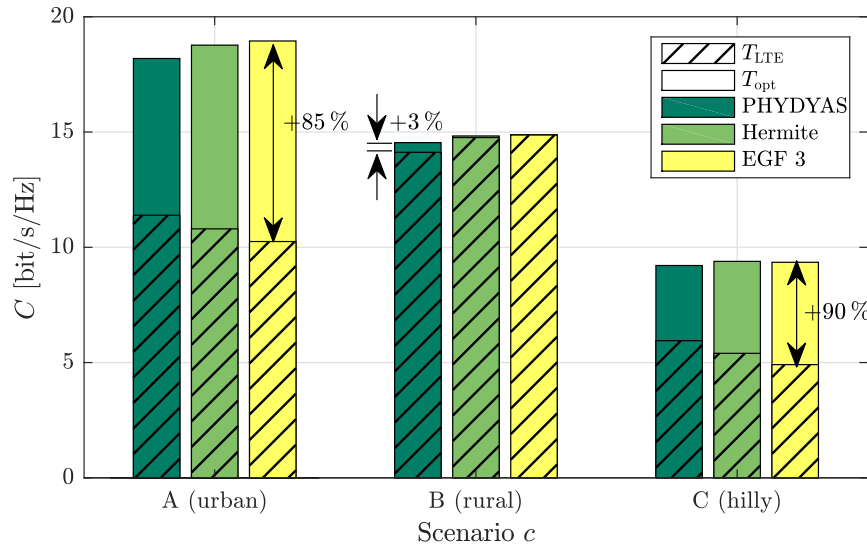


Figure 4.5: Channel capacity C for an FBMC-OQAM system with the symbol duration of LTE T_{LTE} (crosshatched) in comparison with the one for optimized symbol durations T_{opt} in different channel scenarios (ref. Table 4.11) and the different PFFs. In urban and hilly environments, CAW improves the channel capacity by up to 90%.

4.4 CAW WITH IMPERFECT CSIR

In the previous section, perfect channel knowledge at the receiver has been assumed. In practical applications however, the current channel state has to be estimated, which in MC systems is usually performed with pilot symbols. There are two principle schemes for the configuration of pilot symbols which are commonly known as *preamble* and *scattered pilots*. As shown in Section 3.2, all transmitted data and pilot symbols suffer from interference induced by neighboring symbols. For data symbols, the main proportion of the interference is removed as only the real part is considered after channel equalization (cf. (4.4)). In contrast, channel estimation is performed on complex symbols to estimate the channel gain and phase shift. Thus, after demodulation the channel estimation for FBMC-OQAM system is affected by the imaginary interference on the pilot symbols. Therefore, in literature lots of algorithms and pilot patterns are suggested to mitigate the interference induced to pilot symbols (cf. [52, 78]). Generally, preamble based channel estimation techniques enable better interference mitigation compared to scattered pilots, as preambles usually do not contain random data and thus have the advantage of known interference. Various schemes have been proposed in literature to minimize the interference in preambles [37, 52, 53, 95, 97]. However, some systems such as LTE and DVB-T don't have a dedicated preamble. Additionally, practically every wireless communication system requires reference symbols embedded within the data part for the purpose of residual CFO estimation and channel tracking. Therefore, in this thesis, the influence of imperfect channel estimation based on scattered pilots on the performance of CAW is investigated. To combat the intrinsic interference in FBMC-OQAM systems, in literature

several interference mitigation schemes for scattered pilots have been proposed [4, 13, 14, 49, 56–58, 65, 71, 109, 115]. These can be categorized as follows:

- Auxiliary Pilot (AP) [49, 71]
- Data Spreading (DS) / Precoding [4, 14, 58, 71]
- Pairs of Pilots (POP) [13, 57]
- Pilot Clustering (PC) [65, 109]
- Basic Iterative Interference Mitigation (BIIM) [56]
- Composite Pilot Pairs (CPP) [115].

To obtain a lower performance bound for the performance of CAW with imperfect CSIR, a low complexity receiver structure is considered. In this way minimal implementation cost and extended battery life time are supported. Accordingly, the following requirements and features in the considered system design are defined:

- The CAW parameters, e.g. PFF and symbol duration T , are chosen at the transmitter.
- The amount of redundant data transmission for interference mitigation should be kept to a minimum, thus only a maximum redundancy of one real symbol is tolerated.
- Channel estimation is performed by the method of Least Squares (LS).
- ZF equalizer is used for the channel equalization, which additionally enables a comparison with the results in Section 4.2.
- No iterative interference rejection schemes shall be applied at the receiver to keep mobile equipment hardware simple and low cost.

Both the BIIM and CPPs schemes are based on iterative channel estimation, equalization and data symbol detection. Thus, referring to the system requirements defined above, these schemes are not within the scope of this investigation. The channel estimation schemes proposed in [4, 14, 65, 71, 109] require more than one redundant symbol or do not provide a closed form solution which complicates the investigation of the impact of channel estimation errors on the performance gains of CAW. Therefore, these schemes are not considered in this thesis.

The POP scheme [57] and the modified version of it [13] provide a closed form LS estimation for the equalizer, whereas both the AP [49] and DS [58] approaches considered within the context of this thesis deliver a LS estimate of the channel. In fact, even though the estimation technique is similar for all of these schemes, it should be made clear that two different LS problem formulations (cost functions) are being raised. In other words,

the POP scheme additionally requires the inverse equalizer determination, which might result in further errors, e.g. noise enhancement. Therefore, as a first step of the evaluation of CAW in combination with imperfect CSIR, the focus of this thesis is guided by the evaluation of AP and DS interference mitigation performance in terms of the channel estimation error for various PFFs.

As mentioned before, in MC systems the channel estimation is usually carried out in the frequency domain and is based on a transmitted reference sequence, which is either a separate preamble sequence or a certain number of pilots scattered over the whole transmission frame as done in LTE or DVB-T. Using the LS estimator, the estimated channel coefficients $\tilde{H}_{\tilde{m},\tilde{k}}$ are calculated by comparing the received pilot symbol, i.e. $\tilde{a}_{\tilde{m},\tilde{k}} = \tilde{p}_{\tilde{m},\tilde{k}}$ and the reference pilot symbol $p_{\tilde{m},\tilde{k}}$ according to

$$\tilde{H}_{\tilde{m},\tilde{k}} = \frac{\tilde{p}_{\tilde{m},\tilde{k}}}{p_{\tilde{m},\tilde{k}}}. \quad (4.8)$$

The resulting channel estimation error ε_H can be determined using the Mean-Squared Error (MSE) defined by

$$\varepsilon_H = \mathbf{E} \left[\left| \tilde{H}_{\tilde{m},\tilde{k}} - H_{\tilde{m},\tilde{k}} \right|^2 \right]. \quad (4.9)$$

As shown in (3.7), each received data or pilot symbol can be considered as a superposition of a desired part and an interference part, which degrades the channel estimation accuracy.

To enable a precise channel estimation, the transmission of each pilot symbol requires special processing to mitigate the interference. Therefore, the estimated channel coefficient $\tilde{H}_{\tilde{m},\tilde{k}}$ can be considered as a linear combination as follows:

$$\tilde{H}_{\tilde{m},\tilde{k}} = H_{\tilde{m},\tilde{k}} + C_{\tilde{m},\tilde{k}} + R_{\tilde{m},\tilde{k}}, \quad (4.10)$$

such that (4.9) can be rewritten as

$$\varepsilon_{H,AP} = \mathbf{E} \left[\left| C_{\tilde{m},\tilde{k}} + R_{\tilde{m},\tilde{k}} \right|^2 \right]. \quad (4.11)$$

Here, $C_{\tilde{m},\tilde{k}}$ represents the residual interference induced by the symbols considered by an arbitrary interference mitigation scheme to combat the interference on the pilot symbol $\tilde{p}_{\tilde{m},\tilde{k}}$. $R_{\tilde{m},\tilde{k}}$ is the interference imposed by all symbols not included in the interference mitigation.

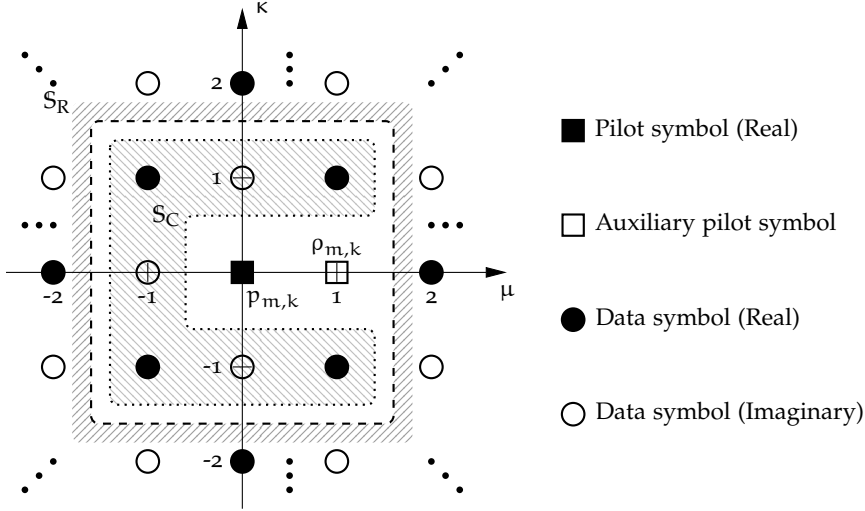


Figure 4.6: Allocation pattern of pilot $p_{m,k}$ and auxiliary symbol $\rho_{m,k}$ for $(\mu_a, \kappa_a) = (1, 0)$, respectively. Data symbols within the inner hatched area are used for the AP calculation as reported in [49].

4.4.1 Scattered pilots based on AP

To reduce the interference on pilot symbols, Javaudin et al. [49] proposed the usage of a dedicated symbol $\rho_{m,k}$, which counteracts the interference on a pilot symbol inflicted by neighboring data symbols. The more common naming Auxiliary Pilot (AP) has been introduced in [95]. The AP is placed at the lattice position with symbol offset μ_a and subcarrier offset κ_a relative to the associated pilot symbol position, as depicted in Figure 4.6. With the assumption of a flat channel around the pilot symbol, i.e. $\tau_{rms} \ll T$ and $f_D \ll 1/T$, and with $S_C \subseteq \{S_N \setminus (\mu_a, \kappa_a)\}$ being the set of symbols considered for interference mitigation, the AP approach of Javaudin et al. is specified by

$$\underbrace{\sum_{(\mu, \kappa) \in S_C} \theta_{\mu, \kappa} a_{m+\mu, k+\kappa} A_{\mu, \kappa}^k [0, 0]}_{\text{Approximated interference } i_{m,k}} + \rho_{m,k} A_{\mu_a, \kappa_a}^k [0, 0] = 0. \quad (4.12)$$

For this approach, the interference induced by the symbols at positions $(\mu, \kappa) \in S_C$ is counteracted by the interference induced by the AP located at any arbitrary lattice position (μ_a, κ_a) . Therefore, the AP $\rho_{m,k}$ of pilot symbol $p_{m,k}$ yields

$$\rho_{m,k} = -\frac{1}{A_{\mu_a, \kappa_a}^k [0, 0]} \sum_{(\mu, \kappa) \in S_C} \theta_{\mu, \kappa} a_{m+\mu, k+\kappa} A_{\mu, \kappa}^k [0, 0], \quad (4.13)$$

whereby the average power σ_{AP}^2 of $\rho_{m,k}$ is

$$\sigma_{\text{AP}}^2 = \mathbf{E}[\rho_{m,k}\rho_{m,k}^*] = \sigma_{\text{d}}^2 \sum_{(\mu,\kappa) \in \mathcal{S}_{\text{C}}} \frac{|\mathcal{A}_{\mu,\kappa}[0,0]|^2}{|\mathcal{A}_{\mu_a,\kappa_a}[0,0]|^2}, \quad (4.14)$$

with the average data symbol power $\sigma_{\text{d}}^2 = \mathbf{E}[|a_{m,k}|^2]$. It can be seen, that the average power σ_{AP}^2 of the AP depends on the value of the ambiguity function at the position of the AP. To minimize the additional power requirements, the lattice position (μ_a, κ_a) of the AP should be selected such that

$$(\mu_a, \kappa_a) = \arg \max_{(\mu,\kappa)} |\mathcal{A}_{\mu,\kappa}[0,0]|. \quad (4.15)$$

Applying this generalized approach for APs, each component of the effective channel coefficient $\tilde{H}_{\tilde{m},\tilde{k}}$ given in (4.10) can be defined by

$$H_{\tilde{m},\tilde{k}} = H_{\tilde{m},\tilde{k}}(0,0) \quad (4.16a)$$

$$C_{\tilde{m},\tilde{k}} = \frac{\rho_{\tilde{m},\tilde{k}}}{p_{\tilde{m},\tilde{k}}} H_{\tilde{m},\tilde{k}}(\mu_a, \kappa_a) + \sum_{(\mu,\kappa) \in \mathcal{S}_{\text{C}}} \theta_{\mu,\kappa} \frac{a_{\tilde{m}+\mu,\tilde{k}+\kappa}}{p_{\tilde{m},\tilde{k}}} H_{\tilde{m},\tilde{k}}(\mu, \kappa) \quad (4.16b)$$

$$R_{\tilde{m},\tilde{k}} = \sum_{(\mu,\kappa) \in \mathcal{S}_{\text{R}}} \theta_{\mu,\kappa} \frac{a_{\tilde{m}+\mu,\tilde{k}+\kappa}}{p_{\tilde{m},\tilde{k}}} H_{\tilde{m},\tilde{k}}(\mu, \kappa), \quad (4.16c)$$

where $\mathcal{S}_{\text{R}} = \mathcal{S}_{\text{N}} \setminus \{\mathcal{S}_{\text{C}}, (\mu_a, \kappa_a)\}$. According to (4.11), the channel estimation error $\varepsilon_{\text{H,AP}}$ for the AP scheme is calculated by

$$\varepsilon_{\text{H,AP}} = \mathbf{E} \left[\left| \sum_{(\mu,\kappa) \in \mathcal{S}_{\text{R}}} \theta_{\mu,\kappa} \frac{a_{\tilde{m}+\mu,\tilde{k}+\kappa}}{p_{\tilde{m},\tilde{k}}} H_{\tilde{m},\tilde{k}}(\mu, \kappa) + \sum_{(\mu,\kappa) \in \mathcal{S}_{\text{C}}} \theta_{\mu,\kappa} \frac{a_{\tilde{m}+\mu,\tilde{k}+\kappa}}{p_{\tilde{m},\tilde{k}}} \hat{H}_{\tilde{m},\tilde{k}}(\mu, \kappa) \right|^2 \right], \quad (4.17)$$

with

$$\hat{H}_{\tilde{m},\tilde{k}}(\mu, \kappa) = H_{\tilde{m},\tilde{k}}(\mu, \kappa) - \frac{\mathcal{A}_{\mu,\kappa}^{\tilde{k}+\kappa}[0,0]}{\mathcal{A}_{\mu_a,\kappa_a}^{\tilde{k}+\kappa_a}[0,0]} H_{\tilde{m},\tilde{k}}(\mu_a, \kappa_a). \quad (4.18)$$

In [49] only OQAM symbols next to the pilot symbol are considered for the calculation of $\rho_{m,k}$, i.e. $\mathcal{S}_{\text{C}} = (\{-1, 0, 1\} \times \{-1, 0, 1\}) \setminus \{(0,0), (\mu_a = 1, \kappa_a = 0)\}$. Referring to the derivations in Appendix A.3 and A.4, $\varepsilon_{\text{H,AP}}$ yields

$$\varepsilon_{\text{H,AP}} = \frac{1}{b} \sum_{l=0}^{L-1} \int_{-f_{\text{D}} T_{\text{s}}}^{f_{\text{D}} T_{\text{s}}} S[\tau_l, \nu] \alpha[\tau_l, \nu] d\nu, \quad (4.19a)$$

with the pilot boost factor $b = \sigma_p^2/\sigma_d^2$, the average pilot symbol power $\sigma_p^2 = \mathbb{E}[|p_{m,k}|^2]$ and the effective ambiguity function $\alpha[\tau_l, \nu]$ defined according to

$$\alpha[\tau_l, \nu] = \sum_{(\mu, \kappa) \in \mathcal{S}_C} |\alpha_{\mu, \kappa}[\tau_l, \nu]|^2 + \sum_{(\mu, \kappa) \in \mathcal{S}_R} |A_{\mu, \kappa}[\tau_l, \nu]|^2. \quad (4.19b)$$

Similar to (4.10), the channel estimation error can be separated into the cancellation error $\varepsilon_{c,AP}$ and the residual estimation error $\varepsilon_{r,AP}$:

$$\varepsilon_{H,AP} = \varepsilon_{c,AP} + \varepsilon_{r,AP}. \quad (4.20a)$$

The cancellation error $\varepsilon_{c,AP}$ represents the error induced by the symbols taken into account for interference mitigation. It is given by

$$\varepsilon_{c,AP} = \frac{1}{b} \sum_{l=0}^{L-1} \int_{-f_D T_s}^{f_D T_s} S[\tau_l, \nu] \sum_{(\mu, \kappa) \in \mathcal{S}_C} |\alpha_{\mu, \kappa}[\tau_l, \nu]|^2 d\nu. \quad (4.20b)$$

The residual estimation error $\varepsilon_{r,AP}$ induced by symbols not considered by the interference mitigation scheme is obtained by:

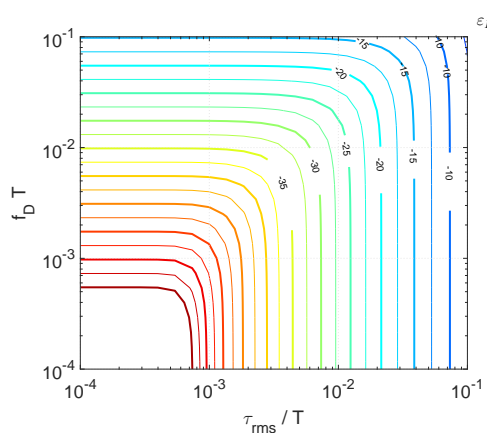
$$\varepsilon_{r,AP} = \frac{1}{b} \sum_{l=0}^{L-1} \int_{-f_D T_s}^{f_D T_s} S[\tau_l, \nu] \sum_{(\mu, \kappa) \in \mathcal{S}_R} |A_{\mu, \kappa}[\tau_l, \nu]|^2 d\nu. \quad (4.20c)$$

Here, the effective ambiguity function $\alpha_{\mu, \kappa}[\tau_l, \nu]$ is calculated as

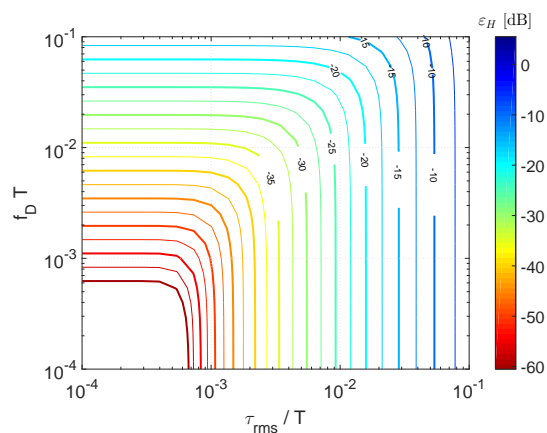
$$\alpha_{\mu, \kappa}[\tau_l, \nu] = A_{\mu, \kappa}[\tau_l, \nu] - \frac{A_{\mu, \kappa}[0, 0]}{A_{\mu_a, \kappa_a}[0, 0]} A_{\mu_a, \kappa_a}[\tau_l, \nu]. \quad (4.20d)$$

It has to be noted that in (4.19b) and (4.20d) the discrete-time ambiguity function according to 3.9c can be applied, as the delay and subcarrier specific phase shifts are either canceled out or removed due to the calculation of the absolute value.

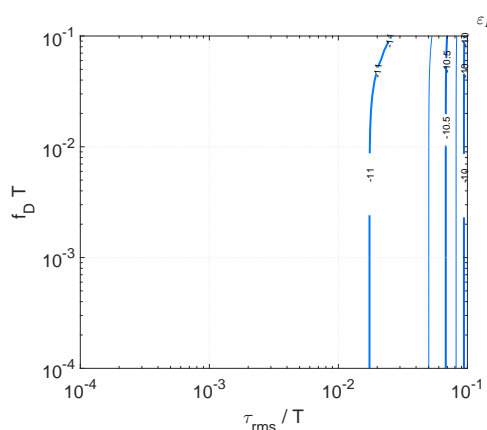
The total channel estimation error $\varepsilon_{H,AP}$ of the AP scheme and both its parts $\varepsilon_{c,AP}$ and $\varepsilon_{r,AP}$ are depicted in Figure 4.7 for different PFFs. Considering the cancellation error $\varepsilon_{c,AP}$ in Figures 4.7a, 4.7b and 4.7g, the AP scheme can provide a close to perfect interference mitigation for small values of the normalized delay spread τ_{rms}/T and maximum Doppler shift $f_D T$. As the utilized channel is not considered by the AP scheme, the channel estimation error increases similar to the SIR of received data symbols shown in Figure 3.9. However, the overall channel estimation error $\varepsilon_{H,AP}$ is severely limited, as the estimation error is bounded by $\varepsilon_{r,AP}$ (cf. Figure 4.7c, 4.7d and 4.7h). For isotropic PFFs (i.e. Hermite), the AP scheme delivers a minimum $\varepsilon_{H,AP}$ of approximately -18 dB. For non-isotropic PFFs, $R_{\tilde{m}, \tilde{k}}$ causes an increase of the channel estimation error to -11 dB and -14 dB for the PHYDYAS and EGF $\alpha = 3$ PFFs, respectively. Additionally, the trans-



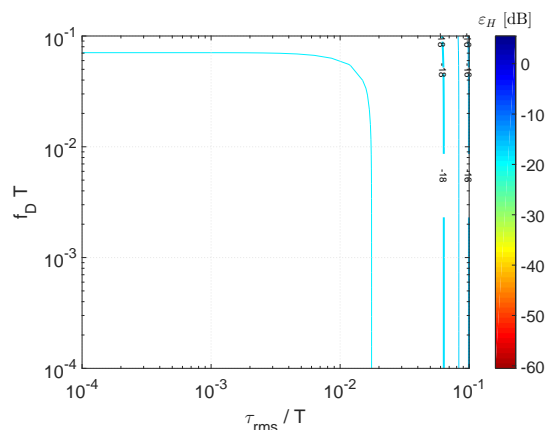
(a) $\epsilon_{C,AP}$ with PHYDYAS



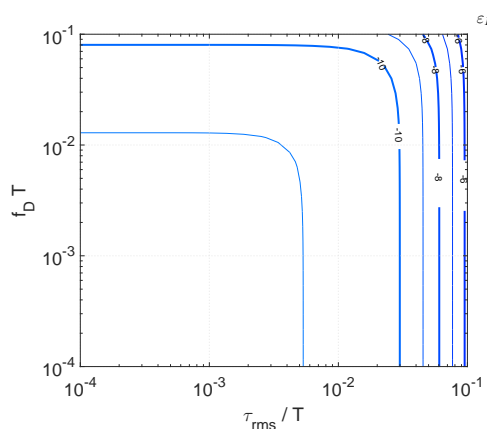
(b) $\epsilon_{C,AP}$ with Hermite



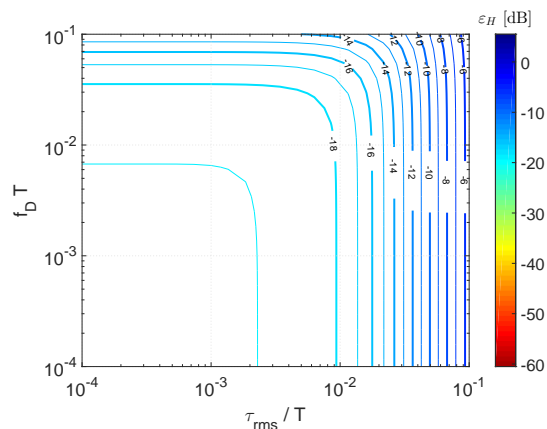
(c) $\epsilon_{r,AP}$ with PHYDYAS



(d) $\epsilon_{r,AP}$ with Hermite



(e) $\epsilon_{H,AP}$ with PHYDYAS (2.76 dB)



(f) $\epsilon_{H,AP}$ with Hermite (6.19 dB)

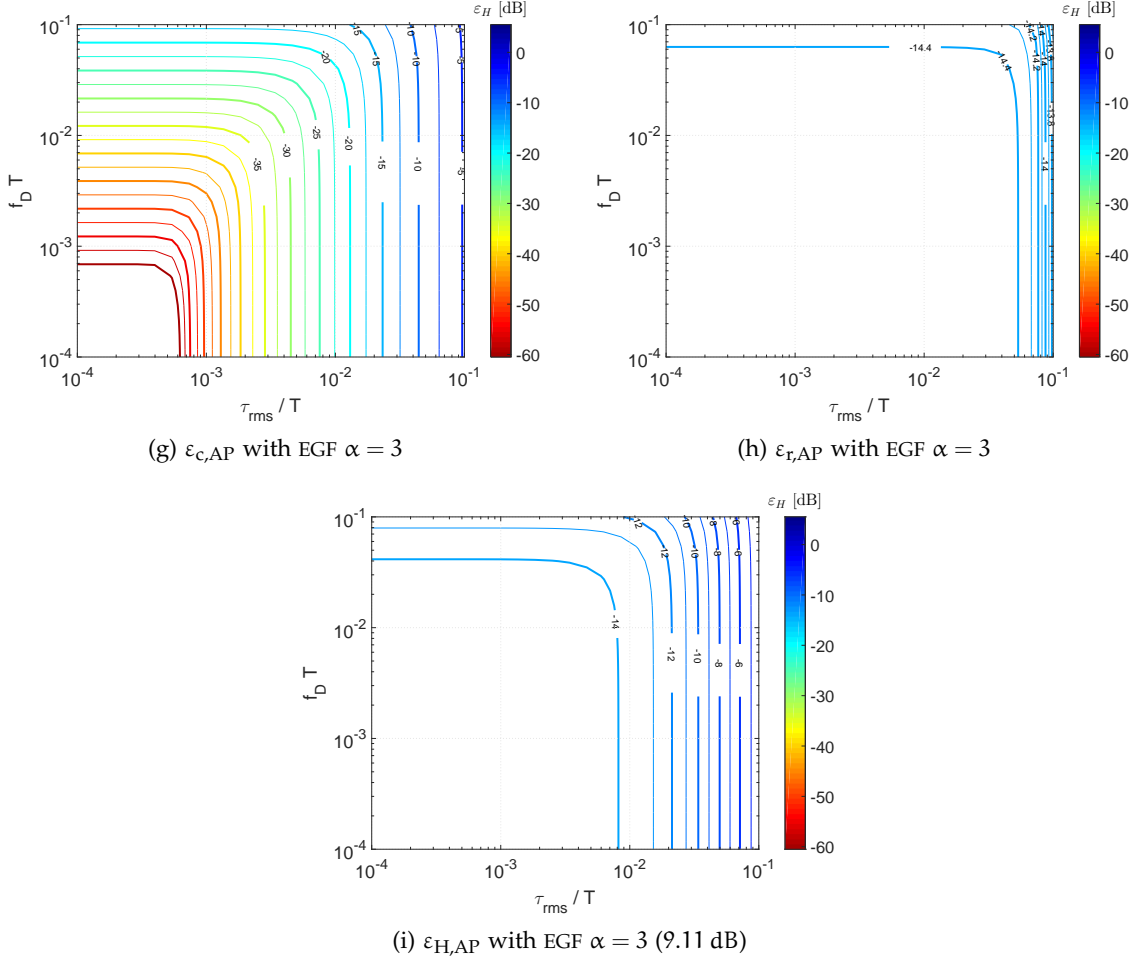


Figure 4.7: Scattered pilot based channel estimation error and its components (cancellation error $\varepsilon_{c,AP}$, residual estimation error $\varepsilon_{r,AP}$) of FBMC-OQAM systems for AP based interference mitigation operating in various channel environments with $K = 256$, $\gamma = 4$, $b = 1$ and $(\mu_a, \kappa_a) = (1, 0)$. The values in parentheses indicate the required AP power increase per pilot symbol in relation to the data symbols $a_{m,k}$.

mit power is increased, as compared to classical CP-OFDM the pilot pair ($p_{m,k}$ and $\rho_{m,k}$) power is in average about 3 to 9 dB higher. This may become an issue for high pilot pattern densities, as the remaining power for data symbols is reduced and thus the effective SINR on data symbols is decreased. For all PFFs, the channel estimation performance is limited by the residual estimation error $\varepsilon_{r,AP}$ in the region of $\tau_{rms}/T \leq 9 \cdot 10^{-3}$ and $f_D T \leq 3 \cdot 10^{-2}$. However, at the cost of increased system complexity and potentially latency, the channel estimation performance can be improved significantly if $R_{\bar{m},\bar{k}}$ is reduced. This can be achieved by either considering more symbols in interference mitigation as suggested in [50] or by boosting the pilot power.

4.4.2 Scattered pilots based on DS

Instead of using only one symbol to combat the interference on the pilot symbol as done in the AP scheme, in [58] L    et al. proposed to impose the zero forcing condition on a certain number of neighboring symbols $\Lambda > 1$, with $S_C \subseteq S_N$. Herefore, all data symbols neighboring a pilot symbol are pre-coded to avoid the intrinsic interference on it. This concept has been extended in [14, 71] to avoid the use of the auxiliary pilot and to improve the algorithms for the coding matrices design. In this thesis, the focus lies on the performance of the algorithm proposed in [58]. To simplify the notation, spread data symbols are indexed as depicted in Figure 4.8, with $\lambda : \{1, \dots, \Lambda\} \rightarrow \{(\mu, \kappa)_\lambda\}$. Accordingly, the approach to mitigate the interference can be formulated as

$$\sum_{(\mu, \kappa) \in S_C} \theta_{\mu, \kappa} a_{m+\mu, k+\kappa} A_{\mu, \kappa}^k [0, 0] = \sum_{\lambda=1}^{\Lambda} \theta_\lambda a_\lambda A_\lambda^k [0, 0] = 0, \quad (4.21)$$

where a_λ are the spread data symbols calculated by

$$a_\lambda = \underline{\chi}_\lambda \underline{d}. \quad (4.22)$$

Here, \underline{d} is a vector of the original OQAM symbols and \underline{C} is the spreading matrix including different spreading codes \underline{c}_λ and $\underline{\chi}_\lambda$ defined by

$$\underline{C} = \begin{bmatrix} \underline{c}_1 & \dots & \underline{c}_\lambda & \dots & \underline{c}_\Lambda \end{bmatrix} \quad (4.23a)$$

$$= \begin{bmatrix} \underline{\chi}_1 & \dots & \underline{\chi}_\lambda & \dots & \underline{\chi}_\Lambda \end{bmatrix}^T \quad (4.23b)$$

$$\underline{c}_\lambda = \begin{bmatrix} c_{1,\lambda} & \dots & c_{\lambda',\lambda} & \dots & c_{\Lambda,\lambda} \end{bmatrix}^T \quad (4.23c)$$

$$\underline{\chi}_\lambda = \begin{bmatrix} c_{\lambda,1} & \dots & c_{\lambda,\lambda'} & \dots & c_{\lambda,\Lambda} \end{bmatrix} \quad (4.23d)$$

$$\underline{d} = \begin{bmatrix} d_1 & \dots & d_\lambda & \dots & d_\Lambda \end{bmatrix}^T. \quad (4.23e)$$

Accordingly, the vector of spread data symbols \underline{a} is defined by

$$\underline{a} = \underline{C} \underline{d} \quad (4.23f)$$

$$= \begin{bmatrix} a_1 & \dots & a_\lambda & \dots & a_\Lambda \end{bmatrix}^T. \quad (4.23g)$$

To ensure that all d_λ can be recovered on the receiver side as well as to avoid transmission power waste and noise enhancement, \underline{C} has to be orthonormal [58]. Similar to the AP

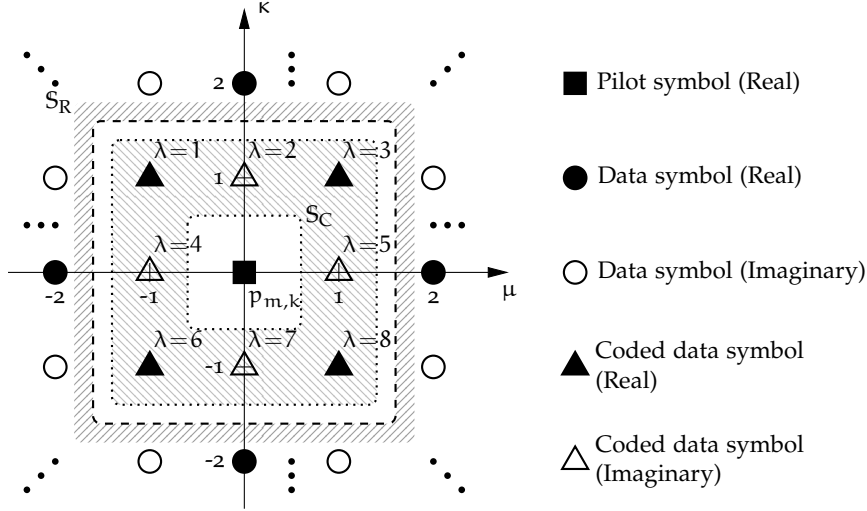


Figure 4.8: Allocation and index pattern of pilot and data symbols for the DS scheme. All data symbols within the inner hatched area (i.e. $\Lambda = 8$) are spread to reduce the interference induced onto the pilot symbol $p_{m,k}$ [58].

scheme, the DS approach requires a specific symbol d_Λ such that (4.21) is fulfilled for all d_λ . Here, d_Λ is a linear combination of all data symbols d_λ , i.e.

$$d_\Lambda = \sum_{\lambda=1}^{\Lambda-1} \beta_\lambda d_\lambda, \quad (4.24)$$

where β_λ is a weighting factor, which is an element of the weighting vector $\underline{\beta}$:

$$\underline{\beta} = [\beta_1 \quad \dots \quad \beta_{\Lambda-1}]. \quad (4.25)$$

With regard to this, the average power σ_{DS}^2 of d_Λ is given by

$$\sigma_{DS}^2 = \mathbf{E}[d_\Lambda d_\Lambda^*] = \sigma_d^2 \underline{\beta} \underline{\beta}^T = \sigma_d^2 \sigma_\beta^2, \quad (4.26)$$

where σ_β^2 is the average amplification factor of the auxiliary data symbol d_Λ . Considering the set S_C , the different parts of (4.10) for the DS scheme are obtained as below:

$$H_{\tilde{m}, \tilde{k}} = H_{\tilde{m}, \tilde{k}}(0, 0) \quad (4.27a)$$

$$\begin{aligned} C_{\tilde{m}, \tilde{k}} &= \sum_{(\mu, \kappa) \in S_C} \theta_{\mu, \kappa} \frac{a_{\tilde{m}+\mu, \tilde{k}+\kappa}}{p_{\tilde{m}, \tilde{k}}} H_{\tilde{m}, \tilde{k}}(\mu, \kappa) \\ &= \sum_{\lambda=1}^{\Lambda} H_\lambda \frac{a_\lambda}{p_{\tilde{m}, \tilde{k}}} = \sum_{\lambda=1}^{\Lambda} H_\lambda \frac{\chi_\lambda \underline{d}}{p_{\tilde{m}, \tilde{k}}} \end{aligned} \quad (4.27b)$$

$$R_{\tilde{m}, \tilde{k}} = \sum_{(\mu, \kappa) \in S_R} \theta_{\mu, \kappa} \frac{a_{\tilde{m}+\mu, \tilde{k}+\kappa}}{p_{\tilde{m}, \tilde{k}}} H_{\tilde{m}, \tilde{k}}(\mu, \kappa), \quad (4.27c)$$

with $H_\lambda = \theta_{(\mu,\kappa)_\lambda} H_{\tilde{m},\tilde{k}}(\mu, \kappa)_\lambda$. According to (4.11), $\varepsilon_{H,DS}$ is specified as

$$\varepsilon_{H,DS} = \mathbf{E} \left[\left| \sum_{(\mu,\kappa) \in \mathcal{S}_R} \theta_{\mu,\kappa} \frac{a_{\tilde{m}+\mu, \tilde{k}+\kappa}}{p_{\tilde{m},\tilde{k}}} H_{\tilde{m},\tilde{k}}(\mu, \kappa) + \sum_{\lambda=1}^{\Lambda} H_\lambda \frac{\underline{X}_\lambda \underline{d}}{p_{\tilde{m},\tilde{k}}} \right|^2 \right]. \quad (4.28)$$

Utilizing the derivations given in Appendix A.3 and C.1, $\varepsilon_{H,DS}$ yields

$$\varepsilon_{H,DS} = \frac{1}{b} \sum_{l=0}^{L-1} \int_{-f_D T_s}^{f_D T_s} S[\tau_l, \nu] \left(\sum_{(\mu,\kappa) \in \{\mathcal{S}_C, \mathcal{S}_R\}} |A_{\mu,\kappa}[\tau_l, \nu]|^2 + \underline{\alpha}[\tau_l, \nu] \underline{X} \underline{\alpha}[\tau_l, \nu]^H \right) d\nu, \quad (4.29)$$

which again can be separated into a cancellation error $\varepsilon_{c,DS}$ and a residual estimation error $\varepsilon_{r,DS}$:

$$\varepsilon_{H,DS} = \varepsilon_{c,DS} + \varepsilon_{r,DS}. \quad (4.30a)$$

Here, the cancellation error $\varepsilon_{c,DS}$ and the residual estimation error $\varepsilon_{r,DS}$ are given by

$$\varepsilon_{c,DS} = \frac{1}{b} \sum_{l=0}^{L-1} \int_{-f_D T_s}^{f_D T_s} S[\tau_l, \nu] \left(\sum_{(\mu,\kappa) \in \mathcal{S}_C} |A_{\mu,\kappa}[\tau_l, \nu]|^2 + \underline{\alpha}[\tau_l, \nu] \underline{X} \underline{\alpha}[\tau_l, \nu]^H \right) d\nu \quad (4.30b)$$

and

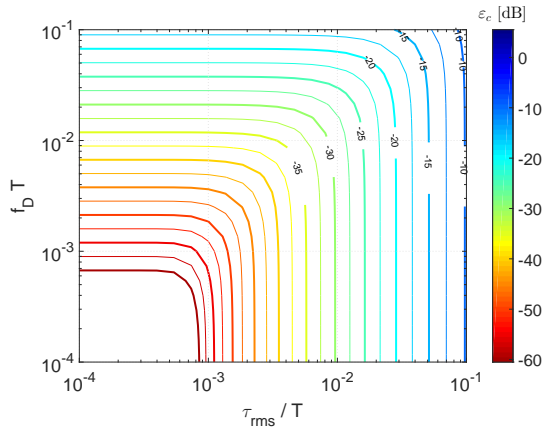
$$\varepsilon_{r,DS} = \frac{1}{b} \sum_{l=0}^{L-1} \int_{-f_D T_s}^{f_D T_s} S[\tau_l, \nu] \sum_{(\mu,\kappa) \in \mathcal{S}_R} |A_{\mu,\kappa}[\tau_l, \nu]|^2 d\nu = \varepsilon_{c,AP}, \quad (4.30c)$$

with $\underline{\alpha}_{\tau_l, \nu}$, \underline{B}_l and \underline{X} as provided in Appendix C.1 (cf. (C.7) and (C.10)). Similar to the AP scheme, [58] proposed the usage of the OQAM symbols next to the pilot symbol, i.e. $\Lambda = 8$ and $\mathcal{S}_C = (\{-1, 0, 1\} \times \{-1, 0, 1\}) \setminus (0, 0)$, such that the residual channel estimation errors for both interference mitigation schemes are equal, i.e. $\varepsilon_{r,DS} = \varepsilon_{r,AP}$. The appropriate spreading codes and the derived matrix \underline{X} are provided in appendix C.3.

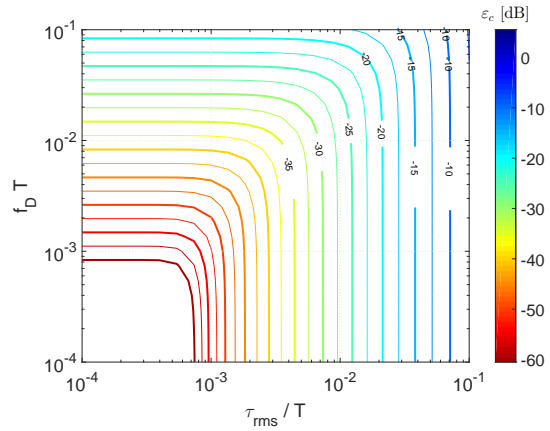
The resulting cancellation $\varepsilon_{c,DS}$ and total channel estimation errors $\varepsilon_{H,DS}$ are depicted in Figure 4.9, which additionally presents the cancellation performance ratio $\Delta\varepsilon_c$ between the DS and AP schemes defined as below:

$$\Delta\varepsilon_c = \frac{\varepsilon_{c,DS}}{\varepsilon_{c,AP}}. \quad (4.31)$$

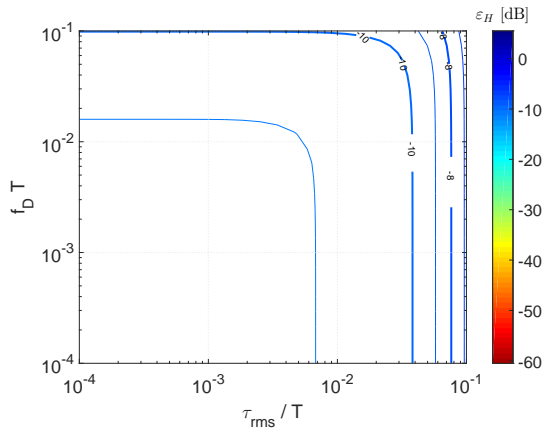
As the residual estimation error is equal for both investigated interference mitigation schemes, i.e. $\varepsilon_{r,DS} = \varepsilon_{r,AP}$, the graphical presentation of $\varepsilon_{r,DS}$ is omitted. Since the utilized channel is not considered in the design of the auxiliary data symbol d_Λ and the spreading matrix \underline{C} , the increase in channel estimation error is in line with the SIR of the data symbols shown in Figure 3.9. Similar to the AP scheme, the overall channel estimation



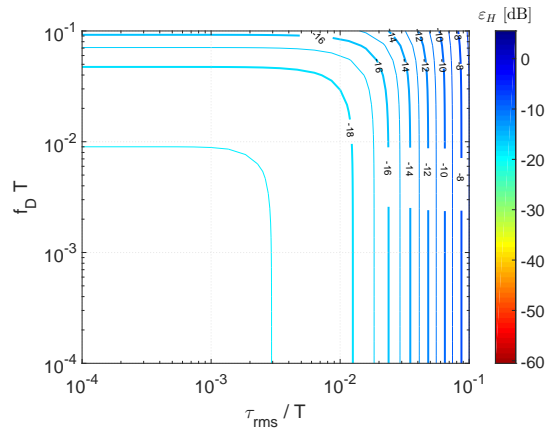
(a) $\epsilon_{c,DS}$ with PHYDYAS



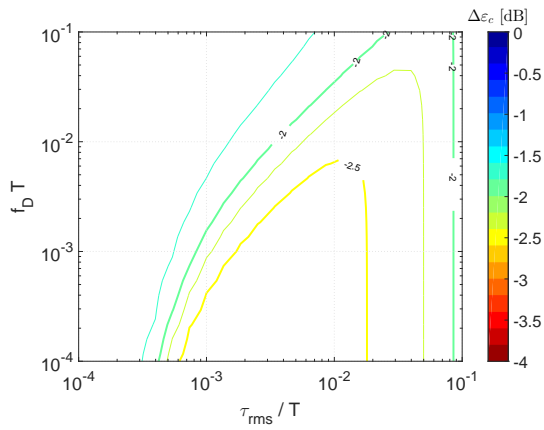
(b) $\epsilon_{c,DS}$ with Hermite



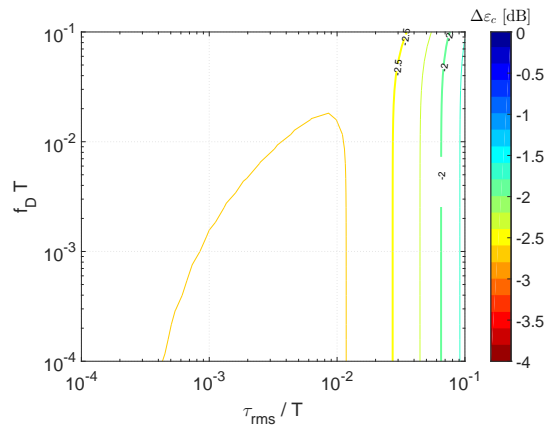
(c) $\epsilon_{H,DS}$ with PHYDYAS (-3.51 dB)



(d) $\epsilon_{H,DS}$ with Hermite (-5.39 dB)



(e) $\Delta\epsilon_c$ with PHYDYAS



(f) $\Delta\epsilon_c$ with Hermite

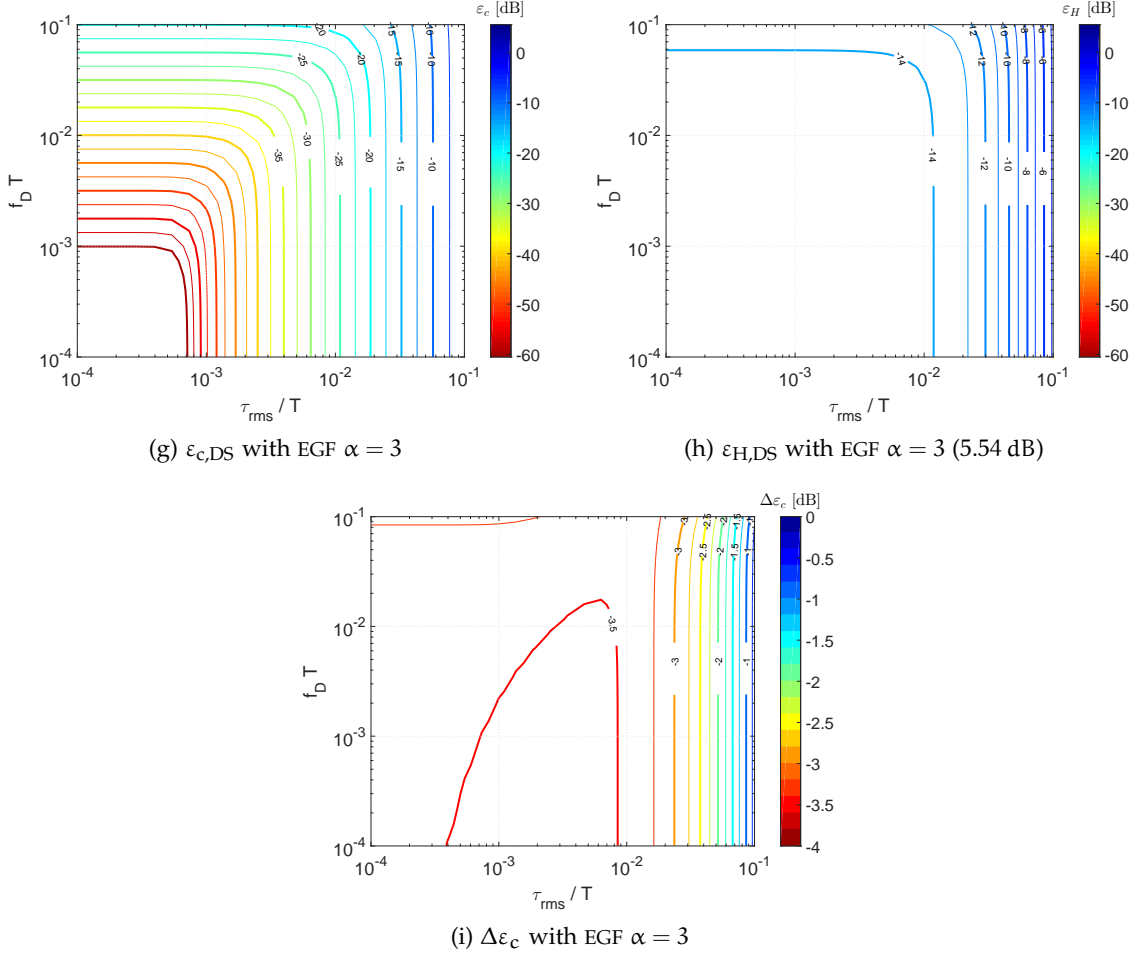


Figure 4.9: Scattered pilot based channel estimation error $\varepsilon_{H,DS}$, the cancellation error $\varepsilon_{c,DS}$ and the estimation error reduction $\Delta\varepsilon_c$ of FBMC-OQAM systems with DS interference mitigation operating in various channel environments with $K = 256$, $\gamma = 4$ and $b = 1$. The values in parentheses determine the required DS power overhead per pilot symbol compared to the data symbols $a_{m,k}$.

performance $\varepsilon_{H,DS}$ of the DS scheme is severely limited, as it is bounded by $\varepsilon_{r,DS}$. For isotropic PFFs, i.e. Hermite, the DS scheme can deliver a minimum $\varepsilon_{H,DS}$ of approximately -18 dB. For non-isotropic PFFs, i.e. PHYDYAS and EGF $\alpha = 3$, $R_{\tilde{m},\tilde{k}}$ leads to an increase of the total estimation error to -11 dB and -14 dB, respectively. Additionally, the transmit power is increased. Compared to CP-OFDM the pilot pair ($p_{m,k}$ and $\rho_{m,k}$) has an average power rise of about -5.5 to 5.5 dB, which is significantly less than the power overhead of the AP scheme. The high value of 5.5 dB for the EGF PFF with $\alpha = 3$ can be reduced by a proper design of $\underline{\beta}$ and \underline{C} . For all PFFs, the channel estimation performance is limited by the residual estimation error $\varepsilon_{r,DS}$ in the region of $\tau_{rms}/T \leq 9 \cdot 10^{-3}$ and $f_D T \leq 3 \cdot 10^{-2}$. This may be improved by increasing the set S_C as proposed in [14, 71].

Comparing the AP and DS schemes, i.e. considering the cancellation error $\Delta\varepsilon_c$, depending on the applied PFF the DS scheme offers a superior channel estimation performance

of 2 to 3.5 dB gain compared to the AP scheme as depicted in Figures 4.9e, 4.9f and 4.9i. However, simulations proved that due to the presence of $R_{\bar{m},\bar{k}}$, the performance ratio $\Delta\epsilon_H$ defined as

$$\Delta\epsilon_H = \frac{\epsilon_{H,DS}}{\epsilon_{H,AP}} \quad (4.32)$$

yields 0 dB for approximately $\tau_{\text{rms}}/T \leq 9 \cdot 10^{-3}$ and $f_D T \leq 3 \cdot 10^{-2}$. Beyond this region the performance gain $-\Delta\epsilon_H$ of the DS scheme is limited to 0.5 to 2 dB.

4.4.3 System level simulations

In this section, the influence of the channel estimation error ϵ_H on the system level performance in terms of uncoded BER with application of the AP and DS interference mitigation schemes is evaluated. Therefore, the ϵ_H results obtained analytically (cf. Section 4.4.1 and Section 4.4.2) and via Monte-Carlo simulations as well as the BER performance with perfect and imperfect CSIR are compared for selected modulation orders M . Additionally, the available modulation order M is evaluated based on the channel estimation error ϵ_H achieved by the AP and DS interference mitigation schemes. Therefore, the influence of the noise on the SINR is not considered to obtain the upper performance limits of the scattered pilot based channel estimation in combination with the AP or DS interference mitigation schemes.

The Monte-Carlo simulations are carried out for $2 \cdot 10^3$ channel realizations, each having $5 \cdot 10^3$ transmitted FBMC-OQAM symbols. To avoid undersampling and thus aliasing of the channel impulse response and transfer function for high delay and Doppler spreads as well as to minimize the interference between adjacent pilot symbols, the pilot symbols are placed in a checker pattern at every 8th subcarrier and real valued OQAM symbol, such that $2 \cdot 10^5$ pilot symbols are evaluated per channel realization. In order to equalize the data symbols, a two-dimensional linear interpolation of the time-variant CTF is applied. For the channel scenarios $s_c = \{A, B, C\}$, Figure 4.10 depicts the comparison of ϵ_H values, which are obtained analytically and via Monte-Carlo based simulations for $K = 256$. The dashed verticals indicates the position of a system configuration with LTE symbol duration. For both interference mitigation schemes, i.e. AP and DS, the results obtained analytically are in line with those based on Monte-Carlo simulations, thus verifying the accuracy of the derived expressions for the channel estimation error ϵ_H . Again, the results clearly show the performance floor of the channel estimation error due to the residual channel estimation error ϵ_r . The small deviations between the analytical results and those based on simulations are supposed to be caused by insufficient simulation statistics.

Similar to the estimation of the required SINR introduced in Section 4.2, a maximum channel estimation error $\epsilon_{H,\text{max}}$ for a given modulation order M and its required BER can

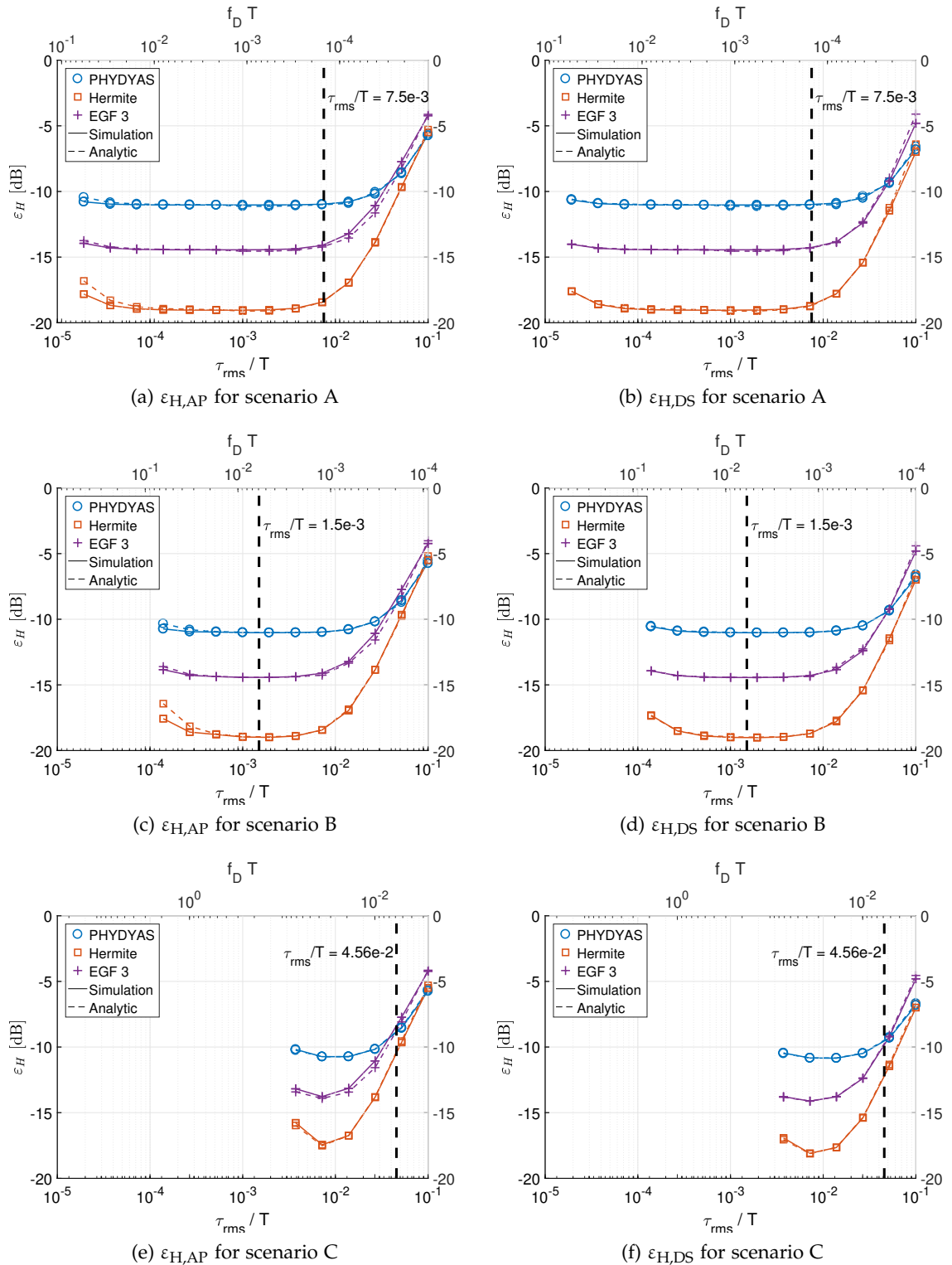


Figure 4.10: Comparison of analytical and Monte-Carlo simulations based channel estimation error ϵ_H for FBMC-OQAM systems, utilizing scattered pilots (left: AP, right: DS) with pilot boost factor $b = 1$ operating in channel scenarios A to C (cf. Table 4.11). The dashed verticals indicate the equivalent normalized delay spread and maximum Doppler shift for the LTE subcarrier spacing, respectively.

M-QAM	4	16	64	256	1024	4096
SINR [dB]	9.3	15.1	20.2	25.2	30.2	35.2
$\varepsilon_{H,\max}$ [dB]	-6.8	-12.2	-17.2	-22.2	-27.2	-32.2

Table 4.10: Approximated SIR values for a target uncoded BER of $5 \cdot 10^{-2}$ for an LTE system operating in a Rayleigh fading channel (cf. Table 4.4) and the related maximum channel estimation error $\varepsilon_{H,\max}$ for SINR = SIR.

be derived. In [42], Guo et al. presented a relationship between the SINR and the resulting channel estimation error ε_H for complex valued transmit symbols $a_{m,k}$, which is given by

$$\varepsilon_H = \frac{1}{1 + \text{SINR}}. \quad (4.33a)$$

Although (4.33a) has been derived for the MMSE estimator, it can serve as an upper performance bound for the LS estimation. Thus, without noise, i.e. SINR = SIR, the maximum channel estimation error $\varepsilon_{H,\max}$ for FBMC-OQAM systems can be derived as follows

$$\varepsilon_{H,\max} \cong \frac{2}{1 + \text{SIR}} \quad (4.33b)$$

and the required SIR can be estimated by

$$\text{SIR} \cong \frac{2}{\varepsilon_{H,\max}} - 1. \quad (4.33c)$$

Here, a factor of two is introduced, which accounts for the fact that only a fraction of the estimation error affects the OQAM data symbols, since only the real part of demodulated symbols bears information and the imaginary part is dropped after channel equalization. The resulting maximum channel estimation error $\varepsilon_{H,\max}$ based on the required SINR values for a given modulation order M (cf. Table 4.4) are summarized in Table 4.10.

From the channel estimation error results depicted in Figures 4.7, 4.9 and 4.10, the maximum modulation order M in dependence on the PFF and channel scenario can be derived, which are provided in Table 4.11. For reference, Table 4.11 also contains the SIR values for the optimal symbol duration T_{opt} as well as the related channel estimation errors and modulation orders (cf. Section 4.2). In Figure 4.11 the related BER curves are contrasted with the BER results under assumption of perfect CSIR. It can be seen, that channel estimation based on the LS method in combination with the discussed AP or DS interference mitigation schemes results in a significant loss of BER performance of more than one order of magnitude.

In all considered scenarios, the residual interference on pilot symbols and thus MSE of the LS channel estimation is minimized for isotropic PFFs. Therefore, for these scenarios

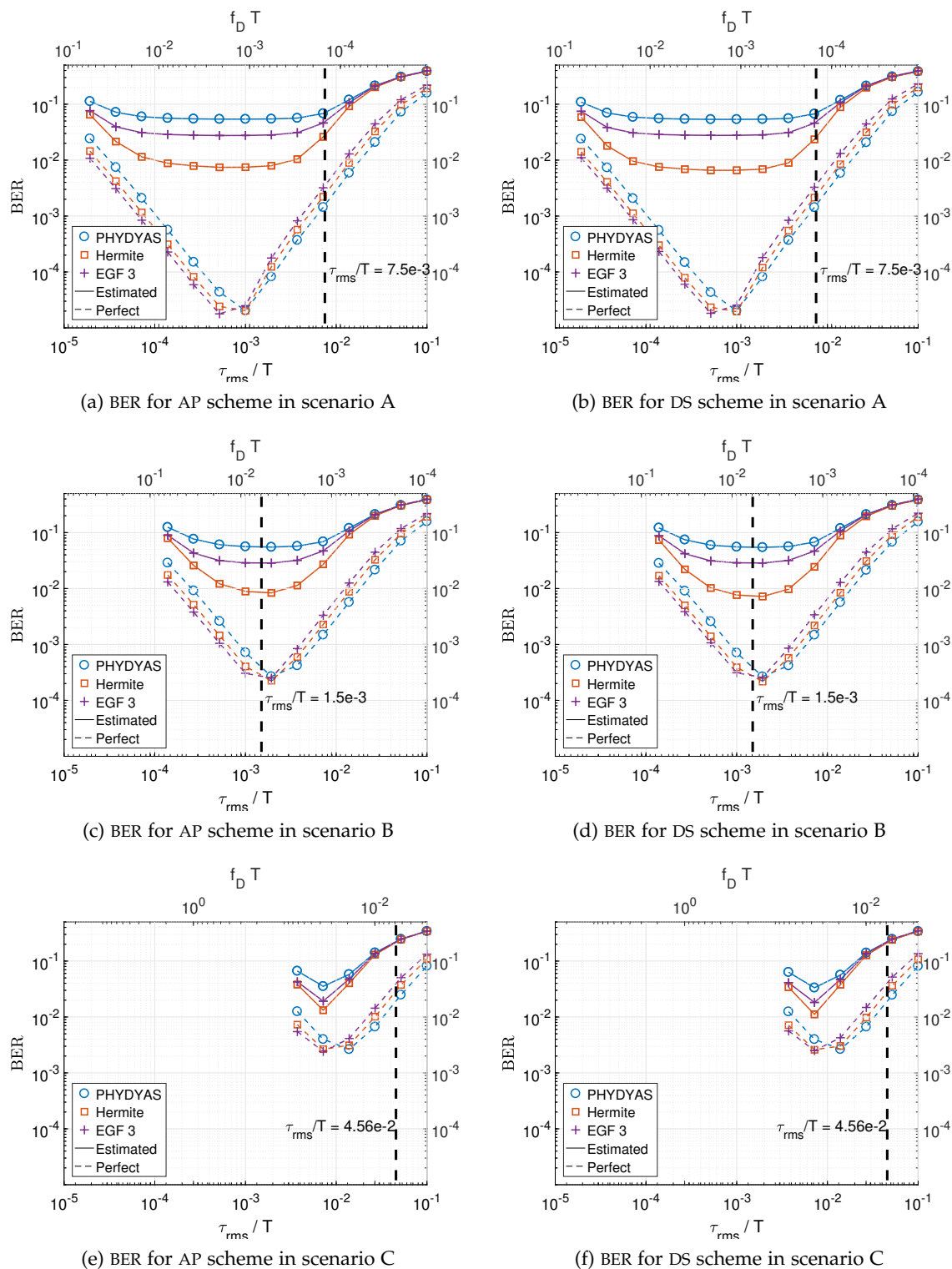


Figure 4.11: Comparison of BERs for FBMC-OQAM systems with perfect and imperfect CSIR, utilizing scattered pilots (left: AP, right: DS) with pilot boost factor $b = 1$ operating in channel scenarios A to C (cf. Table 4.11). The dashed verticals indicate the equivalent normalized delay spread and maximum Doppler shift for the LTE subcarrier spacing, respectively.

s_c	PFF	imperfect CSIR			perfect CSIR		
		$\varepsilon_{H,\max}$ [dB]	equiv. SIR [dB]	M	SIR [dB]	equiv. $\varepsilon_{H,\max}$ [dB]	M
A	PHYDYAS	-11	13.8	16	54.8	-51.8	4096
	Hermite	-19	22	64	56.5	-53.5	4096
	EGF 3	-14.4	17.3	16	57.1	-54.1	4096
B	PHYDYAS	-11	13.8	16	43.8	-40.8	4096
	Hermite	-19	22	64	44.6	-41.6	4096
	EGF 3	-14.4	17.3	16	44.8	-41.8	4096
C	PHYDYAS	-10.7	13.5	4	27.7	-24.7	256
	Hermite	-17.5	20.5	16	28.3	-25.3	256
	EGF 3	-13.9	16.8	16	28.1	-25.1	256

Table 4.11: Selected scenarios for the performance evaluation at 800 MHz carrier frequency including the theoretically obtained M-QAM based on the approximated SIR as well as the applied M-QAM limited by the channel estimation error $\varepsilon_{H,\max}$. (Note that modulation order for perfect CSIR holds only for interference limited scenarios, i.e. $SIR \gg SNR$)

with the considered system design, CAPS cannot provide the uncoded BER performance gains as shown for perfect CSIR. For the scenarios A and C, CASS can still retrieve some performance enhancements, which however are much less as for perfect CSIR.

As shown by the previous results, both investigated interference mitigation schemes are able to reach the BER performance levels required by LTE. To support higher order modulation schemes, e.g. 256-QAM in LTE Advanced (Rel. 12), further improvements in the system design need to be found to reduce the channel estimation error. Without increasing the receiver complexity, the channel estimation error and the related system performance can be improved by using boosted pilots ($b > 1$) or by reducing the residual estimation error by consideration of a higher number of neighboring symbols. Unfortunately, this in turn results in higher system complexity and might increase latency [14, 50, 71]. Additionally, further interference mitigation schemes, e.g. POP methods [13, 57] may provide a better channel estimation and equalization performance.

4.5 CONCLUDING REMARKS

In this chapter, the practical feasibility of FBMC-OQAM systems with homogeneous CAW has been investigated. Therefore, the performance gains in terms of SIR, BER and channel capacity have been evaluated. Additionally, the impact of scattered pilot based channel estimation according to the LS approach has been considered. In this regard, analytical descriptions of interference mitigation on pilot symbols based on the AP and DS schemes have been derived and evaluated. The related outcomes have been compared with Monte-

Carlo simulation based results. These results confirm that for the specified system design, homogeneous CAW can provide significant performance gains compared to a “one-fits-all” system design approach like LTE. However, the performance gains may be reduced significantly, if channel estimation based on scattered pilots is utilized, as it is subject to shortcomings concerning the residual channel estimation error. In this case, the best performance for each considered scenario has been achieved by isotropic PFFs.

In this chapter the extension of the homogeneous CAW approach discussed in the preceding chapter to heterogeneous configurations per cell is evaluated. Here, different groups of users (or even single users) within a cell may utilize a specific system configuration according to their environment and behavior in terms of velocity. An exemplary presentation of different lattice grids in the T-F domain is provided in Figure 5.1. It can be seen clearly, that due to the various lattice grids and PFFs, the orthogonality between different user groups is not guaranteed. Therefore, based on a signal model extended for multi-user DL and UL setups with user-specific system configurations, in this chapter the general optimization problem for the maximization of the channel capacity in a cell is formulated and investigated for an exemplary scenario. Additionally, the amount of inter-user guard bands is discussed briefly. Parts of this chapter have been published in [33]. For simplicity, in this chapter the term “user” encloses a single or a group of users with a common system configuration in terms of PFF and symbol duration.

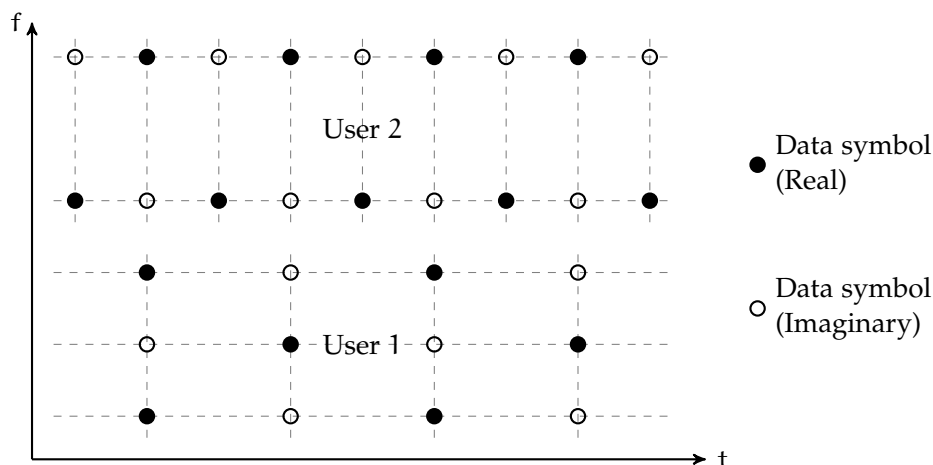


Figure 5.1: Exemplary lattice grids of users with different subcarrier spacing (Symbol duration T_1 of user 1 is twice the one of user 2 (T_2), i.e. $T_1 = 2T_2$).

For the consideration of multi-user scenarios with user-specific system configurations, the system model introduced in Chapter 3 has to be extended. Therefore, throughout this chapter the indices u and u' are used to indicate variables specific to a certain user or user group. \mathcal{U} and $\mathcal{U}_{c,u} = \mathcal{U} \setminus u$ are the sets of all users and the related co-users, respectively. To ease the interference investigation of systems with different subcarrier spacings, a joint virtual lattice grid with K_v virtual subcarriers is introduced, such that all subcarriers of all users can be represented by both user specific and virtual subcarriers.

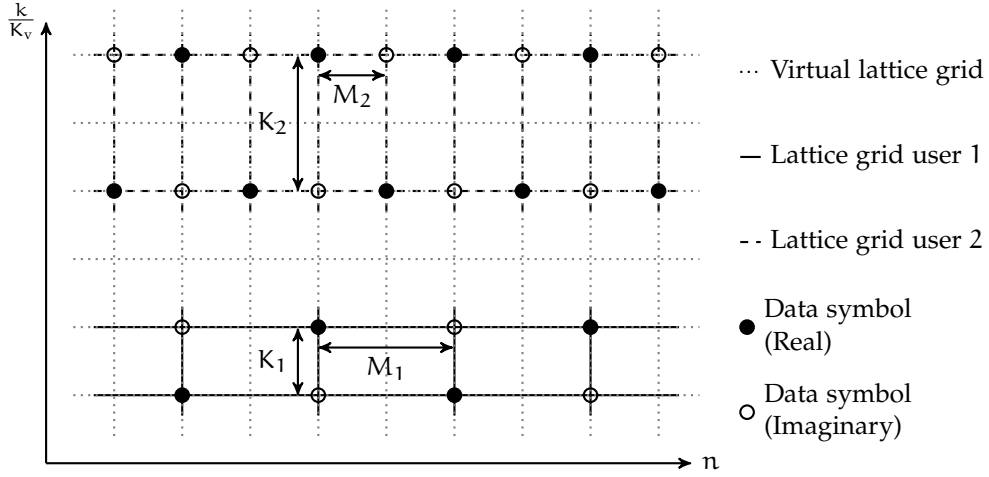


Figure 5.2: Mapping of user specific lattice grids of Figure 5.1 onto the virtual lattice grid. The intersections of the virtual lattice determine all available sampling points in the T-F plane.

Therefore, for each user with discrete-time subcarrier spacing K_u a frequency domain oversampling factor $\zeta_u \in \mathbb{N}$ is introduced with

$$\zeta_u = \frac{K_v K_u}{\nu_0}. \quad (5.1a)$$

To ensure that all lattice points of all users are located at integer multiples of the base sample rate T_s , the effective symbol spacing $M_u \in \mathbb{N}^+$ and symbol duration T_u are defined according to

$$M_u = \frac{\tau_0 K_v}{\zeta_u} \quad (5.1b)$$

$$T_u = \frac{K_v T_s}{\zeta_u}. \quad (5.1c)$$

For illustration, the resulting virtual lattice grid related to the scenario of Figure 5.1 is presented in Figure 5.2.

5.1 HETEROGENEOUS CAW IN CELLULAR DL

In this section, the performance of heterogeneous CAW is investigated for a cellular DL scenario. Therefore, the system model introduced in Chapter 3 is extended to a multi-user setup. Afterwards, the optimization problem and constraints for an improvement of the cell-specific channel capacity applying heterogeneous CAW is formulated, followed by a discussion of simulation results for a selected cell scenario.

5.1.1 System model

Based on the introduced virtual lattice grid and considering the user specific time-variant multipath channel $h_u[\tau, n]$ of path delay τ , in cellular DL the discrete-time signal $r_u[n]$ received by user u is obtained by

$$r_u[n] = \sum_{\tau} h_u[\tau, n] \sum_{u' \in \mathcal{U}} s_{u'}[n - \tau], \quad (5.2)$$

which comprises a superposition of the user specific FBMC-OQAM transmit signals $s_u[n]$ given by

$$s_u[n] = \sum_{(m,k) \in \mathbb{T}_u} \theta_{m,k} a_{u,m,k} f_u[n - mM_u] e^{j2\pi k K_u n}. \quad (5.3)$$

Here, the i.i.d. real valued OQAM symbols $a_{u,m,k}$ of user u are transmitted at time index m and at subcarrier index k out of the user-specific sets of allocated symbols \mathbb{M}_u and subcarriers \mathbb{K}_u , respectively. The set $\mathbb{T}_u = \mathbb{M}_u \times \mathbb{K}_u$ denotes the set of transmit position tuples (m, k) and $f_u[n]$ is the PFF utilized by user u .

After matched filtering at the receiver, the symbol $\tilde{a}_{u,\tilde{m},\tilde{k}}$ received by user u at time index \tilde{m} and subcarrier index \tilde{k} yields

$$\begin{aligned} \tilde{a}_{u,\tilde{m},\tilde{k}} &= \theta_{\tilde{m},\tilde{k}}^* \left(r_u[n] * f_u^*[\tilde{m}M_u - n] e^{-j2\pi\tilde{k}K_u n} \right) \Big|_{M_u} \\ &= \sum_{u' \in \mathcal{U}} \sum_{(\mu,\kappa) \in \mathbb{S}_{u'}} \theta_{\mu,\kappa} a_{u',\tilde{m}+\mu,\tilde{k}+\kappa} H_{\tilde{m},\tilde{k}}^{u,u'}(\mu, \kappa) \end{aligned} \quad (5.4)$$

with the sets of available offsets $\tilde{\mathbb{M}}_u = \mathbb{M}_u - \tilde{m}$ and $\tilde{\mathbb{K}}_u = \mathbb{K}_u - \tilde{k}$. The $\tilde{a}_{u,\tilde{m},\tilde{k}}$ related lattice grid is described by the set of lattice position tuples $(\mu, \kappa) \in \mathbb{S}_u$ with $\mathbb{S}_u = \tilde{\mathbb{M}}_u \times \tilde{\mathbb{K}}_u$. The resulting effective channel coefficient $H_{\tilde{m},\tilde{k}}^{u,u'}(\mu, \kappa)$ for a multi-user scenario is given by

$$\begin{aligned} H_{\tilde{m},\tilde{k}}^{u,u'}(\mu, \kappa) &= \sum_{\tau} \int_{-f_D T_s}^{f_D T_s} D_u[\tau, \nu] e^{j2\pi\tilde{m}M_u\nu} A_{\tilde{m},\tilde{k}}^{u,u'}[\mu M_{u'} + \tau, \kappa K_{u'} + \nu] \\ &\quad \cdot e^{-j2\pi K_u(\tilde{k}+\kappa)(\mu M_u - \tilde{m}M_{u,u'} + \tau)} d\nu, \end{aligned} \quad (5.5)$$

where the channel spreading function $D_u[\tau, \nu]$ of user u is the DTFT of $h_u[\tau, n]$ at frequency ν (cf. (3.8)). $A_{\tilde{m},\tilde{k}}^{u,u'}[\tau, \nu]$ is the discrete-time (cross-)ambiguity function defined by

$$A_{\tilde{m},\tilde{k}}^{u,u'}[\tau, \nu] = \sum_{n=-\infty}^{\infty} f_{u'}[n + \tilde{m}M_{u,u'} - \tau] f_u^*[n] e^{j2\pi n(\nu - \tilde{k}K_{u,u'})}. \quad (5.6)$$

To account for the lattice position (\tilde{m}, \tilde{k}) dependent symbol and virtual subcarrier offsets between two users, the virtual lattice grid based co-user symbol and subcarrier offsets $M_{u,u'}$ and $K_{u,u'}$ are introduced. They are defined according to (cf. Appendix A.5)

$$\text{Symbol offset:} \quad M_{u,u'} = \tau_0 K_v \left(\frac{1}{\zeta_u} - \frac{1}{\zeta_{u'}} \right) \quad (5.7a)$$

$$\text{Subcarrier offset:} \quad K_{u,u'} = \frac{\nu_0}{K_v} (\zeta_u - \zeta_{u'}). \quad (5.7b)$$

Similar to the scenario of homogeneous CAW (cf. Section 3.2), the received symbol $\tilde{a}_{u,\tilde{m},\tilde{k}}$ can be interpreted as a superposition of a desired part $\check{a}_{u,\tilde{m},\tilde{k}}$ and an interference part, which in this case is composed by the intrinsic interference $\check{i}_{u,\tilde{m},\tilde{k}}$ and the co-user interference $u_{u,\tilde{m},\tilde{k}}$:

$$\tilde{a}_{u,\tilde{m},\tilde{k}} = \check{a}_{u,\tilde{m},\tilde{k}} + \check{i}_{u,\tilde{m},\tilde{k}} + u_{u,\tilde{m},\tilde{k}} \quad (5.8a)$$

with

$$\check{a}_{u,\tilde{m},\tilde{k}} = a_{u,\tilde{m},\tilde{k}} H_{\tilde{m},\tilde{k}}^{u,u}(0,0) \quad (5.8b)$$

$$\check{i}_{u,\tilde{m},\tilde{k}} = \sum_{(\mu,\kappa) \in S_{N,u}} \theta_{\mu,\kappa} a_{u,\tilde{m}+\mu,\tilde{k}+\kappa} H_{\tilde{m},\tilde{k}}^{u,u}(\mu,\kappa) \quad (5.8c)$$

$$u_{u,\tilde{m},\tilde{k}} = \sum_{u' \in \mathcal{U}_{c,u}} \sum_{(\mu,\kappa) \in S_{u'}} \theta_{\mu,\kappa} a_{u',\tilde{m}+\mu,\tilde{k}+\kappa} H_{\tilde{m},\tilde{k}}^{u,u'}(\mu,\kappa). \quad (5.8d)$$

As for homogeneous CAW, $S_{N,u} = S_u \setminus (0,0)$ is the set of lattice position tuples (μ,κ) of user u neighboring the demodulated symbol $\tilde{a}_{u,\tilde{m},\tilde{k}}$. Compared to the critically sampled system model in Chapter 3 the amount of intrinsic as well as co-user interference depends on the investigated symbol position (\tilde{m}, \tilde{k}) . Thus, with the assumption of i.i.d. data and pilot symbols $a_{u,m,k}$ and WSSUS channels, the reconstruction performance $\text{SIR}_u(\tilde{m}, \tilde{k})$ at a given lattice position of user u in a multi-user scenario can be defined as

$$\text{SIR}_u(\tilde{m}, \tilde{k}) = \frac{\sigma_{S,u}^2}{\sigma_{I,u}^2(\tilde{m}, \tilde{k}) + \sigma_{U,u}^2(\tilde{m}, \tilde{k})}. \quad (5.9)$$

Here, the average data $\sigma_{S,u}^2$, intrinsic interference $\sigma_{I,u}^2(\tilde{m}, \tilde{k})$ and co-user interference power $\sigma_{U,u}^2(\tilde{m}, \tilde{k})$ are obtained by

$$\sigma_{S,u}^2 = P_{0,0}^{u,u}(0,0) \quad (5.10a)$$

$$\sigma_{I,u}^2(\tilde{m}, \tilde{k}) = \sum_{(\mu,\kappa) \in S_{N,u}} P_{\mu,\kappa}^{u,u}(\tilde{m}, \tilde{k}) \quad (5.10b)$$

$$\sigma_{U,u}^2(\tilde{m}, \tilde{k}) = \sum_{u' \in \mathcal{U}_{c,u}} \sum_{(\mu,\kappa) \in S_{u'}} P_{\mu,\kappa}^{u,u'}(\tilde{m}, \tilde{k}), \quad (5.10c)$$

with the average power $P_{\mu,\kappa}^{u,u'}(\tilde{m}, \tilde{k})$ obtained from lattice point (μ, κ) of user u' defined as follows

$$P_{\mu,\kappa}^{u,u'}(\tilde{m}, \tilde{k}) = \sigma_a^2 \sum_{\tau} \int_{-f_D T_s}^{f_D T_s} S_u[\tau, \nu] \Re\{\theta_{\mu,\kappa} A_{\tilde{m}, \tilde{k}}^{u,u'} [\mu M_{u'} + \tau, \kappa K_{u'} + \nu]\}^2 d\nu. \quad (5.11)$$

Accordingly, the channel scattering function $S_u[\tau, \nu] = \mathbf{E}[|D_u[\tau, \nu]|^2]$ of user u is given by (cf. (3.34b))

$$S_u[\tau, \nu] = \sum_{l=0}^{L-1} \frac{1}{\pi \tau_{\text{rms}} f_D} e^{-\frac{\zeta_u \tau_l}{K_v \tau_{\text{rms}} / T}} \frac{1}{\sqrt{1 - \left(\frac{K_v \nu}{\zeta_u f_D T}\right)^2}} \delta[\tau - \tau_l]. \quad (5.12)$$

5.1.2 Channel capacity gains

As discussed before, the current investigation targets scenarios in which each user in a cell may have an environmental specific system configuration. To account for the increased parameter space compared to a setup with homogeneous CAW, the sets \mathbb{T}_s , \mathbb{F} and \mathbb{K} of user-specific symbol durations $T_u \in \mathbb{T}_s$, PFF configuration $f_u[n] \in \mathbb{F}$ and subcarrier allocation pattern $\mathbb{K}_u \in \mathbb{K}$ have to be considered. Thus, with a given amount of virtual subcarriers K_v , the optimization problem to maximize the cell-wide capacity $C_{u,\text{opt}}$ can be formulated as

$$C_{u,\text{opt}} = \max_{\mathbb{T}_s, \mathbb{K}, \mathbb{F}} \frac{1}{K_v} \sum_{u \in \mathbb{U}} \zeta_u |\mathbb{K}_u| C_{\text{opt}}(u) \quad (5.13a)$$

subject to the constraint of limited bandwidth

$$K_v \geq \sum_{u \in \mathbb{U}} \left(|\mathbb{K}_u| \zeta_u + \sum_{u'} \frac{|\mathbb{K}_g^{u,u'}|}{2} \right). \quad (5.13b)$$

Here, $C_{\text{opt}}(u)$ is the capacity of the u -th user averaged over all allocated subcarriers and K_v and $\mathbb{K}_g^{u,u'}$ are the amount of virtual subcarriers available in the cell and the set of guard bands between two users, respectively. To avoid double counting of the guard bands $|\mathbb{K}_g^{u,u'}|$ during the summation for user u and u' , each user considers half of the guard bands.

As mentioned before, utilizing different symbol durations and PFFs for different users inhibits orthogonality and the capacity becomes dependent on the allocated subcarrier and time index, which influences the relative time offset between neighboring symbols of two users. The amount of different relative time offsets can be determined by analysis of the time domain sampling positions of the cross-ambiguity function, which are the lattice positions of user u' ($\mu M_{u'}$) shifted by a symbol specific offset ($\tilde{m} M_{u,u'}$) and

some channel tap delay τ . From the definition of K_V and ζ_u it can be deduced, that a specific symbol constellation in terms of relative positions at time instance n is repeated at $n + \tau_0 K_V$. Due to the separate transmission of either real or imaginary symbols it can happen that the phase relation (real/imaginary) between the lattice position and thus the inflicted interference of the users is changed. After twice this period the phase relation is guaranteed to be reestablished. Therefore, after a period of $2\tau_0 K_V$ all different sampling positions of the cross-ambiguity function have occurred. Accordingly, the resulting number of different sampling patterns N_P is

$$\begin{aligned} N_P &= 2 \frac{\tau_0 K_V}{M_u} \\ &= 2 \frac{\tau_0 K_V}{\frac{\tau_0 K_V}{\zeta_u}} \\ &= 2\zeta_u. \end{aligned} \quad (5.14)$$

For simplicity, in DL transmissions it is reasonable to assume that all transmitter AFBs have been started simultaneous such that at the receiver there is at least one time-instance at which symbols of all user could be demodulated coincidentally, i.e.

$$\forall u \exists \tilde{m} : \tilde{m} M_u = \text{const.} \quad (5.15)$$

Without loss of generality, in this thesis this time instance is assumed to be $\forall u : \tilde{m} = 0$. Thus, and with equal transmit power for all users and allocated subcarriers, the normalized channel capacity $C_{\text{opt}}(\mathbf{u})$ averaged over all allocated subcarriers and possible time-offsets N_P can be calculated as

$$C_{\text{opt}}(\mathbf{u}) = \frac{1}{N_P |\mathbb{K}_u|} \sum_{\tilde{m}=0}^{N_P-1} \sum_{\tilde{k} \in \mathbb{K}_u} \log_2 (1 + \text{SIR}_u(\tilde{m}, \tilde{k})). \quad (5.16)$$

For a first evaluation of the capacity gains obtained by heterogeneous CAW, the effects for a scenario with two users in different channel environments $s_{c,u}$ is investigated. The considered evaluation scenario in this thesis is a cell located at a site with heterogeneous wave propagation and user behavior properties, e.g. city outskirts with a passing highway. Therefore, user group 1 is defined to consist of pedestrians walking between the buildings of the city, which corresponds to channel scenario A of this thesis. User group 2 comprises car drivers passing the city along a highway (scenario B). To restrict the search space for the optimization process to a reasonable scale, the sets \mathbb{T}_s and \mathbb{K} are restricted as follows:

- Contiguous subcarrier allocation for all users, i.e. all users in the cell with equal channel environment and thus system configuration are grouped in frequency domain to minimize the guard band overhead.

- The search space of available subcarrier spacings is restricted to integer ratios based on the power of 2 as suggested in [36], which additionally reduces implementation complexity, i.e.

$$\forall u \forall u' : \log_2 \left(\frac{\zeta_u}{\zeta_{u'}} \right) \in \mathbb{Z}. \quad (5.17a)$$

As the investigations in this thesis are compared to the state-of-the-art LTE system and additionally, the subcarrier spacing of LTE proved to be close to optimal in channel scenario B, the subcarrier spacings considered in the optimization process are integer multiples or fractions of the one of LTE:

$$\log_2 \left(\frac{K_v T_s}{T_{\text{LTE}}} \right) \in \mathbb{Z}. \quad (5.17b)$$

For any given scenario, the general optimization problem formulated in (5.13) requires additional constraints, as it does not consider any kind of user fairness or other application or scenario specific requirements. Here, the optimization constraints are amended to

1. ensure some kind of fairness between the different user groups, as the optimization problem given in (5.13) always results in an unfair “one-takes-all” capacity distribution. Thus, to overcome this problem each user group shall retain a suitable fraction γ_f of its capacity before the optimization process, hereinafter also referred to as fairness factor

$$C_{\text{opt}}(\mathbf{u}) \geq \gamma_f C_{\text{LTE}}^{\text{sc},u}. \quad (5.18)$$

2. position the inter-user guard bands $K_g^{u,u'}$ to equally distribute the thereof resulting capacity losses to both users. Therefore, with the initial sets of allocated subcarriers \mathbb{K}_u^I of user u and the initial allocation ratio K_r defined by

$$K_r = \frac{|\mathbb{K}_1^I|}{|\mathbb{K}_2^I|}, \quad (5.19a)$$

the additional optimization constraint can be defined as

$$\arg \min_{\mathbb{K}_1, \mathbb{K}_2} \left| \frac{|\mathbb{K}_1|}{|\mathbb{K}_2|} - K_r \right| \quad (5.19b)$$

3. fix the excessive bandwidth at the band edges. Thus, the subcarrier positions of user u can only be changed by integer multiples of ζ_u .

A summary of the scenario and the thereof derived parameters is provided in Table 5.1.

Parameter	Values
Number of users $ \mathbf{U} $	2
Channel scenarios	User 1: A, User 2: B
Allocation pattern	Contiguous
Allocation ratio K_r	1/3, 1/1, 3/1
Bandwidth modes (LTE)	{1.4, 3, 5, 10, 20} MHz
Related number of subcarriers K (LTE)	$12 \cdot \{6, 15, 25, 50, 100\}$
Base symbol duration	T_{LTE} and $\alpha_T T_{\text{LTE}}$ with $\log_2(\alpha_T) \in \{-0.8, -0.6, \dots, 0.8\}$
Symbol duration ratios $T_1/T_2 = \zeta_2/\zeta_1$	$\log_2(\zeta_2/\zeta_1) \in \mathbb{Z}$
Fairness factor γ_f	1

Table 5.1: Parameter setup for the evaluation of the capacity gains in a multi-user CAW scenario.

The cell wide capacity gains for this scenario are compared with a cell configuration based on LTE parameters with the PHYDYAS PFF (cf. Table 4.8 in Section 4.3). The channel capacity gain C_g for a given scenario and allocation ratio can be obtained by

$$C_g = \frac{1}{C_{\text{ref}}} \sum_{\mathbf{u} \in \mathbf{U}} |\mathbb{K}_{\mathbf{u}}| C_{\text{opt}}(\mathbf{u}) \quad (5.20a)$$

$$C_g[\%] = 100(C_g - 1),$$

where for the investigated scenario the reference capacity C_{ref} is given by

$$C_{\text{ref}} = |\mathbb{K}_1^I| C_{\text{LTE}}^A + |\mathbb{K}_2^I| C_{\text{LTE}}^B. \quad (5.20b)$$

In Table 5.2 the resulting channel capacity gains C_g and system configurations for the investigated scenario are quantified and depicted in Figure 5.3 (hatched bar plots). To obtain insight into the impact of the guard band sizes as well as the selected constraints of the optimization problem on the capacity gain, the upper bound \bar{C}_g for the capacity gain in a given scenario is defined according to

$$\bar{C}_g = \frac{1}{C_{\text{ref}}} \sum_{\mathbf{u} \in \mathbf{U}} |\mathbb{K}_{\mathbf{u}}^I| C_{\text{opt}}^{\text{sc},\mathbf{u}} \quad (5.21)$$

$$\bar{C}_g[\%] = 100(\bar{C}_g - 1).$$

Here, $C_{\text{opt}}^{\text{sc},\mathbf{u}}$ are selected for the EGF 3 PFF, which showed the best performance in channel scenarios A and B (cf. Table 4.9). Thus, \bar{C}_g provides a measure for the performance gain for the case that the different optimized system configurations in terms of PFFs and symbol durations can be separated perfectly without the need for intra-cell guard bands. The results show, that the selected restriction for the set of symbol durations \mathbb{T}_s allows

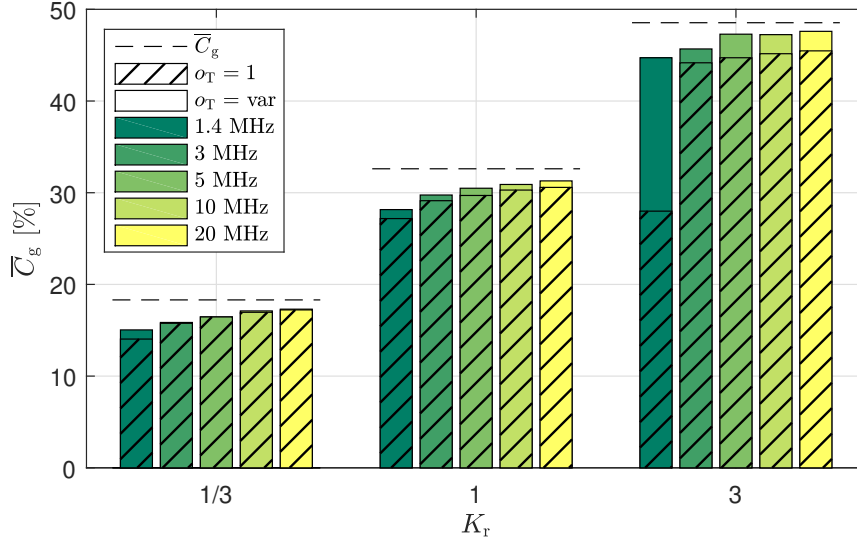


Figure 5.3: Channel capacity gains C_g for a heterogeneous FBMC-OQAM cell with two system configurations, one for users operating in channel scenario A (pedestrian in city outskirts) and the other one for users in scenario B (car on passing highway), compared to a reference system configuration (T_{LTE} and PHYDYAS PFF) utilizing different allocation scenarios as given in Tables 5.2 and 5.3. The dashed horizontals indicated the theoretical upper bound of the capacity gains \bar{C}_g .

for a close to optimal channel capacity utilization. For the given constraints, scenario 11 in Table 5.2 shows a reduced capacity gain, which can be improved using a relaxed fairness constraint. With $\gamma_f = 0.8$ the capacity gain is raised to $C_g = 42.6\%$, which is in the region of the other scenarios with the same initial allocation ratio $K_r = 3$ (12 to 15).

Until now, the symbol durations have been restricted to be integer multiples or fractions of the symbol duration of LTE. Comparing the optimal symbol durations T_{opt} for the given channel scenarios (ref. Table 4.2) with the one of LTE it can be seen, that the ratios between them are not integer powers of two. Thus, the evident question arises if the adjustment of the base symbol duration by some arbitrary factor o_T according to

$$\log_2 \left(\frac{K_v T_s}{o_T T_{\text{LTE}}} \right) \in \mathbb{Z} \quad (5.22)$$

provides an improvement of the capacity gains. In Table 5.3 the resulting channel capacity gains C_g and system configurations for the investigated scenario are quantified for

$$\log_2(o_T) \in \{-0.8, -0.6, \dots, 0.8\}. \quad (5.23)$$

For a comparison with the previous results based on integer ratios or multiples of T_{LTE} , both the results for the scaled symbol duration as well as the LTE based are contrasted in Figure 5.3. The results show, that a proper selection of the base symbol duration can significantly reduce the performance gap between capacity gain C_g and its upper bound \bar{C}_g which is caused by a suboptimal selection of the symbol duration. Here, this especially

Index	K_r	B [MHz]	f_1 [n]	f_2 [n]	ζ_2	$K_g^{1,2}$ ([kHz])	C_g [%]	\bar{C}_g [%]
1	1/3	1.4	Hermite	Hermite	8	12 (22.5)	14.0	18.3
2		3	Hermite	EGF 3	8	12 (22.5)	15.8	
3		5	Hermite	EGF 3	8	12 (22.5)	16.5	
4		10	Hermite	EGF 3	8	12 (22.5)	17.0	
5		20	Hermite	EGF 3	8	12 (22.5)	17.2	
6	1	1.4	Hermite	Hermite	8	10 (18.75)	27.2	32.6
7		3	Hermite	Hermite	8	10 (18.75)	29.1	
8		5	Hermite	EGF 3	8	11 (20.63)	29.7	
9		10	Hermite	EGF 3	8	11 (20.63)	30.3	
10		20	Hermite	EGF 3	8	11 (20.63)	30.6	
11	3	1.4	PHYDYAS	Hermite	4	2 (7.5)	28.0	48.5
12		3	Hermite	Hermite	8	10 (18.75)	44.2	
13		5	Hermite	Hermite	8	10 (18.75)	44.7	
14		10	Hermite	EGF 3	8	11 (20.63)	45.2	
15		20	Hermite	EGF 3	8	11 (20.63)	45.5	

Table 5.2: System configurations for heterogeneous CAW in DL for fairness factor $\gamma_f = 1$ and fixed base symbol durations T_{LTE} , i.e. $\log_2(K_v T_s / T_{LTE}) \in \mathbb{Z}$. All presented scenarios resulted in $\zeta_1 = 1$ and $K_v T_s = 1600/3 \mu s$. In scenario 11, the virtual lattice grid $K_v T_s = 800/3 \mu s$ has been obtained.

Index	K_r	B [MHz]	α_T	f_1 [n]	f_2 [n]	ζ_2	$K_g^{1,2}$ ([kHz])	C_g [%]	\bar{C}_g [%]
1	1/3	1.4	$2^{-0.2}$	Hermite	Hermite	8	12 (25.8)	15.0	18.3
2		3	$2^{-0.2}$	Hermite	Hermite	8	12 (25.8)	15.9	
3		5	$2^{0.2}$	Hermite	EGF 3	8	12 (19.6)	16.5	
4		10	$2^{0.2}$	Hermite	EGF 3	8	12 (19.6)	17.1	
5		20	$2^{0.2}$	Hermite	EGF 3	8	12 (19.6)	17.3	
6	1	1.4	$2^{0.8}$	EGF 3	PHYDYAS	16	15 (8.1)	28.2	32.6
7		3	$2^{0.2}$	Hermite	EGF 3	8	11 (18.0)	29.8	
8		5	$2^{0.4}$	EGF 3	PHYDYAS	16	15 (10.7)	30.5	
9		10	$2^{0.4}$	EGF 3	EGF 3	8	11 (15.6)	30.9	
10		20	$2^{0.2}$	Hermite	EGF 3	8	11 (18.0)	31.3	
11	3	1.4	$2^{0.8}$	EGF 3	PHYDYAS	16	15 (9.2)	44.7	48.5
12		3	$2^{0.2}$	Hermite	Hermite	8	10 (10.4)	45.7	
13		5	$2^{0.4}$	EGF 3	PHYDYAS	16	15 (10.6)	47.3	
14		10	$2^{0.4}$	EGF 3	PHYDYAS	16	15 (10.6)	47.2	
15		20	$2^{0.4}$	EGF 3	EGF 3	8	11 (15.6)	47.6	

Table 5.3: System configurations for heterogeneous CAW in DL for fairness factor $\gamma_f = 1$ and variable base symbol durations $\alpha_T T_{LTE}$, i.e. $\log_2(K_v T_s / \alpha_T T_{LTE}) \in \mathbb{Z}$. All presented scenarios resulted in $\zeta_1 = 1$.

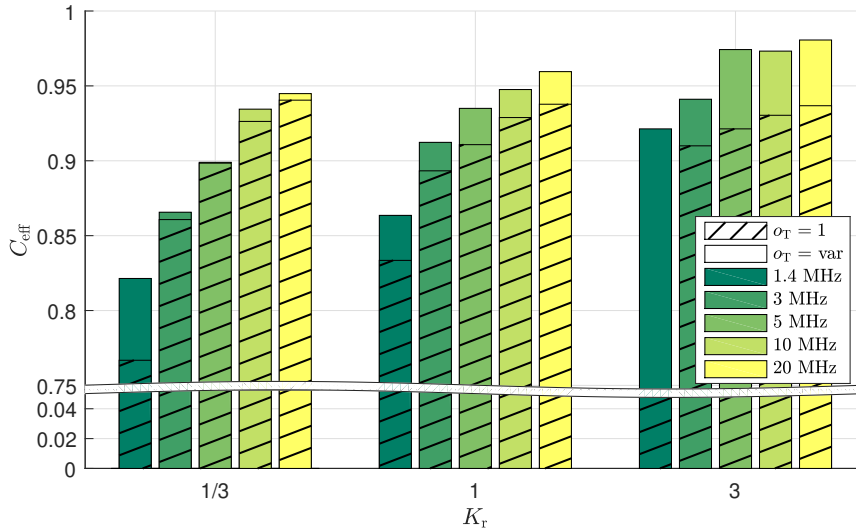


Figure 5.4: Utilization of channel capacity gains C_{eff} for a heterogeneous FBMC-OQAM cell with two different system configurations..

effects the user operating in channel scenario A. Thus, the performance gain is largest for $K_r = 3$, as user 1 utilizes three times the bandwidth of user 2. For a more detailed insight into the performance of the optimization constrains selected in this thesis, the efficiency C_{eff} of the channel capacity gain utilization given by

$$C_{\text{eff}} = \frac{C_g[\%]}{\bar{C}_g[\%]} \quad (5.24)$$

is presented in Figure 5.4. These results show, that with the presented optimization constraints, heterogeneous CAW is able to utilize more than 82 % of the theoretical capacity gains (homogeneous CAW with perfect user separation). This is even true for cell setups with very small bandwidths such as 1.4 and 3 MHz. This is due to the excellent OOB power suppression of FBMC-OQAM, which enables very small inter-user guard bands. For the investigated scenarios, these guard bands are in the range of 10 to 25 kHz, which relates to approximately 1 to 2 subcarrier spacings in an LTE system. Additionally, the results indicate that the selected restriction for the set of available symbol durations \mathbb{T}_s can be a reasonable choice, as the gains obtained by a finer adjustment of \mathbb{T}_s are limited.

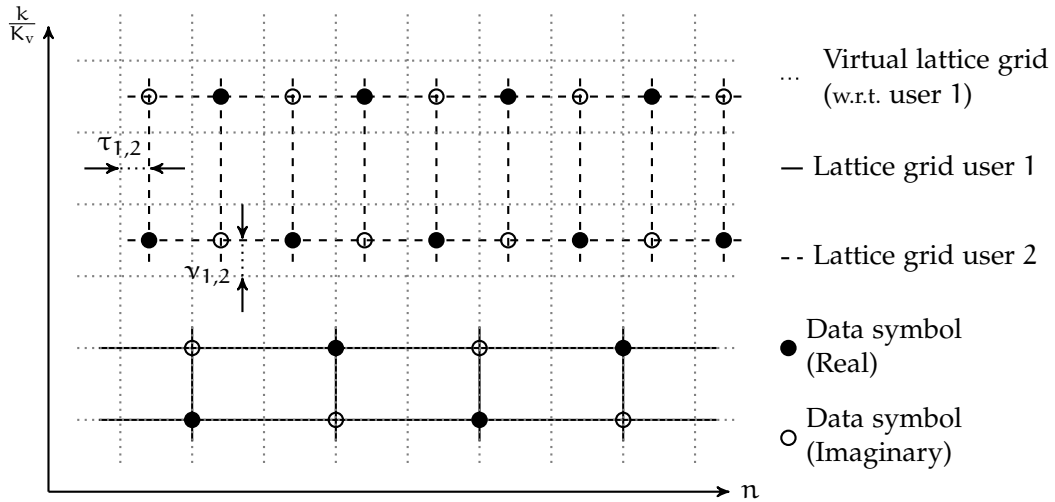


Figure 5.5: Example for asynchronous users and their lattice grids. Here, the virtual lattice grid is given with respect to user 1.

5.2 HETEROGENEOUS CAW IN CELLULAR UL

In multi-user cellular communication systems the main differences between UL and DL are the effects induced by the propagation channel as well as the need for time and frequency synchronization between users. In DL, the signals for all users can be assumed to be perfectly synchronized, as they are generated and transmitted coincidentally by a single signal source. Additionally, the transmit signals $s_u[n]$ of all users are affected by the same propagation channel specific to the currently receiving user. However, in UL each transmit signal $s_u[n]$ is generated and transmitted by a separate signal source. Thus, the transmit signals of each user $s_u[n]$ undergo separate propagation channels and due to arbitrary propagation delays and hardware imperfections, the receiver (base station) observes various user specific STOs and CFOs values (cf. Figure 5.5).

Depending on the architecture of the demodulator, the user-specific STO and CFO are required to be considered or counteracted by system design to achieve a suitable orthogonality between the users. In LTE systems for example, the STO is controlled by the base station, which tunes the transmit timings of each user equipment by so called timing advance messages. To reduce the CFO, all user equipments synchronize their oscillators to the DL reference signals, which are transmitted continuously by the base station. These approaches are suitable for applications with manageable amounts of active users per cell, for which a more or less continuously activated receiver and thus a low power efficiency for the user equipment is not a major issue. However, this system design concept is not suitable for Machine-Type Communication (MTC) with high duty cycles and short-packet transmissions [107]. Here, it may be suitable to choose a system design which separates users by inter-user guard bands, which requires modulation schemes

with excellent OOB power suppression such as FBMC-OQAM or UFMC. Some exemplary investigations for this approach are provided in [23, 36, 106].

In this section, first the approach of perfect synchronization at the UL receiver is discussed based on a system model derived of the DL system model introduced in the preceding sections, followed by a brief analysis of the capacity gains of CAW with heterogeneous system configurations in a cell.

5.2.1 System model

The multi-user system model in an UL scenario is similar to the one derived for the DL. Here, the user specific transmit signals are subject to some STO τ_u , a CFO ν_u and, as mentioned before, a separate propagation channel $h_u[\tau, n]$. Thus, the signal $r[n]$ received at the base station yields

$$r[n] = \sum_{u \in \mathbb{U}} \sum_{\tau} h_u[\tau, n] s_u[n - \tau - \tau_u] e^{j2\pi\nu_u n}, \quad (5.25)$$

which comprises a superposition of the distorted user specific FBMC-OQAM transmit signals $s_u[n]$ given by (5.3).

After matched filtering at the receiver with a time and frequency shifted PFF to combat the STO and CFO, respectively, the symbol $\tilde{a}_{u, \tilde{m}, \tilde{k}}$ of the u -th user at time index \tilde{m} and subcarrier index \tilde{k} yields

$$\begin{aligned} \tilde{a}_{u, \tilde{m}, \tilde{k}} &= \theta_{\tilde{m}, \tilde{k}}^* \left(r[n] * f_u^*[\tilde{m}M_u - n - \tau_u] e^{-j2\pi(\tilde{k}K_u + \nu_u)n} \right) \Big|_{\downarrow M_u} \\ &= \sum_{u' \in \mathbb{U}} \sum_{(\mu, \kappa) \in \mathbb{S}_{u'}} \theta_{\mu, \kappa} a_{u', \tilde{m} + \mu, \tilde{k} + \kappa} \mathcal{H}_{\tilde{m}, \tilde{k}}^{u, u'}(\mu, \kappa, \tau_{u, u'}, \nu_{u, u'}). \end{aligned} \quad (5.26)$$

Here, the resulting effective channel coefficient $\mathcal{H}_{\tilde{m}, \tilde{k}}^{u, u'}(\mu, \kappa, \tau_{u, u'}, \nu_{u, u'})$ for a multi-user UL scenario is given by

$$\begin{aligned} \mathcal{H}_{\tilde{m}, \tilde{k}}^{u, u'}(\mu, \kappa, \tau_{u, u'}, \nu_{u, u'}) &= \sum_{\tau} \int_{-f_D T_s}^{f_D T_s} D_{u'}[\tau, \nu] e^{j2\pi\tilde{m}M_u \nu} \\ &\quad \cdot A_{\tilde{m}, \tilde{k}}^{u, u'}[\mu M_{u'} + \tau + \tau_{u, u'}, \kappa K_{u'} + \nu + \nu_{u, u'}] \nu \\ &\quad \cdot e^{-j2\pi K_u(\tilde{k} + \kappa)(\mu M_u - \tilde{m}M_{u'} + \tau)} d\nu, \end{aligned} \quad (5.27a)$$

where $\tau_{u, u'}$ and $\nu_{u, u'}$ are the relative time- and frequency offsets defined as

$$\tau_{u, u'} = \tau_{u'} - \tau_u \quad (5.27b)$$

and

$$\nu_{u,u'} = \nu_{u'} - \nu_u. \quad (5.27c)$$

As $\mathcal{H}_{\tilde{m},\tilde{k}}^{u,u}(\mu, \kappa) = H_{\tilde{m},\tilde{k}}^{u,u}(\mu, \kappa)$ and $\tau_{u,u'}$ and $\nu_{u,u'}$, the representation of the demodulated symbol $u_{u,\tilde{m},\tilde{k}}$ given in (5.8a) in UL and DL scenarios only differs for the co-user interference $u_{u,\tilde{m},\tilde{k}'}$ which here is given by

$$u_{u,\tilde{m},\tilde{k}} = \sum_{u' \in \mathcal{U}_{c,u}} \sum_{(\mu, \kappa) \in \mathcal{S}_{u'}} \theta_{\mu, \kappa} a_{u', \tilde{m} + \mu, \tilde{k} + \kappa} \mathcal{H}_{\tilde{m}, \tilde{k}}^{u, u'}(\mu, \kappa, \tau_{u, u'}, \nu_{u, u'}). \quad (5.28)$$

Therefore, the related average co-user interference power $\sigma_{\tilde{U}, u}^2(\tilde{m}, \tilde{k})$ in an UL scenario yields

$$\sigma_{\tilde{U}, u}^2(\tilde{m}, \tilde{k}) = \sum_{u' \in \mathcal{U}_{c,u}} \sum_{(\mu, \kappa) \in \mathcal{S}_{u'}} \mathcal{P}_{\mu, \kappa}^{u, u'}(\tilde{m}, \tilde{k}, \tau_{u, u'}, \nu_{u, u'}), \quad (5.29)$$

with the average power $\mathcal{P}_{\mu, \kappa}^{u, u'}(\tilde{m}, \tilde{k})$ obtained from lattice point (μ, κ) of user u' defined as follows

$$\mathcal{P}_{\mu, \kappa}^{u, u'}(\tilde{m}, \tilde{k}, \tau_{u, u'}, \nu_{u, u'}) = \sigma_a^2 \sum_{\tau} \int_{-f_D T_s}^{f_D T_s} S_{u'}[\tau, \nu] \Re \left\{ \theta_{\mu, \kappa} A_{\tilde{m}, \tilde{k}}^{u, u'} [\mu M_{u'} + \tau + \tau_{u, u'}, \kappa K_{u'} + \nu + \nu_{u, u'}] \right\}^2 d\nu. \quad (5.30)$$

5.2.2 Channel capacity gains

Utilizing the equations specific for the cellular UL scenario, the related channel capacity gains can be obtained as for the DL case by solving the optimization problem described in Section 5.1.2. Here, the same cell scenario is investigated to enable a comparison of the results achieved for UL and DL. Additionally, perfect synchronization between users, i.e.

$$\forall u \forall u' : \tau_{u, u'} = \nu_{u, u'} = 0, \quad (5.31)$$

is assumed. For the investigated scenarios, the results show that the performance gains for heterogeneous CAW in cellular UL provided in Tables 5.4 and 5.5 are practically identical to that of the DL scenario (cf. Tables 5.2 and 5.3). The reasons for this are discussed in the following.

The only difference between the DL and UL scenarios is the amount of inflicted co-user interference $\sigma_{\tilde{U}, u}^2(\tilde{m}, \tilde{k})$ or, to be more specific, the applied channel scattering function (cf. Section 5.2.1), which for the considered PFFs with their excellent localization properties

Index	K_r	B [MHz]	f_1 [n]	f_2 [n]	ζ_2	$K_g^{1,2}$ ([kHz])	C_g [%]	\bar{C}_g [%]
1	1/3	1.4	Hermite	Hermite	8	12 (22.5)	14.0	18.3
2		3	Hermite	EGF 3	8	12 (22.5)	15.8	
3		5	Hermite	EGF 3	8	12 (22.5)	16.5	
4		10	Hermite	EGF 3	8	12 (22.5)	17.0	
5		20	Hermite	EGF 3	8	12 (22.5)	17.2	
6	1	1.4	Hermite	Hermite	8	10 (18.75)	27.2	32.6
7		3	Hermite	Hermite	8	10 (18.75)	29.1	
8		5	Hermite	EGF 3	8	11 (20.63)	29.7	
9		10	Hermite	EGF 3	8	11 (20.63)	30.3	
10		20	Hermite	EGF 3	8	11 (20.63)	30.6	
11	3	1.4	PHYDYAS	Hermite	4	2 (7.5)	28.0	48.5
12		3	Hermite	Hermite	8	10 (18.75)	44.2	
13		5	Hermite	Hermite	8	10 (18.75)	44.7	
14		10	Hermite	EGF 3	8	11 (20.63)	45.2	
15		20	Hermite	EGF 3	8	11 (20.63)	45.5	

Table 5.4: System configurations for heterogeneous CAW in UL for fairness factor $\gamma_f = 1$ and fixed base symbol durations T_{LTE} , i.e. $\log_2(K_v T_s / T_{LTE}) \in \mathbb{Z}$. All presented scenarios resulted in $\zeta_1 = 1$ and $K_v T_s = 1600/3 \mu s$. In scenario 11, the virtual lattice grid $K_v T_s = 800/3 \mu s$ has been obtained.

Index	K_r	B [MHz]	o_T	f_1 [n]	f_2 [n]	ζ_2	$K_g^{1,2}$ ([kHz])	C_g [%]	\bar{C}_g [%]
1	1/3	1.4	$2^{-0.2}$	Hermite	Hermite	8	12 (25.8)	15.0	18.3
2		3	$2^{-0.2}$	Hermite	Hermite	8	12 (25.8)	15.9	
3		5	$2^{0.2}$	Hermite	EGF 3	8	12 (19.6)	16.5	
4		10	$2^{0.2}$	Hermite	EGF 3	8	12 (19.6)	17.1	
5		20	$2^{0.2}$	Hermite	EGF 3	8	12 (19.6)	17.3	
6	1	1.4	$2^{0.8}$	EGF 3	PHYDYAS	16	15 (8.1)	28.2	32.6
7		3	$2^{0.2}$	Hermite	EGF 3	8	11 (18.0)	29.8	
8		5	$2^{0.4}$	EGF 3	PHYDYAS	16	15 (10.7)	30.5	
9		10	$2^{0.4}$	EGF 3	EGF 3	8	11 (15.6)	30.9	
10		20	$2^{0.2}$	Hermite	EGF 3	8	11 (18.0)	31.3	
11	3	1.4	$2^{0.8}$	EGF 3	PHYDYAS	16	15 (9.2)	44.7	48.5
12		3	$2^{0.2}$	Hermite	Hermite	8	10 (10.4)	45.7	
13		5	$2^{0.4}$	EGF 3	PHYDYAS	16	15 (10.6)	47.3	
14		10	$2^{0.4}$	EGF 3	PHYDYAS	16	15 (10.6)	47.2	
15		20	$2^{0.4}$	EGF 3	EGF 3	8	11 (15.6)	47.6	

Table 5.5: System configurations for heterogeneous CAW in UL for fairness factor $\gamma_f = 1$ and variable base symbol durations $o_T T_{LTE}$, i.e. $\log_2(K_v T_s / o_T T_{LTE}) \in \mathbb{Z}$. All presented scenarios resulted in $\zeta_1 = 1$.

(cf. Section 3.3) decreases very fast with increasing the frequency spacing to neighboring users. Therefore, only the subcarriers closest to subbands with different system configurations are affected by an increased amount of interference. In Figures 5.6a, 5.6b and 5.6c, exemplary curves for the averaged (over time) but subcarrier specific intrinsic and co-user interference $\sigma_{I,u}^2(\tilde{k})$ and $\sigma_{U,u}^2(\tilde{k})$ are depicted for scenario 6. Here it is assumed, that no guard carriers are spent to separate the users and all users allocate a contiguous spectrum, whereby user 1 allocates the lower and user 2 the upper sub-band. To indicate the improvement of the intrinsic interference, Figure 5.6c additionally depicts the intrinsic interference for an LTE like parametrization of the symbol duration T . The small but significant decrease of the intrinsic interference at the band edges observed in Figures 5.6a, 5.6b and 5.6c is due to the reduced amount of directly neighboring symbols, which cause the main amount of intrinsic interference. The different shape of the intrinsic and co-user interference is caused by the fact, that for the intrinsic interference the ambiguity function is sampled close to its roots, whereas the co-user interference is determined at arbitrary positions of the cross-ambiguity function.

The minor difference between the co-user interference results obtained for DL and UL transmissions is also due to the arbitrary sampling of the cross-ambiguity function. As indicated in Figures 5.6d, 5.6e and 5.6f, compared to the (auto-)ambiguity function the cross-ambiguity function is significantly spread in frequency domain. It can be seen, that the cross-ambiguity function only has a small gradient in both time-offset and frequency-offset direction, especially in the regions of high amplitude. Additionally, for all users u and u' the spread of the applied channel scattering functions is significantly smaller than a subcarrier spacing and symbol duration, i.e.

$$f_D T_s \ll K_u \quad (5.32a)$$

$$\tau_L \ll M_u. \quad (5.32b)$$

Thus, the average powers $P_{\mu,\kappa}^{u,u'}(\tilde{m}, \tilde{k})$ and $\mathcal{P}_{\mu,\kappa}^{u,u'}(\tilde{m}, \tilde{k})$ obtained from lattice point (μ, κ) of user u' are dominated by the shape of the cross-ambiguity function and less dependent on the exact spreading and shape of the channel scattering functions. Furthermore, the co-user interference investigated here is an average value over a set of lattice points of the co-users and relative lattice offsets. Therefore, the co-user interference is dominated by the lattice positions at which the transmit and receive PFFs have higher correlation, i.e. the cross-ambiguity function has larger values, compared to the other considered lattice positions.

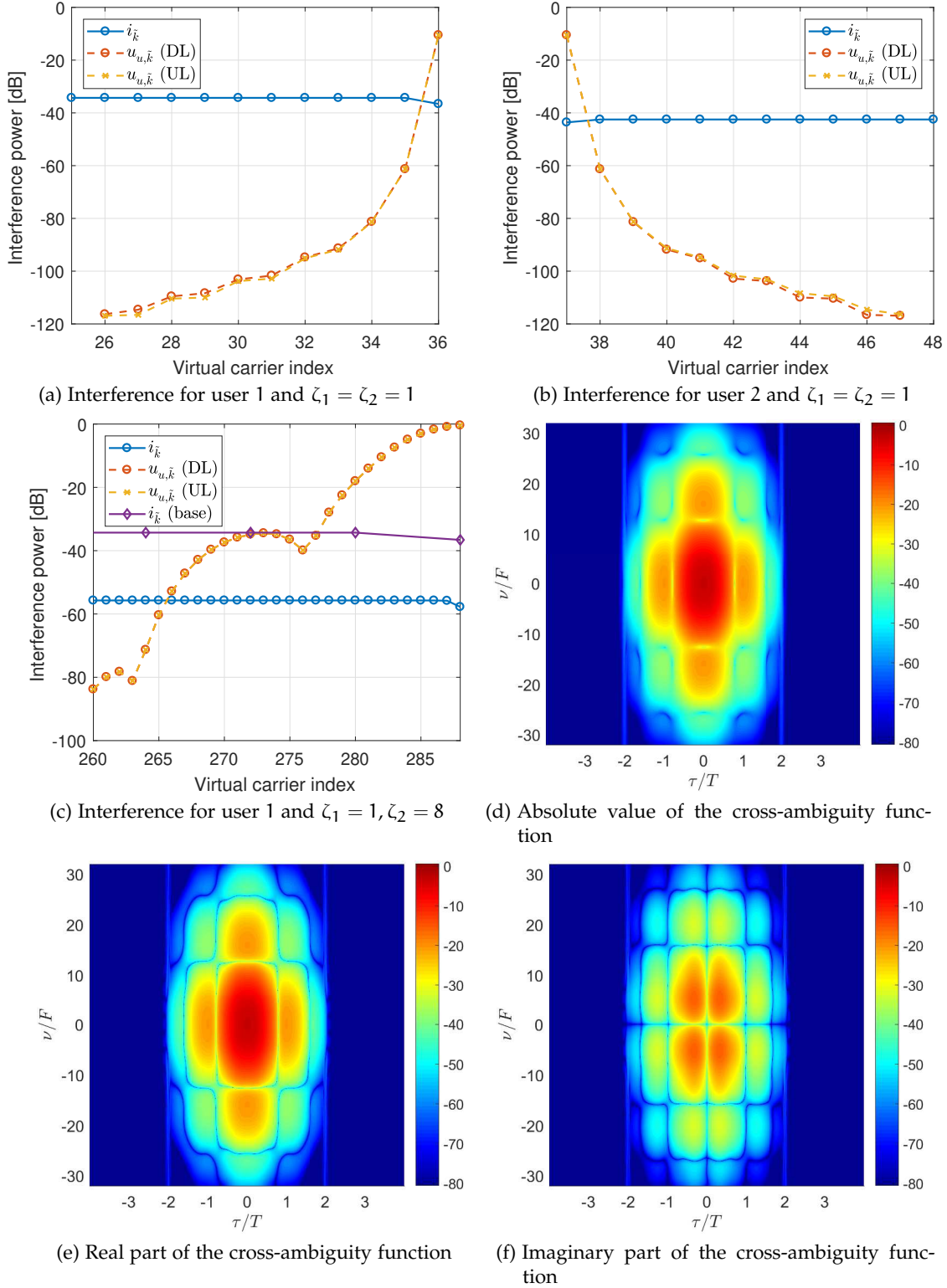


Figure 5.6: Exemplary results for the interference in scenario 6 with $\sigma_T = 1$ (cf. Tables 5.2 to 5.5): Intrinsic interference $\sigma_{T,u}^2(\vec{k})$ and co-user interference $\sigma_{U,u}^2(\vec{k})$ for $\zeta_1 = \zeta_2 = 1$ and $T = T_{\text{LTE}}$ in DL and UL (User 1: (a), User 2: (b)) as well as the ones of user 1 for the optimized system parameters $\zeta_1 = 1, \zeta_2 = 8$ and $T = \zeta_2 T_{\text{LTE}}$ in (c). Figures (d), (e) and (f) depict the absolute value, real and imaginary part of the related cross-ambiguity function, respectively.

5.3 CONCLUDING REMARKS

In this chapter, the capacity gains for heterogeneous CAW in cellular DL and UL scenarios have been investigated. Therefore, the related multi-user system models have been derived and the optimization problem to maximize the capacity within a cell and important constraints, e.g. fairness between users in different channel environments, have been proposed and discussed. Additionally, the capacity gains have been evaluated numerically for a selected scenario. The results show, that heterogeneous CAW with the simple optimization constraints considered here is able to utilize channel capacity gains, which are close to the optimal performance gains ($> 95\%$). Furthermore, the analysis of DL and UL scenarios proved, that the performance of heterogeneous CAW is basically independent from the direction of transmission.

CONCLUSIONS AND FUTURE WORKS

In this thesis the question has been raised if a communication system optimization in terms of a combined lattice grid and PFF adaptation (CAW) to match the properties of the utilized communication channel provides practically relevant performance gains. To answer this question, a novel system design concept for homo- and heterogeneous channel scenarios per cell has been proposed and its performance gains in terms of SIR, BER and capacity have been analyzed and evaluated for an FBMC-OQAM system. To this, the feasibility of the SIR as a performance indicator has been studied. Furthermore, the system performance has been compared with that of state-of-the-art LTE based on CP-OFDM.

In addition, a unified system model for FBMC-OQAM and CP-OFDM systems has been described. The effects on a symbol transmitted over doubly dispersive channels are characterized using the (cross-)ambiguity function and the statistical properties of the communication channel. Various PFFs proposed for FBMC-OQAM systems and their properties have been presented and the SIR performance for FBMC-OQAM and CP-OFDM has been defined and evaluated concerning both AWGN and doubly dispersive channels. Thereof, the parameter space suitable for the evaluation of CAW has been deduced.

For a basic evaluation of the practical feasibility of CAW, it has been investigated for homogeneous setups. Here, all users in a cell utilize the same lattice and PFF configuration, whereby each cell may be configured differently. The evaluation results confirm that for the specified system design, homogeneous CAW can provide significant performance gains compared to a “one-fits-all” system design approach such as LTE. Furthermore, the impact of scattered pilot based channel estimation according to the LS approach has been considered. In this regard, analytical descriptions of the channel estimation error for different scattered pilot schemes proposed in literature have been derived and evaluated. The results have been compared to that obtained by Monte-Carlo simulations. Here, the results prove that the performance gains of homogeneous CAW are significantly reduced, as the investigated scattered pilot schemes are subject to significant residual channel estimation errors. In this case, the best performance for each considered scenario has been achieved by using isotropic PFFs.

Based on these results, the homogeneous CAW approach has been extended to a system setup which allows for heterogeneous system configurations per cell. For that, the related channel capacity gains have been investigated for both DL and UL scenarios. Therefore, the corresponding multi-user system models have been derived and the optimization problem to maximize the capacity within a cell as well as important optimization constraints have been proposed and discussed. Here, the capacity gains have been evaluated numerically for a selected

cell scenario. The results show that heterogeneous CAW with the optimization constraints considered here is able to achieve close to the optimal channel capacity. Furthermore, the analysis of DL and UL scenarios proved that the performance of heterogeneous CAW is basically independent from the direction of transmission.

In conclusion, the outcome of this thesis shows that the application of CAW in communication systems is advantageous to the current "one-fits-all" system design approach. For applications with a high range of channel characteristics such as cellular networks, the results indicate that CAW provides significant performance gains in terms of BER and channel capacity. Due to the excellent localization of the PFFs in FBMC-OQAM systems, it is possible to extend CAW to heterogeneous scenarios without sacrificing the performance gains, as the amount of required guard bands is very limited.

In the future, the system performance of the interference avoidance approach by CAW could be compared with that of multi-tap equalizers, which aim to reduce the induced interference after demodulation. Generally, channel equalization in MC systems relies on channel estimation based on demodulated pilot symbols, and thus is afflicted by interference. Thus, the performance of multi-tap equalizers is suggested to be limited, especially in channel environments with large signal dispersion. In this context, a combination of CAW with multi-tap equalization could be beneficial.

In addition, CAW can be extended to operate on the instantaneous channel state, which requires a closed loop system design to enable the feedback of channel state information. This additionally allows for the combination of CAW with other system adaptation schemes such as CAM and CAL which could provide a further improvement of the communication channel utilization.

Another important research topic is the development of (de-)modulators which are capable of a flexible demodulation of different system configurations to reduce the complexity of transmitter and receiver structures and thus hardware costs. This is even more important for base stations, which are required to demodulate different system configurations coincidentally.

Part II

APPENDIX

MULTICARRIER SYSTEMS

A.1 INHERENT ORTHOGONALITY FOR REAL AND EVEN SYMMETRIC PFFs

Without loss of generality, the proof of inherent orthogonality of real valued and even symmetric PFFs is provided for the case in which one of the “T-F logons” is placed at the center of the lattice grid, i.e. $(m, k) = (0, 0)$. Therefore, utilizing Euler’s formula the T-F shift of a PFF can be written as

$$\begin{aligned} f_{m,k} &= f(t - mT_0)e^{j2\pi kF_0(t - mT_0)} \\ &= f(t - mT_0) \left(\cos(2\pi kF_0(t - mT_0)) + j \sin(2\pi kF_0(t - mT_0)) \right), \end{aligned} \quad (\text{A.1})$$

such that the inner product of two “T-F-logons” yields

$$\langle f_{0,0}, f_{m,k} \rangle = \int f(t)f(t - mT_0) \left(\cos(2\pi kF_0(t - mT_0)) + j \sin(2\pi kF_0(t - mT_0)) \right) dt. \quad (\text{A.2})$$

To obtain orthogonality, the inner product has to be zero at all positions $(m, k) \neq (0, 0)$.

It can be noted that the inner product given in (A.2) is a sum of a product of an even symmetric part $f(t)f(t - mT_0)$, with the symmetry axis at $t = 0.5mT_0$, with either an even (cosine) or odd symmetric (sine) function. Depending on the time shift mT_0 and frequency shift kF_0 , both the cosine and sine functions become odd symmetric with respect to the symmetry axis at $0.5mT_0$, i.e for.

$$0 = \cos(2\pi kF_0(0.5mT_0 - mT_0)) \quad \Rightarrow \quad \forall i \in \mathbb{Z} : kmT_0F_0\pi = \frac{2i+1}{2}\pi \quad (\text{A.3a})$$

$$0 = \sin(2\pi kF_0(0.5mT_0 - mT_0)) \quad \Rightarrow \quad \forall i \in \mathbb{Z} : kmT_0F_0\pi = \frac{2i}{2}\pi. \quad (\text{A.3b})$$

As the inner product of two functions with even and odd symmetry is known to be zero, the real and imaginary parts of (A.2) reduce to zero for

$$\Re \left\{ \langle f_{0,0}, f_{m,k} \rangle \right\} \begin{cases} = 0 & T_0F_0 = \frac{1}{2} \wedge km = \text{odd} \\ \neq 0 & \text{otherwise} \end{cases} \quad (\text{A.4a})$$

$$\Im \left\{ \langle f_{0,0}, f_{m,k} \rangle \right\} \begin{cases} = 0 & T_0F_0 = \frac{1}{2} \wedge km = \text{even} \\ \neq 0 & \text{otherwise} \end{cases} \quad (\text{A.4b})$$

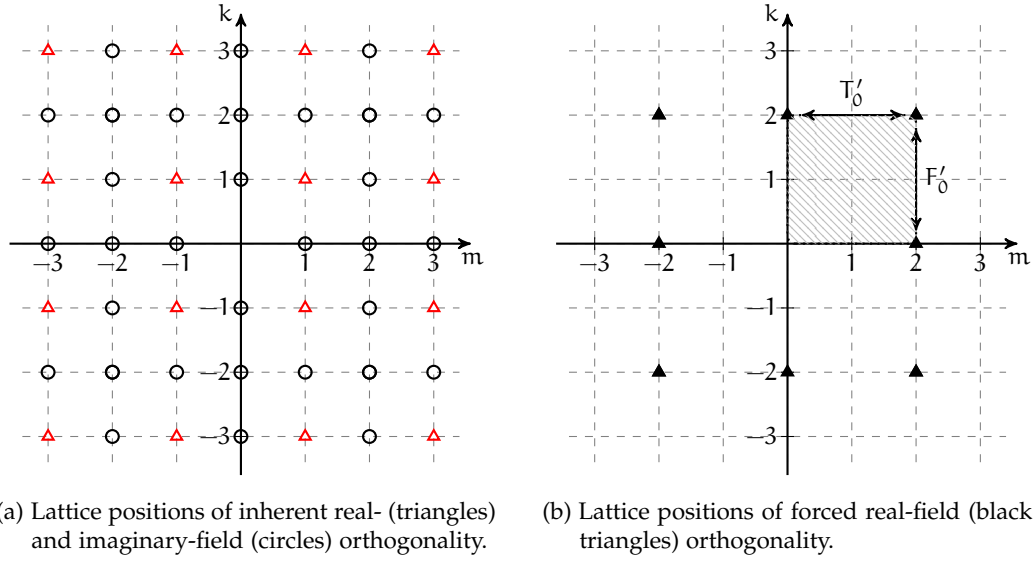


Figure A.1: Lattice positions of inherent and forced real-field orthogonality. The hatching indicates the area spanned by the effective T-F product.

Figure A.1a depicts the lattice positions which provide inherent real or imaginary domain orthogonality. Thus, for transmission of either real or imaginary data symbols, the inner product at the lattice positions marked in Figure A.1b have to be forced to be zero. As stated by the Balian-Low theorem, this can be fulfilled easily by any localized PFF, as the T-F product for this lattice points is greater than 1:

$$\begin{aligned}
 T'_0 \cdot F'_0 &= 2T_0 \cdot 2F_0 \\
 &= 2 \frac{1}{2F_0} \cdot 2F_0 \\
 &= 2.
 \end{aligned} \tag{A.5}$$

A.2 DERIVATION OF THE RECEIVED DEMODULATED SYMBOL

Rewriting (3.4a) in a more general way, $\tilde{a}_{\tilde{m}, \tilde{k}}$ is obtained according to

$$\begin{aligned}
 \tilde{a}_{\tilde{m}, \tilde{k}} &= \theta_{\tilde{m}, \tilde{k}}^* \sum_{n=-\infty}^{\infty} \sum_{(m,k) \in \mathbb{T}} \theta_{m,k} a_{m,k} \left(h[\tau, n] * f_k[n - mM_0] \right) g_{\tilde{k}}^*[n - \tilde{m}M_0] \\
 &= \theta_{\tilde{m}, \tilde{k}}^* \sum_{(m,k) \in \mathbb{T}} \theta_{m,k} a_{m,k} H_{\tilde{m}, \tilde{k}}(m, k)
 \end{aligned} \tag{A.6}$$

with the effective channel coefficient $H_{\tilde{m},\tilde{k}}(m, k)$ given by

$$H_{\tilde{m},\tilde{k}}(m, k) = \sum_{n=-\infty}^{\infty} \left(h[\tau, n] * f_k[n - mM_0] \right) g_{\tilde{k}}^*[n - \tilde{m}M_0] \quad (\text{A.7})$$

Resolving the convolution of the channel $h[\tau, n]$ and the transmit PFF $f_k[n]$ and with definition of $n' = n - \tilde{m}M_0$ and the symbol index offset $\mu = m - \tilde{m}$, (A.7) yields

$$H_{\tilde{m},\tilde{k}}(\mu, k) = \sum_{n'=-\infty}^{\infty} \sum_{\tau} h[\tau, n' + \tilde{m}M_0] f_k[n' - \tau - \mu M_0] g_{\tilde{k}}^*[n']. \quad (\text{A.8})$$

Recalling $f_k[n] = f[n]e^{j2\pi K_0 k n}$ and $g_{\tilde{k}}^*[n] = g^*[n]e^{-j2\pi K_0 \tilde{k} n}$, $H_{\tilde{m},\tilde{k}}(\mu, k)$ can be rewritten as

$$H_{\tilde{m},\tilde{k}}(\mu, k) = \sum_{n'=-\infty}^{\infty} \sum_{\tau} h[\tau, n' + \tilde{m}M_0] \cdot f[n' - \tau - \mu M_0] e^{j2\pi K_0 k (n' - \tau - \mu M_0)} g^*[n'] e^{-j2\pi K_0 \tilde{k} n'}. \quad (\text{A.9})$$

As long as $2f_D T_s < 1$, the DTFT can be applied to $h[\tau, n]$ [67]. Therefore, (A.9) yields

$$H_{\tilde{m},\tilde{k}}(\mu, k) = \sum_{n'=-\infty}^{\infty} \sum_{\tau} \int_{-f_D T_s}^{f_D T_s} D[\tau, \nu] e^{j2\pi(n' + \tilde{m}M_0)\nu} d\nu \cdot f[n' - \tau - \mu M_0] e^{j2\pi K_0 k (n' - \tau - \mu M_0)} g^*[n'] e^{-j2\pi K_0 \tilde{k} n'} \quad (\text{A.10})$$

$$= \sum_{n'=-\infty}^{\infty} \sum_{\tau} \int_{-f_D T_s}^{f_D T_s} D[\tau, \nu] f[n' - \tau - \mu M_0] g^*[n'] \cdot e^{j2\pi K_0 k (n' - \tau - \mu M_0)} e^{-j2\pi K_0 \tilde{k} n'} e^{j2\pi(n' + \tilde{m}M_0)\nu} d\nu. \quad (\text{A.11})$$

$$= \sum_{n'=-\infty}^{\infty} \sum_{\tau} \int_{-f_D T_s}^{f_D T_s} D[\tau, \nu] f[n' - \tau - \mu M_0] g^*[n'] \cdot e^{j2\pi K_0 n' (k - \tilde{k} + \nu)} e^{-j2\pi K_0 k (\tau + \mu M_0)} e^{j2\pi \tilde{m} M_0 \nu} d\nu \quad (\text{A.12})$$

$$= \sum_{\tau} \int_{-f_D T_s}^{f_D T_s} D[\tau, \nu] e^{j2\pi \tilde{m} M_0 \nu} e^{-j2\pi K_0 k (\tau + \mu M_0)} \cdot \sum_{n'=-\infty}^{\infty} f[n' - \tau - \mu M_0] g^*[n'] e^{j2\pi K_0 n' (k - \tilde{k} + \nu)} d\nu. \quad (\text{A.13})$$

With the subcarrier index offset $\kappa = k - \tilde{k}$ and for the tapped delay line channel model (3.3), the system dependent channel coefficient $H_{\tilde{m}, \tilde{k}}(\mu, \kappa)$ is obtained as given in (3.8), (3.9a) and (3.9c):

$$\begin{aligned}
 H_{\tilde{m}, \tilde{k}}(\mu, \kappa) &= \sum_{\tau} \int_{-f_D T_s}^{f_D T_s} \underbrace{D[\tau, \nu] e^{j2\pi \tilde{m} M_0 \nu}}_{\mathcal{F}_n \{h[\tau, n + \tilde{m} M_0]\}} \\
 &\quad \cdot \underbrace{\sum_{n=-\infty}^{\infty} f[n - \tau - \mu M_0] g^*[n] e^{j2\pi K_0 n (\kappa + \nu)}}_{A_{\mu, \kappa}[\tau, \nu]} \\
 &\quad \cdot e^{-j2\pi K_0 (\kappa + \tilde{k}) (\tau + \mu M_0)} d\nu. \tag{A.14}
 \end{aligned}$$

$$= \sum_{\tau} \int_{-f_D T_s}^{f_D T_s} \mathcal{F}_n \{h[\tau, n + \tilde{m} M_0]\} \underbrace{A_{\mu, \kappa}[\tau, \nu] e^{-j2\pi K_0 (\kappa + \tilde{k}) (\tau + \mu M_0)}}_{A_{\mu, \kappa}^{\tilde{k}}[\tau, \nu]} d\nu. \tag{A.15}$$

Finally, the demodulated symbol $\tilde{a}_{\tilde{m}, \tilde{k}}$ is obtained according to

$$\tilde{a}_{\tilde{m}, \tilde{k}} = \sum_{(\mu, \kappa) \in \mathcal{S}} \theta_{\mu, \kappa} a_{\tilde{m} + \mu, \tilde{k} + \kappa} \sum_{\tau} \int_{-f_D T_s}^{f_D T_s} \mathcal{F}_n \{h[\tau, n + \tilde{m} M_0]\} A_{\mu, \kappa}^{\tilde{k}}[\tau, \nu] d\nu. \tag{A.16}$$

A.3 MEAN INTERFERENCE POWER OF RECEIVED SYMBOL

Considering (3.7), the mean power σ_I^2 of $i_{\tilde{m}, \tilde{k}}$ is given by

$$\begin{aligned}
 \sigma_I^2 &= \mathbf{E} \left[\left(\sum_{(\mu, \kappa) \in \mathcal{S}_N} \theta_{\mu, \kappa} a_{\tilde{m} + \mu, \tilde{k} + \kappa} H_{\tilde{m}, \tilde{k}}(\mu, \kappa) \right) \right. \\
 &\quad \left. \cdot \left(\sum_{(\mu', \kappa') \in \mathcal{S}_N} \theta_{\mu', \kappa'} a_{\tilde{m} + \mu', \tilde{k} + \kappa'}^* H'_{\tilde{m}, \tilde{k}}(\mu', \kappa') \right)^* \right]. \tag{A.17}
 \end{aligned}$$

Performing the multiplication in consideration of statistical independence of $H_{\tilde{m}, \tilde{k}}(\mu, \kappa)$ and $a_{\tilde{m} + \mu, \tilde{k} + \kappa}$, σ_I^2 is obtained as

$$\begin{aligned}
 \sigma_I^2 &= \sum_{(\mu, \kappa) \in \mathcal{S}_N} \sum_{(\mu', \kappa') \in \mathcal{S}_N} \theta_{\mu, \kappa} \theta_{\mu', \kappa'}^* \mathbf{E} \left[a_{\tilde{m} + \mu, \tilde{k} + \kappa} a_{\tilde{m} + \mu', \tilde{k} + \kappa'}^* \right] \\
 &\quad \cdot \underbrace{\mathbf{E} \left[H_{\tilde{m}, \tilde{k}}(\mu, \kappa) H_{\tilde{m}, \tilde{k}}'^*(\mu', \kappa') \right]}_{\sigma_{\mu, \mu'}^{\kappa, \kappa'}(\tilde{m}, \tilde{k})}, \tag{A.18}
 \end{aligned}$$

with $\sigma_{\mu,\mu'}^{\kappa,\kappa'}(\tilde{m}, \tilde{k})$ being the cross-correlation of any combination of $H_{\tilde{m},\tilde{k}}(\mu, \kappa)$ and $H_{\tilde{m},\tilde{k}}^*(\mu', \kappa')$. Recalling (3.8), $\sigma_{\mu,\mu'}^{\kappa,\kappa'}(\tilde{m}, \tilde{k})$ can be written as

$$\sigma_{\mu,\mu'}^{\kappa,\kappa'}(\tilde{m}, \tilde{k}) = \sum_{l=0}^{L-1} \sum_{l'=0}^{L-1} \int_{-f_D T_s}^{f_D T_s} \int_{-f_D T_s}^{f_D T_s} \mathbf{E} [D[\tau_l, \nu] D^*[\tau_{l'}, \nu']] e^{j2\pi \tilde{m} M_0 (\nu - \nu')} \cdot A_{\mu,\kappa}^{\tilde{k}}[\tau_l, \nu] \left(A_{\mu',\kappa'}^{\tilde{k}}[\tau_{l'}, \nu'] \right)^* d\nu d\nu'. \quad (\text{A.19})$$

From the WSSUS condition of the propagation channel, $\mathbf{E} [D[\tau_l, \nu] D^*[\tau_{l'}, \nu']] = S[\tau_l, \nu](\nu) \delta_{l,l'} \delta_{\nu,\nu'}$ follows and (A.19) yields

$$\sigma_{\mu,\mu'}^{\kappa,\kappa'}(\tilde{m}, \tilde{k}) = \sum_{l=0}^{L-1} \int_{-f_D T_s}^{f_D T_s} S[\tau_l, \nu] A_{\mu,\kappa}^{\tilde{k}}[\tau_l, \nu] \left(A_{\mu',\kappa'}^{\tilde{k}}[\tau_l, \nu] \right)^* d\nu. \quad (\text{A.20})$$

It should be noticed that a term in (A.18) is only zero in case the modulated symbols are i.i.d., i.e. $\mathbf{E} \left[a_{\tilde{m}+\mu, \tilde{k}+\kappa} a_{\tilde{m}+\mu', \tilde{k}+\kappa'}^* \right] = \sigma_a^2 \delta_{\mu,\mu'} \delta_{\kappa,\kappa'}$, which is not guaranteed for all interference mitigation schemes investigated in this contribution. With $a_{m,k}$ being i.i.d., (A.18) yields

$$\sigma_I^2 = \sigma_a^2 \sum_{(\mu,\kappa) \in \mathcal{S}_N} \sum_{l=0}^{L-1} \int_{-f_D T_s}^{f_D T_s} S[\tau_l, \nu] |A_{\mu,\kappa}[\tau_l, \nu]|^2 d\nu. \quad (\text{A.21})$$

A.4 SYMBOL MODULATION FOR SCATTERED PILOTS

In (4.17), the pilot symbol $p_{\tilde{m},\tilde{k}}$ is statistically independent of $a_{\tilde{m}+\mu, \tilde{k}+\kappa}$ and $H_{\tilde{m},\tilde{k}}(\mu, \kappa)$. Therefore, $\varepsilon_{H,AP}$ can be expressed by

$$\varepsilon_{H,AP} = \mathbf{E} \left[|\tilde{p}_{\tilde{m},\tilde{k}}|^2 \right] \mathbf{E} \left[\frac{1}{|p_{\tilde{m},\tilde{k}}|^2} \right], \quad (\text{A.22})$$

with

$$\tilde{p}_{\tilde{m},\tilde{k}} = \sum_{(\mu,\kappa) \in \mathcal{S}_R} \theta_{\mu,\kappa} a_{\tilde{m}+\mu, \tilde{k}+\kappa} H_{\tilde{m},\tilde{k}}(\mu, \kappa) + \sum_{(\mu,\kappa) \in \mathcal{S}_C} \theta_{\mu,\kappa} a_{\tilde{m}+\mu, \tilde{k}+\kappa} \hat{H}(\mu, \kappa). \quad (\text{A.23})$$

Applying Jensen's inequality for convex functions, (A.22) can be written as

$$\varepsilon_{H,AP} \geq \frac{\mathbf{E} \left[|\tilde{p}_{\tilde{m},\tilde{k}}|^2 \right]}{\mathbf{E} \left[|p_{\tilde{m},\tilde{k}}|^2 \right]}. \quad (\text{A.24})$$

Having this in regard, $\varepsilon_{H,AP}$ is minimized if

$$\mathbb{E} \left[\frac{1}{|p_{\tilde{m},\tilde{k}}|^2} \right] \equiv \frac{1}{\mathbb{E} [|p_{\tilde{m},\tilde{k}}|^2]}. \quad (\text{A.25})$$

This is only fulfilled for $|p_{\tilde{m},\tilde{k}}| = \text{const.}$, such as for BPSK modulated pilots. Accordingly, (4.17) yields

$$\varepsilon_H = \frac{1}{\sigma_p^2} \mathbb{E} \left[\left| \tilde{p}_{\tilde{m},\tilde{k}} \right|^2 \right]. \quad (\text{A.26})$$

A.5 CO-USER SYMBOL AND SUBCARRIER OFFSETS

Extending (A.6) to a multi-user scenario, $\tilde{a}_{u,\tilde{m},\tilde{k}}$ is obtained according to

$$\tilde{a}_{u,\tilde{m},\tilde{k}} = \theta_{\tilde{m},\tilde{k}}^* \sum_{u' \in \mathcal{U}(m,k)} \sum_{\ell \in \mathbb{T}_{\theta_{m,k}}} a_{u',m,k} H_{\tilde{m},\tilde{k}}^{u,u'}(m,k) \quad (\text{A.27})$$

with the effective channel coefficient $H_{\tilde{m},\tilde{k}}^{u,u'}(m,k)$ given by

$$H_{\tilde{m},\tilde{k}}^{u,u'}(m,k) = \sum_{n=-\infty}^{\infty} \left(h_u[\tau,n] * f_{u',k}[n - mM_{u'}] \right) g_{u,\tilde{k}}^*[n - \tilde{m}M_u] \quad (\text{A.28})$$

Resolving the convolution of the channel $h_u[\tau,n]$ and the transmit PFF $f_{u',k}[n]$ and with definition of $n' = n - \tilde{m}M_u$, (A.28) yields

$$H_{\tilde{m},\tilde{k}}^{u,u'}(\mu,k) = \sum_{n'=-\infty}^{\infty} \sum_{\tau} h_u[\tau,n' + \tilde{m}M_u] f_{u',k}[n' - \tau - mM_{u'} + \tilde{m}M_u] g_{u,\tilde{k}}^*[n']. \quad (\text{A.29})$$

Recalling $f_{u',k}[n] = f_u[n]e^{j2\pi K_{u'}kn}$ and $g_{u,\tilde{k}}^*[n] = g_u^*[n]e^{-j2\pi K_u kn}$, $H_{\tilde{m},\tilde{k}}(\mu,k)$ can be rewritten as

$$\begin{aligned} H_{\tilde{m},\tilde{k}}^{u,u'}(\mu,k) &= \sum_{n'=-\infty}^{\infty} \sum_{\tau} h[\tau,n' + \tilde{m}M_u] f_{u'}[n' - \tau - mM_{u'} + \tilde{m}M_u] g_u^*[n'] \\ &\quad \cdot e^{j2\pi K_{u'}k(n' - \tau - mM_{u'} + \tilde{m}M_u)} e^{-j2\pi K_u \tilde{k}n'} \\ &= \sum_{n'=-\infty}^{\infty} \sum_{\tau} h[\tau,n' + \tilde{m}M_u] f_{u'}[n' - \tau - mM_{u'} + \tilde{m}M_u] g_u^*[n'] \\ &\quad \cdot e^{j2\pi K_{u'}k(\tilde{m}M_u - mM_{u'} - \tau)} e^{j2\pi n'(K_{u'}k - K_u \tilde{k})}. \end{aligned} \quad (\text{A.30})$$

Here, the effective channel coefficient depends on different lattice grids and such different coordinate systems. To ease the calculation of the effective channel coefficients it is useful to remove the dependency on the real symbol positions (m,k) and (\tilde{m},\tilde{k}) by in-

roduction of the symbol and subcarrier index offsets $\mu = m - \tilde{m}$ and $\kappa = k - \tilde{k}$ (as done on Appendix A.2). Thus, the time and frequency offsets between users in (A.30) can be calculated as follows:

$$\begin{aligned}
\tilde{m}M_u - mM_{u'} &= \tilde{m}\tau_0 \frac{K_v}{\zeta_u} - m\tau_0 \frac{K_v}{\zeta_{u'}} \\
&= \tilde{m}\tau_0 \frac{K_v}{\zeta_u} - (\mu + \tilde{m})\tau_0 \frac{K_v}{\zeta_{u'}} \\
&= \tilde{m}\tau_0 K_v \left(\frac{1}{\zeta_u} - \frac{1}{\zeta_{u'}} \right) - \mu\tau_0 \frac{K_v}{\zeta_{u'}} \\
&= \tilde{m}M_{u,u'} - \mu\tau_0 \frac{K_v}{\zeta_{u'}} = \tilde{m}M_{u,u'} - \mu M_{u'} \tag{A.31a}
\end{aligned}$$

with

$$M_{u,u'} = \tau_0 K_v \left(\frac{1}{\zeta_u} - \frac{1}{\zeta_{u'}} \right) \tag{A.31b}$$

and

$$\begin{aligned}
kK_{u'} - \tilde{k}K_u &= \kappa\nu_0 \frac{\zeta_{u'}}{K_v} - \tilde{k}\nu_0 \frac{\zeta_u}{K_v} \\
&= (\kappa + \tilde{k})\nu_0 \frac{\zeta_{u'}}{K_v} - \tilde{k}\nu_0 \frac{\zeta_u}{K_v} \\
&= \kappa\nu_0 \frac{\zeta_{u'}}{K_v} + \tilde{k} \frac{\nu_0}{K_v} (\zeta_{u'} - \zeta_u) \\
&= \kappa\nu_0 \frac{\zeta_{u'}}{K_v} - \tilde{k}K_{u,u'} = \kappa K_{u'} - \tilde{k}K_{u,u'} \tag{A.31c}
\end{aligned}$$

with

$$K_{u,u'} = \frac{\nu_0}{K_v} (\zeta_u - \zeta_{u'}). \tag{A.31d}$$

Thus, the effective channel coefficient yields

$$\begin{aligned}
H_{\tilde{m}, \tilde{k}}^{u, u'}(\mu, k) &= \sum_{n'=-\infty}^{\infty} \sum_{\tau} h[\tau, n' + \tilde{m}M_u] f_{u'}[n' - \tau + \tilde{m}M_{u, u'} - \mu M_{u'}] g_u^*[n'] \\
&\quad \cdot e^{j2\pi K_{u'}(\kappa + \tilde{k})(\tilde{m}M_{u, u'} - \mu M_{u'} - \tau)} e^{j2\pi n'(\kappa K_{u'} - \tilde{k}K_{u, u'})} \\
&= \sum_{n'=-\infty}^{\infty} \sum_{\tau} \int_{-f_D T_s}^{f_D T_s} D_u[\tau, \nu] e^{j2\pi(n' + \tilde{m}M_u)\nu} d\nu \\
&\quad \cdot f_{u'}[n' - \tau + \tilde{m}M_{u, u'} - \mu M_{u'}] g_u^*[n'] \\
&\quad \cdot e^{j2\pi K_{u'}(\kappa + \tilde{k})(\tilde{m}M_{u, u'} - \mu M_{u'} - \tau)} e^{j2\pi n'(\kappa K_{u'} - \tilde{k}K_{u, u'})} \\
&= \sum_{\tau} \int_{-f_D T_s}^{f_D T_s} D_u[\tau, \nu] e^{j2\pi \tilde{m}M_u \nu} \\
&\quad \cdot \sum_{n'=-\infty}^{\infty} f_{u'}[n' - \tau + \tilde{m}M_{u, u'} - \mu M_{u'}] g_u^*[n'] e^{j2\pi n'(\nu + \kappa K_{u'} - \tilde{k}K_{u, u'})} \\
&\quad \cdot e^{j2\pi K_{u'}(\kappa + \tilde{k})(\tilde{m}M_{u, u'} - \mu M_{u'} - \tau)} d\nu \\
&= \sum_{\tau} \int_{-f_D T_s}^{f_D T_s} D_u[\tau, \nu] e^{j2\pi \tilde{m}M_u \nu} A_{\tilde{m}, \tilde{k}}^{u, u'}[\mu M_{u'} + \tau, \kappa K_{u'} + \nu] \\
&\quad \cdot e^{-j2\pi K_u(\tilde{k} + \kappa)(\mu M_u - \tilde{m}M_{u, u'} + \tau)} d\nu, \tag{A.32}
\end{aligned}$$

where the channel spreading function $D_u[\tau, \nu]$ is the DTFT of $h_u[\tau, n]$ at frequency ν (cf. (3.8)). $A_{\tilde{m}, \tilde{k}}^{u, u'}[\tau, \nu]$ is the discrete-time (cross-)ambiguity function defined by

$$A_{\tilde{m}, \tilde{k}}^{u, u'}[\tau, \nu] = \sum_{n=-\infty}^{\infty} f_{u'}[n + \tilde{m}M_{u, u'} - \tau] f_u^*[n] e^{j2\pi n(\nu - \tilde{k}K_{u, u'})}. \tag{A.33}$$

CHANNEL MODELING

The channel scenarios used within this thesis are based on the models defined for LTE [20]. Due to the amount of the therein contained scenarios and models, they are harmonized and reduced to a suitable set as described in the following sections.

B.1 HARMONIZATION OF CHANNEL MODELS

In [20], three different channel models have been defined to reflect a large variety of real world environments. Besides the delay spread τ_{rms} and maximum Doppler shift f_D , in [20] the number of channel clusters and fading type, i.e. Rayleigh or Rician fading, is varied to model the different environments. To reduce the complexity of the channel models for the analytic derivations and to ease the performance comparison of different channel environments, in this thesis all channel scenarios are modeled by a single-cluster exponential PDP with Jakes DPSD and Rayleigh fading. Therefore, the derived τ_{rms} is calculated based on the path delays and their related power, which in [20] is provided in Table 5.2 to 5.4. The delay spreads τ_{rms} of the resulting channel models are given in Table B.1.

Environment	Acronym	τ_{rms} [μs]
Typical Urban	Tux	0.5
Rural Area	Rax	0.1
Hilly Terrain	HTx	3

Table B.1: Reduced complexity channel models derived from [20]

B.2 CHANNEL SCENARIOS

Besides the PDP and Doppler PSD shape, the influence of a communication channel on the performance of a communication channel depends on the velocity v of a user and the carrier frequency f_c . Typical carrier frequencies for cellular radios in Europe are approximately at $f_c = \{800, 1800, 2600\}$ MHz [98]. In this thesis, the investigations are conducted for $f_c = 800$ MHz. The amount of user velocities defined in [20] are reduced to reflect the most common movement behavior of mobile user, which are pedestrians

in urban and suburban environments and people traveling by car in rural and hilly environments. For this mobility scenarios, the velocities $v = \{3, 120\}$ km/h have been defined in [20]. The thereof resulting channel scenarios are provided in Table B.2.

Scenario s_c	Acronym	τ_{rms} [μs]	Velocity [km/h]	f_D [Hz]	δ	B_c [kHz]	T_c [ms]
A	Tux	0.5	3	2.2	$1.1 \cdot 10^{-6}$	2000	643
B	Rax	0.1	120	88.8	$8.8 \cdot 10^{-6}$	10 000	15.9
C	HTx	3	120	88.8	$2.6 \cdot 10^{-4}$	333.3	15.9

Table B.2: Channel scenarios and the resulting delay-Doppler products δ for the carrier frequency $f_c = 800$ MHz.

B.3 CONSIDERATIONS FOR MONTE-CARLO SIMULATIONS

For the generation of Monte-Carlo simulation based results, the computer-aided calculation of the effective channel coefficients $H_{\bar{m},\bar{k}}(\mu, \kappa)$ according to (3.8), which is based on the channel spreading function $D(\tau, \nu)$, can result in a huge resource consumption in terms of RAM. To provide an adequate resolution $N_{\text{bin, DPSD}}$ in frequency domain, the time-variant CIR has to have a sufficient length N_{CIR} , which in dependance of the investigated channel parameters and required frequency bins per subcarrier N_{bin} can require a lot of RAM. Table B.3 provides exemplary values for CIR length L and memory consumption $N_{\text{Byte, CIR}}$ for the channel scenarios defined in Table B.2 and the symbol duration of LTE, which are defined in the following. The number of samples per channel tap of $h[\tau, n]$ depends on the required solution of the Doppler PSD

$$N_{\text{bin, DPSD}} \propto 1/f_D T \quad (\text{B.1a})$$

as well as the investigated normalized maximum Doppler shift $f_D T$

$$N_{\text{bin}} = \left\lceil \frac{N_{\text{bin, DPSD}}}{f_D T} \right\rceil, \quad (\text{B.1b})$$

$$N_{\text{CIR}} = N_{\text{bin}} K. \quad (\text{B.1c})$$

The number of channel taps depends on the investigated normalized delay spread as well as the amount of considered energy, which can be adjusted by a factor L_t .

$$L = \lceil L_t K \tau_{\text{rms}} / T \rceil. \quad (\text{B.1d})$$

In this thesis, the PDP truncation is selected such that truncation error is below 10^{-4} , which can be reached by selecting $L_t = 10$.

With double precision, i.e. 8 Byte for each in- and quadrature-phase sample, the required amount of memory can be calculated as

$$N_{\text{Byte,cir}} = 2 \cdot 8 \cdot N_{\text{CIR}}L. \quad (\text{B.1e})$$

In this thesis, the number of Doppler PSD samples $N_{\text{bin, DPSD}}$ is selected to be 501. Therefore, in Monte-Carlo based simulations $H_{\tilde{m},\tilde{\kappa}}(\mu, \kappa)$ is calculated based on the usage of the time-variant CIR $h[\tau, n]$ and (A.9), which is rearranged as

$$H_{\tilde{m},\tilde{\kappa}}(\mu, \kappa) = \sum_{\tau} \sum_{n=-\infty}^{\infty} h[\tau, n + \tilde{m}M_0]f[n - \tau - \mu M_0]f^*[n]e^{j2\pi K_0 \kappa (n - \tau - \mu M_0)}. \quad (\text{B.2})$$

s_c	Frequency domain				Time domain		$N_{\text{Byte,CIR}}$ [GiB]
	$f_D T$	$N_{\text{bin, DPSD}}$	N_{bin}	N_{CIR}	τ_{rms}/T	L	
A	$1.48 \cdot 10^{-4}$	11	$7.43 \cdot 10^4$	$1.9 \cdot 10^7$	$7.5 \cdot 10^{-3}$	20	5.66
		101	$6.82 \cdot 10^5$	$1.75 \cdot 10^8$			52.01
		501	$3.38 \cdot 10^6$	$8.66 \cdot 10^8$			258.01
B	$5.9 \cdot 10^{-3}$	11	$1.86 \cdot 10^3$	$4.76 \cdot 10^5$	$1.5 \cdot 10^{-3}$	4	0.03
		101	$1.7 \cdot 10^4$	$4.35 \cdot 10^6$			0.26
		501	$8.45 \cdot 10^4$	$2.16 \cdot 10^7$			1.29
C	$5.9 \cdot 10^{-3}$	11	$1.86 \cdot 10^3$	$4.76 \cdot 10^5$	$4.56 \cdot 10^{-2}$	116	0.82
		101	$1.7 \cdot 10^4$	$4.35 \cdot 10^6$			7.54
		501	$8.45 \cdot 10^4$	$2.16 \cdot 10^7$			37.41

Table B.3: Estimated RAM requirements for the effective channel coefficient $H_{\tilde{m},\tilde{\kappa}}(\mu, \kappa)$ calculation according to (3.8) with $K = 256$ and $T = T_{\text{LTE}}$.

DS SCHEME RELATED DERIVATIONS

C.1 CHANNEL ESTIMATION ERROR FOR DS SCHEME

Similar to Appendix A.3, the mean square error $\varepsilon_{H,DS}$ for scattered pilot based channel estimation with DS based interference mitigation is defined by

$$\begin{aligned} \varepsilon_{H,DS} &= \mathbf{E} \left[\left| \sum_{(\mu,\kappa) \in \mathcal{S}_R} \theta_{\mu,\kappa}^* \frac{\mathbf{a}_{\tilde{m}+\mu, \tilde{k}+\kappa}}{p_{\tilde{m}, \tilde{k}}} H_{\tilde{m}, \tilde{k}}(\mu, \kappa) + \sum_{\lambda=1}^{\wedge} H_{\lambda} \frac{\underline{\chi}_{\lambda} \underline{d}}{p_{\tilde{m}, \tilde{k}}} \right|^2 \right] \\ &= \mathbf{E} \left[\left(\sum_{(\mu,\kappa) \in \mathcal{S}_R} \theta_{\mu,\kappa}^* \frac{\mathbf{a}_{\tilde{m}+\mu, \tilde{k}+\kappa}}{p_{\tilde{m}, \tilde{k}}} H_{\tilde{m}, \tilde{k}}(\mu, \kappa) + \sum_{\lambda=1}^{\wedge} H_{\lambda} \frac{\underline{\chi}_{\lambda} \underline{d}}{p_{\tilde{m}, \tilde{k}}} \right) \right. \\ &\quad \cdot \left. \left(\sum_{(\mu',\kappa') \in \mathcal{S}_R} \theta_{\mu',\kappa'}^* \frac{\mathbf{a}_{\tilde{m}+\mu', \tilde{k}+\kappa'}}{p_{\tilde{m}, \tilde{k}}} H_{\tilde{m}, \tilde{k}}(\mu', \kappa') + \sum_{\lambda'=1}^{\wedge} H_{\lambda'} \frac{\underline{\chi}_{\lambda'} \underline{d}}{p_{\tilde{m}, \tilde{k}}} \right)^* \right]. \quad (\text{C.1}) \end{aligned}$$

Considering appendix A.4 and with the assumption of i.i.d. data symbols, i.e. $\mathbf{E}[\mathbf{a}_{\tilde{m}+\mu, \tilde{k}+\kappa} \mathbf{a}_{\lambda}^*] = 0$ and $\mathbf{E}[\mathbf{a}_{\tilde{m}+\mu, \tilde{k}+\kappa} \mathbf{a}_{\tilde{m}+\mu', \tilde{k}+\kappa'}^*] = \sigma_d^2 \delta_{\mu, \mu'} \delta_{\kappa, \kappa'}$, pilot boost factor $b = \sigma_p^2 / \sigma_d^2$ and BPSK modulated pilot symbols (cf. Appendix A.4), (C.1) can be simplified as

$$\varepsilon_{H,DS} = \varepsilon_{c,DS} + \varepsilon_{r,DS} \quad (\text{C.2})$$

with

$$\begin{aligned} \varepsilon_{c,DS} &= \frac{1}{\sigma_p^2} \sum_{(\lambda, \lambda')} \mathbf{E}[H_{\lambda} H_{\lambda'}^*] \mathbf{E}[a_{\lambda} a_{\lambda'}^*] \\ &= \frac{1}{\sigma_p^2} \sum_{(\lambda, \lambda')} \mathbf{E}[H_{\lambda} H_{\lambda'}^*] \underline{\chi}_{\lambda} \mathbf{E}[\underline{d} \underline{d}^H] \underline{\chi}_{\lambda'}^T \end{aligned} \quad (\text{C.3})$$

and

$$\begin{aligned} \varepsilon_{r,DS} &= \frac{1}{b} \sum_{(\mu, \kappa) \in \mathcal{S}_R} \mathbf{E} \left[|H_{\tilde{m}, \tilde{k}}(\mu, \kappa)|^2 \right] \\ &= \varepsilon_{r,AP}. \end{aligned} \quad (\text{C.4})$$

Taking into account that

$$\mathbf{E}[d_\lambda d_{\lambda'}^*] = \begin{cases} \sigma_d^2, & \lambda = \lambda' \neq \Lambda \\ \sigma_d^2 \sigma_\beta^2, & \lambda = \lambda' = \Lambda \\ \sigma_d^2 \beta_{\lambda'}, & \lambda \neq \Lambda \wedge \lambda' = \Lambda, \\ \sigma_d^2 \beta_\lambda, & \lambda = \Lambda \wedge \lambda' \neq \Lambda \\ 0 & \text{otherwise} \end{cases} \quad (\text{C.5})$$

the cancellation error $\varepsilon_{c,DS}$ yields

$$\begin{aligned} \varepsilon_{c,DS} &= \frac{1}{b} \sum_{(\lambda, \lambda')} \mathbf{E}[H_\lambda H_{\lambda'}^*] \underline{\mathbf{X}}_\lambda \underline{\mathbf{B}}_I \underline{\mathbf{X}}_{\lambda'}^T \\ &= \frac{1}{b} \sum_{(\lambda, \lambda')} \mathbf{E}[H_\lambda H_{\lambda'}^*] \left(\delta_{\lambda, \lambda'} + \underline{\mathbf{X}}_\lambda \underline{\mathbf{B}} \underline{\mathbf{X}}_{\lambda'}^T \right) \\ &= \frac{1}{b} \sum_{\lambda} \mathbf{E}[|H_\lambda|^2] + \frac{1}{b} \sum_{(\lambda, \lambda')} \mathbf{E}[H_\lambda H_{\lambda'}^*] \left(\underline{\mathbf{X}}_\lambda \underline{\mathbf{B}} \underline{\mathbf{X}}_{\lambda'}^T \right), \end{aligned} \quad (\text{C.6})$$

with $\underline{\mathbf{B}}_I$ and $\underline{\mathbf{B}}$ being correlation matrices defined by

$$\begin{aligned} \underline{\mathbf{B}}_I &= \begin{bmatrix} \underline{\mathbf{I}}_{\Lambda-1} & \underline{\beta}^T \\ \underline{\beta} & \sigma_\beta^2 \end{bmatrix} \\ &= \underline{\mathbf{I}}_\Lambda + \underline{\mathbf{B}} = \underline{\mathbf{I}}_\Lambda + \begin{bmatrix} \underline{\mathbf{Q}}_{\Lambda-1} & \underline{\beta}^T \\ \underline{\beta} & \sigma_\beta^2 - 1 \end{bmatrix}. \end{aligned} \quad (\text{C.7})$$

Here, $\underline{\mathbf{I}}_{\Lambda-1}$ and $\underline{\mathbf{Q}}_{\Lambda-1}$ are the identity and zero matrix of size $\Lambda - 1$, respectively. As both $\varepsilon_{c,DS}$ and $\varepsilon_{r,DS}$ include a term for the full interference induced by a symbol, $\varepsilon_{H,DS}$ can be rewritten as

$$\varepsilon_{H,DS} = \frac{1}{b} \sum_{(\mu, \kappa) \in \mathcal{S}_N} \mathbf{E}[|H_{\tilde{m}, \tilde{k}}(\mu, \kappa)|^2] + \frac{1}{b} \sum_{(\lambda, \lambda')} \mathbf{E}[H_\lambda H_{\lambda'}^*] \left(\underline{\mathbf{X}}_\lambda \underline{\mathbf{B}} \underline{\mathbf{X}}_{\lambda'}^T \right). \quad (\text{C.8})$$

Utilizing (A.20) results in

$$\begin{aligned}
 \varepsilon_{H,DS} &= \frac{1}{b} \sum_{l=0}^{L-1} \int_{-f_D T_s}^{f_D T_s} S[\tau_l, \nu] \left(\sum_{(\mu, \kappa) \in \mathcal{S}_N} |A_{\mu, \kappa}[\tau_l, \nu]|^2 \right. \\
 &\quad \left. + \sum_{(\lambda, \lambda')} \left(\theta_\lambda A_{\lambda}^{\tilde{\kappa}}[\tau_l, \nu] x_{\lambda, \lambda'} (\theta_{\lambda'} A_{\lambda'}^{\tilde{\kappa}}[\tau_l, \nu])^* \right) \right) d\nu \\
 &= \frac{1}{b} \sum_{l=0}^{L-1} \int_{-f_D T_s}^{f_D T_s} S[\tau_l, \nu] \left(\sum_{(\mu, \kappa) \in \mathcal{S}_N} |A_{\mu, \kappa}[\tau_l, \nu]|^2 + \underline{\alpha}[\tau_l, \nu] \underline{X} \underline{\alpha}[\tau_l, \nu]^H \right) d\nu \quad (C.9)
 \end{aligned}$$

with $x_{\lambda, \lambda'}$, \underline{X} and $\underline{\alpha}_{\tau_l, \nu}$ being defined according to

$$x_{\lambda, \lambda'} = \underline{x}_\lambda \underline{B} \underline{x}_{\lambda'}^T \quad (C.10a)$$

$$\underline{\alpha}[\tau_l, \nu] = \begin{bmatrix} \theta_1 \phi_d(\kappa_1, \tau_l) A_1[\tau_l, \nu] \\ \theta_2 \phi_d(\kappa_2, \tau_l) A_2[\tau_l, \nu] \\ \vdots \\ \theta_\Lambda \phi_d(\kappa_\Lambda, \tau_l) A_\Lambda[\tau_l, \nu] \end{bmatrix}^T \quad (C.10b)$$

$$\begin{aligned}
 \underline{X} &= \begin{bmatrix} x_{1,1} & \dots & x_{1,\lambda'} & \dots & x_{1,\Lambda} \\ \vdots & \ddots & \vdots & \ddots & \vdots \\ x_{\lambda,1} & \dots & x_{\lambda,\lambda'} & \dots & x_{\lambda,\Lambda} \\ \vdots & \ddots & \vdots & \ddots & \vdots \\ x_{\Lambda,1} & \dots & x_{\Lambda,\lambda'} & \dots & x_{\Lambda,\Lambda} \end{bmatrix} \\
 &= \underline{C} \underline{B} \underline{C}^T = \underline{X}^T. \quad (C.10c)
 \end{aligned}$$

As shown in C.2, similar to the AP scheme the phase shift $\phi_d(\tilde{\kappa}, \tau_l)$ is canceled out in $\underline{\alpha}_{\tau_l, \nu} \underline{X} \underline{\alpha}_{\tau_l, \nu}^H$, so that the channel estimation error $\varepsilon_{H,DS}$ is independent of the subcarriers allocated for pilot symbols. However, it is shown, that the code matrix \underline{C} has to be designed appropriately with consideration of $\phi_p(k, \kappa, \mu)$ and $\theta_{\mu, \kappa}$. Due to the induced correlation of the symbols a_λ , the phase shifts $\phi_d(\kappa_\lambda, \tau_l)$ have to be considered. For the scenarios investigated in this thesis, $\phi_d(\kappa_\lambda, \tau_l)$ may be neglected as done in [32], as the discrepancies to the correct values have been shown to be very small.

C.2 CHANNEL ESTIMATION ERROR DEPENDENCIES IN THE DS SCHEME

As presented in (4.21), the interference mitigation condition for the DS scheme is given by

$$\forall k \forall \alpha_\lambda : i_{\bar{m}, \bar{k}} = \sum_{\lambda=1}^{\Lambda} \theta_\lambda \alpha_\lambda A_\lambda^k [0, 0] = 0, \quad (\text{C.11})$$

which can be rewritten as

$$\forall k \forall d_\lambda : i_{\bar{m}, \bar{k}} = \sum_{\lambda=1}^{\Lambda} \underline{\alpha}^k \underline{c}_\lambda d_\lambda = 0, \quad (\text{C.12})$$

with

$$\underline{\alpha}^k = \begin{bmatrix} \theta_1 \phi_p(k, \kappa_1, \mu_1) A_1 [0, 0] \\ \theta_2 \phi_p(k, \kappa_2, \mu_2) A_2 [0, 0] \\ \vdots \\ \theta_\Lambda \phi_p(k, \kappa_\Lambda, \mu_\Lambda) A_\Lambda [0, 0] \end{bmatrix}^T, \quad (\text{C.13})$$

as $\tau_l = 0 : \phi_d(k, \tau_l) = \phi_d(\kappa_\lambda, \tau_l) = 1$. To obtain $\forall d_\lambda : i_{\bar{m}, \bar{k}} = 0$, i.e.

$$\forall k : 0 = \sum_{\lambda=1}^{\Lambda-1} \underline{\alpha}^k \underline{c}_\lambda d_\lambda + \underline{\alpha}^k \underline{c}_\Lambda d_\Lambda, \quad (\text{C.14})$$

the linear relationship (4.24) [57] is introduced. Therefore, for a given spreading matrix C the interference mitigation condition yields

$$\forall k \forall \lambda : 0 = \underline{\alpha}^k \underline{c}_\lambda d_\lambda + \underline{\alpha}^k \underline{c}_\Lambda \beta_\lambda d_\lambda. \quad (\text{C.15})$$

Therefore, C has to be designed such that

$$\forall k \forall \lambda : \beta_\lambda = -\frac{\underline{\alpha}^k \underline{c}_\lambda}{\underline{\alpha}^k \underline{c}_\Lambda}; \quad \underline{\alpha}^k \underline{c}_\Lambda \neq 0. \quad (\text{C.16})$$

For both isotropic and non-isotropic pulse shapes and irrespective to the value of k, $\theta_{\mu, \kappa} A_{\mu, \kappa}^k [0, 0]$ has the following symmetry properties

$$\theta_{\mu, \kappa} A_{\mu, \kappa}^k [0, 0] = \begin{cases} r_1, & |\mu| = |\kappa| = 1 \\ -\theta_{\mu, -\kappa} A_{\mu, -\kappa}^k [0, 0] = r_2, & \mu = 0 \\ -\theta_{-\mu, \kappa} A_{-\mu, \kappa}^k [0, 0] = r_3, & \kappa = 0. \end{cases} \quad (\text{C.17a})$$

This can be shown easily by utilizing the symmetry properties of the ambiguity function $A[\tau, \nu]$ as well as the phase factors $\theta_{\mu, \kappa}$ and $\phi_p(k, \kappa, \mu)$:

$$A[\tau, \nu] = e^{j2\pi\tau\nu} A^*[-\tau, -\nu] \quad (\text{C.17b})$$

$$\theta_{\mu, \kappa} = \theta_{-\mu, -\kappa}^* \quad (\text{C.17c})$$

$$\theta_{\mu, \kappa} = -\theta_{\mu, -\kappa} = -\theta_{-\mu, \kappa} \quad (\text{C.17d})$$

$$\phi_p(k, \kappa, \mu) = \phi_p(k, -\kappa, \mu) = \phi_p(k, \kappa, -\mu) = \phi_p(k, -\kappa, -\mu). \quad (\text{C.17e})$$

Therefore, for the indexing scheme used in [57], an alternative representation of $\underline{\alpha}^k$ is given by

$$\underline{\alpha}^k = [r_1 \ r_2 \ r_1 \ r_3 \ -r_3 \ r_1 \ -r_2 \ r_1]. \quad (\text{C.18})$$

Recalling (C.8), the subcarrier \tilde{k} specific channel estimation error $\varepsilon_{\text{H,DS}}(\tilde{k})$, is given by

$$\varepsilon_{\text{H,DS}}(\tilde{k}) = \frac{1}{b} \left(\varepsilon_{\text{H,a}}^{\text{DS}} + \varepsilon_{\text{H,c}}^{\text{DS}}(\tilde{k}) \right), \quad (\text{C.19a})$$

where the auto- and cross-interference errors $\varepsilon_{\text{H,a}}^{\text{DS}}$ and $\varepsilon_{\text{H,c}}^{\text{DS}}$ are defined by

$$\varepsilon_{\text{H,a}}^{\text{DS}} = \sum_{(\mu, \kappa) \in \mathcal{S}_N} \mathbf{E} \left[|H_{\tilde{m}, \tilde{k}}(\mu, \kappa)|^2 \right] \quad (\text{C.19b})$$

$$\varepsilon_{\text{H,c}}^{\text{DS}}(\tilde{k}) = \sum_{(\lambda, \lambda')} \mathbf{E} [H_\lambda H_{\lambda'}^*] \left(\underline{\chi}_\lambda \underline{\mathbf{B}} \underline{\chi}_{\lambda'}^T \right). \quad (\text{C.19c})$$

Utilizing (A.20), $\varepsilon_{\text{H,c}}^{\text{DS}}$ yields

$$\begin{aligned} \varepsilon_{\text{H,c}}^{\text{DS}}(\tilde{k}) &= \sum_{l=0}^{L-1} \int_{-f_D T_s}^{f_D T_s} S[\tau_l, \nu] \left(\sum_{(\lambda, \lambda')} \theta_{(\mu, \kappa)_\lambda} A_{(\mu, \kappa)_\lambda}^{\tilde{k}}[\tau_l, \nu] \chi_{\lambda, \lambda'} \right. \\ &\quad \left. \cdot (\theta_{(\mu, \kappa)_{\lambda'}} A_{(\mu, \kappa)_{\lambda'}}^{\tilde{k}}[\tau_l, \nu])^* \right) d\nu \\ &= \sum_{l=0}^{L-1} \int_{-f_D T_s}^{f_D T_s} S[\tau_l, \nu] \left(\underline{\alpha}_p^{\tilde{k}}[\tau_l, \nu] \underline{\mathbf{X}} \underline{\alpha}_p^{\tilde{k}}[\tau_l, \nu]^H \right) d\nu \\ &= \sum_{l=0}^{L-1} \int_{-f_D T_s}^{f_D T_s} S[\tau_l, \nu] \alpha[\tau_l, \nu] d\nu, \end{aligned} \quad (\text{C.20a})$$

with

$$\begin{aligned}
 \underline{\alpha}_p^{\tilde{\kappa}}[\tau_l, \nu] &= \begin{bmatrix} \theta_{(\mu, \kappa)_1} \mathbf{A}_{(\mu, \kappa)_1}^{\tilde{\kappa}}[\tau_l, \nu] \\ \theta_{(\mu, \kappa)_2} \mathbf{A}_{(\mu, \kappa)_2}^{\tilde{\kappa}}[\tau_l, \nu] \\ \vdots \\ \theta_{(\mu, \kappa)_\lambda} \mathbf{A}_{(\mu, \kappa)_\lambda}^{\tilde{\kappa}}[\tau_l, \nu] \end{bmatrix}^T \\
 &= \begin{bmatrix} \theta_{(\mu, \kappa)_1} \phi_p(\tilde{\kappa}, \mu_1, \kappa_1) \phi_d(\tilde{\kappa}, \tau_l) \phi_d(\kappa_1, \tau_l) \mathbf{A}_{(\mu, \kappa)_1}[\tau_l, \nu] \\ \theta_{(\mu, \kappa)_2} \phi_p(\tilde{\kappa}, \mu_2, \kappa_2) \phi_d(\tilde{\kappa}, \tau_l) \phi_d(\kappa_2, \tau_l) \mathbf{A}_{(\mu, \kappa)_2}[\tau_l, \nu] \\ \vdots \\ \theta_{(\mu, \kappa)_\lambda} \phi_p(\tilde{\kappa}, \mu_\lambda, \kappa_\lambda) \phi_d(\tilde{\kappa}, \tau_l) \phi_d(\kappa_\lambda, \tau_l) \mathbf{A}_{(\mu, \kappa)_\lambda}[\tau_l, \nu] \end{bmatrix}^T \\
 &= \phi_d(\tilde{\kappa}, \tau_l) \begin{bmatrix} \theta_{(\mu, \kappa)_1} \phi_p(\tilde{\kappa}, \mu_1, \kappa_1) \phi_d(\kappa_1, \tau_l) \mathbf{A}_{(\mu, \kappa)_1}[\tau_l, \nu] \\ \theta_{(\mu, \kappa)_2} \phi_p(\tilde{\kappa}, \mu_2, \kappa_2) \phi_d(\kappa_2, \tau_l) \mathbf{A}_{(\mu, \kappa)_2}[\tau_l, \nu] \\ \vdots \\ \theta_{(\mu, \kappa)_\lambda} \phi_p(\tilde{\kappa}, \mu_\lambda, \kappa_\lambda) \phi_d(\kappa_\lambda, \tau_l) \mathbf{A}_{(\mu, \kappa)_\lambda}[\tau_l, \nu] \end{bmatrix}^T \\
 &= \phi_d(\tilde{\kappa}, \tau_l) \underline{\alpha}_p^{\tilde{\kappa}}[\tau_l, \nu] \tag{C.20b}
 \end{aligned}$$

and

$$\underline{\alpha}_p^{\tilde{\kappa}}[\tau_l, \nu] = \begin{bmatrix} \theta_{(\mu, \kappa)_1} \phi_p(\tilde{\kappa}, \mu_1, \kappa_1) \phi_d(\kappa_1, \tau_l) \mathbf{A}_{(\mu, \kappa)_1}[\tau_l, \nu] \\ \theta_{(\mu, \kappa)_2} \phi_p(\tilde{\kappa}, \mu_2, \kappa_2) \phi_d(\kappa_2, \tau_l) \mathbf{A}_{(\mu, \kappa)_2}[\tau_l, \nu] \\ \vdots \\ \theta_{(\mu, \kappa)_\lambda} \phi_p(\tilde{\kappa}, \mu_\lambda, \kappa_\lambda) \phi_d(\kappa_\lambda, \tau_l) \mathbf{A}_{(\mu, \kappa)_\lambda}[\tau_l, \nu] \end{bmatrix}^T. \tag{C.20c}$$

$$\tag{C.20d}$$

In consideration of (C.10c), $\alpha[\tau_l, \nu]$ holds

$$\begin{aligned}
 \alpha[\tau_l, \nu] &= \phi_d(\tilde{\kappa}, \tau_l) \underline{\alpha}_p^{\tilde{\kappa}}[\tau_l, \nu] \underline{\mathbf{X}} \underline{\alpha}_p^{\tilde{\kappa}}[\tau_l, \nu]^H \phi_d(\tilde{\kappa}, \tau_l)^* \\
 &= \underline{\alpha}_p^{\tilde{\kappa}}[\tau_l, \nu] \underline{\mathbf{X}} \underline{\alpha}_p^{\tilde{\kappa}}[\tau_l, \nu]^H. \tag{C.21}
 \end{aligned}$$

Thus, the estimation error is independent of the allocated subcarriers used for transmitting the pilot symbols.

C.3 DS SCHEME MATRICES

In order of completeness, the spreading matrices $\underline{\mathbf{C}}$ reported in [57] and the calculation of the auxiliary data symbols d_λ and the variables $\underline{\beta}$ and $\underline{\mathbf{X}}$ are outlined with the notation

used in this thesis. Therefore, the indexing λ of the lattice position tuples is done as shown in Figure 4.8.

C.3.1 General solution

For both isotropic and non-isotropic pulse shapes, \underline{C} and d_λ can be defined according to

$$\underline{C} = \frac{1}{2} \begin{bmatrix} 1 & 0 & 1 & 0 & 1 & 1 & 0 & 0 \\ 0 & \sqrt{2} & 0 & 0 & 0 & 0 & -\sqrt{2} & 0 \\ 1 & 0 & -1 & 0 & 1 & -1 & 0 & 0 \\ 0 & 0 & 0 & \sqrt{2} & 0 & 0 & 0 & -\sqrt{2} \\ 0 & 0 & 0 & \sqrt{2} & 0 & 0 & 0 & \sqrt{2} \\ -1 & 0 & 1 & 0 & 1 & -1 & 0 & 0 \\ 0 & \sqrt{2} & 0 & 0 & 0 & 0 & \sqrt{2} & 0 \\ -1 & 0 & -1 & 0 & 1 & 1 & 0 & 0 \end{bmatrix} \quad (\text{C.22})$$

$$d_\lambda = d_8 = -j\sqrt{2} \frac{A_{1,1}^k[0,0]}{A_{1,0}^k[0,0]} d_5 - \frac{A_{0,1}^k[0,0]}{A_{1,0}^k[0,0]} d_7, \quad (\text{C.23})$$

and subsequently,

$$\beta_\lambda = \begin{cases} -j\sqrt{2} \frac{A_{1,1}^k[0,0]}{A_{1,0}^k[0,0]}, & \lambda = 5 \\ -\frac{A_{0,1}^k[0,0]}{A_{1,0}^k[0,0]}, & \lambda = 7 \\ 0, & \text{otherwise.} \end{cases} \quad (\text{C.24})$$

Through this, \underline{X} of (4.29) can be written as

$$\underline{X} = \frac{1}{4} \begin{bmatrix} \underline{Q}_3 & \underline{X}_1^T & -\underline{X}_1^T & \underline{Q}_3 \\ \underline{X}_1 & \chi & -\chi & -\underline{X}_2 \\ -\underline{X}_1 & -\chi & \chi & \underline{X}_2 \\ \underline{Q}_3 & -\underline{X}_2^T & \underline{X}_2^T & \underline{Q}_3 \end{bmatrix}, \quad (\text{C.25})$$

where \underline{X}_1 , \underline{X}_2 and χ are given by

$$\underline{X}_1 = [-\sqrt{2}\beta_5 \quad 2\beta_7 \quad -\sqrt{2}\beta_5] \quad (\text{C.26a})$$

$$\underline{X}_2 = [\sqrt{2}\beta_5 \quad 2\beta_7 \quad \sqrt{2}\beta_5] \quad (\text{C.26b})$$

$$\chi = 2(\beta_5^2 + \beta_7^2 - 1). \quad (\text{C.26c})$$

c.3.2 Solution specific to isotropic PFFs

In [57], a solution specific for isotropic PFFs is given, which enables a multiplication free (de-)spreading of the transmitted and received data, as it only contains the elements -1 , 0 and 1 . However, this solution is only valid for $k = \text{even}$, as for $k = \text{odd}$ $\underline{\alpha}_{\tau_1, \nu \underline{c}_\Lambda}^k = 0$.

c.3.2.1 Even subcarriers

For isotropic pulse shapes and $k = \text{even}$, \underline{C} and d_Λ are defined according to

$$d_\Lambda = d_8 = -2 \frac{-jA_{1,1}^k[0,0]}{A_{1,0}^k[0,0] + A_{0,1}^k[0,0]} d_7 = j \frac{A_{1,1}^k[0,0]}{A_{1,0}^k[0,0]} d_7 \quad (\text{C.27})$$

$$\underline{C} = \frac{1}{2} \begin{bmatrix} 1 & 0 & 1 & 0 & 0 & 1 & 1 & 0 \\ 0 & 1 & 0 & 1 & 1 & 0 & 0 & -1 \\ 1 & 0 & -1 & 0 & 0 & -1 & 1 & 0 \\ 0 & 1 & 0 & -1 & -1 & 0 & 0 & -1 \\ 0 & 1 & 0 & 1 & -1 & 0 & 0 & 1 \\ -1 & 0 & 1 & 0 & 0 & -1 & 1 & 0 \\ 0 & 1 & 0 & -1 & 1 & 0 & 0 & 1 \\ -1 & 0 & -1 & 0 & 0 & 1 & 1 & 0 \end{bmatrix}. \quad (\text{C.28})$$

From this follows that

$$\beta_\lambda = \begin{cases} j \frac{A_{1,1}^k[0,0]}{A_{1,0}^k[0,0]}, & \lambda = 7 \\ 0, & \text{otherwise} \end{cases}. \quad (\text{C.29})$$

Through this, \underline{X} in (4.29) can be written as

$$\underline{X} = \frac{1}{4} \begin{bmatrix} \underline{X}_1 & \underline{X}_1 & \underline{X}_2 & \underline{X}_2 \\ \underline{X}_1 & \underline{X}_1 & \underline{X}_2 & \underline{X}_2 \\ \underline{X}_2^T & \underline{X}_2^T & \underline{R}^T \underline{X}_1 \underline{R} & \underline{R}^T \underline{X}_1 \underline{R} \\ \underline{X}_2^T & \underline{X}_2^T & \underline{R}^T \underline{X}_1 \underline{R} & \underline{R}^T \underline{X}_1 \underline{R} \end{bmatrix}, \quad (\text{C.30})$$

where \underline{X}_1 , \underline{X}_2 and the rotation matrix \underline{R} are given by

$$\underline{X}_1 = \begin{bmatrix} 0 & -\beta_7 \\ -\beta_7 & \beta_7^2 - 1 \end{bmatrix} \quad (\text{C.31a})$$

$$\underline{X}_2 = \begin{bmatrix} \beta_7 & 0 \\ -\beta_7^2 + 1 & -\beta_7 \end{bmatrix} \quad (\text{C.31b})$$

$$\underline{R} = \begin{bmatrix} 0 & 1 \\ -1 & 0 \end{bmatrix}. \quad (\text{C.31c})$$

c.3.2.2 Odd subcarriers

For isotropic pulse shapes and $k = \text{odd}$, \underline{C} and d_λ are defined according to

$$d_\lambda = d_8 = -2 \frac{-jA_{1,1}^k[0,0]}{A_{1,0}^k[0,0] - A_{0,1}^k[0,0]} d_7 = j \frac{A_{1,1}^k[0,0]}{A_{1,0}^k[0,0]} d_7 \quad (\text{C.32})$$

$$\underline{C} = \frac{1}{2} \begin{bmatrix} 1 & 0 & 1 & 0 & 0 & 1 & 1 & 0 \\ 0 & 1 & 0 & -1 & 1 & 0 & 0 & 1 \\ 1 & 0 & -1 & 0 & 0 & -1 & 1 & 0 \\ 0 & 1 & 0 & -1 & -1 & 0 & 0 & -1 \\ 0 & 1 & 0 & 1 & -1 & 0 & 0 & 1 \\ -1 & 0 & 1 & 0 & 0 & -1 & 1 & 0 \\ 0 & 1 & 0 & 1 & 1 & 0 & 0 & -1 \\ -1 & 0 & -1 & 0 & 0 & 1 & 1 & 0 \end{bmatrix}. \quad (\text{C.33})$$

Here, columns four and eight are swapped compared to the solution for even subcarriers. From this follows that

$$\beta_\lambda = \begin{cases} j \frac{A_{1,1}^k[0,0]}{A_{1,0}^k[0,0]}, & \lambda = 7 \\ 0, & \text{otherwise} \end{cases}. \quad (\text{C.34})$$

Through this, \underline{X} in (4.29) can be written as

$$\underline{X} = \frac{1}{4} \begin{bmatrix} \underline{X}_1 & \underline{X}_1 & \underline{X}_2 & \underline{X}_2 \\ \underline{X}_1 & \underline{X}_1 & \underline{X}_2 & \underline{X}_2 \\ \underline{X}_2^T & \underline{X}_2^T & \underline{R}^T \underline{X}_1 \underline{R} & \underline{R}^T \underline{X}_1 \underline{R} \\ \underline{X}_2^T & \underline{X}_2^T & \underline{R}^T \underline{X}_1 \underline{R} & \underline{R}^T \underline{X}_1 \underline{R} \end{bmatrix} \quad (\text{C.35})$$

where \underline{X}_1 , \underline{X}_2 and the rotation matrix \underline{R} are given by

$$\underline{X}_1 = \begin{bmatrix} 0 & -\beta_7 \\ -\beta_7 & \beta_7^2 - 1 \end{bmatrix} \quad (\text{C.36a})$$

$$\underline{X}_2 = \begin{bmatrix} \beta_7 & 0 \\ -\beta_7^2 + 1 & -\beta_7 \end{bmatrix} \quad (\text{C.36b})$$

$$\underline{R} = \begin{bmatrix} 0 & 1 \\ -1 & 0 \end{bmatrix}. \quad (\text{C.36c})$$

BIBLIOGRAPHY

- [1] J. Abdoli, M. Jia, and J. Ma. "Filtered OFDM: A new waveform for future wireless systems." In: *2015 IEEE 16th Int. Work. Signal Process. Adv. Wirel. Commun.* Vol. 2015-Augus. IEEE, June 2015, pp. 66–70. ISBN: 978-1-4799-1931-4. DOI: 10.1109/SPAWC.2015.7227001.
- [2] M. Alard. "Construction of a multicarrier signal." WO 96/35278. 1996.
- [4] J. Bazzi, P. Weitkemper, and K. Kusume. "Power efficient scattered pilot channel estimation for FBMC/OQAM." In: *SCC 2015; 10th Int. ITG Conf. Syst. Commun. Coding; Proc. VDE*, 2015, pp. 1–6.
- [5] M. G. Bellanger. "Specification and design of a prototype filter for filter bank based multicarrier transmission." In: *2001 IEEE Int. Conf. Acoust. Speech, Signal Process. Proc. (Cat. No.01CH37221)*. Vol. 4. IEEE, 2001, pp. 2417–2420. ISBN: 0-7803-7041-4. DOI: 10.1109/ICASSP.2001.940488.
- [6] P. Bello. "Characterization of Randomly Time-Variant Linear Channels." In: *IEEE Trans. Commun.* 11.4 (Dec. 1963), pp. 360–393. ISSN: 0096-2244. DOI: 10.1109/TCOM.1963.1088793.
- [7] B. Boashash. *Time Frequency Signal Analysis and Processing*. 2nd. Academic Press Inc, 2015, p. 1056. ISBN: 9780123984999.
- [8] H. Bölcskei. "Efficient design of pulse-shaping filters for OFDM systems." In: *Proc. SPIE Wavelet Appl. Signal Image Process. VII*. Ed. by M. A. Unser, A. Aldroubi, and A. F. Laine. Vol. 3813. July 1999. Oct. 1999, pp. 625–636. DOI: 10.1117/12.366818.
- [9] H. Bölcskei. "Orthogonal Frequency Division Multiplexing Based on Offset QAM." In: *Adv. Gabor Anal.* Ed. by H. G. Feichtinger and T. Strohmer. Boston, MA: Birkhäuser Boston, 2003, pp. 321–352. ISBN: 978-1-4612-0133-5. DOI: 10.1007/978-1-4612-0133-5_12.
- [10] R. W. Chang. "Synthesis of Band-Limited Orthogonal Signals for Multichannel Data Transmission." In: *Bell Syst. Tech. J.* 45.10 (1966), pp. 1775–1796. DOI: 10.1002/j.1538-7305.1966.tb02435.x.
- [11] *Channel models for HIPERLAN/2 in different indoor scenarios*. Tech. rep. EP BRAN 3ER1o85B. ETSI, 1998, pp. 1–8.
- [12] G. Cherubini, E. Eleftheriou, and S. Ölcer. "Filtered multitone modulation for VDSL." In: *Glob. Telecommun. Conf. 1999. GLOBECOM '99*. Rio de Janeiro: IEEE, 1999, pp. 1139–1144. DOI: 10.1109/GL0COM.1999.829951.

- [13] J.-M. Choi, Y. Oh, H. Lee, and J.-S. Seo. "Interference-dependent pair of pilots for channel estimation in FBMC systems." In: *2016 IEEE Int. Symp. Broadband Multimed. Syst. Broadcast.* IEEE, June 2016, pp. 1–4. ISBN: 978-1-4673-9044-6. DOI: 10.1109/BMSB.2016.7521983.
- [14] W. Cui, D. Qu, T. Jiang, and B. Farhang-Boroujeny. "Coded auxiliary pilots for channel estimation in FBMC-OQAM systems." In: *IEEE Trans. Veh. Technol.* 65.5 (May 2016), pp. 2936–2946. ISSN: 0018-9545. DOI: 10.1109/TVT.2015.2448659.
- [15] S. Das and P. Schniter. "Max-SINR ISI / ICI-Shaping Multicarrier Communication Over the Doubly Dispersive Channel." In: *IEEE Trans. Signal Process.* 55.12 (2007), pp. 5782–5795. DOI: 10.1109/TSP.2007.901660.
- [16] S. S. Das, E. De Carvalho, and R. Prasad. "Performance Analysis of OFDM Systems with Adaptive Sub Carrier Bandwidth." In: *IEEE Trans. Wirel. Commun.* 7.4 (Apr. 2008), pp. 1117–1122. ISSN: 1536-1276. DOI: 10.1109/TWC.2008.060761.
- [17] R. Datta, G. Fettweis, Z. Kollár, and P. Horváth. "FBMC and GFDM Interference Cancellation Schemes for Flexible Digital Radio PHY Design." In: *Digit. Syst. Des. (DSD), 2011 14th Euromicro Conf.* Oulu: IEEE, 2011, pp. 335–339. DOI: 10.1109/DSD.2011.48.
- [18] I. Daubechies. "The wavelet transform, time-frequency localization and signal analysis." In: *IEEE Trans. Inf. Theory* 36.5 (1990), pp. 961–1005. DOI: 10.1109/18.57199.
- [19] I. Daubechies, S. Jaffard, and J.-L. Journé. "A Simple Wilson Orthonormal Basis with Exponential Decay." In: *SIAM J. Math. Anal.* 22.2 (Mar. 1991), pp. 554–573. DOI: 10.1137/0522035.
- [20] *Deployment aspects (Release 10)*. Tech. rep. TR 25.943 V10.0.0. 3GPP, 2011, pp. 1–13.
- [21] *Digital Radio Mondiale (DRM); System Specification*. Tech. rep. ES 201 980 - V3.1.1. ETSI, 2009, pp. 1–221.
- [22] *Digital Video Broadcasting (DVB); Framing structure, channel coding and modulation for digital terrestrial television*. Tech. rep. EN 300 744 v1.6.1. ETSI, 2009, pp. 1–66.
- [23] J.-B. Doré, V. Berg, N. Cassiau, and D. Ktéas. "FBMC receiver for multi-user asynchronous transmission on fragmented spectrum." In: *EURASIP J. Adv. Signal Process.* 2014.1 (2014), p. 41. ISSN: 1687-6180. DOI: 10.1186/1687-6180-2014-41.
- [24] J. Du and S. Signell. "Pulse shape adaptivity in OFDM/OQAM systems." In: *Proc. 2008 Int. Conf. Adv. Infocomm Technol. - ICAIT '08*. New York, New York, USA: ACM Press, 2008, pp. 1–5. ISBN: 9781605580883. DOI: 10.1145/1509315.1509446.

- [25] S. E. El Ayoubi, M. Boldi, Ö. Bulakci, P. Spapis, M. Schellmann, P. Marsch, M. Säily, J. F. Monserrat, T. Rosowski, G. Zimmermann, I. D. Silva, M. Tesanovic, M. Shariat, and Ahmed M. Ibrahim. "Preliminary views and initial considerations on 5G RAN architecture and functional design." In: *White Pap. METIS II* (2016), pp. 1–27.
- [26] M. Failli. *Digital land mobile radio-communications*. Tech. rep. ICT COST Action 207. Commission of the European Communities, 1989, pp. 1–404.
- [27] Fang-ming Han and Xian-da Zhang. "Wireless multicarrier digital transmission via weyl-heisenberg frames over time-frequency dispersive channels." In: *IEEE Trans. Commun.* 57.6 (June 2009), pp. 1721–1733. ISSN: 0090-6778. DOI: 10.1109/TCOMM.2009.06.070406.
- [28] B. Farhang-Boroujeny. "OFDM Versus Filter Bank Multicarrier." In: *IEEE Signal Process. Mag.* 28.3 (May 2011), pp. 92–112. ISSN: 1053-5888. DOI: 10.1109/MSP.2011.940267.
- [29] B. Farhang-Boroujeny and C. (George) Yuen. "Cosine Modulated and Offset QAM Filter Bank Multicarrier Techniques: A Continuous-Time Prospect." In: *EURASIP J. Adv. Signal Process.* 2010.1 (Dec. 2010), p. 165654. ISSN: 1687-6180. DOI: 10.1155/2010/165654.
- [30] H. G. Feichtinger and T. Strohmer. *Gabor Analysis and Algorithms*. Ed. by H. G. Feichtinger and T. Strohmer. Boston, MA: Birkhäuser Boston, 1998. ISBN: 978-1-4612-7382-0. DOI: 10.1007/978-1-4612-2016-9.
- [31] G. Fettweis, M. Krondorf, and S. Bittner. "GFDM - Generalized Frequency Division Multiplexing." In: *VTC Spring 2009 - IEEE 69th Veh. Technol. Conf. IEEE*, Apr. 2009, pp. 1–4. ISBN: 9781424425174. DOI: 10.1109/VETECS.2009.5073571.
- [32] M. Fuhrwerk, S. Moghaddamnia, and J. Peissig. "Scattered pilot-based channel estimation for channel adaptive FBMC-OQAM systems." In: *IEEE Trans. Wirel. Commun.* 16.3 (Mar. 2017), pp. 1687–1702. ISSN: 1536-1276. DOI: 10.1109/TWC.2017.2651806.
- [33] M. Fuhrwerk and J. Peissig. "Capacity Gains for Single- and Multi-User CAW in FBMC-OQAM Systems." In: *IEEE Commun. Lett.* 22.1 (2018), pp. 61–64. DOI: 10.1109/LCOMM.2017.2761387.
- [34] M. Fuhrwerk, J. Peissig, and M. Schellmann. "Channel adaptive pulse shaping for OQAM-OFDM systems." In: *2014 22nd Eur. Signal Process. Conf.* Sept. 2014, pp. 181–185.
- [35] M. Fuhrwerk, J. Peissig, and M. Schellmann. "Performance comparison of CP-OFDM and OQAM-OFDM systems based on LTE parameters." In: *2014 IEEE 10th Int. Conf. Wirel. Mob. Comput. Netw. Commun. IEEE*, Oct. 2014, pp. 604–610. ISBN: 978-1-4799-5041-6. DOI: 10.1109/WiM0B.2014.6962232.

- [36] M. Fuhrwerk, J. Peissig, and M. Schellmann. "On the design of an FBMC based air interface enabling channel adaptive pulse shaping per sub-band." In: *2015 23rd Eur. Signal Process. Conf. IEEE, Aug. 2015*, pp. 384–388. DOI: 10.1109/EUSIPCO.2015.7362410.
- [37] T. Fusco, A. Petrella, and M. Tanda. "Data-aided symbol timing and CFO synchronization for filter bank multicarrier systems." In: *IEEE Trans. Wirel. Commun.* 8.5 (May 2009), pp. 2705–2715. ISSN: 1536-1276. DOI: 10.1109/TWC.2009.080860.
- [38] D. Gabor. "Theory of Communication. Part 1: The Analysis of Information." In: *J. Inst. Electr. Eng. - Part III Radio Commun. Eng.* 93.26 (Nov. 1946), pp. 429–441. ISSN: 2054-0604. DOI: 10.1049/ji-3-2.1946.0074.
- [39] I. Gaspar, N. Michailow, A. Navarro, E. Ohlmer, S. Krone, and G. Fettweis. "Low Complexity GFDM Receiver Based On Sparse Frequency Domain Processing." In: *Veh. Technol. Conf. (VTC Spring), 2013 IEEE 77th. IEEE, 2013*. DOI: 10.1109/VTCSpring.2013.6692619.
- [40] A. Goldsmith. *Wireless Communications*. Cambridge: Cambridge University Press, 2005. ISBN: 9780511841224. DOI: 10.1017/CB09780511841224.
- [41] K. Gröchenig. *Foundations of Time-Frequency Analysis*. Applied and Numerical Harmonic Analysis. Boston, MA: Birkhäuser Boston, 2001. ISBN: 978-1-4612-6568-9. DOI: 10.1007/978-1-4612-0003-1.
- [42] D. Guo, S. Shamai, and S. Verdú. "Mutual information and minimum mean-square error in Gaussian channels." In: *IEEE Trans. Inf. Theory* 51.4 (Apr. 2005), pp. 1261–1282. ISSN: 0018-9448. DOI: 10.1109/TIT.2005.844072. arXiv: 0412108 [cs].
- [43] R. Haas and J.-C. Belfiore. "Multiple carrier transmission with time-frequency well-localized impulses." In: *IEEE Second Symp. Commun. Veh. Technol. Benelux. 2. Univ. Catholique de Louvain, 1994*, pp. 187–193. DOI: 10.1109/SCVT.1994.574163.
- [44] F.-M. Han and X.-D. Zhang. "Hexagonal Multicarrier Modulation: A Robust Transmission Scheme for Time-Frequency Dispersive Channels." In: *IEEE Trans. Signal Process.* 55.5 (May 2007), pp. 1955–1961. DOI: 10.1109/TSP.2006.890884.
- [45] L. Hanzo, Y. J. Akhtman, L. Wang, and M. Jiang. *MIMO-OFDM for LTE, Wi-Fi and WiMAX*. Chichester, UK: John Wiley & Sons, Ltd, Oct. 2010. ISBN: 9780470711750. DOI: 10.1002/9780470711750.
- [46] F. Harris. "On the use of windows for harmonic analysis with the discrete Fourier transform." In: *Proc. IEEE* 66.1 (1978), pp. 51–83. ISSN: 0018-9219. DOI: 10.1109/PROC.1978.10837.

- [47] *IEEE Standard for Information technology -Telecommunications and information exchange between systems Local and metropolitan area networks - Specific requirements Part 11: Wireless LAN Medium Access Control (MAC) and Physical Layer (PHY) Specifications*, IEEE Std. 802.11-2012 2012.
- [48] *IMT Vision - Framework and overall objectives of the future development of IMT for 2020 and beyond*. Tech. rep. M.2083-0 (09/2015). Geneva: ITU-R, 2015.
- [49] J.-P. Javaudin, D. Lacroix, and A. Rouxel. "Pilot-aided channel estimation for OFDM/OQAM." In: *57th IEEE Semiannu. Veh. Technol. Conf. 2003. VTC 2003-Spring*. Vol. 3. 3. IEEE, 2003, pp. 1581–1585. ISBN: 0-7803-7757-5. DOI: 10.1109/VETECS.2003.1207088.
- [50] Jérôme Louveaux, L. Baltar, D. S. Waldhauser, M. Renfors, M. Tanda, C. Bader, and E. Kofidis. *Equalization and demodulation in the receiver (single antenna)*. Tech. rep. ICT-211887 PHYDYAS Deliverable D3.1. EU Project, 2008, pp. 1–59.
- [51] R. Kattenbach. *Charakterisierung zeitvarianter Indoor-Funkkanäle anhand ihrer System- und Korrelationsfunktionen*. Shaker Verlag, 1997. ISBN: 3826528727.
- [52] E. Kofidis. "Channel estimation in filter bank-based multicarrier systems: Challenges and solutions." In: *2014 6th Int. Symp. Commun. Control Signal Process*. IEEE, May 2014, pp. 453–456. ISBN: 978-1-4799-2890-3. DOI: 10.1109/ISCCSP.2014.6877911.
- [53] E. Kofidis, D. Katselis, A. Rontogiannis, and S. Theodoridis. "Preamble-based channel estimation in OFDM/OQAM systems: A review." In: *Signal Processing* 93:7 (July 2013), pp. 2038–2054. ISSN: 01651684. DOI: 10.1016/j.sigpro.2013.01.013. arXiv: 1306.2581.
- [54] W. Kozek and A. F. Molisch. "Nonorthogonal pulseshapes for multicarrier communications in doubly dispersive channels." In: *IEEE J. Sel. Areas Commun.* 16:8 (1998), pp. 1579–1589. ISSN: 07338716. DOI: 10.1109/49.730463.
- [55] B. Le Floch, M. Alard, and C. Berrou. "Coded orthogonal frequency division multiplex [TV broadcasting]." In: *Proc. IEEE* 83:6 (June 1995), pp. 982–996. ISSN: 00189219. DOI: 10.1109/5.387096.
- [56] C. Lélé. "Iterative scattered-based channel estimation method for OFDM/OQAM." In: *EURASIP J. Adv. Signal Process.* 2012:1 (2012), p. 42. ISSN: 1687-6180. DOI: 10.1186/1687-6180-2012-42.
- [57] C. Lélé, J.-P. Javaudin, R. Legouable, A. Skrzypczak, and P. Siohan. "Channel estimation methods for preamble-based OFDM/OQAM modulations." In: *Eur. Trans. Telecommun.* 19:7 (Nov. 2008), pp. 741–750. ISSN: 1124318X. DOI: 10.1002/ett.1332.

- [58] C. L el e, R. Legouable, and P. Siohan. "Channel estimation with scattered pilots in OFDM/OQAM." In: *2008 IEEE 9th Work. Signal Process. Adv. Wirel. Commun.* 2. IEEE, July 2008, pp. 286–290. ISBN: 978-1-4244-2045-2. DOI: 10.1109/SPAWC.2008.4641615.
- [59] A. D. Liveris and C. N. Georghiades. "Exploiting Faster-Than-Nyquist Signaling." In: *IEEE Trans. Commun.* 51.9 (2003), pp. 1502–1511. DOI: 10.1109/TCOMM.2003.816943.
- [60] *LTE physical layer; General description (Release 9)*, 3GPP Std. TS 36.201 v9.1.0 2010.
- [61] K. W. Martin. "Small side-lobe filter design for multitone data-communication applications." In: *IEEE Trans. Circuits Syst. II Analog Digit. Signal Process.* 45.8 (1998), pp. 1155–1161. ISSN: 10577130. DOI: 10.1109/82.718830.
- [62] G. Matz, H. B olcskei, and F. Hlawatsch. "Time-Frequency Foundations of Communications: Concepts and Tools." In: *IEEE Signal Process. Mag.* 30.6 (Nov. 2013), pp. 87–96. ISSN: 1053-5888. DOI: 10.1109/MSP.2013.2269702.
- [63] G. Matz and F. Hlawatsch. "Fundamentals of Time-Varying Communication Channels." In: *Wirel. Commun. Over Rapidly Time-Varying Channels*. Elsevier, 2011, pp. 1–63. ISBN: 9780123744838. DOI: 10.1016/B978-0-12-374483-8.00001-7.
- [64] G. Matz, D. Schafhuber, K. Grochenig, M. Hartmann, and F. Hlawatsch. "Analysis, Optimization, and Implementation of Low-Interference Wireless Multicarrier Systems." In: *IEEE Trans. Wirel. Commun.* 6.5 (May 2007), pp. 1921–1931. ISSN: 1536-1276. DOI: 10.1109/TWC.2007.360393.
- [65] X. Mestre and E. Kofidis. "Pilot-based channel estimation for FBMC/OQAM systems under strong frequency selectivity." In: *2016 IEEE Int. Conf. Acoust. Speech Signal Process.* IEEE, Mar. 2016, pp. 3696–3700. ISBN: 978-1-4799-9988-0. DOI: 10.1109/ICASSP.2016.7472367.
- [66] S. Mirabbasi and K. Martin. "Design of prototype filter for near-perfect-reconstruction overlapped complex-modulated transmultiplexers." In: *2002 IEEE Int. Symp. Circuits Syst. Proc. (Cat. No.02CH37353)*. Vol. 1. IEEE, 2002, pp. I-821–I-824. ISBN: 0-7803-7448-7. DOI: 10.1109/ISCAS.2002.1009967.
- [67] A. F. Molisch. *Wireless Communications*. 2nd. Wiley - IEEE, 2010, pp. 1–827. ISBN: 9781119992806.
- [68] N. Moret and A. M. Tonello. "Design of orthogonal filtered multitone modulation systems and comparison among efficient realizations." In: *EURASIP J. Adv. Signal Process.* 2010 (2010), pp. 1–19. ISSN: 1687-6172. DOI: 10.1155/2010/141865.
- [69] H. Nam, M. Choi, S. Han, C. Kim, S. Choi, and D. Hong. "A New Filter-Bank Multicarrier System With Two Prototype Filters for QAM Symbols Transmission and Reception." In: *IEEE Trans. Wirel. Commun.* 15.9 (Sept. 2016), pp. 5998–6009. DOI: 10.1109/TWC.2016.2575839.

- [70] H. Nam, M. Choi, C. Kim, D. Hong, and S. Choi. "A New Filter-Bank Multicarrier System for QAM Signal Transmission and Reception." In: *ICC 2014*. 2014, pp. 5227–5232. ISBN: 9781479920037.
- [3] NGMN. *5G White Paper*. Tech. rep. 2015.
- [71] R. Nissel and M. Rupp. "On pilot-symbol aided channel estimation in FBMC-OQAM." In: *2016 IEEE Int. Conf. Acoust. Speech Signal Process.* IEEE, Mar. 2016, pp. 3681–3685. ISBN: 978-1-4799-9988-0. DOI: 10.1109/ICASSP.2016.7472364.
- [72] R. Nissel and M. Rupp. "OFDM and FBMC-OQAM in Doubly-Selective Channels: Calculating the Bit Error Probability." In: *IEEE Commun. Lett.* 21.6 (2017), pp. 1297–1300. ISSN: 10897798. DOI: 10.1109/LCOMM.2017.2677941.
- [73] R. Nissel, S. Schwarz, and M. Rupp. "Filter Bank Multicarrier Modulation Schemes for Future Mobile Communications." In: *IEEE J. Sel. Areas Commun.* 35.8 (Aug. 2017), pp. 1768–1782. DOI: 10.1109/JSAC.2017.2710022.
- [74] A. Osseiran, F. Boccardi, V. Braun, K. Kusume, P. Marsch, M. Maternia, O. Queuth, M. Schellmann, H. Schotten, H. Taoka, H. Tullberg, M. A. Uusitalo, B. Timus, and M. Fallgren. "Scenarios for 5G mobile and wireless communications: the vision of the METIS project." In: *IEEE Commun. Mag.* 52.5 (May 2014), pp. 26–35. ISSN: 0163-6804. DOI: 10.1109/MCOM.2014.6815890.
- [75] *Physical channels and modulation (Release 12)*. Tech. rep. TS 36.211 v12.3.0. ETSI, 2014, pp. 1–126.
- [76] J. Proakis. *Digital Communications*. 3rd. McGraw-Hill Inc., 1995. ISBN: 9780071138147.
- [77] *Radio frequency (RF) system scenarios (Release 13)*. Tech. rep. TR 36.942 v13.0.0. 3GPP, 2016, pp. 1–109.
- [78] M. Renfors, X. Mestre, E. Kofidis, and F. Bader. *Orthogonal Waveforms and Filter Banks for Future Communication Systems*. 1st. Academic Press Inc, 2017, p. 590. ISBN: 978-0-12-810384-5.
- [79] C. Roche and P. Siohan. "A Family of Extended Gaussian Functions with a Nearly Optimal Localization Property." In: *Multi-Carrier Spread-Spectrum*. Boston, MA: Springer US, 1997, pp. 179–186. ISBN: 978-1-4615-6231-3. DOI: 10.1007/978-1-4615-6231-3_21.
- [80] F. Rusek and J. B. Anderson. "The Two Dimensional Mazo Limit." In: *Inf. Theory, 2005. ISIT 2005. Proceedings. Int. Symp.* Adelaide: IEEE, 2005. DOI: 10.1109/ISIT.2005.1523482.
- [81] F. Rusek and J. B. Anderson. "Successive Interference Cancellation in Multistream Faster-than-Nyquist Signaling Categories and Subject Descriptors." In: *Proc. 2006 Int. Conf. Wirel. Commun. Mob. Comput.* 2. Vancouver, 2006, pp. 1021–1026. DOI: 10.1145/1143549.1143753.

- [82] F. Rusek and J. B. Anderson. "Multistream Faster than Nyquist Signaling." In: *IEEE Trans. Commun.* 57.5 (2009), pp. 1329–1340. DOI: 10.1109/TCOMM.2009.05.070224.
- [83] A. Sahin, I. Guvenc, and H. Arslan. "A Survey on Multicarrier Communications: Prototype Filters, Lattice Structures, and Implementation Aspects." In: *IEEE Commun. Surv. Tutorials* 16.3 (2014), pp. 1312–1338. ISSN: 1553-877X. DOI: 10.1109/SURV.2013.121213.00263. arXiv: 1212.3374.
- [84] B. R. Saltzberg. "Performance of an Efficient Parallel Data Transmission System." In: *IEEE Trans. Commun. Technol.* 15.6 (1967), pp. 805–811. DOI: 10.1109/TCOM.1967.1089674.
- [85] F. Schaich and T. Wild. "Subcarrier spacing - a neglected degree of freedom?" In: *2015 IEEE 16th Int. Work. Signal Process. Adv. Wirel. Commun.* (June 2015), pp. 56–60. DOI: 10.1109/SPAWC.2015.7226999.
- [86] F. Schaich, T. Wild, and R. Ahmed. "Subcarrier Spacing - How to Make Use of This Degree of Freedom." In: *2016 IEEE 83rd Veh. Technol. Conf. (VTC Spring)*. Vol. 2016-July. IEEE, May 2016, pp. 1–6. ISBN: 978-1-5090-1698-3. DOI: 10.1109/VTCspring.2016.7504496.
- [87] M. Schellmann, Z. Zhao, H. Lin, P. Siohan, N. Rajatheva, V. Luecken, and A. Ishaque. "FBMC-based air interface for 5G mobile: Challenges and proposed solutions." In: *Proc. 9th Int. Conf. Cogn. Radio Oriented Wirel. Networks*. i. ICST, 2014, pp. 102–107. ISBN: 978-1-63190-003-7. DOI: 10.4108/icst.crowncom.2014.255708.
- [88] Seong Taek Chung and A. Goldsmith. "Degrees of freedom in adaptive modulation: a unified view." In: *IEEE Trans. Commun.* 49.9 (2001), pp. 1561–1571. ISSN: 00906778. DOI: 10.1109/26.950343.
- [89] C. E. Shannon. "Communication in the Presence of Noise." In: *Proc. IRE* 37.1 (Jan. 1949), pp. 10–21. ISSN: 0096-8390. DOI: 10.1109/JRPROC.1949.232969.
- [90] C. Siclet and P. Siohan. "Design of BFDN/OQAM systems based on biorthogonal modulated filter banks." In: *Globecom '00 - IEEE. Glob. Telecommun. Conf.* Vol. 2. IEEE, 2000, pp. 701–705. ISBN: 0-7803-6451-1. DOI: 10.1109/GLOCOM.2000.891230.
- [91] M. K. Simon and M.-S. Alouini. *Digital Communication Over Fading Channels*. New York, USA: John Wiley & Sons, Inc., 2000, pp. 1–550. ISBN: 0471317799. DOI: 10.1002/0471200697.
- [92] P. Siohan and C. Roche. "Cosine-modulated filterbanks based on extended Gaussian functions." In: *IEEE Trans. Signal Process.* 48.11 (2000), pp. 3052–3061. ISSN: 1053587X. DOI: 10.1109/78.875463.
- [93] P. Siohan, C. Siclet, and N. Lacaille. "Analysis and design of OFDM/OQAM systems based on filterbank theory." In: *IEEE Trans. Signal Process.* 50.5 (May 2002), pp. 1170–1183. ISSN: 1053587X. DOI: 10.1109/78.995073.

- [94] T. Starr, J. M. Cioffi, and P. J. Silverman. *Understanding Digital Subscriber Line Technology*. Prentice Hall PTR, 1999. ISBN: 0-13-780545-4.
- [95] T. H. Stitz, T. Ihalainen, A. Viholainen, and M. Renfors. "Pilot-based synchronization and equalization in filter bank multicarrier communications." In: *EURASIP J. Adv. Signal Process.* 2010 (2010), pp. 1–19. ISSN: 1687-6172. DOI: 10.1155/2010/741429.
- [96] T. Strohmer and S. Beaver. "Optimal OFDM design for time-frequency dispersive channels." In: *IEEE Trans. Commun.* 51.7 (July 2003), pp. 1111–1122. ISSN: 0090-6778. DOI: 10.1109/TCOMM.2003.814200.
- [97] C. Thein, M. Schellmann, and J. Peissig. "Analysis of frequency domain frame detection and synchronization in OQAM-OFDM systems." In: *EURASIP J. Adv. Signal Process.* 2014.1 (2014), p. 83. ISSN: 1687-6180. DOI: 10.1186/1687-6180-2014-83.
- [98] *User Equipment (UE) radio transmission and reception (Release 13)*. Tech. rep. TS 36.101 v13.3.0. 3GPP, 2013, pp. 1–931.
- [99] V. Vakilian, T. Wild, F. Schaich, S. ten Brink, and J.-F. Frigon. "Universal-filtered multi-carrier technique for wireless systems beyond LTE." In: *2013 IEEE Globecom Work. (GC Wkshps)*. Dec. 2013, pp. 223–228. ISBN: 978-1-4799-2851-4. DOI: 10.1109/GLOCOMW.2013.6824990.
- [100] A. Viholainen, M. Bellanger, and M. Huchard. *Prototype filter and structure optimization*. Tech. rep. ICT-211887 PHYDYAS Deliverable D5.1. EU Project, 2009, pp. 1–102.
- [101] D. S. Waldhauser, L. G. Baltar, and J. A. Nossek. "MMSE subcarrier equalization for filter bank based multicarrier systems." In: *2008 IEEE 9th Work. Signal Process. Adv. Wirel. Commun. ICI. IEEE*, July 2008, pp. 525–529. ISBN: 978-1-4244-2045-2. DOI: 10.1109/SPAWC.2008.4641663.
- [102] X. Wang, T. Wild, and F. Schaich. "Universal Filtered Multi-Carrier with Leakage-Based Filter Optimization." In: *Eur. Wirel. 2014; 20th Eur. Wirel. Conf. Proc. VDE*, 2014, pp. 963–967. ISBN: 9783800736218.
- [103] X. Wang, T. Wild, and F. Schaich. "Filter Optimization for Carrier-Frequency- and Timing-Offset in Universal Filtered Multi-Carrier Systems." In: *2015 IEEE 81st Veh. Technol. Conf. (VTC Spring)*. Barcelona: IEEE, May 2015, pp. 1–6. ISBN: 978-1-4799-8088-8. DOI: 10.1109/VTCSpring.2015.7145842.
- [104] S. B. Weinstein and P. M. Ebert. "Transmission Frequency-Division." In: *IEEE Trans. Commun. Technol.* 19.5 (1971), pp. 628–634. DOI: 10.1109/TCOM.1971.1090705.

- [105] T. A. Weiss and F. K. Jondral. "Spectrum pooling: an innovative strategy for the enhancement of spectrum efficiency." In: *IEEE Commun. Mag.* 42.3 (Mar. 2004), pp. 8–14. DOI: 10.1109/MCOM.2004.1273768.
- [106] T. Wild, F. Schaich, and Y. Chen. "5G air interface design based on Universal Filtered (UF-)OFDM." In: *2014 19th Int. Conf. Digit. Signal Process.* August. IEEE, Aug. 2014, pp. 699–704. ISBN: 978-1-4799-4612-9. DOI: 10.1109/ICDSP.2014.6900754.
- [107] G. Wunder, P. Jung, M. Kasparick, T. Wild, F. Schaich, Y. Chen, S. Brink, I. Gaspar, N. Michailow, A. Festag, L. Mendes, N. Cassiau, D. Ktenas, M. Dryjanski, S. Pietrzyk, B. Eged, P. Vago, and F. Wiedmann. "5GNOW: Non-orthogonal, asynchronous waveforms for future mobile applications." In: *IEEE Commun. Mag.* 52.2 (Feb. 2014), pp. 97–105. ISSN: 0163-6804. DOI: 10.1109/MCOM.2014.6736749.
- [108] G. Wunder, M. Kasparick, T. Wild, F. Schaich, Y. Chen, M. Dryjanski, M. Buczkowski, S. Pietrzyk, N. Michailow, M. Matthe, I. Gaspar, L. Mendes, A. Festag, G. Fettweis, J.-B. Doré, N. Cassiau, D. Ktenas, V. Berg, B. Eged, and P. Vago. "5GNOW: Intermediate frame structure and transceiver concepts." In: *2014 IEEE Globecom Work. (GC Wkshps)*. IEEE, Dec. 2014, pp. 565–570. ISBN: 978-1-4799-7470-2. DOI: 10.1109/GLOCOMW.2014.7063492.
- [109] T. W. Yoon, S. B. Im, S. H. Hwang, and H. J. Choi. "Pilot structure for high data rate in OFDM/OQAM-IOTA system." In: *2008 IEEE 68th Veh. Technol. Conf.* IEEE, Sept. 2008, pp. 1–5. ISBN: 978-1-4244-1721-6. DOI: 10.1109/VETECF.2008.227.
- [110] Y. H. Yun, C. Kim, K. Kim, Z. Ho, B. Lee, and J.-Y. Seol. "A new waveform enabling enhanced QAM-FBMC systems." In: *2015 IEEE 16th Int. Work. Signal Process. Adv. Wirel. Commun.* Vol. 2015-Augus. IEEE, June 2015, pp. 116–120. ISBN: 978-1-4799-1931-4. DOI: 10.1109/SPAWC.2015.7227011.
- [111] R. Zakaria and D. Le Ruyet. "On Maximum Likelihood MIMO Detection in QAM-FBMC Systems ." In: *Pers. Indoor Mob. Radio Commun. (PIMRC), 2010 IEEE 21st Int. Symp.* Istanbul, 2010, pp. 183–187. ISBN: 9781424480166. DOI: 10.1109/PIMRC.2010.5671632.
- [112] R. Zakaria and D. Le Ruyet. "A novel filter-bank multicarrier scheme to mitigate the intrinsic interference: Application to MIMO systems." In: *IEEE Trans. Wirel. Commun.* 11.3 (Mar. 2012), pp. 1112–1123. ISSN: 1536-1276. DOI: 10.1109/TWC.2012.012412.110607.
- [113] X. Zhang, M. Jia, L. Chen, J. Ma, and J. Qiu. "Filtered-OFDM - Enabler for Flexible Waveform in The 5th Generation Cellular Networks." In: *2015 IEEE Glob. Commun. Conf.* San Diego: IEEE, 2015. DOI: 10.1109/GLOCOM.2015.7417854.
- [114] Z. Zhao, M. Schellmann, Q. Wang, X. Gong, R. Boehnke, and W. Xu. "Pulse shaped OFDM for asynchronous uplink access." In: *2015 49th Asilomar Conf. Sig-*

- nals, Syst. Comput.* Vol. 2015. 1. IEEE, Nov. 2015, pp. 3–7. ISBN: 978-1-4673-8576-3. DOI: 10.1109/ACSSC.2015.7421048.
- [115] Z. Zhao, N. Vucic, and M. Schellmann. “A simplified scattered pilot for FBM-C/OQAM in highly frequency selective channels.” In: *2014 11th Int. Symp. Wirel. Commun. Syst.* IEEE, Aug. 2014, pp. 819–823. ISBN: 978-1-4799-5863-4. DOI: 10.1109/ISWCS.2014.6933466.

INDEX

- Ambiguity function, 26, 83
 - phase shifted, 26
- Balian-Low theorem, 12, 17
- Biorthogonality condition, 12
- Channel (linear), 7
- Channel adaptivity schemes, 19
 - Adaptive Subcarrier Bandwidth (ASB), 20
 - Channel Adaptive Loading (CAL), 20
 - Channel Adaptive Modulation and coding (CAM), 19
 - Channel Adaptive Pulse Shaping (CAPS), 20, 59
 - Channel Adaptive Subcarrier Spacing (CASS), 20, 21
 - Channel Adaptive Waveform (CAW), 20
- Channel capacity, 59
 - CP-OFDM, 59
 - FBMC-OQAM, 59
 - heterogenous CAW, 85
 - homogeneous CAW, 61
- Channel delay
 - maximum, 10
 - mean, 10
 - spread, 10
- Channel estimation error, 64
 - AP, 66
 - DS, 72
 - maximum, 77
- Channel scattering function, 9
 - Rayleigh fading, 42, 85
- Characteristic functions
 - Channel spreading function, 7
 - Doppler-variant Channel Transfer Function (CTF), 8
 - Time-variant Channel Impulse Response (CIR), 8
 - Time-variant Channel Transfer Function (CTF), 8
- Cosine-modulated MultiTone (CMT), 17
- Delay-Doppler product, 44
- Demodulation, 11, 24, 83, 93, 104, 108
- Direction parameter, 14, 31
 - normalized, 14, 31, 47
- Doppler Power Spectral Density (DPSD)
 - Jakes, 42
- Doppler Power Spectral Density (DPSD), 9
- Doppler shift, 44
 - maximum, 10
 - mean, 10
 - spread, 10
- Effective channel coefficient, 26, 83, 93, 105, 108
- Faster Than Nyquist (FTN), 18
- FilterBank MultiCarrier (FBMC)
 - FBMC-OQAM, 17, 27
 - FBMC-QAM, 17
 - FFT-FBMC, 17
- Filtered MultiTone (FMT), 17
- Generalized Frequency-Division Multiplexing (GFDM), 18
- Guard bands, 85, 87, 91
- Heisenberg-Gabor uncertainty, 30

- Interference mitigation schemes
 - Auxiliary Pilot (AP), 63, 65
 - Basic Iterative Interference Mitigation (BIIM), 63
 - Composite Pilot Pairs (CPP), 63
 - Data Spreading (DS), 63, 70
 - Pilot Clustering (PC), 63
 - Pairs of Pilots (POP), 63
- Lattice staggering, 13, 17
- Least Squares (LS) estimator, 64
- Matched filtering, 14
- Orthogonal Frequency-Division
 - Multiplexing (OFDM), 15
 - Cyclic Prefix (CP), 16, 28, 36
 - Discrete Fourier Transform (DFT) spread, 16
 - Filtered OFDM (F-OFDM), 16
 - Lattice-OFDM (LOFDM), 21
 - Non-Contiguous OFDM (NC-OFDM), 17, 31
 - plain, 15, 28
 - Pulse-shaped OFDM (P-OFDM), 17, 21
 - Single-Carrier Frequency-Division Multiple Access (SC-FDMA), 16
 - windowed, 16
 - Zero-Padded (ZP), 16
- Prototype Filter Function (PFF)
 - band-limited, 29
 - localized, 30
 - time-limited, 29
- PFF energy spread, 15, 47
 - Frequency Domain (FD) spread, 15
 - isotropic, 15
 - Time Domain (TD) spread, 15
- Prototype Filter Function (PFF) Types
 - Blackman (exact), 29
 - Gaussian, 30
 - Hamming, 29
 - Hanning, 29
 - Hermite, 30, 36
 - PHYDYAS, 29, 31
 - Rectangular, 29, 36
 - EGF, 30, 31
 - IOTA, 30, 31
 - Raised Cosine (RC), 30
 - Root Raised Cosine (RRC), 30
 - Cardinal sine (sinc), 30
- Power Delay Profile (PDP), 9
 - Exponential decay, 42
- Reconstruction performance, 39, 49, 84
- Signal-to-Interference-plus-Noise Ratio (SINR), 13
- Signal-to-Interference Ratio (SIR), 39, 49, 77, 84
 - CP-OFDM, 39
 - FBMC-OQAM, 39
- Staggered MultiTone (SMT), 17
- System adaptation, 14
 - Lattice, 14
 - Prototype Filter Function (PFF), 14
- Time-Frequency (T-F) correlation function, 8
- Time-Frequency (T-F)-localization, 30
- Time-Frequency (T-F)-logon, 10
- Universal-Filtered MultiCarrier (UFMC), 16, 21
- Weyl-Heisenberg (WH) set, 11
- Wide Sense Stationary Uncorrelated Scattering (WSSUS), 8

LIST OF FIGURES

Figure 2.1	Subset of characteristic functions, parameters and relationships of WSSUS communication channels used within this thesis.	11
Figure 2.2	Sampling of the T-F plane.	12
Figure 2.3	Classification of popular MC modulation schemes based on T-F grid, PFF localization and orthogonality.	16
Figure 2.4	System complexity categorization of channel adaptivity schemes based on the utilized degrees of freedom.	19
Figure 3.1	Generic discrete-time and filtering (convolution) based transceiver chain for a (bi-)orthogonal multicarrier scheme.	24
Figure 3.2	Sets of lattice position for TX symbols (left) and the ones related to the RX symbol at position (\tilde{m}, \tilde{k}) (right).	25
Figure 3.3	Sign change patterns of the intrinsic interference in FBMC-OQAM systems.	28
Figure 3.4	Ambiguity functions and the related transfer functions $F(\nu) = \mathcal{F}_n\{f[n]\}$ for PHYDYAS PFFs with $\gamma = [3, 5]$	32
Figure 3.5	Ambiguity functions for EGF PFFs with $\gamma = [3, 5]$ and $\alpha \in \{1, 2, 3\}$ as well as the related transfer functions $F(\nu) = \mathcal{F}_n\{f[n]\}$	35
Figure 3.6	Ambiguity functions for Hermite PFFs with $\gamma = [3, 5]$ and the related transfer functions $F(\nu) = \mathcal{F}_n\{f[n]\}$	37
Figure 3.7	Ambiguity functions for rectangular PFFs with $T_{CP}/T \in \{0, 0.25\}$ and the related transfer functions $F(\nu) = \mathcal{F}_n\{f[n]\}$	38
Figure 3.8	Reconstruction performance of FBMC-OQAM systems with different PFFs in dependence on the overlapping factor γ in an AWGN channel.	41
Figure 3.9	SIR in dB for CP-OFDM with $T_{CP}/T = 0.07$ and FBMC-OQAM for overlapping factor $\gamma = 4$, $K = 256$ and different PFFs.	43
Figure 3.10	SIR in doubly dispersive channels including considerations for CAW.	46
Figure 4.1	SIR of FBMC-OQAM systems in dependence on symbol duration T and channel scenarios s_c	50
Figure 4.2	Work flow for the determination of practically relevant BER and SINR values for Rayleigh fading channels.	53
Figure 4.3	BER of FBMC-OQAM systems with selected modulation order M in dependence on symbol duration T and channel scenarios s_c	56
Figure 4.4	SIR and related channel capacity C of FBMC-OQAM systems in dependence on symbol duration T and channel scenarios s_c	60

Figure 4.5	Channel capacity C for an FBMC-OQAM system with the symbol duration of LTE T_{LTE} (crosshatched) in comparison with the one for optimized symbol durations T_{opt} in different channel scenarios.	62
Figure 4.6	Allocation pattern of pilot $p_{m,k}$ and AP $\rho_{m,k}$ for $(\mu_a, \kappa_a) = (1, 0)$, respectively.	65
Figure 4.7	Scattered pilot based channel estimation error of FBMC-OQAM systems for AP interference mitigation operating in various channel environments with $K = 256$, $\gamma = 4$, $b = 1$ and $(\mu_a, \kappa_a) = (1, 0)$	69
Figure 4.8	Allocation and index pattern of pilot and data symbols for the DS scheme.	71
Figure 4.9	Scattered pilot based channel estimation error $\varepsilon_{\text{H,DS}}$ of FBMC-OQAM systems with DS interference mitigation operating in various channel environments with $K = 256$, $\gamma = 4$ and $b = 1$	74
Figure 4.10	Comparison of analytical and Monte-Carlo simulations based channel estimation error ε_{H} for FBMC-OQAM systems, utilizing scattered pilots with pilot boost factor $b = 1$ operating in channel scenarios A to C (cf. Table 4.11).	76
Figure 4.11	Comparison of BERs for FBMC-OQAM systems with perfect and imperfect CSIR, utilizing scattered pilots with pilot boost factor $b = 1$ operating in channel scenarios A to C (cf. Table 4.11).	78
Figure 5.1	Exemplary lattice grids of users with different subcarrier spacing.	81
Figure 5.2	Mapping of the user specific lattice grids of Figure 5.1 onto the virtual lattice grid.	82
Figure 5.3	Channel capacity gains C_g for a heterogeneous FBMC-OQAM cell with two system configurations.	89
Figure 5.4	Utilization of channel capacity gains C_{eff} for a heterogeneous FBMC-OQAM cell with two different system configurations.	91
Figure 5.5	Example for two asynchronous users and their lattice grids.	92
Figure 5.6	Exemplary results for the interference in scenario 6 with $\sigma_T = 1$ (cf. Tables 5.2 to 5.5)	97
Figure A.1	Lattice positions of inherent and forced real-field orthogonality.	104

LIST OF TABLES

Table 3.1	Coefficients for the parametrization of the PHYDYAS PFF given in (3.23) and the resulting direction and T-F localization parameters.	31
Table 3.2	Direction and T-F localization parameters for the EGF PFF with $\alpha \in \{1, 2, 3\}$ and $\gamma \in [3, 5]$	33
Table 3.3	Weighting factors q_{4i} for the calculation of the Hermite PFF given in (3.26).	36
Table 3.4	Direction and T-F localization parameters of the Hermite PFF for $\gamma \in [3, 5]$	36
Table 3.5	PFF energy spreadKey characteristics of the PFFs discussed in Section 3.3	47
Table 4.1	SIR for an FBMC-OQAM or CP-OFDM based LTE system operating in channel scenarios s_c	51
Table 4.2	SIR and corresponding $\tau_{\text{rms}}/T_{\text{opt}}$ in dependence on PFFs and channel scenarios.	51
Table 4.3	Approximated SINR values in AWGN and Rayleigh fading channels and the related uncoded BERs required for $> 90\%$ throughput for certain LTE MCSs according to [77].	54
Table 4.4	Target SINR and the related minimum SIR values for 1% and 10% SINR tolerance (SINR_e) for an uncoded BER of $5 \cdot 10^{-2}$ in Rayleigh fading channels.	54
Table 4.5	Estimated available modulation order M in dependence on the channel scenario and SINR tolerances.	54
Table 4.6	BERs floors for FBMC-OQAM and CP-OFDM systems with LTE or channel specific symbol duration operating in channel scenarios s_c	57
Table 4.7	Equivalent SINR for the obtained BER values and the SINR estimation error ΔSINR	57
Table 4.8	$C_{\text{LTE}}^{s_c}$ (and SIR) for an FBMC-OQAM or CP-OFDM based LTE system operating in channel scenarios s_c	59
Table 4.9	SIR and $C_{\text{opt}}^{s_c}$ and corresponding $\tau_{\text{rms}}/T_{\text{opt}}$ in dependence on PFFs and channel scenarios.	61
Table 4.10	Approximated SIR values for a target uncoded BER of $5 \cdot 10^{-2}$ for an LTE system operating in a Rayleigh fading channel (cf. Table 4.4) and the related maximum channel estimation error $\varepsilon_{H,\text{max}}$ for $\text{SINR} = \text{SIR}$	77

Table 4.11	Selected scenarios for the performance evaluation at 800 MHz carrier frequency including the theoretically obtained M-QAM based on the approximated SIR as well as the applied M-QAM limited by the channel estimation error $\varepsilon_{H,\max}$	79
Table 5.1	Parameter setup for the evaluation of the capacity gains in a multi-user CAW scenario.	88
Table 5.2	System configurations for heterogeneous CAW in DL for fairness factor $\gamma_f = 1$	90
Table 5.3	System configurations for heterogeneous CAW in DL for fairness factor $\gamma_f = 1$ and variable base symbol durations $\sigma_T T_{\text{LTE}}$	90
Table 5.4	System configurations for heterogeneous CAW in UL for fairness factor $\gamma_f = 1$	95
Table 5.5	System configurations for heterogeneous CAW in UL for fairness factor $\gamma_f = 1$ and variable base symbol durations $\sigma_T T_{\text{LTE}}$	95
Table B.1	Reduced complexity channel models derived from [20]	111
Table B.2	Channel scenarios and the resulting delay-Doppler products δ for the carrier frequency $f_c = 800$ MHz.	112
Table B.3	Estimated RAM requirements for the effective channel coefficient $H_{\tilde{m},\tilde{k}}(\mu, \kappa)$ calculation according to (3.8) with $K = 256$ and $T = T_{\text{LTE}}$	113

SCIENTIFIC CAREER

Name	Martin Fuhrwerk
Date of birth	17.02.1982
Working Experience	
since 01/2011	<p>Research assistant and PhD student: Institute of Communications Technology at Leibniz Universität Hannover</p> <p>Research in the field of system adaptivity to mobile communication channels and coexistence for FBMC with OQAM subcarrier modulation (FBMC-OQAM) modulation schemes</p> <p>Research in the field of adaptive predistortion of high power amplifiers</p>
since 01/2009	<p>Senior Development Engineer and Project Management: “Embedded Software & Protocols” Department at Signalion GmbH, Dresden</p> <p>Development of testing-solutions for mobile communication networks with focus on 3rd Generation Partnership Project (3GPP) Long-Term Evolution (LTE)</p> <p>Project management and technical coordination in the area of layer 2 implementation</p> <p>Elaboration of design and execution planning of the layer 2 implementation with focus on Medium Access Control (MAC) layer and Radio Link Control (RLC) layer</p> <p>DSP implementation, integration and test in the area of 3GPP LTE Layer 2 and Layer 1</p>

since 04/2007 Development Engineer: "Embedded Software & Protocols" Department at Signalion GmbH, Dresden

Development of testing-solutions for mobile communication networks with focus on 3GPP LTE

DSP implementation, integration and test in the area of 3GPP LTE Layer 2 and Layer 1

Teaching Experience

since 10/2015 Stand-in lecturer for "Signals and systems"

since 10/2011 Exercises on "Signals and systems"

Lab exercises on "Physical layer transmission techniques"

Supervision of 7 student thesis (Master, Bachelor, Student project)

Education

10/2001 - 02/2007 Studies: Electrical engineering at Technische Universität Dresden

Diploma thesis at the Vodafone Chair Mobile Communications Systems at the Communications Laboratory at Technische Universität Dresden

Publications & Patents

3 journals, 1 book contribution and 14 conference publications

2 patents granted and 2 additional patent applications filed

PUBLICATIONS

JOURNAL ARTICLES

- [J1] M. Fuhrwerk and J. Peissig. "Capacity Gains for Single- and Multi-User CAW in FBMC-OQAM Systems." In: *IEEE Commun. Lett.* 22.1 (2018), pp. 61–64. DOI: 10.1109/LCOMM.2017.2761387.
- [J2] M. Fuhrwerk, S. Moghaddamnia, and J. Peissig. "Scattered pilot-based channel estimation for channel adaptive FBMC-OQAM systems." In: *IEEE Trans. Wirel. Commun.* 16.3 (Mar. 2017), pp. 1687–1702. ISSN: 1536-1276. DOI: 10.1109/TWC.2017.2651806.
- [J3] S. Moghaddamnia, A. Waal, M. Fuhrwerk, C. Le, and J. Peissig. "On the efficiency of PAPR reduction schemes deployed for DRM systems." In: *EURASIP J. Wirel. Commun. Netw.* (Dec. 2016). ISSN: 1687-1499. DOI: 10.1186/s13638-016-0747-5.

BOOK CONTRIBUTIONS

- [B1] J. Louveaux, M. Fuhrwerk, D. Mattera, M. Renfors, and M. Tanda. "FBMC Synchronization Techniques." In: *Orthogonal Waveforms and Filter Banks for Future Communication Systems*. Ed. by M. Renfors, X. Mestre, E. Kofidis, and F. Bader. 1st. Academic Press Inc, 2017. Chap. 10, pp. 221–255. ISBN: 978-0-12-810384-5. DOI: 10.1016/B978-0-12-810384-5.00010-4.

CONFERENCE PAPERS

- [C1] M. Fuhrwerk, J. Peissig, and M. Schellmann. "On the design of an FBMC based air interface enabling channel adaptive pulse shaping per sub-band." In: *2015 23rd Eur. Signal Process. Conf. IEEE*, Aug. 2015, pp. 384–388. DOI: 10.1109/EUSIPCO.2015.7362410.
- [C2] M. Fuhrwerk, J. Peissig, and M. Schellmann. "Performance comparison of CP-OFDM and OQAM-OFDM systems based on LTE parameters." In: *2014 IEEE 10th Int. Conf. Wirel. Mob. Comput. Netw. Commun.* IEEE, Oct. 2014, pp. 604–610. ISBN: 978-1-4799-5041-6. DOI: 10.1109/WiMOB.2014.6962232.
- [C3] M. Fuhrwerk, J. Peissig, and M. Schellmann. "Channel adaptive pulse shaping for OQAM-OFDM systems." In: *2014 22nd Eur. Signal Process. Conf.* Sept. 2014, pp. 181–185.

- [C4] M. Fuhrwerk, C. Thein, and J. Peissig. "Audio quality measurements for wireless microphones in spectrum pooling scenarios." In: *2013 IEEE Int. Conf. Commun.* IEEE, June 2013, pp. 2823–2828. ISBN: 978-1-4673-3122-7. DOI: 10.1109/ICC.2013.6654968.
- [C5] M. Fuhrwerk, C. Thein, and L. Häring. "Performance comparison of CP-OFDM and OQAM-OFDM based WiFi systems." In: *Proc. 16th Int. OFDM-Workshop.* May 2011, pp. 11–15. arXiv: 1605.01434.
- [C6] C. Le, M. Fuhrwerk, M. Schellmann, and J. Peissig. "Faster than Nyquist—an enabler for achieving maximum spectral efficiency in coexistence scenarios?" In: *2015 23rd Eur. Signal Process. Conf. IEEE*, Aug. 2015, pp. 2142–2146. ISBN: 978-0-9928-6263-3. DOI: 10.1109/EUSIPCO.2015.7362763.
- [C7] C. Le, M. Schellmann, M. Fuhrwerk, and J. Peissig. "On the practical benefits of faster-than-Nyquist signaling." In: *2014 Int. Conf. Adv. Technol. Commun. (ATC 2014)*. Vol. 52. 13. IEEE, Oct. 2014, pp. 208–213. ISBN: 978-1-4799-6956-2. DOI: 10.1109/ATC.2014.7043385.
- [C8] S. Moghaddamnia, M. Fuhrwerk, and J. Peissig. "Use of Statistical Signal Properties for Adaptive Predistortion of High Power Amplifiers." In: *2018 15th Int. Symp. Wirel. Commun. Syst.* Lisbon: IEEE, Aug. 2018, pp. 1–6. ISBN: 978-1-5386-5005-9. DOI: 10.1109/ISWCS.2018.8491222.
- [C9] M. Penner, M. Fuhrwerk, and J. Peissig. "A measurement based evaluation of feedback-less MTC using FBMC-OQAM." In: *2016 Int. Symp. Wirel. Commun. Syst.* IEEE, Sept. 2016, pp. 543–549. ISBN: 978-1-5090-2061-4. DOI: 10.1109/ISWCS.2016.7600964.
- [C10] C. Thein, M. Fuhrwerk, and J. Peissig. "About the use of different processing domains for synchronization in non-contiguous FBMC systems." In: *2013 IEEE 24th Annu. Int. Symp. Pers. Indoor, Mob. Radio Commun.* 1. IEEE, Sept. 2013, pp. 791–795. ISBN: 978-1-4673-6235-1. DOI: 10.1109/PIMRC.2013.6666244.
- [C11] C. Thein, M. Fuhrwerk, and J. Peissig. "Frequency-domain processing for synchronization and channel estimation in OQAM-OFDM systems." In: *2013 IEEE 14th Work. Signal Process. Adv. Wirel. Commun.* IEEE, June 2013, pp. 634–638. ISBN: 978-1-4673-5577-3. DOI: 10.1109/SPAWC.2013.6612127.
- [C12] C. Thein, M. Fuhrwerk, and J. Peissig. "Practical Evaluation of NC-OFDM System Designs in Dynamic Spectrum Access with Narrow-Band Interference." In: *2013 Int. Symp. Wirel. Commun. Syst.* Aug. 2013, pp. 753–757.
- [C13] C. Thein, M. Fuhrwerk, and J. Peissig. "CFO estimation algorithm for OQAM-OFDM systems based on the conjugate symmetry property." In: *2012 20th Eur. Signal Process. Conf.* 2012, pp. 470–473. ISBN: 9781467310680.

- [C14] C. Thein, M. Fuhrwerk, J. Peissig, and M. Schellmann. "Opportunistic spectrum access in TVWS: A comparative coexistence study for LTE." In: *2012 IEEE Int. Symp. Dyn. Spectr. Access Networks*. IEEE, Oct. 2012, pp. 289–298. ISBN: 978-1-4673-4448-7. DOI: 10.1109/DYSPAN.2012.6478152.

PATENTS

- [P1] M. Fuhrwerk, C. Thein, J. Peissig, M. Schellmann, and Z. Zhao. "Sub-band allocation signaling in a non-contiguous multi-carrier communication system." WO 2016 015782. Feb. 2016. published.
- [P2] S. Moghaddamia, C. Thein, M. Fuhrwerk, and J. Peissig. "Verfahren und System zur Übertragung von Daten in einem Erdbohrloch sowie mobile Einheit und Basiseinheit hierzu." DE 10 2012 109 556. Aug. 2014. issued.
- [P3] M. Schellmann, Z. Zhao, C. Thein, and M. Fuhrwerk. "Method and apparatus for accessing a wireless network." WO 2018 050214. Mar. 2018. published.
- [P4] C. Thein, M. Fuhrwerk, J. Peissig, M. Schellmann, and Z. Zhao. "Filterbank-based multicarrier transmitter for transmitting a multicarrier signal." WO 2014 198346. Feb. 2017. issued.